

# Dissertation

submitted to the

Combined Faculties of the Natural Sciences and Mathematics  
of the Ruperto-Carola-University of Heidelberg, Germany

for the degree of

Doctor of Natural Sciences

Put forward by

**Diplom-Physiker Jochen Tackenberg**

born in: Dinslaken, Germany

Oral examination: April, the 22nd, 2013



---

---

# Early Stages of High-Mass Star Formation

---

---

Referees:           Priv.-Doz. Henrik Beuther  
                          Priv.-Doz. Simon Glover



# Abstract

This thesis is dedicated to the formation of high-mass stars. In particular, we are interested in the initial conditions that allow massive stars to form. Therefore, we first examine the very initial stage of massive star formation.

Based on a statistical survey study over  $20 \text{ deg}^2$  from mid-infrared to sub-millimeter wavelengths, we show that dense and massive starless clumps exist. Assuming that they will form stellar clusters instead of single objects, we estimate their lifetime to be between 15 kyr and 60 kyr.

In order to understand such short lifetimes, we investigate the large-scale dynamical structure of high-mass star-forming regions. Using  $\text{N}_2\text{H}^+$  observations we find smooth large-scale velocity gradients in a number of filaments, which are consistent with gas flowing along the filament. Analyzing  $\text{HCO}^+$  and  $\text{H}^{13}\text{CO}^+$  spectra, we find global supersonic gas infall onto a few regions.

To understand whether the dynamics of an expanding HII region can trigger star formation, we select a starless clump located on the rim of a bubble which is infrared-dark up to  $160 \mu\text{m}$ . In a multi-wavelengths approach we search for imprints of the bubble on the gas. While an expanding HII region might favor the formation of high-mass stars, we find no evidence that it triggers the collapse.

In summary, this thesis emphasizes that high-mass star formation is a fast and dynamic process.

# Zusammenfassung

Diese Doktorarbeit untersucht die Entstehung massereicher Sterne. Unseren Fokus legen wir auf die Frühstadien schwerer Sterne, und die Bedingungen, unter denen diese entstehen können.

Zuerst identifizieren und charakterisieren wir das Vorstadium massereicher Sternentstehung, die sternlosen und dichten Klumpen. Wir zeigen, dass dieses Vorstadium existiert, aber eine sehr begrenzte Lebenszeit von nur 15 kyr bis 60 kyr hat.

Diese kurze Lebenszeit weist auf eine dynamische Strukturentwicklung hin. Mit Hilfe von  $\text{N}_2\text{H}^+$  Beobachtungen innerhalb verschiedener massereicher Sternentstehungsregionen untersuchen wir deren Kinematik. Wir finden Geschwindigkeitsgradienten, die sich mit Gasflüssen entlang der Filamente erklären lassen. Ausserdem zeigen wir, dass auf einige Regionen weiteres dichtes Gas einfällt.

Um herauszufinden, ob sich ausdehnende HII Regionen ebenfalls Sternentstehung anstoßen können haben wir einen sternlosen Klumpen ausgewählt und untersucht. Mit Hilfe von Daten verschiedener Wellenlaenge zeigen wir zunächst, dass er keine Punktquelle enthält und sich auf dem Rand einer HII Region befindet. Danach suchen wir nach Anzeichen, die auf eine Wechselwirkung zwischen HII Region und sternlosem Klumpen hinweisen. Sich ausdehnende HII Regionen könnten die Entstehung massereicher Sterne begünstigen, wir finden aber keine Hinweise dafür, dass der Kollaps dadurch angestoßen wird.

Mit unseren Resultaten zeigen wir, dass die Entstehung massereicher Sterne ein schneller Prozess ist, an dem der gesamte Klumpen beteiligt ist.



# Contents

<b>Contents</b>	<b>iii</b>
<b>1 Introduction</b>	<b>1</b>
1.1 Low-mass star formation . . . . .	1
1.2 High-mass star formation . . . . .	2
1.3 Clump and cloud formation - a dynamical evolution . . . . .	3
1.4 The onset of star formation . . . . .	4
1.5 Rareness of high-mass star-forming regions . . . . .	5
1.6 Observations of high-mass star-forming regions . . . . .	5
1.7 Observations used in this thesis . . . . .	7
1.8 Subject of the thesis . . . . .	8
<b>2 A search for starless clumps</b>	<b>11</b>
2.1 Introduction . . . . .	11
2.2 Employed data . . . . .	12
2.3 Classification . . . . .	13
2.3.1 Clump extraction . . . . .	13
2.3.2 Identification of starless clumps . . . . .	16
2.3.3 Limitations and observational biases . . . . .	16
2.3.4 Verification of classification by comparison to other tracers and studies	18
2.4 Distance independent results . . . . .	21
2.4.1 Results based on the classification . . . . .	21
2.4.2 Column densities . . . . .	22
2.5 Distances . . . . .	24
2.6 Masses and clump mass function . . . . .	26

2.6.1	Masses . . . . .	26
2.6.2	Observational biases for clumps on the far side . . . . .	27
2.6.3	Clump-mass function (CMF) . . . . .	28
2.7	Lifetimes . . . . .	30
2.7.1	Mass of the most massive star . . . . .	30
2.7.2	Lifetime of clumps . . . . .	31
2.8	Discussion . . . . .	32
2.8.1	Discussion of the clump-mass function . . . . .	32
2.8.2	Discussion of the lifetimes . . . . .	33
2.8.3	Comparison to other surveys . . . . .	34
2.9	Conclusion . . . . .	35
2.10	A full classification - the absolute time scales in high-mass star formation . . . . .	36
2.10.1	Tracers of ongoing star formation . . . . .	36
2.10.2	An attempt of a full classification . . . . .	37
2.10.3	A classification based on the far-IR properties . . . . .	39
2.10.4	Discussion of the attempt of a full classification . . . . .	41
<b>3</b>	<b>Kinematics in high-mass star forming regions</b>	<b>45</b>
3.1	Introduction . . . . .	45
3.2	Observations and analysis . . . . .	46
3.2.1	EPoS - A <i>Herschel</i> Key Project . . . . .	46
3.2.2	Nobeyama 45m observations . . . . .	47
3.2.3	MOPRA observations . . . . .	48
3.2.4	Dust continuum . . . . .	48
3.2.5	$N_2H^+$ hyperfine fitting . . . . .	49
3.2.6	Identification of dust peaks . . . . .	50
3.2.7	Abundance ratio . . . . .	51
3.3	Morphology of the dense gas . . . . .	51
3.3.1	Comparing integrated $N_2H^+$ and dust continuum emission . . . . .	53
3.3.2	$N_2H^+$ abundance . . . . .	54
3.3.3	The large scale velocity structure of clumps and filaments . . . . .	60

3.3.4	The $\text{N}_2\text{H}^+$ linewidth in context of young PACS sources and column density peaks . . . . .	62
3.4	Discussion of $\text{N}_2\text{H}^+$ dense gas properties . . . . .	65
3.4.1	Dense clumps and cores . . . . .	65
3.4.2	Abundance ratios . . . . .	66
3.4.3	Signatures of overlapping dense cores within clumps . . . . .	67
3.4.4	Accretion flows along filaments? . . . . .	68
3.4.5	Discussion of the linewidth distribution . . . . .	74
3.5	Infall and outflow signatures . . . . .	76
3.5.1	Comparing the $\text{HCO}^+$ self-absorption to $\text{H}^{13}\text{CO}^+$ . . . . .	76
3.5.2	Discussion of the global infall . . . . .	79
3.6	Conclusions . . . . .	79
<b>4</b>	<b>Triggered star formation?</b>	<b>81</b>
4.1	Introduction . . . . .	81
4.2	Description and implications of observations and data . . . . .	84
4.2.1	The cold dust tracing the molecular hydrogen, ATLASGAL . . . . .	84
4.2.2	IRAM 30 m observations . . . . .	84
4.2.3	The large scale cloud complex in HI, VGPS . . . . .	85
4.2.4	A large-scale view of the molecular cloud, GRS . . . . .	85
4.2.5	The stellar component of the complex, UKIDSS, GLIMPSE and MIPS GAL . . . . .	86
4.2.6	The peak of the SED, HiGal . . . . .	87
4.2.7	The ionized gas, MAGPIS and SHS . . . . .	87
4.3	Results . . . . .	87
4.3.1	A massive IRDC in the vicinity of a bubble . . . . .	87
4.3.2	Disentangling the spatial relations of G18.93 and EGO G19.01 . . . . .	88
4.3.3	Details and aspects of the G18.93 complex . . . . .	89
4.3.4	The bubble . . . . .	93
4.3.5	The photon-dominated region: a layered structure . . . . .	95

4.4	Imprints of triggering? Discussing the interaction between G18.93/m and the expanding HII region . . . . .	96
4.4.1	Comparison of G18.93/m with typical high-mass starless clumps . . .	97
4.4.2	The photon dominated region: a layered structure . . . . .	98
4.4.3	The temperature distribution . . . . .	99
4.4.4	Does the HII region change the shape of the IRDC? . . . . .	100
4.4.5	Imprints of the shock in the dense gas? . . . . .	101
4.5	Conclusion . . . . .	103
<b>5</b>	<b>Summary, conclusion, and outlook</b>	<b>105</b>
5.1	Summary . . . . .	105
5.2	Conclusion . . . . .	107
5.3	Outlook . . . . .	108
	<b>Bibliography</b>	<b>111</b>
<b>A</b>	<b>Supplementary material for Chapter 'Starless clumps'</b>	<b>120</b>
A.1	Errors and uncertainties . . . . .	120
A.2	Full table of starless clumps . . . . .	121
A.3	Omitted regions . . . . .	129
A.4	Stamps of starless regions . . . . .	129
<b>B</b>	<b>Supplementary material for Chapter 'Kinematics of high-mass star-forming regions'</b>	<b>144</b>
B.1	Description of the linewidth distribution . . . . .	144
B.2	Parameter maps of omitted regions . . . . .	146
B.2.1	Nobeyama 45 m data . . . . .	146
B.2.2	MOPRA data . . . . .	147
B.3	MOPRA data: Comparing integrated intensities of 5 chemical species . . .	147
<b>C</b>	<b>Co-authored papers</b>	<b>154</b>
C.1	The earliest phases of star formation - A Herschel key project. The thermal structure of low-mass molecular cloud cores . . . . .	154
C.2	G048.66-0.29: Physical State of an Isolated Site of Massive Star Formation	155

C.3	ATLASGAL - compact source catalogue: $330^\circ < l < 21^\circ$ . . . . .	155
C.4	The Earliest Phases of Star Formation (EPoS): a Herschel key program. The precursors to high-mass stars and clusters . . . . .	156
C.5	Multiple episodes of star formation in the CN15/16/17 molecular complex .	157
C.6	Galactic Structure Based on the ATLASGAL $870\ \mu\text{m}$ Survey . . . . .	158
C.7	The onset of high-mass star formation in the direct vicinity of the Galactic mini-starburst W43 . . . . .	158
<b>D</b>	<b>List of Figures</b>	<b>160</b>
<b>E</b>	<b>List of Tables</b>	<b>168</b>



# Chapter 1

## Introduction

Massive stars undoubtedly play a crucial role throughout their whole lifetime for the physical and chemical processes of the whole universe. On the largest scales they regulate and shape entire galaxies, but also emit the only observable light besides radiation from active galactic nuclei (AGN) from distant galaxies. On the smallest scales, rare isotopes in meteorites in the solar system suggest that a super nova might have triggered the formation of the sun (Gritschneider et al., 2012). In between, their luminous radiation at all wavelengths, massive jets and outflows, and their highly energetic final stages of evolution affect their direct vicinity, as well as the larger-scale environment. Therefore, massive star formation needs to be understood if we wish to make progress in our understanding of processes on all scales.

Tremendous progress has been made in understanding high-mass star formation within the last decade (cf. reviews by Beuther et al. 2007 and Zinnecker & Yorke 2007). Nevertheless, despite their importance there is still no consistent scenario describing how massive stars form, nor is the impact of massive stars on their environment fully understood. To improve on that situation, this thesis is dedicated to the early evolutionary phases in high-mass star formation.

In the following we will use high-mass or massive stars synonymous for all stars with masses larger than  $8 M_{\odot}$ .

### 1.1 Low-mass star formation

At the end of the 20<sup>th</sup> century a picture on the formation of low-mass stars emerged on the basis of both analytical, observational, and numerical work. In the classical picture, described by Shu (1977) and Shu et al. (1987), density fluctuations in molecular clouds provide seeds for the gravitational formation of slowly-rotating cores. Such cores have masses on the order of  $1 M_{\odot}$  -  $10 M_{\odot}$  and sizes of  $\sim 0.1$  pc. Once a core becomes gravitationally unstable and starts to collapse to a single, isolated object, I call it a protostar. It will collapse in almost isothermal free-fall motion until the central regions become optically thick. Then the released gravitational energy cannot be radiated away efficiently any more. The gas heats up, and the internal pressure can counteract the gravitation; a hydro-static core forms. During the core contraction a disk forms due to angular momentum conservation.

Yet, the protostar has only a very small fraction of its final mass. Both protostar and disk are still surrounded by an envelope from which material continues to fall onto the system. At the same time, material gets ejected from the system in outflows. Therefore, accretion has to exceed the outflow rate. However, while accretion onto the star is believed to work via the disk, the details of e.g. how material can enter the disk, migrate inwards within the disk, or overcome the gap between disk and protostar are not fully understood. Within the protostar, further gravitational contraction will increase the temperature and eventually will allow the ignition of hydrogen burning.

However, the details of low-mass star formation are still not fully understood. Only recently, a possible paradigm change from isolated quasi-static cores to dynamic evolution of cores has occurred. The cores and envelopes are not necessarily as decoupled from their environment as previously assumed and may still interact (André et al., 2010; Hacar & Tafalla, 2011; Lee et al., 2012; Peretto et al., 2012; Tobin et al., 2012).

A similar paradigm change has emerged in high-mass star formation within the past few years. Nevertheless, while low-mass stars may still form in isolation, it seems to be clear that high-mass star formation is a highly dynamic process and occurs exclusively in dense regions in which interactions are likely.

## 1.2 High-mass star formation

As mentioned above, high-mass star formation is very important for understanding processes on all scales, within the Milky Way Galaxy and beyond. Still, there is no agreement on how massive stars form. The main issues in developing theories of high-mass star formation are:

- **How to overcome the radiation pressure barrier?** Adapting the classical picture of low-mass star formation, the core’s hydrogen burning begins once the core mass becomes larger than  $\sim 8 M_{\odot}$ . The radiation pressure might then prevent further material from falling onto the core, thus stopping accretion and halting further mass increase.
- **How to prevent massive gas reservoirs from fragmenting?** In almost all theoretical models (e.g. Bonnell & Bate, 2006; Krumholz et al., 2007; Seifried et al., 2011), density fluctuations within high-mass star-forming cores and clumps will lead to fragments, too small to form high-mass stars.

While there are several theories to tackle each problem independently (e.g. accretion via a massive disk to overcome the radiation pressure, or magnetic fields to avoid fragmentation), three main scenarios have been discussed over the last decade:

**Monolithic collapse and disk accretion** “Monolithic collapse” refers to an up-scaled version of low-mass star formation, in which the mass is accreted from a massive envelope. While the radiation pressure problem mainly originates from a symmetrically, one-dimensional treatment (Shu, 1977; Shu et al., 1987), both analytical calculations and numerical simulations have shown that two-dimensional (axis symmetric)

and full three dimensional models which include disks reduce the radiation pressure significantly. Considering the anisotropic radiation fields (“flashlight effect”, Yorke & Bodenheimer 1999) allows further accretion beyond  $8 M_{\odot}$  (Yorke & Sonnhalter, 2002). Magnetic fields, or radiation could directly prevent fragmentation. Dynamical aspects like triggering or colliding flows could allow the formation of dense cores faster than fragmentation occurs.

**Competitive accretion and runaway growth** The competitive accretion model assumes large gas reservoirs from which clusters form. Within these, higher density seeds accrete mass faster and more efficiently than others (Bonnell et al., 2004). Therefore, the more massive cores can attract more material, while other cores “starve”.

**Stellar collisions and mergers** Here, the formation of the cores and protostars is identical to the formation of low-mass objects, but in a strongly clustered mode (Bonnell et al., 1998). If the stellar densities and cross sections are high enough, cores and young stars merge and build more massive objects.

In the last few years a more dynamical formation scenario has emerged (Heitsch et al., 2009; Smith et al., 2009; André et al., 2010; Schneider et al., 2010; Hartmann et al., 2012; Smith et al., 2012). High-sensitivity observations from *Spitzer* and *Herschel* suggest that both low- and high-mass star-forming regions are embedded in large complexes and filaments. Observations of gas dynamics show large-scale flows and steady feeding of the clumps. High-resolution interferometric observations resolve individual centrally-condensed dense objects, but find no isolated cores decoupled from their harboring clumps. Within those cores, a mixture of “monolithic collapse” and “competitive accretion” takes place, in which the collapsing objects form disks and drive outflows, and at the same time still accrete dynamically onto the disk from its surrounding gas.

### 1.3 Clump and cloud formation - a dynamical evolution

Independent of the actual star formation scenario, there is agreement that forming stars not only requires large gas reservoirs, but also high (column) densities. In addition, high-mass stars do not form in isolation, but in dense clusters, and the star-formation efficiency is not 100% (in the sense that not all gas will end up in stars). Therefore, the available gas mass needs to be even larger.

The build-up of structures massive and dense enough to harbor high-mass star formation is not fully understood, either. However, most mass within our Galaxy resides in the diffuse interstellar medium. Therefore, before star formation begins, the diffuse gas of the interstellar medium needs to be collected into dense and massive structures. Independent of whether gravity, large-scale flows, large-scale turbulence, etc., is the driving force, the interstellar medium becomes compressed and forms first atomic, and then molecular clouds.

For the formation of molecules within clouds, high column densities are required ( $\sim 1 \times 10^{21} \text{ cm}^{-2}$ , McKee & Ostriker 2007; Wilson et al. 2009) to shield the dissociating UV radiation of nearby stars. The shielding is provided by a layer of atomic gas

surrounding molecular clouds. Molecular clouds are entities with sizes between 5 pc and 100 pc, average densities of around  $10^3 \text{ cm}^{-3}$  (Ferrière, 2001; Bergin & Tafalla, 2007), and their temperatures are relatively cold (between 10 K to 20 K). The cool temperatures are important for the existence of molecules as well, since at higher temperatures collisions may dissociate the molecules.

Already during the mass assembly of the larger scale cloud, turbulence and/or density fluctuations start building dense sub-structures. These are often referred to as clumps (Williams et al., 2000) and have sizes between 0.3 pc to 1.0 pc. Their average particle densities of  $10^4 \text{ cm}^{-3}$  to  $10^5 \text{ cm}^{-3}$  are a factor 10-100 larger than the average densities for entire clouds.

Note that both entities are not necessarily gravitationally bound, and can be transient objects that dissolve, without forming stars. However, even if they are not gravitationally bound they might contain dense and bound, sub-structure capable of forming stars.

The star forming structures within clouds and clumps are often called cores. They are gravitationally bound, have typical sizes below 0.1 pc, and even higher densities ( $> 10^5 \text{ cm}^{-3}$ ). Their masses range from a few  $M_{\odot}$  to several tens of  $M_{\odot}$  (Bontemps et al., 2010b). In this picture, originally introduced by Williams et al. (2000) and adopted by Beuther et al. (2007), while cores form individual stars or multiple systems, clumps form entire clusters.

## 1.4 The onset of star formation

As explained above, clumps and cores form likely in a dynamical process, with mass being constantly added. At some point, the densities might be high enough to form massive stars, but star formation has not had time to begin, yet. These clumps are cold,  $\sim 15 \text{ K}$ , and have low luminosities. Once individual cores within dense clumps start to collapse, their gravitational energy begins to be released. The cores are still optically thin, thus the energy can be radiated away efficiently. Only when the cores become optically thick, their temperatures rise, the pressure slows down the collapse and will eventually stop the free-fall contraction of the material. At the same time, the radiation produced increases over time, and becomes detectable at shorter and shorter wavelengths.

An alternative tracer of ongoing star formation within dense clumps is shocked gas. While most other tracers are sensitive to more evolved objects, shocked gas traces outflows which are produced throughout the entire star-formation process, both in low- and in high-mass star formation.

Clumps without a detected infrared counterpart are often referred to as “infrared quiet”. If, in addition, no classical shock tracer is present, those clumps are often called “starless”. However, for observational reasons (see 2.3) I call all clumps without mid-IR counterpart starless.

## 1.5 Rareness of high-mass star-forming regions

One important aspect of the studies of high-mass star formation are the time scales involved. While the lifetime of giant molecular clouds can be several million years, once the clumps and cores become dense enough they must evolve rapidly. Both Motte et al. (2007) and (Russeil et al., 2010) estimate the lifetime of the initial phase, before star formation sets in, to be on the order of  $\sim 10^4$  yr.

The time scale for the formation of massive stars is so far unknown, but probably on the order of a few hundred thousand years (Zinnecker & Yorke, 2007). A lower limit for the formation time of massive stars is given by the free-fall time scale, which describes the gravitational collapse of a spherical object if no other forces are present. This depends only on the density, and for typical values for dense clumps ( $\rho \sim 10^5 \text{ cm}^{-3}$ ) the free-fall timescale is  $\sim 1.2 \times 10^4$  yr.

In low-mass star formation, while the onset of star formation is not as clear, the end of the formation phase is defined by the moment when hydrogen burning ignites. In contrast, high-mass stars still accrete mass after hydrogen burning has ignited. Nevertheless, lifetime estimates of massive stars usually start with the onset of hydrogen burning and range from a few million years for the most massive objects, to several tens of millions of years for  $8 M_{\odot}$  stars.

While the stellar evolution of high-mass stars is short, their number distribution is controlled by the stellar initial mass function (IMF). Empirical studies, beginning with that of Salpeter (1955), show that the number distribution of stars formed is a function of mass, following a power-law distribution,  $dN / dM \propto M^{-\alpha}$ . It has been shown that the slope of the low-mass end of the IMF is different from the high-mass regime, for which the original value of  $\alpha = 2.3$  is still valid (Kroupa, 2001; Chabrier, 2003). Although highly debated, there is observational evidence that the initial mass function is universal on most scales (for a detailed discussion see Bastian et al. 2010).

Based on the Galactic star formation rate of  $\sim 2 M_{\odot}/\text{yr}$  (Robitaille & Whitney, 2010), one can estimate that within the entire Milky Way Galaxy every  $\sim 125$  yr a star more massive than  $10 M_{\odot}$  forms. In combination with the short timescales involved, only a very limited number of regions with ongoing active high-mass star formation can be observed. Therefore, in contrast to low-mass star formation, the few observable high-mass star forming regions are relatively far away, at distances beyond  $\sim 1$  kpc.

## 1.6 Observations of high-mass star-forming regions

Due to the low luminosities of massive starless clumps, the earliest evolutionary stages of high-mass star formation were undetectable for many years. It was suspected that they are embedded within giant molecular clouds, but the most abundant constituent, molecular hydrogen is difficult to observe directly.  $\text{H}_2$  is symmetric and therefore has no permanent dipole moment, resulting in a lack of both pure rotationally and vibrationally transitions, and ro-vibrational transitions are too energetic to become populated within cold and dense molecular clouds. Thus, it is impractical as a tracer of cold dense structure.

Alternative to directly tracing the dense gas, extinction has been established as a tracer of dense clouds and clumps. Similar to the dark patches in optical images reported by Barnard (1919), both Perault et al. (1996) and Egan et al. (1998) found extinction patches in mid-IR images of the *Infrared Space Observatory* (ISO) and *Midcourse Space Experiment* (MSX), respectively, which are a result of dust absorbing the Galactic background emission. However, while the extinction patches observed by Barnard (1919) in optical images are connected to nearby low-mass clouds, the high extinction of the newly detected objects even at near- and mid-IR wavelengths led to the conclusion that they had to be of very high column density (because extinction  $A_\lambda \propto \lambda^{-2}$ ). Follow-up observations by Carey et al. (1998) established the so-called infrared dark clouds (IRDCs) as precursors of massive star formation. While they found dense gas tracers along the extinction patches, only a few objects showed tracers of ongoing high-mass star formation (Carey et al., 1998). Later, it has been shown that many of these regions contain embedded sources (Motte et al., 2007; Peretto & Fuller, 2009).

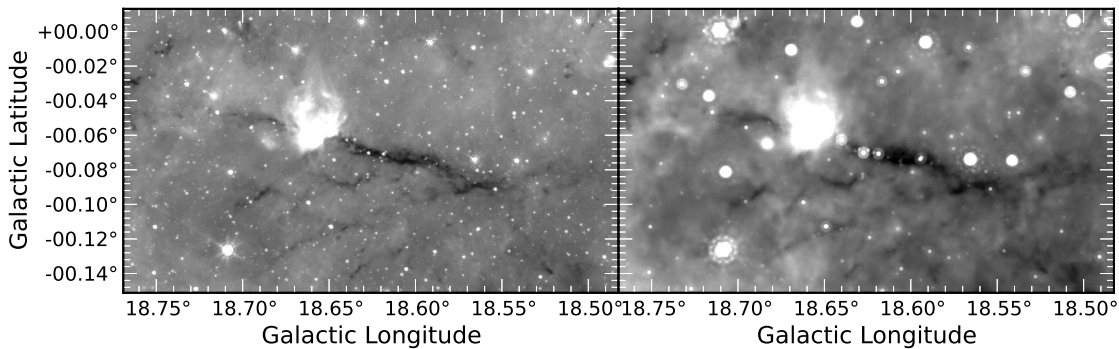


**Figure 1.1:** The GLIMPSE  $8\mu\text{m}$  and MIPSGAL  $24\mu\text{m}$  maps of IRDC 18223, named after the bright young stellar object IRAS 18223-1243. In both images, the extinction is clearly visible as dark patch in the center of the image.

The mid-IR Galactic plane surveys from MSX and Spitzer made systematic searches for IRDCs on large scales feasible, and both surveys revealed numerous new sites of ongoing massive star formation (Simon et al., 2006; Peretto & Fuller, 2009). An example of an IRDC is shown in Fig. 1.1. From east to west, IRDC 18223 absorbs the otherwise almost homogenous background emission and becomes visible as dark patch.

However, identifying IRDCs by their absorption relies on homogeneous Galactic background emission, which is not applicable in all cases. A more straight forward approach is mapping the thermal dust emission. Although only about 1% of the mass in molecular clumps is dust (Spitzer, 1978; Draine & Li, 2007), the molecular gas can be traced by the dust's thermal emission. This is visualized in Fig. 1.2. It shows the same IRDC as Fig. 1.1, but as three-color image of the two mid-IR images plus the  $870\mu\text{m}$  sub-millimeter (sub-mm) emission. The region that has been seen in absorption before is now filled by the sub-mm. Assuming that the dust emission is optically thin, it has been worked out by Hildebrand (1983) that sub-mm continuum observations can be used to estimate both the column density and mass of molecular gas. Nevertheless, this method requires the knowledge of the dust temperature, the gas-to-dust ratio, and the dust absorption coefficient. The latter depends on the dust properties such as grain size, grain mass density, and dust

emissivity index, all of which are not well known. This introduces large uncertainties on the so derived gas masses, on the order of a factor of 5 (for a discussion of the error see Sect. A.1).

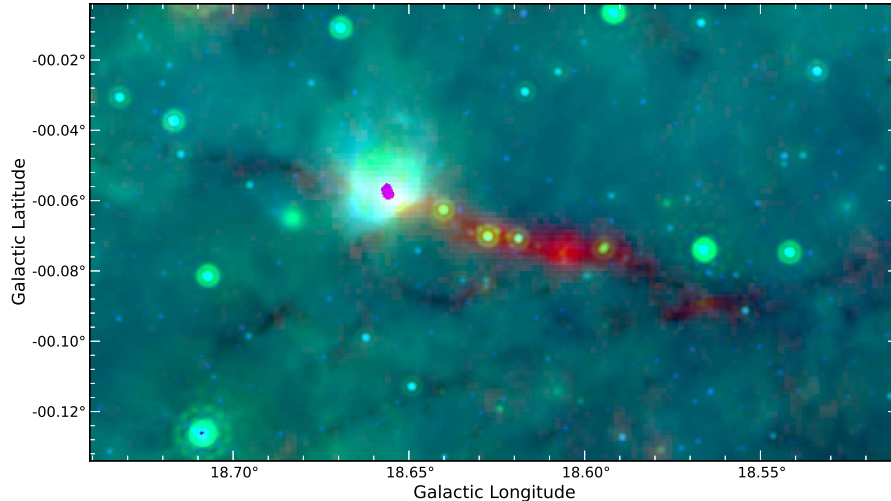


**Figure 1.2:** Three color image of IRDC 18223, with  $8\ \mu\text{m}$ ,  $24\ \mu\text{m}$ , and  $870\ \mu\text{m}$  in blue, green, and red, respectively.

The stellar content within molecular clouds and clumps can be viewed at mid-IR wavelength. Light at shorter wavelengths is absorbed by the interstellar dust (interstellar extinction) and the embedding cloud. In addition, the cold objects are not yet visible at short wavelength. In this context, surveys of the mid-IR sky by the *Infrared Astronomical Satellite* (IRAS), and MSX have provided crucial knowledge about the young protostellar objects within high-mass star-forming regions. The two infrared surveys GLIMPSE at 4 wavelength bands from  $3.6\ \mu\text{m}$  to  $8\ \mu\text{m}$ , and the MIPS GAL survey at  $24\ \mu\text{m}$ , conducted with the *Spitzer Space Telescope* (Spitzer), have exceeded all previous mid-IR surveys both in resolution and sensitivity. Therefore, they currently provide the best view of the youngest protostellar objects. Working at even longer wavelength, the *Herschel Space Observatory* (*Herschel*) sheds light onto the even earlier evolutionary stages. It works at wavelengths from  $70\ \mu\text{m}$  to  $500\ \mu\text{m}$ , but at a by far superior resolution and sensitivity compared to IRAS (e.g. at  $100\ \mu\text{m}$   $\sim 300\times$  more sensitive at a spatial resolution  $\sim 40$  times better than IRAS, Neugebauer et al. 1984; Poglitsch et al. 2010.)

## 1.7 Observations used in this thesis

In the following I will describe briefly the main surveys we utilized in this thesis. Throughout the thesis I introduce additional surveys which we incorporate to address specific questions.

## ATLASGAL

The APEX telescope large area survey of the Galaxy (ATLASGAL, Schuller et al. 2009) is a systematic survey of the Galactic plane at  $870\ \mu\text{m}$  with LABOCA (Siringo et al., 2009), covering the Galactic latitude range  $-60^\circ \leq l \leq 60^\circ$  and Galactic longitude  $b \leq \pm 1$ , with a beam size of  $19.2''$ , a pixel size of  $6''$ , and an average rms noise of below 50 mJy. This is the first survey of the full inner Galactic plane at sub-mm wavelength. A limitation one should mention is the spatial filtering. Imposed by the use of the bolometer array, all emission on scales larger than  $2.5'$  is filtered out due to technical reasons.

## GLIMPSE and MIPS GAL

The *Spitzer Space Telescope* (Spitzer) is an infrared space telescope with a 0.85 m mirror.

The Galactic Legacy Infrared Mid-Plane Survey Extraordinaire (GLIMPSE, Benjamin et al. 2003) and the MIPS Galactic plane survey (MIPSGAL, Carey et al. 2009) are *Spitzer* Legacy Programs. The GLIMPSE survey provides maps of the inner Galactic plane for  $-60^\circ \leq l \leq 60^\circ$  at  $3.8\ \mu\text{m}$ ,  $4.5\ \mu\text{m}$ ,  $5.8\ \mu\text{m}$ , and  $8.0\ \mu\text{m}$ . The resolution is  $1.7''$ ,  $1.7''$ ,  $1.9''$ ,  $2.0''$ , respectively. For GLIMPSE, a point source catalog exists containing  $\sim 5 \times 10^7$  sources. Among other criteria, the GLIMPSE source catalog requires a minimum flux of 0.6 mJy, 0.4 mJy, 2 mJy, or 10 mJy in either the 3.8, 4.5, 5.8, or  $8.0\ \mu\text{m}$  band, respectively. The IRAC pointing accuracy is better than  $1''$  and the pixel resolution is  $0.6''$ .

From MIPSGAL we used the  $24\ \mu\text{m}$  images with a resolution of  $6''$ , which have an rms noise of  $\sim 0.67$  mJy (Carey et al., 2009).

## Herschel/EPoS

The *Herschel Space Observatory* (*Herschel*, Pilbratt et al. 2010) is a far-IR and sub-millimeter satellite with imaging capabilities ranging from  $70\ \mu\text{m}$  to  $500\ \mu\text{m}$ . It has a 3.5 m mirror and was funded by the European Space Agency and NASA.

The *Earliest Phases of Star formation* (EPOS), is a guaranteed-time project. It uses the PACS (Poglitsch et al., 2010) and SPIRE (Griffin et al., 2010) instruments to image 15 isolated, low-mass objects (Stutz et al., 2010; Nielbock et al., 2012; Launhardt et al., 2013), as well as 45 high-mass regions, which are known to harbor the earliest stages of star formation (Beuther et al., 2010; Henning et al., 2010; Linz et al., 2010; Ragan et al., 2012).

## 1.8 Subject of the thesis

While almost all theories of massive star formation predict the existence of dense and massive starless clumps, previous observational studies failed to identify a significant number of such objects. It was thus concluded that star formation begins as soon as the density is high enough (Motte et al., 2007).

In the last ten years, new surveys of the Galactic plane at different wavelengths have allowed systematic studies of a broad range of phenomena connected to massive star formation. For example unbiased studies of YSOs (Allen et al., 2004; Robitaille et al., 2006; Robitaille & Whitney, 2010), Galactic star formation rates (Robitaille & Whitney, 2010), or IRDCs (Peretto & Fuller, 2009) to name a few. In particular, the ATLASGAL 870  $\mu\text{m}$  survey of the full inner Galactic plane makes it possible to search for cold, dense structures. The angular resolution of  $19.2''$  corresponds to  $< 0.3 \text{ pc}$  at a distance of 3 kpc. Therefore, it is well suited for tracing typical scales of massive star-forming clumps of  $\sim 0.5\text{-}1 \text{ pc}$ , making it possible to extend the search for starless clumps to a statistically significant portion of the Galactic plane.

In combination with the GLIMPSE and MIPS GAL surveys, we ask in Chapter 2: *Do starless clumps exist?*

Next to the clump mass function, we use our statistical approach to answer a closely-related question: *What is the lifetime of dense starless clumps?*

Using *Herschel* it has been shown that high-mass star formation takes place in large blobs and filaments of dense gas. As discussed in Sec. 1.2, a highly-dynamic picture of star formation has emerged. However, in order to constrain the clump formation scenario, kinematic observations of the dense gas are crucial. Therefore, we map a sample of high-mass star-forming regions in  $\text{N}_2\text{H}^+$ , a dense gas tracer, and study their kinematic properties in Chapter 3. For a subset of this sample, we also compare the optically-thick  $\text{HCO}^+$  emission lines to the optically-thin  $\text{H}^{13}\text{CO}^+$  emission, and obtain additional dynamical signatures of our star-forming regions.

As final step, we wish to understand whether external dynamical triggering has an effect on starless clumps. We address the question: *Do O/B stars and massive clusters trigger star-formation?* In contrast to previous studies, which mainly searched for populations of stars formed by triggering, we select a "pristine" starless clump on the edge of an expanding bubble. In Chap. 4, we conduct a multi-wavelength study, using both publicly-available survey data as well as IRAM 30 m observations of  $\text{H}^{13}\text{CO}^+$  to search for imprints of the expanding bubble on the starless clump.

Finally, a summary of the thesis and conclusions are given in Chap. 5, along with an outlook.



## Chapter 2

# A search for starless clumps in the ATLASGAL survey

This chapter has been published in A&A (Tackenberg et al., 2012a). However, our calculations of the H<sub>2</sub> column density and mass from the sub-mm ATLASGAL data are based on a wrong main beam solid angle of the APEX telescope. While we assumed a circular beam with the opening angle of the full-width half-maximum (FWHM), the correct main beam solid angle needs to be derived from the integration of a Gaussian function with FWHM of our beam. Using the corrected beam, both the gas column density (see Eqn. 2.1) and the integrated fluxes become smaller by a factor of  $\sim 1.44$ . Note, the gas mass scales linearly with the integrated flux. In addition, due to inconsistencies in the documentation we first used a beam FWHM of 18.22'', while 19.2'' is the canonical value. In total, both column densities and gas masses are overestimated by a factor of 1.6. In other words, one has to multiply all previous values by a factor of 0.63. This issue will be addressed in an erratum (Tackenberg et al., in prep.).

It is interesting to note that recent estimates of the gas-to-dust mass ratio  $R$  (see Eqns. 2.1 and 2.2) find a ratio of 154 (Draine, 2011, B. Draine, priv. communication). In contrast, we here assumed a gas-to-dust mass ratio of 100 (Spitzer, 1978; Hildebrand, 1983). If one assumes the more recent gas-to-dust mass ratio from B. Draine, it compensates the error in our column densities and mass calculations. The error then becomes less than five percent.

However, to be consistent with the assumptions we used in the original publication, we here present the values based on the correct main beam solid angle and a gas-to-dust mass ratio of 100. All subsequent quantities and the discussion have been adopted accordingly.

The results presented in Sect. 2.10 have not been published before.

### 2.1 Introduction

Independent of the actual high-mass star formation scenario (e.g. Keto, 2003; McKee & Tan, 2003; Bonnell & Bate, 2005; Commerçon et al., 2011), there is agreement that the

most massive stars form in clusters. Therefore, it is probable that we can detect an initial stage of a high-mass gas clump without any star formation signatures.

The discovery of infrared-dark clouds (IRDCs) with ISO, MSX, and Spitzer data provided an interesting sample of objects with which to characterize the earliest stages of massive star formation (e.g. Perault et al. 1996; Carey et al. 1998). The systematic study of IRDCs provided potential precursors of massive stars and allowed the characterization of their physical and chemical parameters (e.g. Simon et al. 2006; Peretto & Fuller 2009; Vasyunina et al. 2009, 2011). Although Peretto & Fuller (2009) reported that more than 30 % of the IRDCs have no IR counterparts at  $24\ \mu\text{m}$ , follow-up studies of IRDCs often revealed signs of ongoing star formation (Beuther & Sridharan, 2007; Cyganowski et al., 2008; Vasyunina et al., 2011).

All IRDC studies are biased by the variation of the background, foreground confusion, and extinction caused by variations in the dust properties. Longward of  $200\ \mu\text{m}$ , the thermal emission from dust grains in IRDCs is optically thin and can be measured at mm and sub-mm wavelengths (Hildebrand, 1983). This can be used to obtain extinction-independent mass measurements of the cold gas inside these objects.

Until recently, there were no available systematic surveys of the Galactic plane directly tracing the cold dust associated with molecular clumps. Now, the Bolocam Galactic Plane Survey (BGPS, Aguirre et al. 2011) at  $1.1\ \text{mm}$ , as well as the APEX Telescope Large Area Survey of the GALaxy (ATLASGAL, Schuller et al. 2009) at  $870\ \mu\text{m}$ , offer surveys of the Galactic plane's cold dust. Only ATLASGAL covers the full range  $l = -60^\circ$  to  $60^\circ$  of the inner Galactic plane at  $19''$  resolution.

In this paper, we present a compilation of clumps of high column density, located in a region of Galactic longitude  $10^\circ < l < 20^\circ$  and latitude  $-1^\circ < b < 1^\circ$ , showing no signs of star formation. To confirm their starless nature, we carefully examined each clump for GLIMPSE (Benjamin et al., 2003) and MIPS GAL  $24\ \mu\text{m}$  (Carey et al., 2009) sources, either of which would indicate that star formation had already started. The column density threshold we imposed on our survey is  $6.6 \times 10^{22}\ \text{cm}^{-2}$ .

After a short description of the surveys we employed (Sect. 2.2), we describe the individual steps of the classification and its limitations in Sect. 2.3. In Sect. 2.4, we present both the results of the classification and the direct clump properties and discuss the clump column densities. Using the ammonia velocities given in Wienen et al. (2012, submitted), we derived distances to  $\sim 71\ \%$  of the clumps (Sect. 2.5). Sect. 2.6 presents the clump masses and the clump mass function. Next we estimated the lifetimes of starless clumps (Sect. 2.7). In Sect. 2.8, we discuss our results and compare them to other surveys (Sect. 2.8.3). Our conclusions, in Sect. 2.9, summarizes the main results of this work.

## 2.2 Employed data

All data for this study were taken from large surveys, most of them publicly available. Clumps were identified by searching for continuum peaks at  $870\ \mu\text{m}$  in the ATLASGAL survey (Schuller et al., 2009) and then classified using both the GLIMPSE point source catalog and MIPS GAL  $24\ \mu\text{m}$  images.

In contrast to most other searches for massive prestellar clumps of high column density using extinction maps (Simon et al., 2006; Peretto & Fuller, 2009; Kainulainen et al., 2011), we used emission at  $870\ \mu\text{m}$  as a tracer of cold dust. The APEX telescope large area survey of the Galaxy (ATLASGAL, Schuller et al. 2009) is a systematic survey of the Galactic plane at  $870\ \mu\text{m}$  with LABOCA (Siringo et al., 2009). Its beam size is  $19.2''$ , the pixel size in the maps is  $6''$ , and the average rms noise of the selected maps is below 50 mJy. To obtain a statistically meaningful sample, we covered  $20\ \text{deg}^2$  on the sky, the region of Galactic longitude  $10^\circ < l < 20^\circ$  and Galactic latitude  $|b| < 1^\circ$ .

As described in Sect. 2.3.2, we extracted young stellar objects from the GLIMPSE 1 Spring '07 catalog (Benjamin et al., 2003). Among other criteria, the GLIMPSE source catalog requires a minimum flux of 0.6 mJy, 0.4 mJy, 2 mJy, or 10 mJy in either the 3.8, 4.5, 5.8, or  $8.0\ \mu\text{m}$  band, respectively, for a source to be taken into account. For the region given, we investigated more than 5.6 million GLIMPSE sources. The IRAC/*Spitzer* pointing accuracy is better than  $1''$  and the pixel resolution is  $0.6''$ . As an additional tracer of ongoing star formation, we used the MIPS GAL  $24\ \mu\text{m}$  survey (Carey et al., 2009). The rms noise of the MIPS GAL images is  $\sim 0.67\text{mJy}$  and its resolution is  $6''$ .

## 2.3 Classification

The naming of clumps in the literature refers to various physical objects. Research groups working on high- and low-mass star formation have different naming schemes for the objects named clumps and cores, including the sub-categories starless and prestellar (Enoch et al., 2008). An often used nomenclature tries to bind things to physical properties, denoting gravitationally bound objects “cores” and unbound objects “clumps” (Chabrier & Hennebelle, 2010). In this paper, we use the term clumps for all emission peaks revealed by the CLUMPFIND algorithm (Williams et al., 1994). Typically, these are massive and large enough to form massive clusters. As shown in Fig. 2.5, typical sizes derived from the effective radii of these clumps range from  $18''$  to  $70''$ . These can either be bound or unbound systems, but are assumed to be coherent in lbv space (Galactic longitude and latitude, and radial velocity, thus distance, Williams et al. 2000). In the remainder of this paper, clumps are called starless if they host no mid-IR tracers of ongoing star formation. Nevertheless, as mentioned in Sect. 2.1 and Sect. 2.3.3, many IRDCs not hosting  $24\ \mu\text{m}$  sources have been shown to host star formation using other tracers such as SiO emission. In this study, we cannot completely rule out the presence of star formation, but only present starless clump candidates. In this context, the MALT90 survey (Foster et al., 2011) will improve future classifications. However, all previous surveys searching for IR pointsources within clumps were not as sensitive as this study is. Therefore, we expect that the SiO detection rate is lower than in previous studies.

### 2.3.1 Clump extraction

To identify starless clumps, we first employed the CLUMPFIND algorithm by Williams et al. (1994) to search for dust condensations. It has been reported that CLUMPFIND is less reliable in very crowded regions (Kainulainen et al., 2009) and that the extracted clump parameters strongly depend on the distance (Smith et al., 2008). The second point

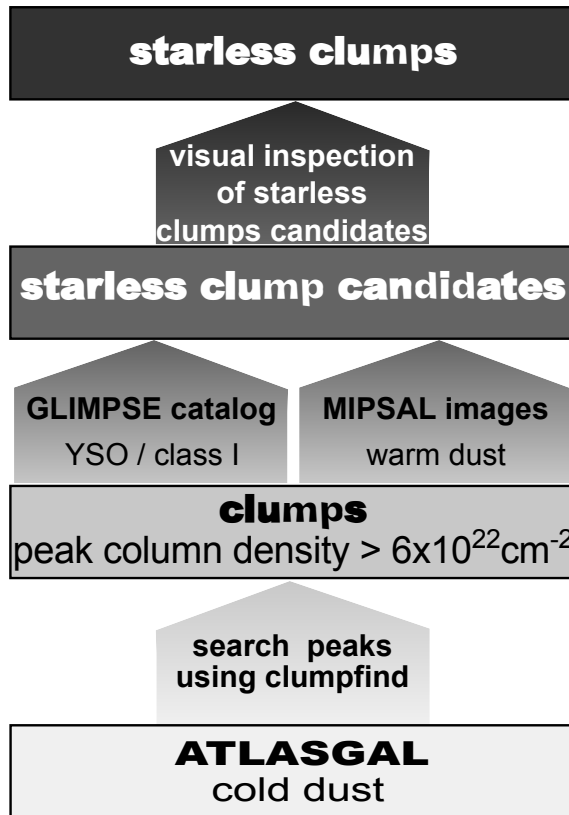


**Figure 2.1:** Schematic visualization of classification.

is unavoidable in observed data and is discussed further in Sect. 2.6.2. Nevertheless, we are interested in column-density peak positions and the associated fluxes/masses, which CLUMPFIND can extract reliably. Pineda et al. (2009) demonstrated that the exponent of the derived mass function is not very sensitive to the chosen step size.

We set the lowest detection level to  $6\sigma$ , or 0.3 Jy. The additional thresholds, 0.3, 0.4, 0.5, 0.7, 0.9, 1.3, 1.8, 2.5, 4, and 7 Jy, were chosen (1) to account for the degree of variation relative to the actual emission level and (2) to trace the structures recognized by observers. The use of non-constant intervals for the various emission levels in CLUMPFIND prevents bright clumps from being artificially sub-divided because of brightness changes that are very small relative to the flux level of the clump.

To test the robustness of the chosen thresholds, we compared the integrated clump fluxes of our clump extraction to classical  $3\sigma$  spaced thresholds as proposed in Kainulainen et al. (2009). The two right columns of Fig. 2.2 compare the flux distributions along the lines plotted in the left column. The upper row shows our clump definition, the lower row shows the clumps of a pure  $3\sigma$  spacing of the contour levels. While some regions do not differ at all, e.g. as shown by the right-most column of Fig. 2.2, the additional contours in the evenly spaced situation can subdivide large clumps into a number of smaller ones, shown by the middle column of Fig. 2.2.

While flux level spacings that are not bound to some objective criteria introduce subjectivity, Fig. 2.2 shows that the chosen levels trace structures that we call clumps. In

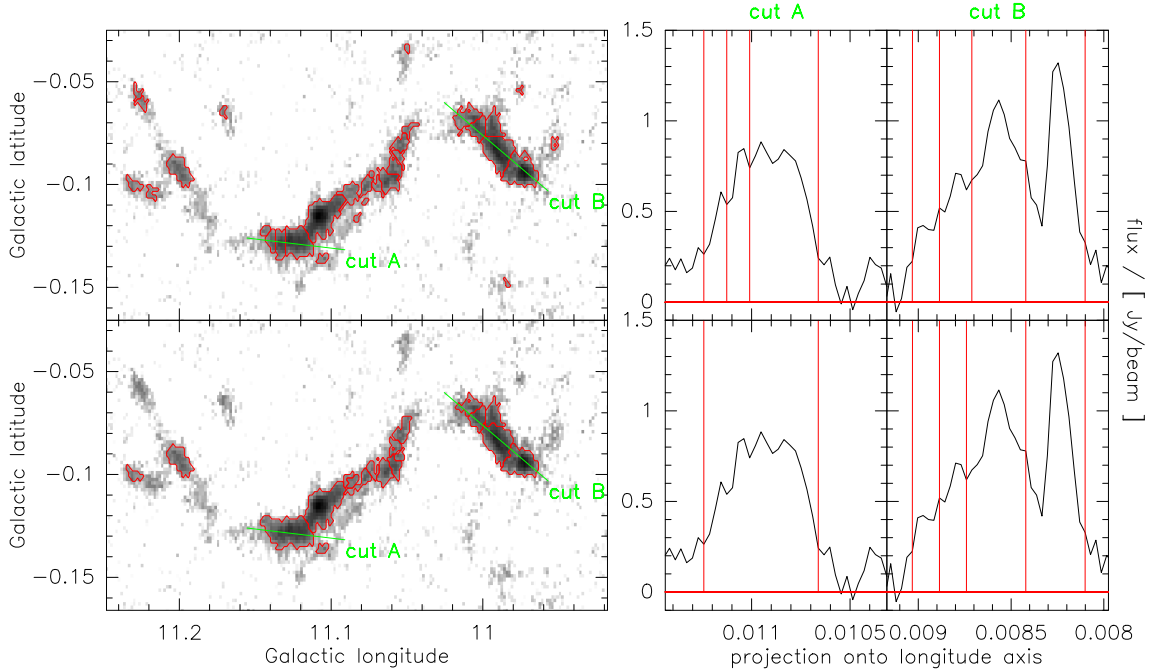


**Figure 2.2:** The figures show the clump definition as used in this paper (bottom row), compared to 'classical'  $3\sigma$  spacing contour levels (top row). While the left most column shows the ATLASGAL image of G11.11 with the clump definitions (red), the other columns show two profiles along the lines shown in the left panel ('cut A' and 'cut B'). The red lines indicate the clump borders.

addition, we compared the fluxes of our clumps to the fluxes of the  $3\sigma$  extraction and could not find an excess of bright clumps, as might have been expected. Furthermore, we compared our CLUMPFIND sources to sources found by Contreras (priv. communication) using SExtractor as described in Schuller et al. (2009). For fluxes above our thresholds, almost all sources identified by Contreras had a counterpart within our clumps with matching peak fluxes. In addition to this, the comparison shows that we identified smaller fragments of lower mass, and the integrated fluxes in our catalog are lower than the integrated fluxes of the corresponding SExtractor clumps. This assures us that we do not produce sources with artificially high fluxes.

To concentrate on potential regions of high-mass star formation we estimate the initial peak column density of the Orion nebula cluster (ONC).

Its stellar mass is about  $1800 M_{\odot}$  (Hillenbrand & Hartmann, 1998). To be consistent with estimates carried out in Sect. 2.7.1, we assumed a star formation efficiency of 30% and, therefore, estimated the initial gas mass of the ONC to be  $6000 M_{\odot}$ . As the cluster has dispersed over its lifetime, we set its initial radius to the typical radius we found for our most massive clumps, hence 0.7 pc (cf. Sect. 2.7.1). With the assumptions made and a spherically symmetric mass distribution, the initial peak column density in the ONC has been  $1.8 \times 10^{23} \text{ cm}^{-2}$ , or  $0.6 \text{ g cm}^{-3}$ . This agrees with the theoretical values found by Krumholz & McKee (2008). To avoid fragmentation in high-mass star formation, they require column densities of  $1 \text{ g cm}^{-2}$ , or  $3 \times 10^{23} \text{ cm}^{-2}$ .

As we aim to study sites of high-mass star formation we require similar densities as

expected for the Orion nebula cluster. However, the estimated peak column density for the Orion nebula cluster is only crude and an example. In addition we expect that most clumps will contract further before star formation sets in. In order not to exclude potential sites of massive star formation we ignore all clumps with a peak flux of less than 0.5 Jy, corresponding to a column density of  $6.6 \times 10^{22} \text{ cm}^{-2}$ . (For a further discussion of the derivation of column densities, we refer to Sect. 2.4.2.)

### 2.3.2 Identification of starless clumps

Although it is unclear whether high- or low-mass stars form first, starless clumps should not host young stellar objects (class I sources, YSOs). To identify clumps hosting YSOs, we searched the GLIMPSE source catalog for stars with colors similar to known YSOs and compared those to our clumps. To do so, we followed the classification given by Gutermuth et al. (2008). We used additional color criteria, given in Gutermuth et al. (2008) as well, to reject contaminating extragalactic sources and AGNs ‘that masquerade as bona fide YSOs’. Afterwards we selected objects obeying the following IRAC criteria:

$$\begin{aligned} & [4.5] - [5.8] > 1.0 \text{ OR} \\ & ([4.5] - [5.8] > 0.7 \text{ AND } [3.6] - [4.5] > 0.7). \end{aligned}$$

In addition, we required a source to be detected at  $8 \mu\text{m}$ . The identified YSOs were directly compared to the clumps and their extensions according to CLUMPFIND using the CLUMPFIND maps produced. If a YSO is located on a clump (in projection), the clump was considered as star forming and is ignored in the following. Nevertheless, at the onset of star formation, sources may be too cold to be detectable in the GLIMPSE bands, but show weak  $24 \mu\text{m}$  emission. Unfortunately, no MIPS GAL  $24 \mu\text{m}$  point source catalog has been published. Therefore, we used the STARFINDER algorithm by Diolaiti et al. (2000) to search the  $24 \mu\text{m}$  MIPS GAL images for point sources. To avoid mis-identifications we only extracted stars with a detection better than  $7\sigma$ . Again, clumps with a  $24 \mu\text{m}$  source were assumed to host stellar activity. In a last step, all remaining clumps were classified by visual inspection. Here the main focus was on  $24 \mu\text{m}$  objects that had not been identified by STARFINDER. A schematic summary of the classification is given in Fig. 2.1. Parts of M17, in which MIPS GAL is saturated due to extended emission, were omitted as well as a few additional regions. Exact positions of omitted regions are listed in the Appendix, Table A.2.

### 2.3.3 Limitations and observational biases

Although the visual verification of the classification ensures a maximum reliability, technical limitations of the data sets impose various biases. To point out the limitations of this study, next we carefully discuss the biases.

#### ATLASGAL and clump finding limitations

The spatial limitations of ATLASGAL vary with the distance and are discussed in detail in Sect. 2.6.2. The flux threshold for the clump extraction was chosen to be  $\sim 6\sigma$  or

0.3 Jy, and the higher thresholds were chosen to trace clearly recognizable structures. These threshold spacings are larger than the estimated rms. Contours in steps of the noise level are less biased and would generate more substructure, hence clumps. However, noise would, more likely, generate artificial clumps as studied by Reid et al. (2010). The chosen peak flux threshold of 0.5 Jy/beam corresponds to  $6.6 \times 10^{22} \text{ cm}^{-2}$ . In the context of massive star formation, this provides a rough lower limit for potential regions of massive star formation (see Sect. 2.3.1). Sources for which the integrated flux is less than its peak flux are considered as artificial and 28 out of 929 sources were rejected.

### GLIMPSE catalog limitations

The detection thresholds of GLIMPSE and MIPS GAL as well as the point source extraction from the GLIMPSE catalog and the color-color criteria for young sources described in Sect. 2.3.2 have a major impact on the classification. Gutermuth et al. (2008) included criteria to reject contaminating extragalactic sources, but AGB stars have similar colors to YSOs and obey the color-color criteria Gutermuth used to identify YSOs. Their contribution to the list of YSOs may be as high as  $\sim 30\%$  (Robitaille et al., 2008), rejecting potential starless clumps. Nevertheless, their likelihood of being projected onto a clump is significantly lower. Since we expect embedded YSOs to have detectable  $24 \mu\text{m}$  flux for which we will check again, the given sensitivity limits of the GLIMPSE source catalog do not influence the population of starless clumps. Additional sources in the list of YSOs as well as chance alignments could lead to an artificial rejection of clumps, but will not produce artificial starless clumps.

### MIPSGAL $24 \mu\text{m}$ limitations

The situation is different for the  $24 \mu\text{m}$  MIPS GAL images. Here the sensitivity limit is the key parameter and sources hidden in the rms can lead to misidentifications of starless clumps. The brightness of the faintest sources still detectable varies over the images with respect to their surroundings, but for the visual inspection method we estimated it to be  $\sim 1 \text{ mJy}$ . This is slightly smaller than the  $2 \text{ mJy}$  level for a  $3\sigma$  detection given in Carey et al. (2009).

For sources hidden in the dust, one may assume that all flux gets re-emitted by the dust producing a black body spectrum. From this, one can estimate the integrated luminosity of the internal source. Since the faint  $24 \mu\text{m}$  sources in question are not detected at GLIMPSE wavelengths, we used both the GLIMPSE and MIPS GAL detection limits to construct a SED of three data points at  $3.8 \mu\text{m}$ ,  $8.0 \mu\text{m}$ , and  $24 \mu\text{m}$  with  $0.6 \text{ mJy}$ ,  $10.0 \text{ mJy}$ , and  $2.0 \text{ mJy}$ , respectively. Using near- and mid-IR dust opacities from Draine & Lee (1984), we fitted a black body spectrum to the SED, with an integrated luminosity of  $1.1 L_{\odot}$  at 3 kpc, or  $27 L_{\odot}$  at 15 kpc. These luminosities correspond to main sequence stars of  $1.1 M_{\odot}$  or  $2.1 M_{\odot}$  (Siess et al., 2000). Krumholz et al. (2007) found that accretion luminosities in massive star formation reach several hundred solar luminosities very early on, excluding that a massive collapsing core could be hidden in the dust. Furthermore, there have been observations of objects that may form high-mass stars, but are not yet that luminous (Beuther & Steinacker, 2007; Bontemps et al., 2010a; Motte et al., 2010,

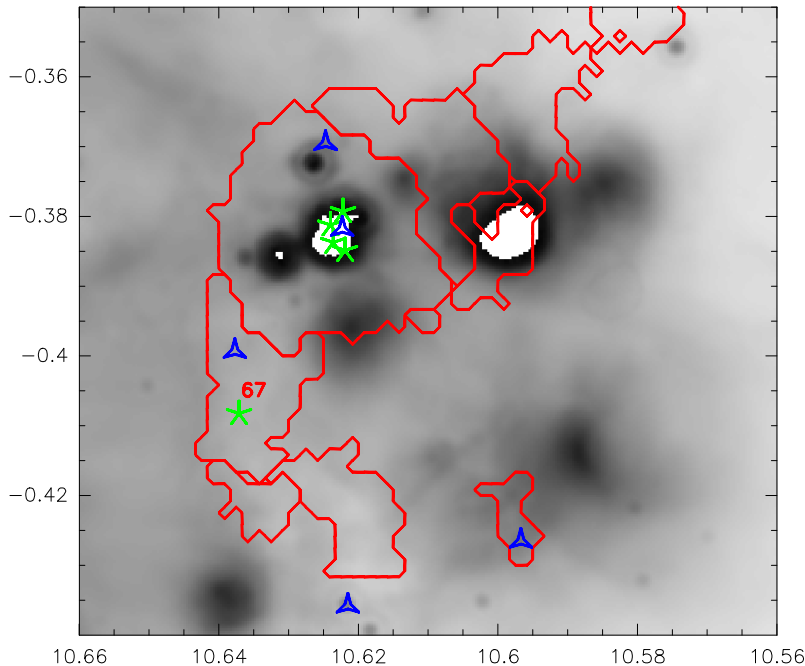


**Figure 2.3:** Clump 67 overplotted on a MIPS GAL  $24\ \mu\text{m}$  image. The clump definition are the red solid lines. Overplotted green asterisks are HII regions (Purcell & Hoare, 2010), and blue triangles are GLIMPSE Red Sources (Robitaille et al., 2008).

Ragan et al., in prep.). Nevertheless, their luminosities are still higher (on the order of several  $10 L_{\odot}$ ) than our detection limit for  $24\ \mu\text{m}$  fluxes on the far side of the Galaxy. Therefore, only low-mass objects can be hidden.

Observations using the Herschel satellite have shown that some  $24\ \mu\text{m}$  dark regions, hence starless clumps already show  $70\ \mu\text{m}$  emission (Beuther et al., 2010; Wilcock et al., 2011). As discussed in Henning et al. (2010), these sources may be either starless or protostellar. Similarly, Motte et al. (2007) and Russeil et al. (2010) find MSX and  $24\ \mu\text{m}$  dark cores, driving SiO outflows. Although Motte et al. (2007) and Russeil et al. (2010) are less sensitive at  $24\ \mu\text{m}$ , future studies will need to disentangle this situation.

### 2.3.4 Verification of classification by comparison to other tracers and studies

To test the classification, a comparison with other tracers and catalogs is helpful.

Similar to Gutermuth et al. (2008), Robitaille et al. (2008) identified Intrinsically Red Sources (R08 in the following) by applying color-color criteria to the Spitzer GLIMPSE catalog. Both sets of color criteria differ and, in addition to a large number of common sources, both catalogs also identify different sources. We take these different identifications as statistical variations that set the approximate uncertainties in the different catalogs. If we now compare the population of starless clumps to the Red Sources given in R08, this gives us a feeling for the classification statistics. As it turns out, only two clumps that we identified as starless have a *Spitzer* Red Source. With knowledge of its position,

we have been able to associate the R08 source in clump 67 with a peak in the  $24\ \mu\text{m}$  image (see Fig. 2.3). The other Red Source is supposed to be in clump 1216, at a ridge of bright continuous emission. This hampers the identification and we cannot identify a  $24\ \mu\text{m}$  counter part. Therefore, it is unclear to us whether this source is still very young.

Another test of our classification is to check the clumps for additional tracers of star formation. HII regions are a well-accepted tracer of ongoing massive-star formation and several surveys have searched the Galactic plane systematically. In this context, CORNISH (Purcell & Hoare, 2010), a Galactic plane survey at 5 GHz with the VLA in B configuration, identified more than 600 HII regions in our region of study. With their high spatial resolution, matches can be made unambiguously. We found HII regions on only three of our clumps. In clump 67 (shown in Fig. 2.3) and clump 87, no  $24\ \mu\text{m}$  source is in the vicinity of the cm emission peak. This suggests that star formation is already taking place, but so embedded that (almost) no light can escape. However, clump 505 has a very bright  $24\ \mu\text{m}$  source at the edge of the clump. This might power the HII region, which is offset by  $11''$  towards the emission peak of clump 505.

A comparison to the Green Bank Telescope HII Region Survey (GBT HRDS, Bania et al., 2010) and the Red MSX Source Survey (RMS, Hoare et al., 2004; Mottram et al., 2011) did not discover any matches.

In summary, since only three incorrect classifications have been found, all tests confirm our classification and establish its credibility. For consistency reasons, we flagged clump 67 as star forming, but kept the other two sources in our sample.

Furthermore, both pointed *Herschel* observations (e.g. EPOS, Krause et al., in prep., Ragan et al., in prep.) and the *Herschel* Galactic plane survey HiGal (Molinari et al., 2010) revealed a new population of very young sources, detectable at  $70\ \mu\text{m}$ , but yet dark at  $24\ \mu\text{m}$ . Comparing the embedded protostars found in Henning et al. (2010) to the starless clumps we found in G11.11, we conclude that one out of six starless clumps harbors an embedded source, that is invisible at  $24\ \mu\text{m}$ . This suggests that not all clumps presented here will be starless at  $70\ \mu\text{m}$ . Future studies will need to clarify the *Herschel* view of our starless clumps.

**Table 2.1:** Properties of starless clumps. The full table is available in the Appendix A.1.

Global identifier	Gal lon	Gal lat	Ra	Dec	Peak flux	R	Total flux	NH <sub>3</sub> velocity	NH <sub>3</sub> flag	HCO <sup>+</sup> velocity	ve-	HCO <sup>+</sup> flag	Near distance	Far distance	Peak umn density	col- den- sity	Near mass	Far mass	Near flag
	[°]	[°]	[°]	[°]	[Jy/beam[ <sup>00</sup> ]]		[Jy]	[km/s]		[km/s]			[kpc]	[kpc]	[10 <sup>23</sup> cm <sup>-2</sup> ]	[M <sub>⊙</sub> ]	[M <sub>⊙</sub> ]		
75	10.6075	-0.3708	272.5993	-19.9382	0.92	36	10.43	-2.9	0	—		0	-0.5	17.0	1.21	0.	37000.	1	
76	10.5958	-0.3642	272.5871	-19.9452	0.92	31	7.23	-2.9	0	—		0	-0.5	17.0	1.21	0.	26000.	1	
80	10.6858	-0.3075	272.5805	-19.8390	0.86	25	3.72	-1.5	1	-1.7		1	-0.2	16.7	1.13	0.	13000.	1	
82	10.1842	-0.4042	272.4125	-20.3249	0.85	21	2.78	10.5	0	9.4		0	1.8	14.7	1.12	110.	7500.	1	
83	10.6208	-0.4225	272.6543	-19.9515	0.83	28	5.64	-2.0	1	—		0	-0.3	16.8	1.09	0.	20000.	1	
86	10.1658	-0.3342	272.3378	-20.3071	0.81	18	2.18	10.5	0	9.4		0	1.8	14.7	1.07	87.	5900.	1	
87	10.1592	-0.3008	272.3032	-20.2968	0.81	18	2.08	10.5	0	9.4		0	1.8	14.7	1.07	83.	5600.	1	
94	10.6225	-0.5092	272.7359	-19.9918	0.78	22	3.44	-4.1	0	-3.6		0	-0.7	17.2	1.03	0.	13000.	1	
95	10.9825	-0.3692	272.7899	-19.6089	0.78	23	3.33	—	0	-0.6		1	—	16.5	1.03	0.	11000.	0	
101	10.1375	-0.3575	272.3449	-20.3432	0.75	17	2.03	10.5	0	9.4		0	1.8	14.7	0.99	81.	5500.	1	
105	10.0675	-0.4075	272.3554	-20.4286	0.75	20	2.43	—	0	11.4		1	1.9	14.6	0.99	110.	6500.	1	
106	10.1775	-0.4025	272.4075	-20.3300	0.74	13	1.11	10.5	0	9.4		0	1.8	14.7	0.98	44.	3000.	1	
111	10.1375	-0.4108	272.3947	-20.3690	0.73	17	1.79	12.9	0	—		0	2.1	14.5	0.96	97.	4700.	1	
114	10.1325	-0.4108	272.3921	-20.3734	0.72	15	1.41	12.9	0	—		0	2.1	14.5	0.95	76.	3700.	1	
118	10.1342	-0.3475	272.3339	-20.3413	0.71	22	3.08	10.5	0	9.4		0	1.8	14.7	0.94	120.	8300.	1	
119	10.5758	-0.3475	272.5613	-19.9547	0.71	17	1.85	-2.9	0	-2.6		1	-0.5	17.0	0.94	0.	6700.	1	
121	10.2992	-0.1658	272.2496	-20.1089	0.71	26	4.79	12.8	0	13.6		0	2.1	14.5	0.94	250.	13000.	1	
122	11.0575	-0.0958	272.5743	-19.4114	0.70	16	1.72	29.8	0	29.0		0	3.5	13.0	0.92	260.	3600.	1	
123	10.5775	-0.3508	272.5653	-19.9548	0.70	19	2.13	-2.9	0	-2.6		1	-0.5	17.0	0.92	0.	7600.	1	
140	10.6625	0.0825	272.2059	-19.6708	0.64	21	2.44	—	0	21.1		1	2.8	13.7	0.84	250.	5700.	0	
143	10.1958	-0.2892	272.3112	-20.2591	0.62	22	2.64	10.5	0	9.4		0	1.8	14.8	0.82	100.	7200.	1	
155	10.6325	-0.4225	272.6603	-19.9412	0.59	18	1.60	-2.9	0	—		0	-0.5	17.0	0.78	0.	5700.	1	
156	10.2475	-0.3358	272.3814	-20.2365	0.59	11	0.72	—	0	11.4		1	1.9	14.7	0.78	32.	1900.	0	
161	10.2542	-0.3392	272.3880	-20.2322	0.59	12	0.86	—	0	11.4		1	1.9	14.7	0.78	38.	2300.	1	
162	11.9139	0.7356	272.2431	-18.2597	0.59	21	2.25	24.0	0	—		0	2.9	13.5	0.78	240.	5100.	1	
167	11.0541	-0.0792	272.5571	-19.4062	0.58	19	2.05	29.8	0	29.0		0	3.5	13.0	0.76	310.	4300.	1	
168	11.9005	0.7206	272.2501	-18.2786	0.58	19	1.94	—	0	—		0	—	—	0.76	0.	0.	1	

Notes: Columns are identifier, galactic longitude, galactic latitude, right ascension, declination, peak flux, radius as calculated by CLUMPFIND, integrated flux, NH<sub>3</sub> velocity from Wielen et al. (submitted), flag indicating presence of direct NH<sub>3</sub> observation, HCO<sup>+</sup> velocity from Schlingman et al. (2011), flag indicating presence of direct HCO<sup>+</sup> observation, calculated near distance, calculated far distance, peak column density, mass calculated for the near distance, mass calculated for the far distance, flag indicating the connection to an IRDC. Negative near distances are meaningless; the velocities of those sources place them in the outer Galaxy, while we are looking towards the inner Galaxy. However, their galactic latitude and velocities are also consistent with the near 3 kpc arm at a distance of 5.2 kpc (Dame & Thaddeus, 2008). The NH<sub>3</sub> flag means that Wielen et al. (submitted) have observed a position within the clump's boundary definition. If the NH<sub>3</sub> flag is absent but a NH<sub>3</sub> velocity is given, the velocity is derived from neighboring clumps (see Sec. 2.5 for details). The same yields for the HCO<sup>+</sup> flag and HCO<sup>+</sup> observations in Schlingman et al. (2011).

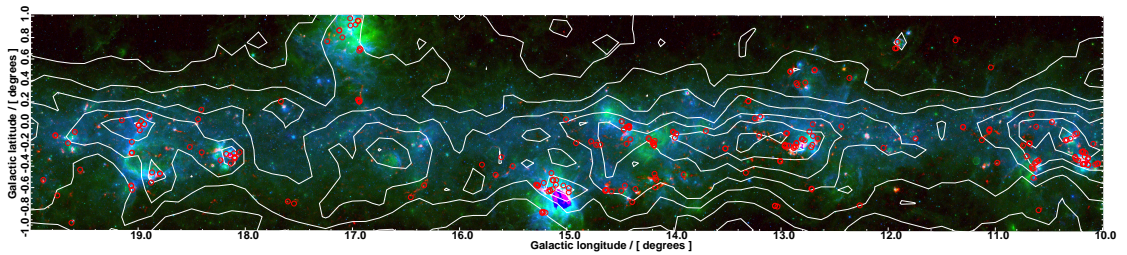


**Figure 2.4:** RGB image of the Galactic plane with Galactic latitude  $l = 10^\circ$  to  $20^\circ$  using GLIMPSE  $8\mu\text{m}$ , MIPS GAL  $24\mu\text{m}$ , and ATLAS GAL  $870\mu\text{m}$ , respectively. Overplotted are CO contours from Dame et al. (2001). Starless cores are indicated as circles.

## 2.4 Distance independent results

Using CLUMPFIND, we therefore extracted 901 clumps with peak column densities above our threshold of  $6.6 \times 10^{22} \text{ cm}^2$ . We found that 291 clumps have a Spitzer counterpart classified as YSO using the Gutermuth criteria. For 238 objects, STARFINDER identified a  $24\mu\text{m}$  (point) source in the MIPS GAL images, which had no YSO inside. During the visual inspection of the remaining 372 clumps, 103 additional  $24\mu\text{m}$  sources were found, while 59 clumps were found to be partially or completely saturated in the MIPS GAL  $24\mu\text{m}$  images. Therefore, 210 clumps, or  $\sim 23\%$ , show no signs of a heating source with the data employed. These can be considered as starless.

The large number of visually identified  $24\mu\text{m}$  sources show that this step was crucial for a reliable source catalog. Unfortunately,  $24\mu\text{m}$  point sources are often hidden in the unsteady background emission, hence algorithmic point source extraction is unable to distinguish the weakest sources. The positions of the starless clumps are shown in a three color image, Fig. 2.4, and full details are given in Table 2.1. These clumps build a sample of potential starless clumps. As we show, most of them can be considered as massive.

### 2.4.1 Results based on the classification

It can be seen from the figures presented in Appendix A.4 that almost all of the clumps are embedded in larger structures (cf. Schuller et al. 2009). These form filaments with lower density gas, indicated by the  $3\sigma$  contour. Only a few clumps seem to be isolated.

The majority of the gas is concentrated towards the Galactic plane, with a small offset towards negative latitudes. Enhanced concentrations of gas/clumps are visible towards known regions, mainly W31, W33, M17, M16, and W39 (from west to east).

A study to identify IRDCs, solely based on *Spitzer*  $8\mu\text{m}$  extinction, was conducted by Peretto & Fuller (2009). They found the fraction of starless IRDCs to be 32%. This is similar to the fraction of 23% found within this work. Nevertheless, as pointed out in Peretto & Fuller (2010), the detection of column densities via *Spitzer*  $8\mu\text{m}$  extinction breaks down at column densities larger than  $\sim 1 \times 10^{23} \text{ cm}^{-2}$ , which is close to the threshold we require as minimum column density in our study. In addition, extinction is very

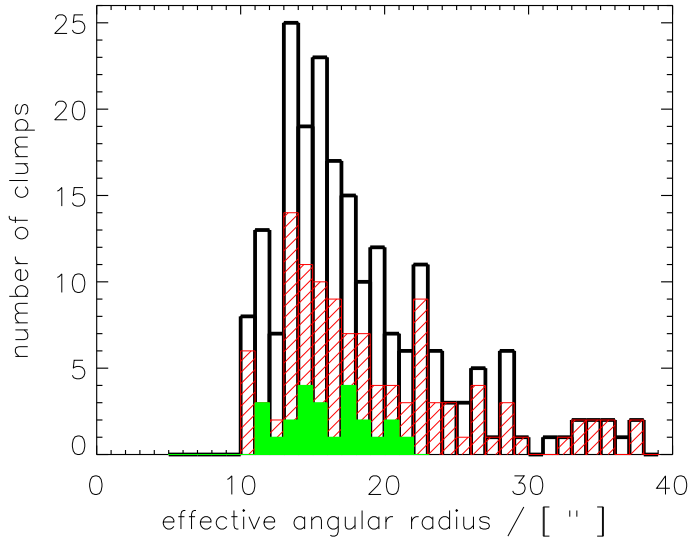


**Figure 2.5:** Histogram of the effective radius derived by CLUMPFIND for all clumps (black), for clumps with IRDC connection (hatched red area), only, and for clumps without any IRDC indication (solid green area).

unlikely to be observed on the far side of the Galaxy. Therefore, more than a quarter of the complexes have no Peretto & Fuller (2009) IRDC close by and are a completely new sample, which is likely at the far side of the Galaxy.

The CLUMPFIND algorithm calculates the effective radius of the clumps by equating the area of a theoretical circular clump to the sum of the pixels. Results for the clump radii are shown in black in Fig. 2.5. The clump radii range between 10" and 40", with an average radius of 18".

### 2.4.2 Column densities

The fluxes at the peak positions of the clumps can be used to derive a beam-averaged peak column density. Within their large  $\text{NH}_3$  survey, Wienen et al. (2012) measured the rotation temperature of 15 of our starless clumps directly. Both the mean and median temperature are  $T = 15$  K at these peak positions. This is in agreement with temperature estimates for IRDCs (Sridharan et al., 2005; Pillai et al., 2006; Vasyunina et al., 2011; Peretto et al., 2010). Since we required all clumps to be devoid of  $24\ \mu\text{m}$  emission, we assumed that all our clumps have similar temperatures. We calculated the column density of the gas via

$$N_{H_2} = \frac{RF_\lambda}{B_\lambda(\lambda, T)m_{H_2}\kappa\Omega} \quad (2.1)$$

for a gas-to-dust ratio of  $R = 100$ , where  $F_\lambda$  is the flux at the given wavelength,  $B(\lambda, T)$  the blackbody radiation as a function of wavelength and temperature,  $m_{H_2}$  the mass per  $H_2$  molecule, and  $\Omega$  the beam size. The mass absorption coefficient  $\kappa = 0.77\ \text{cm}^2\ \text{g}^{-1}$

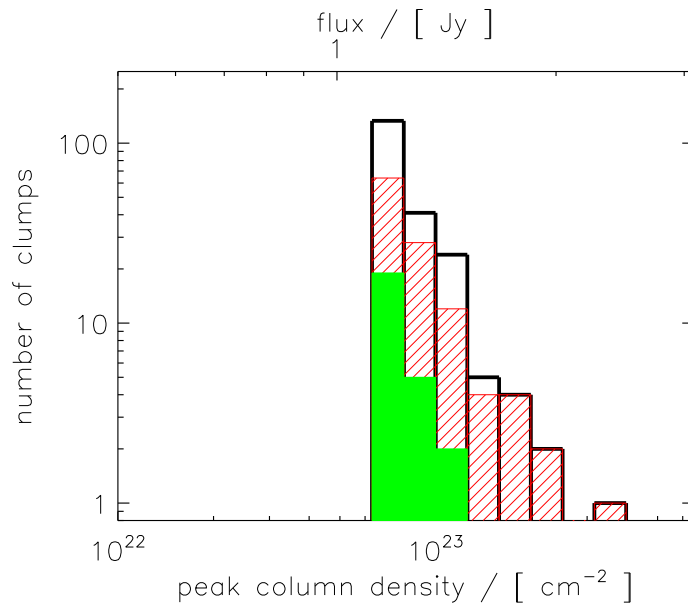


**Figure 2.6:** Logarithmic histogram plot of the column density (lower x-axis) and flux (upper axis). While the black histogram represents the full sample of starless clumps, the hatched red and filled green histograms correspond to the near and far sample, respectively. (For details, cf. Sect. 2.5.)

is adopted from the values given in Hildebrand (1983) using a dust emissivity index  $\beta = 2$  and an emissivity at  $250 \mu\text{m}$  of  $3.75 \times 10^{-4}$ . This is consistent with the value for the diffuse ISM in Ossenkopf & Henning (1994), a frequently used value for dark clouds. The calculated column densities for the starless clumps are given in table 2.1. For volume densities of  $10^6 \text{ cm}^{-3}$  and thin ice mantles, one can extrapolate  $\kappa = 1.85 \text{ cm}^2 \text{ g}^{-1}$  from Ossenkopf & Henning (1994), as, e.g., used by Schuller et al. (2009). Including their different assumption of the mean molecular weight for the ISM, column density estimates in Schuller et al. (2009) would be smaller by a factor of three.

The peak column densities vary only slightly. As shown in Fig. 2.6, 83% of the starless clumps have column densities in the range between our survey threshold  $6.6 \times 10^{22} \text{ cm}^{-2}$  and  $1 \times 10^{23} \text{ cm}^{-2}$ . Only 1 clump has a peak column density larger than  $3 \times 10^{23} \text{ cm}^{-2}$ , which corresponds to  $1 \text{ g cm}^{-2}$ . Nevertheless, the beam at a distance of 3 kpc corresponds to 0.26 pc, hence is too large to resolve individual cores ( $\sim 0.01 \text{ pc} - 0.1 \text{ pc}$ ). The given column densities are beam-averaged over large spatial scales and the actual peak column densities could be considerably larger. This effect preferentially reduces the column densities of clumps further away more significantly than those of nearby clumps, introducing an artificial difference between the clumps on this side and on the far side of the Galaxy. This difference is clearly illustrated by the red and green histograms in Fig. 2.6 for the near and far clumps, respectively (see Sect. 2.5).

To get a feeling for the small-scale peak column densities, Vasyunina et al. (2009) studied the effects of distance and telescope resolution onto the peak column density. First, they produced an artificial  $r^{-1}$  density distribution grid of 2000 AU, or 0.01 pc,

resolution. Secondly, they smoothed the grid with different Gaussian kernels to imitate observations with a  $24''$  beam at different distances. They next compared the obtained column densities to the unsmoothed peak column densities and calculated from these ratios correction factors for different distances, which resemble the peak column density seen with a linear spatial resolution of 2000 AU. The correction factors applied for a distance of  $\sim 2$  kpc start at around  $\sim 17$ , and go up to  $\sim 40$  for distances around 4.5 kpc. Even assuming a minimal correction factor of  $\sim 10$  and applying it to our sample, all clumps should contain smaller subregions of higher column densities, larger than  $3 \times 10^{23} \text{cm}^{-2}$ , following the Krumholz criterion for high-mass star formation. Nevertheless, this procedure cannot be applied to clumps at all distances. For clumps at the far side of the Galaxy in particular, the beam averages over several/many clumps and projection effects become more likely.

## 2.5 Distances

Property reviewed	Near	Far	Only far	Estimated error near / far / only far
number of clumps	115	26	9	
distance / [kpc]	3.1	12.8	16.9	0.5
average effective radius / [pc]	0.3	1.0	2.2	0.28/1.2/1.6
average mass / [ $M_{\odot}$ ]	370	3360	15900	factor of 4
median mass / [ $M_{\odot}$ ]	200	2780	12900	factor of 4
particle density / [ $\text{cm}^{-3}$ ]	$6.1 \times 10^4$	$1.4 \times 10^4$	$0.8 \times 10^4$	factor of 2

**Table 2.2:** Overview of typical clump properties for near and far clumps. The origin of the uncertainties is explained in Appendix A.1.

To determine additional physical parameters, in particular the size and the mass of the clumps, the distance is a major parameter. A Galactic rotation curve was utilized to determine distances from the clumps' radial velocities. In the following, only clumps with a distance estimate are discussed.

As the idea of this study was an unbiased survey of a large area of the sky with continuum data, a priori we have no information about the distances to the clumps found. To tackle this problem, we employed the Galactic rotation curve given in Reid et al. (2009). The necessary velocities are provided by Wienen et al. (2012, submitted). Wienen et al. (2012, submitted) conducted spectroscopic follow-up observations of  $\text{NH}_3$  towards bright peaks in the ATLASGAL survey. If no counterpart was found in Wienen et al. (2012, submitted), we used the  $\text{HCO}^+$  survey of BGPS sources by Schlingman et al. (2011).

To maximize the number of clumps to which we could assign a velocity, all clumps that lie within the same lowest significant contour were assumed to be connected. With this assumption, we were able to assign to connected clumps the same velocities as their neighbors. Incorporating all information at hand, the velocities of 150 starless clumps, or 71%, are known. The uncertainties in the velocities can be estimated by comparing the  $\text{NH}_3$  and  $\text{HCO}^+$  velocities of clumps that have both measurements. We note that 134 of all clumps (not only starless clumps presented here) were observed by both Wienen et al. (2012, submitted) and Schlingman et al. (2011). The average difference between both velocity measurements is 0.5 km/s, while their median difference is 0.3 km/s, with 2.3 km/s being the largest difference. Therefore, we estimated the velocity uncertainties to be 0.5 km/s.

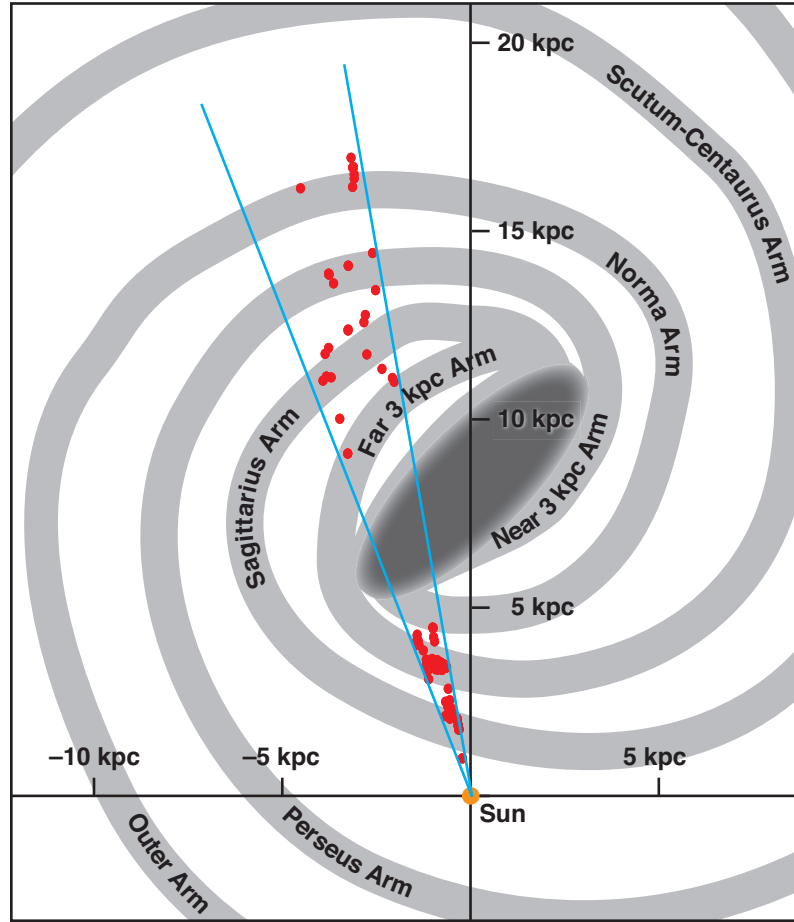


**Figure 2.7:** Artist impression of face-on view of the Milky Way by R. Hurt (SSC-Caltech) / MPIA graphic. Plotted on top are the starless clumps presented here with the distance according to the distance flag in Table 2.1.

Owing to the rotational structure and symmetry of the Galaxy, a Galactic rotation curve usually yields two distance solutions for a given direction and velocity. To solve this distance ambiguity, additional information or assumptions are required. While in studies of IRDCs it has often been argued that all sources lie at the near solution because their identification requires a bright mid-IR background, this argument could not be adopted here. The optically thin dust emission at  $870\ \mu\text{m}$  instead allowed us to identify clumps across the entire Galaxy. Nevertheless, coincidence with an IRDC favors the near solution and we used the catalog of IRDCs given in Peretto & Fuller (2009) to identify nearby objects within our sample. Although they cover a different column density range (for details see section 2.4.1), considerable overlap can still be expected. During the visual inspection of the  $24\ \mu\text{m}$  emission, additional dark patches connected to our clumps were identified and noted as IRDC. In the following, all clumps with an associated IRDC were assumed to be on the near side.

For 9 sources with velocities between  $-5\ \text{km/s}$  and  $-1\ \text{km/s}$ , the rotation curve only allows the far solution, because their near solution is meaningless (it places the source in the outer Galaxy, while we looked in the opposite direction towards the inner Galaxy).

The far solution places them in, or close to, the Norma arm at  $\sim 17$  kpc. However, as discussed in Dame & Thaddeus (2008) and Green et al. (2011), the velocities could also place them in the near 3 kpc arm at  $\sim 5.2$  kpc distance. For consistency with the adopted Galactic rotation model, we prefer the Norma solution. Future studies of these clumps could also use HI self-absorption or  $^{13}\text{CO}$  associations with well-known regions (Liszt et al., 1981) to better solve the distance ambiguity.

In summary, out of the 160 sources with velocity measurements 115 clumps are likely on the near side and 35 clumps are on the far side of the Galaxy (cf. Table 2.2 and Sect. 2.6.2). Only few starless clumps on the far side of the Galaxy have been known previously (Battersby et al., 2011), thus about a quarter of the sources are newly identified. Fig. 2.7 shows the locations of the starless clumps within the Milky Way Galaxy. One notes a clear gap between 5 kpc and 11 kpc in the source distribution, which can be explained in several ways: (1) The elliptical orbits in the bulge of the Milky Way randomize its clouds' velocities and the rotation curve places them at random distances. (2) Circular orbits close to the tangent point have very large  $\frac{d(\text{dist})}{dv}$ , hence small errors in the velocities propagate into large distance offsets. (3) The majority of the cold gas is homogeneously distributed in a molecular ring around the Galactic center with  $4 \text{ kpc} < R_{GC} < 8 \text{ kpc}$  (Solomon & Rivolo, 1989). Therefore, no clumps are expected outside that region.

## 2.6 Masses and clump mass function

### 2.6.1 Masses

Assuming optically thin emission, the mass of these clumps can be calculated from the dust continuum emission via

$$M_{gas} = \frac{Rd^2 F_\lambda}{B_\lambda(\lambda, T)\kappa}, \quad (2.2)$$

where most of the parameters are the same as defined in Sect. 2.4.2, and  $d$  is the distance. Therefore, the mass can only be calculated for sources with distance measurements. For completeness, the mass is calculated for both the near and far solutions produced by the distance ambiguity and listed in Table 2.1. Fig. 2.8 shows the calculated masses for both the near and far solutions. The solid line indicates the theoretical sensitivity limit of our source extraction. The uncertainties in the masses are discussed in Appendix A.1.

We expect the amount of dense gas per volume to be similar on both sides of the Galaxy. We can therefore conduct a consistency check by comparing the mass of the near and far population relative to the volume covered.

All clumps on the near side of the Galaxy have masses below  $5 \times 10^3 M_\odot$  (cf. Fig. 2.8, black dots), while the maximum mass within the far-clumps is a factor of about 2.5 higher than the most massive clump on the near side. The clumps furthest away at calculated distances of up to 17 kpc have even masses up to  $3.7 \times 10^4 M_\odot$ . In addition, when looking at Fig. 2.8, the total number of near objects is clearly higher than the number of far objects. To make a quantitative comparison of both populations, we estimated the common sensitivity limit for distances between 10 kpc and 15 kpc to be  $1 \times 10^3 M_\odot$ . We next calculated the volumes that we cover on the near and the far side using the scale

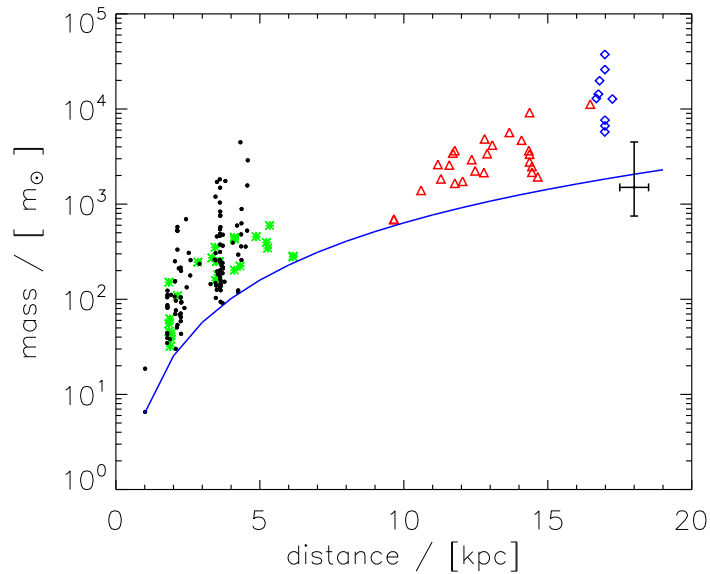


**Figure 2.8:** The mass in solar masses is plotted over the distance in kpc. The solid line indicates the sensitivity/completeness limit of our clump extraction, which depends on the distance. The black filled dots represent sources with IRDC associations, and, therefore, the near distance is plotted. The red triangles represent the far solution of sources without an IRDC for which both a far and a near solution can be calculated; in addition, the green asterisks represent the corresponding near solutions. Blue diamonds show sources with such low velocities that only a single solution can be found in the given direction. The error bar in the top right corner indicates uncertainties of a factor of two for the masses and 0.5 kpc for the distance.

height of  $\sim 40$  pc given in Bronfman et al. (2000). Adding up all masses above the far detection threshold for the near range, 0 kpc to 5 kpc, the total mass of clumps on the near side is  $\sim 18 M_{\odot}$ . Doing the same for the far range 10 kpc to 15 kpc and normalizing it to the volume covered on the near side the total mass becomes  $23 M_{\odot}$ . Both masses agree given this crude estimate, supporting the idea that, statistically, the allocation is reliable.

### 2.6.2 Observational biases for clumps on the far side

The change in resolution over the survey's depth affects the sensitivity and the recognition of substructure significantly. The  $19.2''$  beam corresponds to 0.28 pc linear spatial resolution at a distance of 3 kpc, and in contrast corresponds to 1.4 pc at a distance of 15 kpc. While the distances vary by more than an order of magnitude, the angular sizes of the extracted clumps vary by only a factor 2-3 and show no correlation with distance (cf Fig. 2.5). This results in an almost linear correlation between the physical size and the distance, which is shown in Fig. 2.9. In addition, a single, unresolved source would be 25 times fainter at 15 kpc than at 3 kpc. As indicated by the solid line in Fig. 2.8, the completeness limit changes with distance. Both effects are studied in detail in the

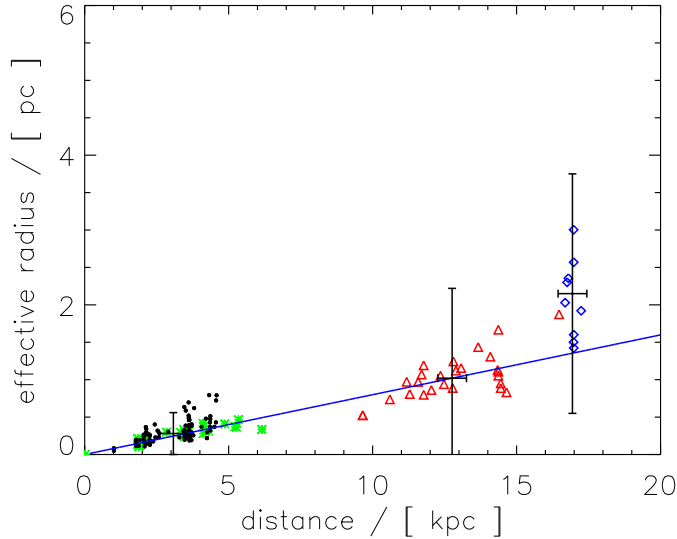


**Figure 2.9:** Effective radius in pc over the distance. Colors and symbols are as in Fig. 2.8.

following.

Taking an ATLASGAL map of  $3^\circ \times 2^\circ$ , we re-extracted all clumps with CLUMPFIND using the same thresholds as explained above and calculated their masses assuming a generic distance of 3 kpc. In addition, we convolved the same map with a Gaussian profile, emulating a resolution of  $96''$ , reducing the resolution by a factor of 5. This resembles the appearance of the same structure as seen at 15 kpc. Once again CLUMPFIND was used to search for clumps using the same parameters, but assuming a distance of 15 kpc when determining the mass.

While 90% of the total mass was recovered in the lower resolution maps, the number of clumps extracted differed significantly. In the full resolution map, 328 clumps were extracted, whereas in the lower resolution map, only 20 clumps were found. This implies that structures, which can be resolved into several clumps on the near side, cannot be resolved on the far side and that their fluxes then add up.

The volumes covered at the two distances differ by a factor of about five. This would add to the probability of chance alignment and since the dust emission is optically thin, several faint clumps within the same beam may add up and may be detectable.

Therefore, one should keep in mind that clumps discovered on the far side are slightly different types of objects.

### 2.6.3 Clump-mass function (CMF)

Mass distributions connected to stellar populations or star formation are very often compared to a power-law distribution, as first stated by Salpeter (1955) and discussed since then. The more recent study of Reid et al. (2010) even found that statistical errors al-

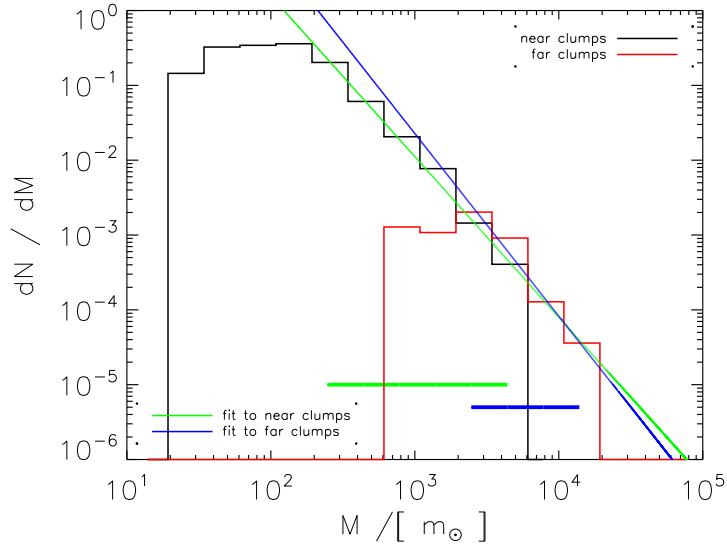


**Figure 2.10:** Clump mass function with the near population plotted in black, the far population plotted in red. Both populations' high-mass tail have been fitted, with the fitting range indicated by the thick horizontal bars at the bottom. The power law indices are fitted to  $-2.1$  and  $-2.4$  for the near and far population, respectively.

low the slope of (m)any sort(s) of astrophysical random distribution(s) to be fitted by a power-law with spectral indices similar to the Salpeter value of 2.35 within the errors. Nevertheless, a clump-mass function (CMF) is of great interest in connecting clumps to core- and star-formation efficiencies. To ensure that our data has sufficiently high quality statistics, we considered all 125 near clumps for a ‘local’ CMF and the 27 far clumps for a CMF on the other side of the Galaxy. As shown in Fig. 2.8, the completeness limit for the near and far populations is lower than  $50 M_{\odot}$  and  $1000 M_{\odot}$ , respectively. The black histogram in Fig. 2.10 represents the number distribution of the near clumps  $dN/dM$ . Owing to the completeness limits, we cannot rely on the low-mass end of the CMF below  $50 M_{\odot}$ , nor do we have sufficient statistics to determine the existence of a broken power-law distribution. We instead only consider the high-mass tail. The green line indicates a fit to the high-mass tail of the near-clump mass function, with a logarithmic slope of  $\alpha = -2.1$ . The red histogram is the far-clump mass function, fitted by the blue line of slope  $\alpha = -2.4$ . Neglecting the uncertainties on the data points, the uncertainties on the slopes calculated by the IDL routine ‘LINFIT’ are 0.1 and 0.3 for the near- and far-clump mass functions, respectively. The thick bars at the bottom indicate the fitting range. If we expand the fitting range of the near population and include lower mass bins, the slope becomes immediately shallower. If we reduce the fitting range, the slope remains constant within the uncertainties. Therefore, we believe that the fitting range is reliable and the uncertainty is reasonable. For the far range, the situation is more difficult because of the smaller number of bins. An enlargement of the fitting range to smaller bins again reduces the slope dramatically. Including the next lower mass bin does not change the result significantly, but excluding additional bins on the low mass end would steepen the slope to  $-2.8$ . This number is almost within the errors and can be entirely explained by the lower

quality statistics. Nevertheless, the fit to the far mass distribution should be interpreted with caution.

## 2.7 Lifetimes

SFR Mass of potential star	H83, diffuse ISM opacity		OH94, cold dense opacities	
	20 $M_{\odot}$	40 $M_{\odot}$	20 $M_{\odot}$	40 $M_{\odot}$
Clump-mass threshold	1065 $M_{\odot}$	2960 $M_{\odot}$	1065 $M_{\odot}$	2960 $M_{\odot}$
Number of clumps above threshold	8	1	2	0
SFR of 1 $M_{\odot}$ / yr	$1.9 \times 10^5$ yr	$6.6 \times 10^4$ yr	$4.8 \times 10^4$ yr	
SFR of 3 $M_{\odot}$ / yr	$6.3 \times 10^4$ yr	$2.2 \times 10^4$ yr	$1.6 \times 10^4$ yr	
SFR of 6 $M_{\odot}$ / yr	$3.2 \times 10^4$ yr	$1.1 \times 10^4$ yr	$8.0 \times 10^3$ yr	

**Table 2.3:** Lifetimes of starless clumps calculated for different sets of parameters. Estimates are calculated using different Milky Way star formation efficiencies for opacities for both the cold ISM (Hildebrand 1983, H83) and dense but cold regions (Ossenkopf & Henning 1994, OH94).

As discussed in Sect. 2.6.2, clumps seen at the far side of the Galaxy are a mixture of clumps seen in chance-alignment or groupings that we would identify as several structures on the near side. To form a more consistent sample, in the following we only consider starless clumps that are identified on the near side.

### 2.7.1 Mass of the most massive star

To place constraints on the lifetime of starless clumps, we first need to estimate what clump mass is required so that the final cluster can house at least one massive star.

Star-formation efficiencies on scales from clumps to stars do not have a common value but a number of studies estimate that it is 23% - 50% (Chabrier & Hennebelle 2010 and references therein). For high-mass star formation, the numbers are even more weakly constrained (5% - 50%, cf. Krumholz et al. 2007, Kuiper et al. 2010).

Following the definition given in Williams et al. (2000) and Beuther et al. (2007), these clumps will most likely form entire clusters instead of single stars. To estimate the required clump mass to form a star of given mass, one must assume a gas-to-star formation efficiency and the initial mass function (IMF) of the cluster produced.

We assume the IMF of Kroupa (2001) and normalize it to the probability that at least one star with a mass higher than 20  $M_{\odot}$  is formed. Integrating the normalized IMF over the expected mass range of stars, from 0.08 to 150  $M_{\odot}$ , the stellar mass of this cluster is on the order of 320  $M_{\odot}$ . With a star formation efficiency (SFE) of 30% (for details see next paragraph), we estimate the mass of a clump with the potential to form at least one star more massive than 20  $M_{\odot}$  to be  $10^3 M_{\odot}$ . A  $3 \times 10^3 M_{\odot}$  clump is required to form a 40  $M_{\odot}$  star (see also Table 2.3).

Since the mass distribution follows a power law, the number of clumps with masses higher than a given threshold is very sensitive to that threshold. In the picture in which these clumps form entire clusters following the IMF, the estimate of the stellar cluster

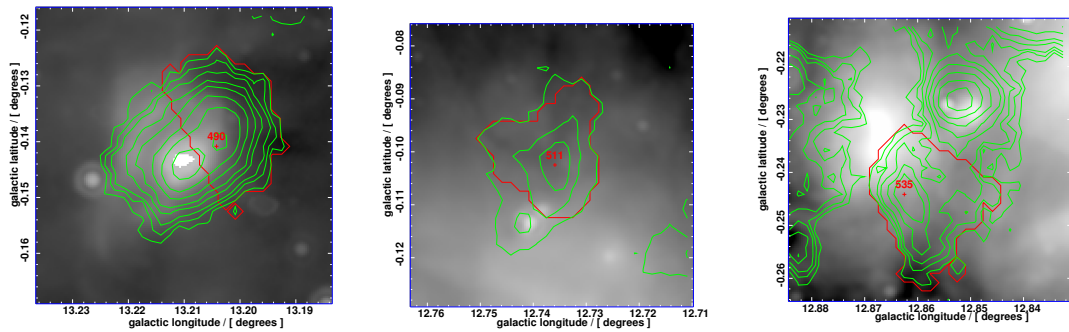


**Figure 2.11:** MIPS GAL images of the three most massive starless clumps found in this survey, with (from left to right )  $7400 M_{\odot}$ ,  $4700 M_{\odot}$ , and  $3000 M_{\odot}$ . Green contours are from ATLAS GAL, red lines mark the borders of the clumps identified by CLUMPFIND.

mass relative to the most massive star seems quite reliable. Nevertheless, the estimates of the SFE vary over a wide range (Lada & Lada, 2003; Alves et al., 2007; Johnston et al., 2009; Bontemps et al., 2010b). Here, we used the SFE given in Lada & Lada (2003), Alves et al. (2007), and Bontemps et al. (2010b) of 30%.

In the near sample derived across  $20 \text{ deg}^2$  of the sky, with this estimate only 8 starless clumps have the potential to form stars more massive than  $20 M_{\odot}$ , and only 1 has the potential to form a  $40 M_{\odot}$  star.

The MIPS GAL images of the 3 most massive clumps are shown in Fig. 2.11. As can be seen, none of the regions are isolated but all are connected to regions already containing  $24 \mu\text{m}$  sources. At the distances to these objects varying between 3.6 kpc and 4.6 kpc, their effective radii become between 0.7 pc and 0.8 pc. Therefore, their particle densities are not among the highest of our sample at only  $2 \times 10^4 \text{ cm}^{-3}$  to  $4 \times 10^4 \text{ cm}^{-3}$ . Nevertheless, these are very interesting objects and very promising in the context of massive star formation.

### 2.7.2 Lifetime of clumps

Since there is no reason to believe that the starless clumps have ages that are correlated with those of other objects in this sample, the sample should span the entire age range expected for these clumps. If this is the case, the oldest clumps will start forming stars as new and similar clumps appear. Therefore, their lifetime can be calculated by comparing the number of these clumps identified to the number of massive stars formed.

To do so, we need to **1)** extrapolate the number of starless clumps we would find in the entire Milky Way galaxy, and **2)** estimate the number/fraction of massive stars formed every year:

**1)** We assume that most star-forming gas is distributed in a ring around the Galactic center, between 4 kpc and 8 kpc Galactocentric distance (Solomon & Rivolo, 1989) with a scale height of 40 pc (Bronfman et al., 2000). Taking into account that we only consider clumps up to a distance of 5 kpc from the Sun within the direction of the survey, and above the clump mass thresholds for  $20 M_{\odot}$  and  $40 M_{\odot}$  stars, for the whole Milky Way Galaxy, we expect to identify 1043 and 223 clumps, respectively.

2) To calculate the fraction of massive stars formed every year, one needs to assume a star-formation rate (SFR) for the Milky Way. The most recent publications suggest a star formation rate of around  $1 - 2 M_{\odot}/\text{yr}$  (Robitaille & Whitney, 2010).

For a SFR of  $1 M_{\odot}/\text{yr}$ , the lifetimes of massive starless clumps become  $2 \times 10^5$  yr and  $7 \times 10^4$  yr calculated for all clumps more massive than  $10^3 M_{\odot}$ , and  $3 \times 10^3 M_{\odot}$ , respectively. For higher SFRs, the lifetimes become shorter in a linear fashion, e.g. for  $6 M_{\odot}/\text{yr}$  the lifetimes become  $3 \times 10^4$  yr and  $1 \times 10^4$  yr, respectively. Lifetimes for different parameters are summarized in Table 2.3. As we discuss in Sect. 2.8.2, we estimate the lifetime of these objects to be between  $1.5 \times 10^4$  yr and  $6 \times 10^4$  yr.

## 2.8 Discussion

### 2.8.1 Discussion of the clump-mass function

The slope of the CMF for starless clumps found in this study,  $\alpha = -2.1$ , is similar to the value of the Salpeter IMF. Nonetheless, as we study clumps that will most likely host small clusters rather than individual stars, we do not propose a one-to-one mapping to the IMF. We emphasize that not all clumps will eventually form clusters or even be transient objects. Another set of massive clumps was presented in Peretto & Fuller (2009), including a subset of clumps without MIPS  $24 \mu\text{m}$  emission. They found the mass function of IRDCs to be similar to the CO clump mass distribution (Simon et al., 2006; Peretto & Fuller, 2010) with  $\alpha = -1.7$ . In addition, they used a derivative of CLUMPFIND to search their extinction maps for structures within the IRDCs. These fragments have a rather Salpeter-like slope (Rathborne et al., 2006; Peretto & Fuller, 2010) which is then similar to our result. Although the extinction method used by Peretto & Fuller (2009) to calculate column densities of IRDCs is sensitive to a lower column density range than that of the starless clumps we present, the  $870 \mu\text{m}$  emission identifies objects similar to fragments Peretto & Fuller (2009) find in IRDCs.

The studies of Williams et al. (2004), Reid & Wilson (2005), and Beltrán et al. (2006) all targeted the more evolved high-mass protostellar objects. They found a common break in the CMF at  $100 M_{\odot}$  and fit power laws to their high-mass end with exponents between  $-2.0$  and  $-2.32$ . Although we did not attempt to fit the exact break, a break point of  $100 M_{\odot}$  or just above seems to be in good agreement with the starless CMF, but that clearly might be biased by the completeness limit close to  $100 M_{\odot}$ . However, the exponent of the near CMF agrees with all values within the errors. Thus, comparing our results to earlier studies of more evolved clumps shows that there is no evidence that the CMF of starless clumps is different from a CMF at later evolutionary stages.

Although the exponent of the CMF for clumps at the far side of the Galaxy agrees with the Salpeter value within the errors, it is larger than most other values of CMFs. Despite the fact that the uncertainty is larger and the difference could be explained by the errors, this trend might equally represent a general scale-dependent trend. Beltrán et al. (2006) distinguished between the populations at  $d < 2$  kpc and  $d < 6$  kpc and found that the exponent for the more clearly resolved population  $< 2$  kpc is shallower than for  $d < 6$  kpc. Our far population is even more distant than their sample and the far

CMF's exponent would continue the trend to steeper slopes. This could be interpreted as a general scale-dependent trend and rather a matter of resolution than of true structure.

Studies of the core mass function for low-mass star formation target significantly smaller objects. To have sufficient spatial resolution, they are typically chosen to be nearby. Nevertheless, whether they present starless cores or more evolved objects, many studies have measured power-law slopes close to the Salpeter value (Motte et al., 1998; Johnstone et al., 2000; Alves et al., 2007; Enoch et al., 2008).

### 2.8.2 Discussion of the lifetimes

The estimates of the lifetimes of starless clumps are based on the SFR of a given mass range and the number of clumps above a corresponding clump mass. Both estimates involve several assumptions, which may introduce errors.

Lifetimes are inversely proportional to the SFR. The SFR varies from  $1 M_{\odot}/\text{yr}$  (Roitaille & Whitney, 2010) to over  $4 M_{\odot}/\text{yr}$  (Diehl et al., 2006) to even larger values, but the most recent publications favor the smaller values. Nevertheless, our own survey looks at a region in the vicinity of the Galactic center for which both Rosolowsky et al. (2010) and Beuther et al. (2011) found that more dense gas is located within the inner  $l < 30^{\circ}$  of the Galactic plane. While most gas is concentrated within a molecular ring around the Galactic center at  $4 \text{ kpc} < R < 8 \text{ kpc}$  (Solomon & Rivolo, 1989), the ring does not seem homogeneous and the outer regions of that ring seem to contain less gas. This might indicate that the extrapolated numbers for the entire Galaxy might be higher than average and therefore require a higher SFR. This would reduce the lifetime estimate.

The lifetimes are also proportional to the number of clumps of given mass and when we use the extrapolated dust opacities from Ossenkopf & Henning (1994) our clump masses decrease and the number of clumps above our threshold is lower. This, in turn, reduces the lifetimes. In addition, one should keep in mind that small number statistics are involved. If one of these objects turns out to already be star-forming, the estimated lifetimes are reduced, while correcting chance alignments of mid-IR sources has the opposite effect.

Another factor contributing to the uncertainties are the star-formation efficiencies, which directly influence the mass thresholds themselves. As explained in Sect. 2.7.1, the number distribution decays as a power of the mass, which makes the lifetime estimates very sensitive to the clump mass thresholds. On the basis of the range of possible lifetimes shown in Table 2.3, we estimated the uncertainties to be one order of magnitude.

In summary, most effects seem to reduce the lifetimes. Based on these arguments, we estimate the lifetime of starless clumps to be between 15 000 yr and 60 000 yr.

For volume-averaged particle densities of  $10^5 \text{ cm}^{-3}$ , the free-fall time becomes  $\sim 1.2 \times 10^5 \text{ yr}$ , and lower densities increase this number. Therefore, the free-fall time is about a factor of two to ten longer than the lifetime we found for starless clumps, but both agree within the errors.

In good agreement with previous studies (Motte et al., 2007; Hatchell & Fuller, 2008; Motte et al., 2010), Table 2.3 shows that the estimated lifetimes of more massive clumps are smaller. Accordingly, it was expected that the lifetimes we found for starless dense

clumps are shorter than the  $3 \times 10^5$  yr found by Kirk et al. (2005) for low-mass cores.

An adequate comparison to the lifetime of high-mass starless clumps is difficult because only a few studies exist. Most deal with slightly different kinds of objects. For example, Motte et al. (2007) studied the nearby Cygnus X region and found cores that cover the same volume densities as our clumps, while their masses are significantly lower (see also Motte et al. 2010). However, they found clumps of similar mass to our objects but with lower volume densities. Using SiO as an additional tracer of star formation, Motte et al. (2007) did not find a single starless massive dense core in their sample. Therefore they proposed that the low-density starless clumps dynamically evolve into star-forming massive dense cores. Their lifetime estimate of starless massive dense cores becomes  $< 10^3$  yr.

A similar study covering more similar entities both in density and mass by Russeil et al. (2010) found one starless clump, hence they derived a statistical lifetime of  $\sim 1 \times 10^4$  yr. This almost agrees with our estimate. The difference could be caused by their inclusion of SiO as a tracer of star formation, which could reduce the number of starless clumps we found.

### 2.8.3 Comparison to other surveys

#### Comparison to the Bolocam Galactic Plane Survey (BGPS)

The Bolocam Galactic Plane Survey (BGPS) performed a systematic study of the inner Galactic plane at 1.1 mm. Although their rms across the region  $10^\circ < l < 20^\circ$  is  $\sim 25$  mJy/beam, their overall  $5 \sigma$  level is 0.4 Jy, at which they have a completeness level of 99%. Their 0.4 Jy completeness threshold converts into a column density threshold of  $\sim 6 \times 10^{22} \text{ cm}^{-2}$  over their  $31''$  beam when using the same assumptions as for our data, while their sensitivity translates into a rms of 64 mJy/beam at  $870 \mu\text{m}$  and their beam width of  $31''$ . With this column density, they found 1211 sources on the same region as we studied here.

For that data set, Dunham et al. (2011) used different point source catalogs to search within all BGPS sources for mid-infrared tracers of star formation activity. As resources they employed the Red Sources (R08, Robitaille et al., 2008), the RMS catalog, the catalog of extended green objects (EGOs, Cyganowski et al. 2008), and the full GLIMPSE catalog. The EGOs have no direct counterpart in this study, but trace shocked gas. To be truly starless, starless clumps should not contain EGOs.

Reviewing the Dunham et al. (2011) source catalog for the same region as surveyed in this study, we found that for  $\sim 70 \%$  of the sources they found neither RMS sources, R08 sources, nor EGOs.

Following a similar approach to Dunham et al. (2011) and using the identical mid-IR tracers, the R08, RMS, and EGO catalogs, for the ATLASGAL clumps, we found R08 counterparts within 163 clumps, 39 RMS counterparts within clumps without R08 sources, and 9 matches among EGOs and clumps without the previous tracers. This leaves 719, or 77%, of our ATLASGAL clumps starless. Both fractions of infrared quiet clumps are significantly larger than those of Peretto & Fuller (2009) (32%) or we found (23%) including all tracers. Even without visual inspection but including MIPS GAL

$24\ \mu\text{m}$  sources found by STARFINDER, we would have found only 42% of the clumps to be starless. These differences in our statistics from both of the latter studies can be explained by the superior sensitivity of the “by eye” source confirmation and the higher spatial resolution of the MIPS GAL survey over the MSX images.

### Comparison to PLANCK’s Early Cold Cores

That Planck’s Early Cold Core Source List (ECC) (Planck Collaboration et al., 2011) does not contain any cold sources in the region of the sky we surveyed here is apparently remarkable. However, the ECC contains only sources colder than  $T < 14\ \text{K}$  averaged over PLANCK’s beam sizes of several arc minutes. Owing to the high gas density and ongoing star formation as well as confusion, no sources are expected to be found within the Galactic plane (Planck Collaboration et al., 2011).

## 2.9 Conclusion

For the first time, we have presented a complete and unbiased sample of high-mass starless clumps on  $20\ \text{deg}^2$  of the sky. To concentrate on the actual potential precursors of massive stars, we imposed a minimum peak column density of  $6.6 \times 10^{22}\ \text{cm}^{-2}$ . From ATLAS GAL, we extracted 901 clumps across the region  $10^\circ < l < 20^\circ$  of the Galactic plane. Using the GLIMPSE source catalog and MIPS GAL  $24\ \mu\text{m}$  images, we compared clumps found at  $870\ \mu\text{m}$  to near- and mid-infrared tracers of ongoing star formation.

Neglecting clumps that are saturated at MIPS GAL  $24\ \mu\text{m}$ , we identified 210 clumps, or 23%, to be starless. Their effective radii range from  $10''$  to  $40''$ , and most of the beam-averaged peak column densities are below  $1.0 \times 10^{23}\ \text{cm}^{-2}$ . However, correcting the single-dish peak column densities to true peak column densities as discussed in Vasyunina et al. (2009) suggests that all clumps should have peak column densities above the fragmentation threshold for massive star formation of  $3 \times 10^{23}\ \text{cm}^{-2}$ , or  $1\ \text{g cm}^{-2}$ , proposed by Krumholz & McKee (2008).

For  $\sim 71\%$  of the starless clumps, we had the velocities and were able to calculate their distance. If a clump is connected to an IRDC, then we assumed a distance on the near side. We found that about a quarter of the starless clumps lie on the far side of the Galaxy and were therefore previously unknown.

We found that the masses of starless clumps on the near side range from  $5\ M_\odot$  to  $4470\ M_\odot$ , and that objects on the far side have masses between  $690\ M_\odot$  to  $11\ 000\ M_\odot$ . The different mass regimes are a consequence of our limited spatial resolution, biasing us towards detecting larger structures as a single clump on the far side, which we would resolve into several clumps on the near side. The mass distributions of the near and far populations could be fitted by power laws with slopes  $\alpha = -2.1$  and  $\alpha = -2.4$ , respectively, and agree within the errors. This shows that the mass distribution of clump populations on the near and far side of the Galaxy do not differ significantly.

Drawn from the population of clumps on the near side, we found that only 8 objects are massive enough to form clusters with stars more massive than  $20\ M_\odot$ . Only a single

starless clump has the potential to form stars even more massive than  $40 M_{\odot}$ . We estimate the minimum clump mass required to form a cluster with a  $20 M_{\odot}$  or  $40 M_{\odot}$  star to be  $10^3 M_{\odot}$  or  $3 \times 10^3 M_{\odot}$ , respectively. Since the star-formation efficiency used is an upper limit, these numbers are lower limits.

Extrapolating the numbers of massive starless clumps from our survey volume to the Milky Way Galaxy, we estimated the lifetime of the most massive starless clumps to be between  $1.5 \times 10^4$  yr and  $6 \times 10^4$  yr. To do so, we assumed a star formation rate of  $1 M_{\odot}$  to  $3 M_{\odot}$  per year for the entire Galaxy. We also discussed a possibly enhanced star formation activity within the surveyed volume and its implications for the assumed global star formation rate.

## 2.10 A full classification - the absolute time scales in high-mass star formation

In addition to determining the evolutionary time scales of the starless clumps, we extend this study to identify additional clump evolutionary stages and to derive relative time scales between them. We do so by placing each evolutionary stage in relation to the estimated absolute lifetime of the starless clumps, to establish absolute time scales for the formation of massive stars within dense clumps.

In the following I will first discuss what additional indicators and tracers of evolution we considered. Next, I describe two approaches to realize a full classification. A third approach based on auxiliary data is presented in Sect. 2.10.3. Finally, I summarize and discuss our results.

### 2.10.1 Tracers of ongoing star formation

To select starless clumps, we removed all clumps that showed either a YSO or a MIPS-GAL  $24 \mu\text{m}$  point source. While all sites of ongoing high-mass star formation should be detected at  $24 \mu\text{m}$ , the YSOs determined by the Gutermuth criteria are Class 0/1 protostars. Robitaille & Whitney (2010) have shown that their sample, selected from similar color-color criteria, consists mainly of low to intermediate mass protostars. However, since we want to focus on the formation of high-mass objects within the clumps, we need tracers of high-mass star formation for a full classification.

### Ionized gas - ultra- and hyper-compact HII regions

Two genuine tracers of ongoing high-mass star formation are ultra- and hyper-compact HII regions. Once the central object is hot enough to produce UV radiation, it ionizes its surrounding gas, and the pressure of the ionized gas leads to an expansion.

The Co-Ordinated Radio 'N' Infrared Survey for High-mass star formation, (COR-NISH, Purcell et al., 2008), of  $110 \text{ deg}^2$  of the sky, conducted VLA observations in B configuration at 5 GHz, or 6 cm, including our survey area  $10^{\circ} < l < 20^{\circ}$ . The sensitivity of the survey  $1.5''$  resolution is better than 2 mJy.

Another survey for HII regions, the HII Region Discovery Survey (HRDS), has been done by Bania et al. (2010). Using the Green Bank Telescope they searched for recombination lines at 9 GHz, or 3 cm. They find 448 HII regions within the Galactic plane, of which 78 fall within the region of our survey. However, the survey was not unbiased but observed a sample selected from 24  $\mu\text{m}$  and 21 cm continuum emission.

### Luminous mid-IR sources

The Infrared Astronomical Satellite (IRAS) performed an all-sky survey at 12  $\mu\text{m}$ , 25  $\mu\text{m}$ , 60  $\mu\text{m}$ , and 100  $\mu\text{m}$ . While we used the 24  $\mu\text{m}$  MIPS GAL data to search for faint objects, IRAS only detected the brightest infrared objects for which the MIPS GAL data is saturated. However, since we are interested in massive YSOs, the most luminous objects are more appropriate. To select the young star-forming IRAS sources we applied the color-color criteria as given by Wood & Churchwell (1989). The positional uncertainty on the IRAS point source catalog is  $\sim 1'$ .

The survey of Red MSX Sources (RMS, Hoare et al., 2004; Mottram et al., 2011) used data from the MSX satellite to search for massive YSOs. MSX has a better resolution and sensitivity at mid-IR wavelengths than IRAS, and is therefore more complete. In order to identify regions of high-mass star formation, the RMS survey carefully identified objects with colors similar to known massive YSOs.

#### 2.10.2 An attempt of a full classification

As discussed above, identification of the evolutionary stages of all clumps within our survey area allows us to derive both relative time scales and a high-mass star formation time scale. In this context, high-mass star formation time scale refers to the time it takes to form massive stars, from dense but yet starless clumps up to the point where the high-mass star has blown away its detectable envelope.

In Sect. 2.10.1, we describe the tracers of ongoing star formation and further evolution that were used. However, the assignment of the evolutionary stages to all clumps is complicated, and ambiguous.

First, the spatial offsets between the sub-mm peaks and the positions of ongoing star formation impose problems. Often, the offsets are a significant fraction of the projected clump radius. In other words, star formation is sometimes taking place right on the edge of a clump. It is unclear whether such clumps should be considered as star forming or starless. CLUMPFIND draws the clump boundaries dependent on the contour levels used to set it up, and therefore the boundaries are observationally biased or somewhat arbitrary. On the other hand, ongoing star formation at a position offset from the clump center implies an unresolved gravitational condensation that will attract further mass and influence the following evolution of the clump. Therefore, no unambiguous classification is possible.

Second, a significant amount of the identified clumps have a low- or intermediate-mass GLIMPSE YSO within their boundaries, but no indication of ongoing high-mass star formation. As discussed in Robitaille & Whitney (2010), the majority of the GLIMPSE

YSO are of intermediate mass. In order to derive relative time scales an unbiased and clean sample is crucial.

### The anchor for absolute lifetimes: the starless phase

Despite the difficulties outlined above, we will try to estimate a star formation time scale. In order to do so, we first establish the starless phase as an absolute reference time scale.

In Sect. 2.7.2, we outlined how we inferred the lifetime of the starless phase of clumps more massive than  $1000 M_{\odot}$ . However, a differentiation between the mass regimes as was performed in Sect. 2.7.2 is not useful, since all stars more massive than  $8 M_{\odot}$  produce ionizing photons. Therefore, we first want to characterize all starless clumps that are capable of forming a cluster with at least one  $8 M_{\odot}$  mass star, not only those with  $> 1000 M_{\odot}$ .

Using the same assumptions as above, that is a star formation efficiency of 30% and a Kroupa IMF, we derive the mass of such a clump to be at least  $300 M_{\odot}$ . Searching the catalog for all clumps with a near kinematic distance, we find that 35 out of our 125 starless clumps of known velocity and with near assigned distances are capable of forming stars more massive than  $8 M_{\odot}$ . Assuming a star formation rate of  $3 M_{\odot}/\text{yr}$ , their lifetime is approximately 80 000 yr.

### Determining the high-mass star formation time scale - a rigorous approach

In the following we consider only clumps that have no GLIMPSE YSO counterpart, as defined in Gutermuth et al. (2008), because they are not necessarily forming high-mass stars. All remaining clumps are either starless, or show signs of ongoing high-mass star formation. With this approach we assume that a certain amount of clumps are not forming high-mass stars and will not in the future. However, this also implies that not all starless clumps will eventually form high-mass stars. Therefore, we need to estimate the number of starless clumps that will potentially not form high-mass stars.

To form a more consistent sample, we follow the same method as outlined in Sect. 2.7 and only consider clumps with known kinematic distances on the near side of the Galaxy. Among these, 197 are more massive than  $306 M_{\odot}$  and are star forming. Independent of other tracers of ongoing star formation, 122 of these clumps have a GLIMPSE YSO, and 75 clumps have no YSO within.

For now we assume that the 197 clumps with signatures of ongoing star formation evolved from clumps similar to the starless clumps presented in Table 2.1. If this is the case, the starless clumps should form the same ratio of low- or intermediate-mass YSOs as the star-forming clumps. Therefore, applying the ratio of star-forming clumps no low- or intermediate-mass YSOs (75:197 or 38%) to the 35 starless clumps selected above, we find that on average 13.3 will not contain GLIMPSE YSOs before the clump is dispersed.

Among the 75 star-forming clumps that have no detectable low- or intermediate-mass objects, we find that 60 clumps have a weak  $24 \mu\text{m}$  detection, but no IRAS or MSX detection. Four clumps contain massive YSOs in the sense that they are infrared bright,

traced by either an RMS source or an IRAS source, and eight clumps already have an HII region.

Taking the lifetime of starless clumps of 80 kyr as reference time scale, we then compare the 13.3 starless clumps to the 75 star forming clumps. From the formation of dense clumps with high column densities until the clump is no longer picked up by our CLUMPFIND detection limits, we estimate the lifetime of massive star formation to be 510 kyr.

However, this estimate of the star formation time scale is imperfect in various aspects. The most important issue relates to the dynamical evolution of clouds and clumps. In one picture of dynamical evolving clouds, clumps become more massive and denser during their lifetime because of mass infall. Therefore, it could be that the clumps that are now forming low-mass YSOs would not have been detected during their starless phase, because they were of too low column density. Only during their evolution after onset of star formation did they reach beam-averaged column densities high enough to become detected by our algorithm. Another issue is the large number of clumps that have a MIPS GAL 24  $\mu\text{m}$  only detection. It is unclear what fraction of these will turn into low-mass stars. Both concerns might artificially prolong the star formation time scale.

### Treating the fraction of clumps with YSOs more carefully

In the previous approach, we rigorously rejected all clumps that contained a low-mass YSO. However, a number of clumps have both a low-mass GLIMPSE YSO and, independently, tracers of ongoing high-mass star formation. We can argue that their progenitors would have been included in our starless sample and, if massive star formation sets in first, they must have had a high-density starless phase. Therefore, to derive the time scales it is more sensible to account for that fraction independently and reject only clumps that will exclusively form low mass stars.

In numbers, we find that 31 of the 197 clumps have both a GLIMPSE YSO, and also an indicator of ongoing high-mass star formation. Therefore, out of the 197 star-forming clumps, and together with the 75 clumps that have no GLIMPSE YSO (see above), 106 of the clumps would have been included in our starless sample. Deriving from this an improved correction fraction, 18.8 of our 35 starless clumps should form high-mass stars in the future. Finding 130 clumps with a 24  $\mu\text{m}$  detection, 19 clumps with a massive YSO inside, and 24 clumps with an HII region, the time to form high-mass stars becomes 810 kyr. This is almost a factor of 2 larger than the value found in Sect. 2.10.2, when rigorously removing all clumps with low-mass YSOs.

Nevertheless, we still do not account for clumps that have a low-mass YSO now, but still may form massive stars. In addition, neither of the approaches attempted so far can take the spatial offsets between the sub-mm peaks and signposts of ongoing star formation into account.

### 2.10.3 A classification based on the far-IR properties

One can expect that ongoing star formation should leave an imprint on the physical condition of the clump. For example Sridharan et al. (2002) find a trend in the luminosity

over mass ratio for clumps with an without embedded ultracompact HII regions. Clumps with an embedded ultra compact HII region have larger luminosities than clumps of the same mass with an embedded HMPO.

To study the physical parameters of the clumps we fit a black-body function to HiGal data (see Sect. 2.10.3) of each clump. In combination with the classification of the clumps we described above, we then try to identify similar trends as found by Sridharan et al. (2002) to determine a classification independent of individual star formation tracers.

### HiGal - a mid- to far-IR view of the clumps

Covering the peak emission of the spectral energy distribution (SED) of cold dust, the HiGal/*Herschel* survey (Molinari et al., 2010) provides far-IR observations at  $70\ \mu\text{m}$  and  $160\ \mu\text{m}$ , and at submm wavelength  $250\ \mu\text{m}$ ,  $350\ \mu\text{m}$ , and  $500\ \mu\text{m}$ . Therefore, they connect the ATLASGAL submm observations of the cold dust at  $870\ \mu\text{m}$  to the near- and mid-IR observations of the hot dust and stellar radiation. The observations were carried out in parallel mode with a scanning speed of  $60''/\text{s}$ . Since the official, fully reduced HiGal fields are not yet available, Anika Schmiedeke reduced the HiGal raw data using HIPE (level 0 to 1, build 8.0.3287, Ott 2010) and SCANAMORPHOS (level 1 to 2, v16 Roussel 2012). The angular resolutions at the given wavelengths are  $10.2''$ ,  $13.6''$ ,  $23.4''$ ,  $30.3''$ , and  $42.5''$ , respectively (Traficante et al., 2011).

To determine the clump temperature, mass, and luminosity we fit a single temperature modified Planck function (graybody) to the SED of the each clump in the range  $70\ \mu\text{m}$  to  $500\ \mu\text{m}$ . In contrast to how we determined the masses above, here we use dust emission coefficients from Ossenkopf & Henning (1994), assuming thin ice mantels and average volume densities of  $10^6\ \text{cm}^{-3}$ . To determine the flux at each wavelength we first smooth the HiGal data to a common resolution of  $42.5''$ , and then calculate the total flux over each clump. Therefore, the clump parameters refer to rather large-scale entities.

As we will explain in more detail in Sect. 4.3.3, we refrain from subtracting background levels. While the derived temperature is not affected at all, the masses and luminosities change slightly. However, since we only compare values derived from the same HiGal data, general offsets do not affect our results.

### Clump parameters

In Fig. 2.12 we show the results of the single Planck function fit to the clumps as derived from the HiGal data. Note that in this figure the mass cut of  $306\ M_{\odot}$  is applied to the masses calculated with the fitted HiGal temperature and dust opacities from Ossenkopf & Henning (1994). Looking at the temperature distribution of the clumps, it is obvious that starless clumps have on average lower luminosities and temperatures than both the MYSO sample and the clumps with embedded HII regions. If we assume that in high-mass star formation MYSOs form first (or high-mass proto-stellar objects, HMPOs), and that they later develop an ultra-compact HII region while being still IR bright, the plot suggests that UCHII regions are again warmer and more luminous than the MYSOs. However, all populations have large overlap and no clear distinction between them is visible.

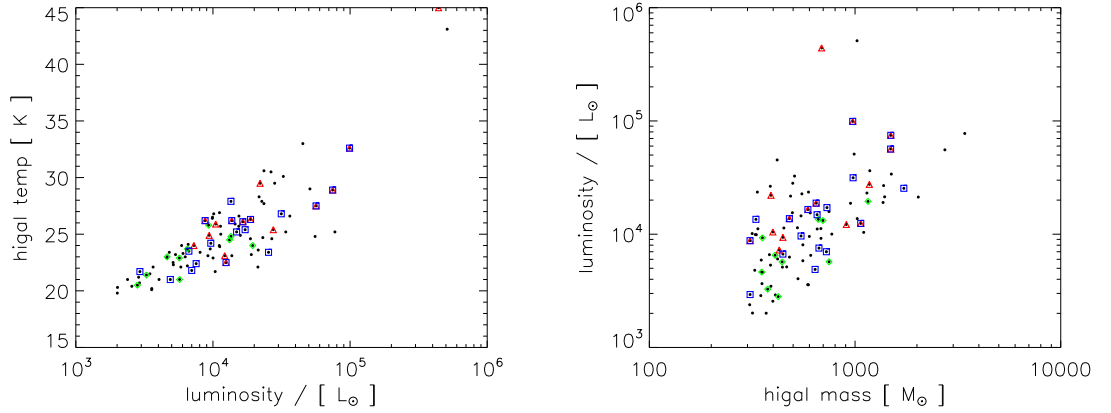


**Figure 2.12:** Comparison of the fitted HiGal clump parameters to the evolutionary stage derived from star formation tracers. The left panel shows the temperature distribution of the clumps over the luminosity, the right panel displays the luminosity over the clump mass. The green diamonds represent the starless clumps, the blue squares are infrared bright clumps, and the red triangles indicate the presence of an HII region.

To directly compare our luminosities to the distribution of luminosities found in Sridharan et al. (2002), the right panel of Fig. 2.12 shows the clump luminosity versus the fitted mass. While the starless clumps have lower luminosities than clumps of comparable mass but with an embedded HII region, the infrared bright objects that have no HII region, yet are not distinguishable from the starless clumps. Therefore, we find a similar trend for the luminosities as was found by Sridharan et al. (2002). However, the rise in luminosity seems to be connected to the time-evolution of the HII region. The IR bright and dark sources are not distinguishable from a single component fit to the far-IR portion of their SED.

#### 2.10.4 Discussion of the attempt of a full classification

As we have discussed in Sect. 2.10.2, the main issue with a full classification derived from tracers of ongoing star formation are their correlation to the column density peaks. At the given resolution, both appear at different positions. But it is unclear how to treat clumps that show signatures of star formation on their edges, compared to clumps that show star formation at their center. However, we still try two different approaches to define a clean sample of clumps. As it turns out, the intermediate phase of star formation in which a faint  $24\ \mu\text{m}$  point source indicates activity is the longest. Assuming that the starless phase lasts about 80 kyr as an average for all clumps that may form  $8\ M_{\odot}$  stars and taking the average of both approaches presented above, their lifetime becomes  $\sim 450$  kyr. That is several times the free-fall time for regions of  $1 \times 10^5\ \text{cm}^{-3}$ . The HMPO phase prior to the build-up of an detectable HII region is the shortest, with an estimated lifetime of about  $\sim 50$  kyr. The phase with an embedded HII region is short as well,  $\sim 75$  kyr, since the expanding HII region clears out the dust from its surroundings and the clump is no longer detected at our sub-mm sensitivities.

The lifetime of the entire star formation cycle, from the time when a clump becomes dense to the point where the clump is no longer detected, is constrained to 510 kyr to 810 kyr. This time agrees very well with observational constraints (Motte et al., 2007; Russeil et al., 2010). However, the efforts to define a clean sample are not sufficient. In our picture of dynamical evolving clumps, we include different clumps in our sample, dependent on their evolutionary stage. In addition, while some initially low column density clumps may still form high-mass stars after further evolution and mass gain, some initially dense clumps may dissolve again. It is also not clear how to deal with clumps that only have a  $24\ \mu\text{m}$  detection. Some of those might be forming low-mass stars as well, but their fraction should be less than we rejected from the starless sample.

In that context it is interesting to note that all IRAS and RMS sources, as well as all HII regions, are found towards the few most massive clumps. Therefore, if we impose a different clump mass limit, e.g.  $1000\ M_{\odot}$ , the number of objects in the more evolved stages do not change, while the number of clumps with a  $24\ \mu\text{m}$  detection is lowered significantly. While it is expected that more massive objects have shorter formation times, it is likely an observational bias that all tracers of the more evolved stages are found exclusively in the most massive clumps. This raises additional questions about the estimated formation time scale.

To obtain a more reliable classification, independent of star formation tracers, we used HiGal mid-IR data to fit the SED of each clump. As expected, the temperatures of starless clumps are on average lower than for the more evolved clumps, but the regions show very large overlap. Here one should keep in mind that we fit the flux integrated over the entire clump.

In the luminosity over mass plot, clumps with an associated HII region have on average larger luminosities than the starless or IR bright clumps. The latter two populations are very similar to each other and cannot be distinguished based on their luminosity. While this seems unexpected at first, it can be explained by the wavelength range we use. The IR bright IRAS and RMS sources heat up their direct vicinity and become distinct from their surrounding dust. To fit their e.g.  $24\ \mu\text{m}$  flux, a second, warm dust component is required. However, the majority of the dust is hardly affected and still at cold temperatures. Therefore, the long wavelength regime at  $70\ \mu\text{m}$  and above does not change its appearance. Once the central object is warm enough to produce Lyman continuum photons and ionizes its environment, the dust is heated up as well, becomes more luminous, and the cold dust component traced by the HiGal data changes its properties.

Nevertheless, no clear distinction between the two more evolved populations is visible. Because of the relatively high temperatures of clumps with an HII region, in combination with the larger dust opacities from Ossenkopf & Henning (1994), their masses are reduced considerably. Therefore, in contrast to what was discussed for the masses prior to the HiGal temperature fitting in Sect. 2.10.4, we find no indication that the sensitivity of the HII region sample is different from the rest of the sample.

In summary, our estimated star-formation time-scale agrees with previous estimates. However, the uncertainties on the formation time scale for high-mass stars are very large. Using the clump luminosities from fitting the SED at HiGal wavelengths  $70\ \mu\text{m}$  to  $500\ \mu\text{m}$ , we cannot find a discriminator for the different evolutionary stages to improve the classi-

fication and reduce the uncertainties.



## Chapter 3

# Kinematics in high-mass star forming regions

A possible explanation for the short lifetime of starless clumps found in the previous chapter could be a highly dynamical evolution clouds, clumps, and cores. Therefore, we now study the large-scale gas dynamics of high-mass star-forming regions.

This chapter will be submitted to A&A for publication.

### 3.1 Introduction

Despite their rareness, high-mass stars are important for all fields of astronomy. Within the Milky Way they e.g. shape and regulate the formation of clusters, influence the chemistry of the interstellar medium, and might have even affected the formation of the solar system (Gritschneider et al., 2012). On the large scales, the light from massive stars is all we see of distant galaxies, and most extragalactic studies are solely based on them. Nevertheless, high-mass star formation is far from understood (Beuther et al., 2007; Zinnecker & Yorke, 2007).

Sensitive mid-IR and (sub-)mm Galactic plane surveys together with results from the *Herschel* space observatory (Pilbratt et al., 2010) have shed new light onto the cradles of massive stars/clusters and their early formation. Perault et al. (1996) and Egan et al. (1998) discovered extinction patches in the bright mid-IR background using the ISO (Kessler et al., 1996) and MSX (Egan et al., 2003) satellites, similar to the dark patches reported by Barnard (1919) which are today known to be connected to low-mass star formation. Soon after, Carey et al. (1998) established the so-called infrared dark clouds (IRDCs) as precursors of high-mass star formation. Today, the Spitzer observatory Galactic plane surveys GLIMPSE at  $3.6\ \mu\text{m}$ ,  $4.5\ \mu\text{m}$ ,  $5.8\ \mu\text{m}$ , and  $8\ \mu\text{m}$  (Benjamin et al., 2003), and MIPS GAL at  $24\ \mu\text{m}$  (Carey et al., 2009) allow the systematic search for IRDCs with unprecedented sensitivity (e.g. Peretto & Fuller, 2009).

While Spitzer improved our mid-IR view of the Galaxy, the *Herschel* satellite allows observations of the far-IR. With the PACS (Poglitsch et al., 2010) and SPIRE (Griffin et al., 2010) photometer, high sensitivity and spatial resolution observations between  $70\ \mu\text{m}$  and

500  $\mu\text{m}$  are possible.

From correlating the various data, the picture emerged that most star-forming regions are filamentary (André et al., 2010; Men'shchikov et al., 2010; Molinari et al., 2010; Schneider et al., 2010; Hill et al., 2011; Hennemann et al., 2012; Peretto et al., 2012).

In numerical studies, the formation of dense cores and clumps is explained by two scenarios. On the one hand, molecular clouds fragment in a self-similar cascade down to the typical size of dense, turbulent supported quasi-static cores. These will then form single or gravitationally bound multiple objects McKee & Tan (2003); Zinnecker & Yorke (2007). On the other hand, the dynamical theory forms molecular clouds from large-scale flows of atomic gas as transient objects. Within, supersonic turbulence compresses part of the gas to filaments, clumps, and dense cores. If gravity becomes dominant, the cores collapse. In contrast to the quasi-static cores, they constantly grow in mass (Mac Low & Klessen, 2004; Klessen et al., 2005; Heitsch & Hartmann, 2008; Clark et al., 2012).

The Earliest Phases of Star formation (EPoS<sup>1</sup>, PI O. Krause) is a Guaranteed Time key Program for investigating 15 low-mass and 45 high-mass star-forming regions. The low-mass observations have been summarized in Launhardt et al (subm.), and the high-mass part has been described in Ragan et al. (2012). Since we want to study details of high-mass star formation we select our sample from the latter.

## 3.2 Observations and analyzis

### 3.2.1 EPoS - A *Herschel* Key Project

All 45 high-mass EPoS sources were observed with the *Herschel* satellite (Pilbratt et al., 2010) at 70  $\mu\text{m}$ , 100  $\mu\text{m}$ , 160  $\mu\text{m}$ , 250  $\mu\text{m}$ , 350  $\mu\text{m}$ , and 500  $\mu\text{m}$  with a spatial resolution of 5.6'', 6.8'', 11.3'', 18.1'', 25.2'', and 36.6'', respectively (Poglitsch et al., 2010; Griffin et al., 2010). The observations were performed in two orthogonal directions and the data reduction has been performed using *HIFE* (Ott, 2010) and *scanamorphos* (Roussel, 2012). A more detailed description of the data reduction is given in Ragan et al. (2012).

Out of the 45 *Herschel* EPoS high-mass sources we selected a sub-sample of 17 regions that cover several important evolutionary stages: From promising candidates for high-mass starless cores over IRDCs that contain weak mid- and far-infrared sources, indicative of early ongoing star formation activity, to known high-mass protostellar objects (HMPOs).

Using *starfinder*, Ragan et al. (2012) extract point sources from the three PACS bands and correlate them to the *Spitzer*/MIPS 24  $\mu\text{m}$  observations, where available. For sources which are saturated at 24  $\mu\text{m}$  they adopt an IRAS 25  $\mu\text{m}$  or MSX 21  $\mu\text{m}$  flux. Then they fit the spectral energy distribution of each point source with a single temperature modified Planck function, using dust opacities from Ossenkopf & Henning (1994). This yields an estimate of the temperature of the point source and, with the distance, of its luminosity.

---

<sup>1</sup>*Herschel* is an ESA space observatory with science instruments provided by European-led Principal Investigator consortia and with important participation from NASA.

### 3.2.2 Nobeyama 45m observations

**Table 3.1:** Observed IRDCs.

Source name	RA(J2000) [hh mm ss.s]	DEC(J2000) [dd mm ss]	Gal. longi- tude [ $^{\circ}$ ]	Gal. lat- itude [ $^{\circ}$ ]	Distance [kpc]	minimum $\text{N}_2\text{H}^+$ detec- tion [ $\times 10^{12} \text{ cm}^{-2}$ ]	minimum $\text{N}_2\text{H}^+$ detec- tion 0.4 km/s [ $\times 10^{12} \text{ cm}^{-2}$ ]
<b>Observed with Nobeyama 45m telescope</b>							
IRDC 18223	18 25 10.7	-12 45 12	18.613	-0.081	3.5	0.8	
IRDC 18310	18 33 44.7	-08 22 36	23.467	0.085	4.9	3.9	
IRDC 18385	18 41 17.1	-05 09 15	27.189	-0.098	3.1	1.2	
IRDC 18454	18 47 58.1	-01 54 41	30.835	-0.100	5.3	4.1	
ISOSS J20153	20 15 21.4	+34 53 52	72.953	-0.027	1.2	8.1	
IRDC 13.90	18 17 26.1	-17 05 26	13.906	-0.473	2.6	1.4	
<b>Observed with Mopra</b>							
IRDC 18102	18 13 12.2	-17 59 34	12.632	-0.016	2.6	5.7	3.3
IRDC 18151	18 17 55.3	-12 07 29	18.335	1.778	2.7	3.9	2.8
IRDC 18182	18 21 12.2	-14 32 46	16.577	-0.069	3.4	3.2	2.2
IRDC 18306	18 33 29.9	-08 32 07	23.298	0.066	3.6	1.5	1.6
IRDC 18308	18 33 33.1	-08 37 46	23.220	0.011	4.4	2.9	2.1
IRDC 18337	18 36 29.6	-07 40 33	24.402	-0.197	3.7	1.8	1.1
IRDC 19.30	18 25 58.1	-12 05 09	19.293	0.060	2.4	7.6	1.3
IRDC 11.11	18 10 20.0	-19 25 05	11.056	-0.107	3.4	2.4	1.6
IRDC 15.05	18 17 40.4	-15 49 12	15.052	0.080	3.0	3.4	1.4
IRDC 28.34	18 42 48.1	-04 01 51	28.361	0.080	4.5	4.5	3.2
IRDC 48.66	19 21 40.7	+13 50 32	48.666	-0.263	2.6	2.3	0.8

Position columns (2-5) give the center coordinate of the maps. The actual areas that have been mapped are displayed in Fig. 3.1 through Fig. 3.4. The distances are adopted from (Ragan et al., 2012) with references therein. The detected  $\text{N}_2\text{H}^+$  minimum the minimum plotted in Fig. 3.1 through Fig. 3.4. For sources observed with MOPRA we also give the improved minimum detection when smoothing the spectra to a velocity resolution of 0.4 km/s. Also observed with the NRO 45m telescope but not detected have been IRDC20081, ISOSSJ19357, ISOSSJ19557, and ISOSSJ20093.

Between April 7th and 12th 2010 the BEam Array Receiver System (BEARS, Sunada et al. 2000) on the Nobeyama Radio Observatory (NRO<sup>2</sup>) 45 m telescope was used to map six of the regions in  $\text{N}_2\text{H}^+$ , the details are given in Table 3.1. At a frequency of the  $\text{N}_2\text{H}^+$  (2-1) transition of 93.173 GHz, the spatial resolution of the NRO 45 m telescope is  $18''$  (HPBW) and the observing mode with a band-width of 32 MHz has a frequency resolution of 62.5 kHz, or 0.2 km/s. All observations were performed using on-the-fly (OTF) mapping in varying weather conditions, with an average system temperature of 280 K and high water vapors between 3 mm and 9 mm. Although the wind conditions contributed to the pointing uncertainties, the pointing is better than a third of the beam.

For the data reduction we used NOSTAR (Sawada et al., 2008), a software package provided by the NRO for OTF data. The data is sampled to a spatial grid of  $7.5''$  and smoothed to a spectral resolution of 0.5 km/s. To account for the different efficiencies of the 25 receivers in the BEARS array we corrected each pixel to the efficiency of the S100 receiver, using individual correction factors and a beam efficiency of  $\eta = 0.46$  to calculate main-beam temperatures. The noisy edges due to less coverage have been removed within NOSTAR by suppressing pixels in the final maps with a rms noise above 0.15 K. The resulting antenna temperature maps have an average rms noise between 0.12 K and 0.13 K per beam.

<sup>2</sup>Nobeyama Radio Observatory is a branch of the National Astronomical Observatory of Japan, National Institutes of Natural Sciences.

### 3.2.3 MOPRA observations

Eleven sources, listed in Table 3.1, were mapped with the 22 m MOPRA radio telescope, operated by the Australia Telescope National Facility (ATNF) in OTF mode. The observations were carried out in 2010, June 1st to 5th and 25th to 27th, as well as July 7th through 9th. High precipitable water vapors during the observations result in system temperatures mostly between 200 K and 300 K. Observations with system temperatures above 500 K were ignored during the data reduction.

We employed 13 of the MOPRA spectrometer (MOPS) zoom bands, each of 138 MHz width and 4096 channels, resulting in a velocity resolution of 0.11 km/s at 90 GHz. The spectral setup covered transitions of  $\text{CH}_3\text{CCH}$ ,  $\text{H}^{13}\text{CN}$ ,  $\text{H}^{13}\text{CO}^+$ ,  $\text{SiO}$ ,  $\text{C}_2\text{H}$ ,  $\text{HNCO}$ ,  $\text{HCN}$ ,  $\text{HCO}^+$ ,  $\text{HNC}$ ,  $\text{HCCCN}$ ,  $\text{CH}_3\text{CN}$ ,  $^{13}\text{CS}$ , and  $\text{N}_2\text{H}^+$  in the 90 GHz regime. At this wavelength, the MOPRA beam FWHM is  $35.5''$  and the beam efficiency is assumed to be constant over the frequency range with  $\eta = 0.49$  (Ladd et al., 2005). The data reduction was done using LIVEDATA and GRIDZILLA, an on-the-fly mapping analysis package provided by the ATNF. In order to improve the signal-to-noise ratio we spatially smoothed the data to a beam FWHM of  $46''$  within (and as suggested by) *gridzilla*. The final maps were smoothed to a spectral resolution of 0.21 km/s - 0.23 km/s (depending on the transition frequency). Spectra with an rms noise above 0.12 K have been removed, affecting pixels at the edges. The resulting average rms noise of the individual maps is then below 0.09 K/beam.

However, the observed regions of interest are dense but still cold. Therefore, with the achieved sensitivity at the given spatial resolution we do not detect the more complex or low-abundance molecules. For example, although SiO has been detected toward several positions that we have mapped (Sridharan et al. 2002; Sakai et al. 2010), the strongest SiO emitter found by Linz et al. (in prep., G28.34-2) is at our noise level and therefore not detected. As we discuss in Sect. 3.2.5, we first concentrate on  $\text{N}_2\text{H}^+$ , a well known cold dense gas tracer. Later, we also discuss the distribution of  $\text{HCO}^+$ ,  $\text{H}^{13}\text{CO}^+$ ,  $\text{N}_2\text{H}^+$ ,  $\text{HNC}$ , and  $\text{HCN}$  for the sources observed with MOPRA. The discussed molecules are dense gas tracers as well and have been successfully mapped in several regions.

### 3.2.4 Dust continuum

In order to trace the total cold gas we use the cold dust emission as a tracer of the molecular gas. As most of the selected sources lie within the Galactic plane, the APEX 870  $\mu\text{m}$  survey ATLASGAL (Schuller et al., 2009; Contreras et al., 2013) covers all but two sources. Its beam size is  $19.2''$  and its average rms noise is 50 mJy/beam. IRDC 18151 with a Galactic latitude of  $\sim 1.7^\circ$  is not covered by ATLASGAL. Instead we use IRAM 30 m MAMBO data (Beuther et al., 2002b). At a wavelength of 1.2 mm, the beam width is  $10.5''$ , and the rms noise in the dust map is 17 mJy/beam. In addition, ISOSS J20153 is too far out to be covered by ATLASGAL. Here we used 850  $\mu\text{m}$  data from the SCUBA camera at the JCMT<sup>3</sup>. The beam width is  $14''$  and the rms noise 14 mJy/beam.

<sup>3</sup>The James Clerk Maxwell Telescope is operated by the Joint Astronomy Centre on behalf of the Particle Physics and Astronomy Research Council of the United Kingdom, the Netherlands Association for Scientific Research, and the National Research Council of Canada.

A summary of the properties of the sub-mm data is given in Table 3.2.

Dust data	wavelength [ $\mu\text{m}$ ]	beam FWHM [ '']	rms noise [ mJy beam <sup>-1</sup> ]	$\kappa_{dust}$ [ cm <sup>2</sup> g <sup>-1</sup> ]	lowest contour [ mJy beam <sup>-1</sup> ]	column density threshold [ cm <sup>-2</sup> ]
ATLASGAL/APEX	870	19.2	50	1.42	310	$1 \times 10^{22}$
MAMBO/IRAM 30 m	1200	10.5	17	0.79	60	$2 \times 10^{22}$
SCUBA/JCMT	850	14.0	14	1.48	176	$1 \times 10^{22}$

**Table 3.2:** Summary of the different dust data used, and the corresponding properties. The column densities have been calculated under the assumptions given in Sec. 3.2.6 for 20 K. The last column is the column density corresponding to the lowest emission contour used within *CLUMPFIND*.

### 3.2.5 N<sub>2</sub>H<sup>+</sup> hyperfine fitting

The molecular line study focuses on the N<sub>2</sub>H<sup>+</sup> J=1-0 line as dense molecular gas tracer. It has a critical density of  $1.7 \times 10^5 \text{ cm}^{-3}$ , and its hyperfine structure allows one to reliably measure its optical depth and thus the distribution over a wide range of densities. In addition, the velocity and linewidth can be measured without being affected by optical depth effects. Finally, it is detected toward both low- and high-mass star-forming regions of various evolutionary stages (Schlingman et al. 2011, Gerner et al., in prep.). Therefore, it is well suited for studies of young high-mass star-forming regions.

To extract the N<sub>2</sub>H<sup>+</sup> line parameters, we fit a N<sub>2</sub>H<sup>+</sup> hyperfine structure to each pixel using *class* from the *GILDAS*<sup>4</sup> package. For every spectrum we calculate the rms and the peak intensity of the brightest component derived from the fit parameters. If the peak is higher than three times the rms value, the fit parameters peak velocity, and linewidth together with an integrated intensity are stored to a parameter map. Otherwise, the pixel is left blank. The low detection threshold of  $3\sigma$  is justified for two reasons. (1) For only a very limited number of pixels that fulfill the  $3\sigma$  criterion, the fitted line-width is twice the channel width or less. Therefore, introducing an additional check on the integrated intensity, e.g. a  $5\sigma$ , does not improve the fit reliability. (2) The resulting parameter maps show only smooth transition in each parameter relative to neighboring pixels. For the same pixels, smoothing over a larger area would increase the signal to noise but worsen the resolution. Therefore, the small scale structure would be lost. For our purposes, fitting the hyperfine structure even in low signal-to-noise maps provides reliable results.

From the integrated intensity ( $\int T_{mb}$ ), determined as the sum over channels times the channel width, and the fitted optical depth  $\tau$ , we calculated the column densities of N<sub>2</sub>H<sup>+</sup>. We used the formula from Tielens (2005),

$$N_J = 1.94 \times 10^3 \frac{\nu^2 \int T_{mb}}{A_u} \times \frac{\tau}{1 - e^{-\tau}} \quad (\text{for } J+1 \text{ to } J) \quad (3.1)$$

$$N_{tot} = \frac{Q}{g_u} \times N_J \times e^{E_u/kT_{ex}}, \quad (3.2)$$

where  $N_J$  is the number of molecules in the the J-th level, and  $N_{tot}$  the total number of molecules.  $A_u$  is the Einstein A coefficient of the upper level,  $E_u/k$  is the excitation energy

<sup>4</sup><http://www.iram.fr/IRAMFR/GILDAS>

of the upper level in K, both adopted from Schöier et al. (2005); Vasyunina et al. (2011), and Q is the partition function of the given level, taken from the Cologne Database for Molecular Spectroscopy (Müller et al., 2005).

The rms of our observations limits the detection of signal, but the  $\text{N}_2\text{H}^+$  column density also depends on the measured opacity and assumed temperature. As we discuss in Sect. 3.3.1, we use a constant gas temperature of 20 K. Varying the temperature by up to 5 K, the calculated column densities vary by less than 25%. Taking also the error on the integrated intensity and the partition function into account, we assume the error on the column density to be on the order of 50%. With the given rms toward the edge of the MOPRA data, our theoretical  $5\sigma$   $\text{N}_2\text{H}^+$  detection limit in the optically thin case is given by  $1.5 \times 10^{12} \text{ cm}^{-2}$  for the velocity resolution of 0.2 km/s. However, since most sources have considerable optical depth, the smallest measured  $\text{N}_2\text{H}^+$  column density is larger. Their minimal calculated values are given in Table 3.1. Similarly, for the Nobeyama 45 m data the  $5\sigma$  detection limit is  $2.1 \times 10^{12} \text{ cm}^{-2}$ . Since some central regions of e.g. IRDC 18223 have a much lower rms of only 0.05 K instead of 0.12 K, here the lowest calculated values are actually smaller.

The uncertainties on the fit parameters velocity and linewidth are mainly constrained by the signal-to-noise ratio and the line shape. Since even the broadest velocity resolution within our sample of 0.5 km/s resolve the lines, the uncertainties on the linewidth are similar for all data. Spectra with a signal-to-noise better than  $7\sigma$  and Gaussian shaped line profiles have typical linewidth uncertainties  $> 5\%$ , while non-Gaussian line profiles and low signal-to-noise ratios may lead to uncertainties of up to 20%. Instead, the recovery of the peak velocity shows an additional slight velocity resolution dependency. Still, both line shape and signal-to-noise ratio dominate, and down to a peak line strength of  $3\sigma$ , the uncertainties on the velocity are below 0.2 km/s.

### 3.2.6 Identification of dust peaks

To put the molecular line data in context to its environment we use the dust continuum to obtain gas column densities and masses. For the calculation of column densities from fluxes we use

$$N_{gas} = \frac{RF_\lambda}{B_\lambda(\lambda, T)\mu m_H \kappa \Omega}, \quad (3.3)$$

with the gas-to-dust mass ratio  $R = 100$ ,  $F_\lambda$  the flux at the given wavelength,  $B_\lambda(\lambda, T)$  the blackbody radiation as a function of wavelength and temperature,  $\mu$  the mean molecular weight of the ISM of 2.8,  $m_H$  the mass of a hydrogen atom, and the beam size  $\Omega$ . Assuming typical beam averaged volume densities in the dense gas of  $10^5 \text{ cm}^{-3}$  and dust grains with thin ice mantles, we can interpolate the dust mass absorption coefficient from Ossenkopf & Henning (1994) to the desired wavelength. The corresponding dust opacities for the different wavelengths are listed in Table 3.2.

The gas and dust temperatures should be coupled at densities typical for dense clump ( $> 10^5 \text{ cm}^{-3}$ ), and have been measured to be between 15 K and 20 K (Sridharan et al., 2005; Pillai et al., 2006; Peretto & Fuller, 2010; Battersby et al., 2011; Wilcock et al., 2011; Vasyunina et al., 2011; Wienen et al., 2012; Wilcock et al., 2012). Since most

regions in our survey show already signs of ongoing star formation, we assume a single temperature value of 20 K for all clumps.

With the distance  $d$  as additional parameter, the mass can be calculated from the integrated flux in a similar way as given above,

$$M_{gas} = \frac{Rd^2 F_\lambda}{B_\lambda(\lambda, T)\kappa}. \quad (3.4)$$

To identify emission peaks and their connected fluxes in the dust maps we use CLUMPFIND (Williams et al., 1994). Since we want to compare our results to the dense gas measured by  $N_2H^+$ , we select a lowest emission contour corresponding to  $1 \times 10^{22} \text{ cm}^{-2}$  ( $> 6\sigma$  for ATLASGAL,  $> 12\sigma$  for SCUBA), or, in the case of ISOSS J20153,  $2 \times 10^{22} \text{ cm}^{-2}$  ( $> 3\sigma$ ). Additional levels are added in steps of  $3\sigma$ , see Table 3.2. All clumps for which we mapped the peak position are listed together with their column density and mass in Table 3.3.

The uncertainties on both the gas column density and mass are dominated by the dust properties. The flux calibration of the ATLASGAL data is reliable within 15%, and typical peak and clump-integrated fluxes are an order of magnitude larger than the rms of the data. The uncertainties on the dust properties are difficult to assess, but from comparison to other values (e.g. Hildebrand 1983) or using slightly different parameters within the same model (Ossenkopf & Henning, 1994) we assume them to be on the order of a factor two. Together with the uncertainties from the dust temperature, we estimate the total uncertainties on the column densities to be a factor of  $\sim 3$ . For the gas mass, the uncertainty of the distance of  $\sim 0.5 \text{ kpc}$  introduces an additional error of  $\sim 50\%$ . Therefore, the total uncertainty of the gas mass we estimate to be on the order of a factor of five.

### 3.2.7 Abundance ratio

For positions where not only dust continuum but also  $N_2H^+$  has been detected we calculate abundance ratios. With a resolution of  $18''$  and  $19.2''$ , the Nobeyama 45 m data have almost the same resolution as the ATLASGAL  $870 \mu\text{m}$  data. Therefore we calculate the  $N_2H^+$  abundance ratio by plain division, correcting for the different spatial beam size but without smoothing the data. To calculate abundance ratios for sources observed with MOPRA at a resolution of  $46''$ , we apply a Gaussian smoothing to the dust data to have both at a common resolution. We then calculate the  $N_2H^+$  abundance for the  $46''$  beam.

## 3.3 Morphology of the dense gas

In the following section we concentrate on the  $N_2H^+$  observations. First we compare the  $N_2H^+$  to the cold dust distribution as measured by ATLASGAL and put it in context with the PACS  $70 \mu\text{m}$  measurements. Then we describe the velocity and linewidth distribution of the dense gas.

Table 3.3: 870  $\mu\text{m}$  ATLASGAL clump properties.

IRDC ident	RA(J2000)	DEC(J2000)	$N_{H_2}$	$M_{dust}$	$R_{eff}$	$N_2H^+$ abun- dance	$v_{N_2H^+}$	$\delta v_{N_2H^+}$	aver. $\Delta v_{N_2H^+}$	$M_{vir,k=12}$	$M_{vir,k=190}$	PACS 70 $\mu\text{m}$ tag	MIPS 24 $\mu\text{m}$ tag
	[ $^\circ$ ]	[ $^\circ$ ]	[ $10^{22}$ $\text{cm}^{-2}$ ]	[ $M_\odot$ ]	[ $''$ ]	[ $10^{-10}$ ]	[km/s]	[km/s]	[ $10^{-10}$ ]	[km/s]	[km/s]		
18102	18 13 11.2	-18 00 06	11.2	1019.	57.1	3.0	21.7	3.2	2.7	680	1026	3	3
18151-1 <sup>1</sup>	18 17 58.2	-12 07 26	32.2	677.	34.5	1.1	33.0	1.9	2.0	232	350	1	0
18151-2 <sup>1</sup>	18 17 50.3	-12 07 54	20.4	524.	32.5	1.3	29.7	3.1	3.1	495	747	1	0
18151-3 <sup>1</sup>	18 17 51.9	-12 06 54	6.6	184.	23.7	—	—	—	0.7	19	29	1	0
18151-4	18 17 55.7	-12 06 54	2.6	21.	9.0	—	—	—	3.0	128	193	0	0
18182-1 <sup>1</sup>	18 21 09.2	-14 31 47	17.2	1032.	36.3	1.4	59.7	2.7	2.6	515	777	1	0
18182-2 <sup>7</sup>	18 21 14.8	-14 33 04	2.9	382.	33.7	5.5	41.0	1.6	1.9	256	387	2	1
18182-4 <sup>7</sup>	18 21 13.8	-14 34 11	1.6	100.	20.3	3.3	41.2	1.9	2.3	217	327	0	0
18223-1 <sup>1</sup>	18 25 10.6	-12 42 24	8.1	975.	43.1	4.7	44.2	1.9	2.0	358	539	3	1
18223-3 <sup>1</sup>	18 25 08.3	-12 45 23	4.9	449.	32.6	9.2	44.6	2.9	2.9	599	904	2	2
18223-2 <sup>1</sup>	18 25 09.5	-12 44 11	3.3	374.	31.6	10.1	44.6	2.5	2.3	361	545	1	1
18306-1	18 33 23.6	-08 33 36	9.0	640.	32.3	4.8	78.0	2.7	2.7	536	809	1	0
18306-2	18 33 31.6	-08 32 36	2.0	107.	18.8	—	—	—	1.6	104	158	0	0
18308-1 <sup>1</sup>	18 33 32.6	-08 39 16	8.2	1483.	40.3	3.9	76.6	3.0	3.4	1271	1916	2	2
18308-3 <sup>1</sup>	18 33 29.8	-08 38 27	2.7	592.	33.7	6.5	74.7	2.7	3.0	796	1201	1	1
18308-4 <sup>1</sup>	18 33 27.0	-08 38 53	1.6	81.	14.0	—	—	—	0.9	33	50	0	0
18308-5	18 33 34.6	-08 35 55	1.4	61.	12.7	10.6	77.8	1.8	1.6	83	125	0	0
18308-6	18 33 36.2	-08 36 41	1.4	57.	12.2	—	—	—	1.2	48	72	0	0
18310-1 <sup>1</sup>	18 33 47.7	-08 23 51	6.5	1100.	33.2	9.0	83.2	1.9	2.4	566	854	2	1
18310-2 <sup>1</sup>	18 33 43.7	-08 21 25	6.3	1236.	33.5	6.0	84.3	3.7	3.5	1209	1824	1	1
18310-4 <sup>1</sup>	18 33 39.2	-08 21 11	2.6	346.	23.2	9.4	86.1	2.4	2.3	384	579	1	0
18310-3 <sup>1</sup>	18 33 43.8	-08 22 13	1.5	221.	21.1	—	—	—	3.1	612	924	0	0
18337-4	18 36 37.0	-07 38 53	2.1	214.	26.0	—	—	—	2.9	497	749	0	0
18337-3 <sup>1</sup>	18 36 18.2	-07 41 06	1.9	177.	24.9	5.4	56.0	2.6	2.6	371	560	2	2
18337-5	18 36 18.7	-07 41 43	1.7	137.	22.4	—	—	—	2.8	394	594	0	0
18337-2 <sup>1</sup>	18 36 26.5	-07 41 15	1.5	44.	12.7	2.9	57.4	1.1	1.1	36	55	0	0
18454- mm1	18 47 46.7	-01 54 26	80.8	16117.	50.6	2.6	95.6	5.4	6.3	6552	9880	1	1
18454-10	18 47 49.4	-01 53 59	8.4	3032.	40.1	12.5	96.6	7.3	6.0	4787	7219	0	0
18454-11	18 47 38.9	-01 56 55	8.0	2641.	38.2	—	—	—	—	NaN	NaN	2	0
18454-3 <sup>2</sup>	18 47 55.4	-01 53 31	6.4	2089.	41.2	8.9	95.3	6.0	6.8	6161	9290	1	1
18454-12	18 47 42.2	-01 56 12	5.3	1358.	35.3	—	—	—	3.9	1729	2608	0	0
18454-13	18 47 40.4	-01 55 59	5.3	1704.	29.9	—	—	—	3.5	1204	1816	1	0
18454-14	18 47 48.2	-01 57 53	4.0	1095.	36.8	6.3	92.8	2.7	3.1	1165	1757	0	0
18454-15	18 47 49.1	-01 57 39	3.6	782.	27.7	7.5	93.9	3.2	3.3	994	1499	0	0
18454-1 <sup>2</sup>	18 48 02.0	-01 54 01	3.4	608.	25.6	6.9	99.3	2.6	2.7	613	925	0	0
18454-4 <sup>2</sup>	18 48 01.1	-01 52 27	3.3	443.	22.4	6.3	100.3	1.8	1.6	179	270	0	0
18454-2 <sup>2</sup>	18 47 59.8	-01 54 12	3.3	666.	27.5	—	—	—	3.2	913	1377	0	0
18454-16	18 47 51.3	-01 53 06	2.5	354.	20.6	—	—	—	8.3	4660	7028	0	0
18454-5b <sup>2</sup>	18 47 57.7	-01 56 18	2.4	261.	18.2	7.5	93.8	2.6	2.7	428	646	0	0
18454-7 <sup>2</sup>	18 47 52.3	-01 55 02	2.4	190.	15.9	10.4	94.2	2.6	2.7	373	563	0	0
18454-17	18 47 52.5	-01 53 09	2.1	240.	18.5	—	—	—	9.3	5237	7897	0	0
18454-6 <sup>2</sup>	18 48 02.1	-01 55 43	1.9	115.	13.1	—	—	—	—	NaN	NaN	1	1
18454-19	18 47 51.6	-01 58 25	1.8	171.	16.6	—	—	—	2.7	399	603	1	0
18454-9 <sup>2</sup>	18 47 57.3	-01 57 35	1.6	199.	18.2	—	—	—	2.6	395	596	0	0
18454-21	18 47 48.5	-01 55 20	1.6	212.	18.8	—	—	—	4.1	1048	1581	0	0
1930-1	18 25 58.4	-12 04 01	4.0	164.	30.1	10.8	26.6	2.7	2.6	299	451	2	2
1930-2	18 25 52.3	-12 04 56	2.9	93.	23.9	7.9	27.0	2.2	2.2	174	263	1	1
1930-3	18 25 53.8	-12 04 40	2.0	94.	26.2	8.9	26.7	2.1	2.1	171	257	0	0
G11.11-1 <sup>3</sup>	18 10 28.1	-19 22 35	5.5	455.	30.1	5.3	29.5	1.9	1.9	234	352	1	1
G11.11-6 <sup>3</sup>	18 10 07.0	-19 29 06	4.3	411.	31.4	4.7	29.8	1.7	1.9	237	358	1	1
G11.11-7 <sup>3</sup>	18 10 06.5	-19 27 40	3.9	458.	31.0	2.9	29.4	2.3	2.4	363	547	0	0
G11.11-2 <sup>3</sup>	18 10 33.3	-19 22 00	3.2	325.	29.3	8.0	30.5	1.9	2.0	249	376	2	2
G11.11-9	18 10 32.9	-19 22 11	3.0	83.	14.0	8.0	30.5	1.9	1.9	104	157	0	0
G11.11-10	18 10 05.2	-19 26 34	2.8	109.	18.2	—	—	—	2.2	178	268	1	1
G11.11-11	18 10 05.7	-19 26 46	2.7	130.	19.1	—	—	—	2.2	198	299	0	0

Table 3.3: continued.

IRDC ident	RA	DEC	$N_{H_2}$	$M_{dust}$	$R_{eff}$	$N_{N_2H^+}$	$v_{N_2H^+}$	$\Delta v_{N_2H^+}$	aver. $\Delta v_{N_2H^+}$	$M_{vir,k=190}$	$M_{vir,k=190}$	PACS 70 $\mu m$ tag	MIPS 24 $\mu m$ tag
	[ $^\circ$ ]	[ $^\circ$ ]	[ $10^{22}$ $cm^{-2}$ ]	[ $M_\odot$ ]	[ $''$ ]	[ $10^{12}$ ]	[km/s]	[km/s]	[km/s]	[ $M_\odot$ ]	[ $M_\odot$ ]		
G11.11-12	18 10 18.0	-19 24 36	2.6	199.	25.1	7.8	29.9	1.7	1.7	158	238	1	1
G11.11-13	18 10 32.3	-19 22 27	2.5	237.	26.9	7.9	30.4	1.8	1.9	194	292	0	0
G11.11-14	18 10 05.4	-19 27 18	2.5	134.	19.1	—	—	—	2.3	205	309	0	0
G11.11-15	18 10 25.7	-19 22 58	2.5	166.	22.2	10.7	29.2	1.0	1.3	74	112	0	0
G11.11-16	18 10 04.8	-19 27 33	2.5	109.	18.5	—	—	—	2.0	158	238	0	0
G11.11-17	18 10 13.9	-19 24 17	2.1	106.	19.7	3.9	30.3	1.4	1.2	59	89	0	0
G11.11-18	18 10 21.4	-19 23 47	1.8	70.	16.3	8.5	29.3	1.6	1.6	86	130	0	0
G11.11-19	18 10 34.2	-19 20 59	1.7	73.	16.9	17.4	31.1	1.7	1.5	82	124	0	0
G11.11-20	18 10 22.0	-19 23 31	1.7	100.	20.3	8.2	29.2	1.6	1.6	110	166	0	0
G11.11-21	18 10 05.8	-19 26 05	1.6	75.	17.9	7.7	28.6	1.9	1.7	112	170	0	0
G11.11-22	18 10 21.0	-19 24 10	1.6	72.	17.3	10.7	29.4	1.6	1.7	102	154	0	0
G11.11-23	18 10 15.5	-19 24 37	1.5	37.	12.2	7.4	30.2	1.5	0.9	19	30	0	0
G13-4 <sup>5</sup>	18 17 34.9	-17 06 43	4.0	370.	42.4	4.7	21.7	2.0	1.5	155	235	2	2
G13-3 <sup>5</sup>	18 17 21.5	-17 09 18	2.0	70.	21.4	6.6	23.3	1.4	1.8	112	169	0	0
G13-1	18 17 19.2	-17 09 41	1.6	54.	19.7	—	—	—	3.5	379	571	0	0
G13-2	18 17 34.0	-17 05 27	1.5	20.	12.2	—	—	—	1.6	52	78	0	0
G1505	18 17 39.0	-15 48 53	1.4	36.	14.8	11.1	29.9	1.3	1.3	47	71	1	1
G2823-2 <sup>6</sup>	18 42 51.9	-03 59 52	15.9	3136.	51.1	3.1	78.1	3.4	3.3	1509	2276	3	2
G2823-3	18 42 37.3	-04 02 09	5.7	890.	35.2	3.6	80.8	2.5	2.5	626	944	1	0
G2823-1 <sup>6</sup>	18 42 50.4	-04 03 15	4.6	919.	37.4	7.7	79.2	3.4	3.5	1234	1861	3	2
G2823-4	18 42 48.9	-04 02 24	3.5	502.	28.9	8.1	80.0	2.7	3.0	722	1089	0	0
G2823-5	18 42 53.6	-04 02 33	3.0	771.	36.3	8.8	79.2	2.6	2.9	860	1298	2	2
G2823-6	18 42 46.5	-04 04 14	2.8	658.	34.2	5.4	79.3	3.0	3.1	883	1331	0	0
G2823-7	18 42 53.3	-04 00 57	1.9	118.	16.3	13.5	79.3	2.2	2.3	247	372	0	0
G2823-8	18 42 42.7	-04 01 43	1.8	176.	20.0	5.1	80.8	2.6	2.6	362	546	2	1
G2823-9	18 42 39.7	-04 00 33	1.8	85.	14.0	13.5	81.4	2.2	2.2	180	272	0	0
G2823-10	18 42 54.7	-04 01 08	1.7	145.	18.2	11.6	79.3	2.1	2.2	240	362	0	0

Notes: The columns are as follows: Clump identifier, as displayed in the figures; Names are adopted from <sup>1</sup>: Beuther et al. (2002b), <sup>7</sup>: Beuther et al. (2007), <sup>2</sup>: Beuther et al. (2012a), <sup>3</sup>: Johnstone et al. (2003), <sup>4</sup>: Motte et al. (wild guess 1998), <sup>6</sup>: Wang et al. (2008), <sup>5</sup>: Vasyunina et al. (2009)

### 3.3.1 Comparing integrated $N_2H^+$ and dust continuum emission

The left panels of Fig. 3.1 through Fig. 3.4 display the PACS 70  $\mu m$  maps with the long-wavelength dust continuum contours on top, the second left panel is the  $N_2H^+$  column density. They clearly show that the  $N_2H^+$  detection and column density agrees in general with the measured dense gas emission, almost independent of the evolutionary state of the clump.

The southern component of IRDC G11.11 appears to be peculiar, see Fig. 3.2. While for the northern component the molecular gas traced by  $N_2H^+$  agrees quite well with the cold gas traced by thermal dust emission, both dense gas tracers seem to disagree for the southern part. Comparing the brightest peak in the ATLASGAL data to the column density peak of the  $N_2H^+$  emission, we find a positional difference of  $37''$ , which is on the order of the beam size. Since the northern and southern component have been observed independently, a pointing error could explain the offset. However, before and in between the OTF observations we checked the pointing and the offset is considerably larger than

the anticipated pointing uncertainty. Therefore, we cannot explain the spatial offset of the southern map well.

For IRDC 18182, the bright north-western component is connected to IRAS 18182-1433 at a velocity of 59.1 km/s (Bronfman et al., 1996) and a distance of 4.5 kpc (Faúndez et al., 2004). Instead, the region of interest is the IRDC in the south-east at a distance of 3.44 kpc with a velocity of 41 km/s (Beuther et al., 2002a; Sridharan et al., 2005).

IRDC 18308 has been selected within this sample for its infrared dark cloud north of the HMPO IRAS 18308-0841. However, at its distance of 4.4 kpc we do not detect the  $\text{N}_2\text{H}^+$  emission from the IRDC with the velocity resolution of 0.2 km/s. To overcome the sensitivity issue we smoothed the velocity resolution to 0.4 km/s and then can trace the dense gas of the IRDC within IRDC 18308. For IRDC 18306 the situation is similar, we trace the HMPO, but not the IRDC. However, even with a velocity resolution of only 0.4 km/s we cannot detect  $\text{N}_2\text{H}^+$  from the IRDC. Therefore, we exclude IRDC 18306 from the discussion and show its dense gas properties in the appendix B.3. To get a better picture of the different regions we display in Fig. 3.1 through Fig. 3.4 the results from the smoothed maps, where helpful. However, because the coverage for many clumps is sufficient in the higher resolution data, we used the 0.2 km/s data to do our analysis.

The total gas peak column densities over the  $19.2''$  APEX  $870 \mu\text{m}$  beam as given in Table 3.3 range from  $1.4 \times 10^{22} \text{ cm}^{-2}$  to  $8 \times 10^{23} \text{ cm}^{-2}$ , and the median averaged peak column density of clumps that have been mapped is  $2.6 \times 10^{22} \text{ cm}^{-2}$ . If we consider only clumps for which the peak position has a detected  $\text{N}_2\text{H}^+$  signal, the median averaged peak column density becomes  $3.0 \times 10^{22} \text{ cm}^{-2}$ . For the lower limit one needs to keep in mind that we require a minimum column density threshold of  $1.0 \times 10^{22} \text{ cm}^{-2}$  for a clump to be detected. The upper limit is set by IRDC 18454-mm1 (adopted from W43-mm1, Motte et al. 2003; Beuther et al. 2012a), the brightest clump within IRDC 18454 and a well known site of massive star formation. All other clumps with peak column densities larger than  $1 \times 10^{23} \text{ cm}^{-2}$  (IRDC 18151-1, IRDC 18182-1, and G 28.34-2) host evolved cores and could be warmer than 20 K. However, to calculate the column densities we assume a constant average dense gas temperature of 20 K. While this is appropriate for most IRDCs in this sample with ongoing early star formation (cf. point sources in Ragan et al. 2012), using a higher temperature would decrease their peak column densities. With the exception of W43-mm1, the upper limit of column densities found within our survey's sources then becomes  $\sim 1 \times 10^{23} \text{ cm}^{-2}$  on scales of the beam size.

### 3.3.2 $\text{N}_2\text{H}^+$ abundance

In order to study the details of the correlation between the dense gas and the related  $\text{N}_2\text{H}^+$  column density, Fig. 3.5 shows the pixel-by-pixel correlation between the  $\text{N}_2\text{H}^+$  abundance ratio versus the flux ratio between the flux at  $70 \mu\text{m}$  and  $160 \mu\text{m}$ . One should keep in mind that, as explained in Sect. 3.2.7, the abundance ratio refers to different beam sizes, dependent on the telescope that has been used for the observations. The flux ratio of the two PACS bands, or color temperature, can be considered as a proxy of the dust temperature. For higher temperatures, the peak of the SED moves to shorter wavelengths, the  $70 \mu\text{m}$  becomes stronger compared to the  $160 \mu\text{m}$  flux. Therefore, higher temperatures have higher far-IR flux ratios. However, in order to derive proper temperatures, a pixel

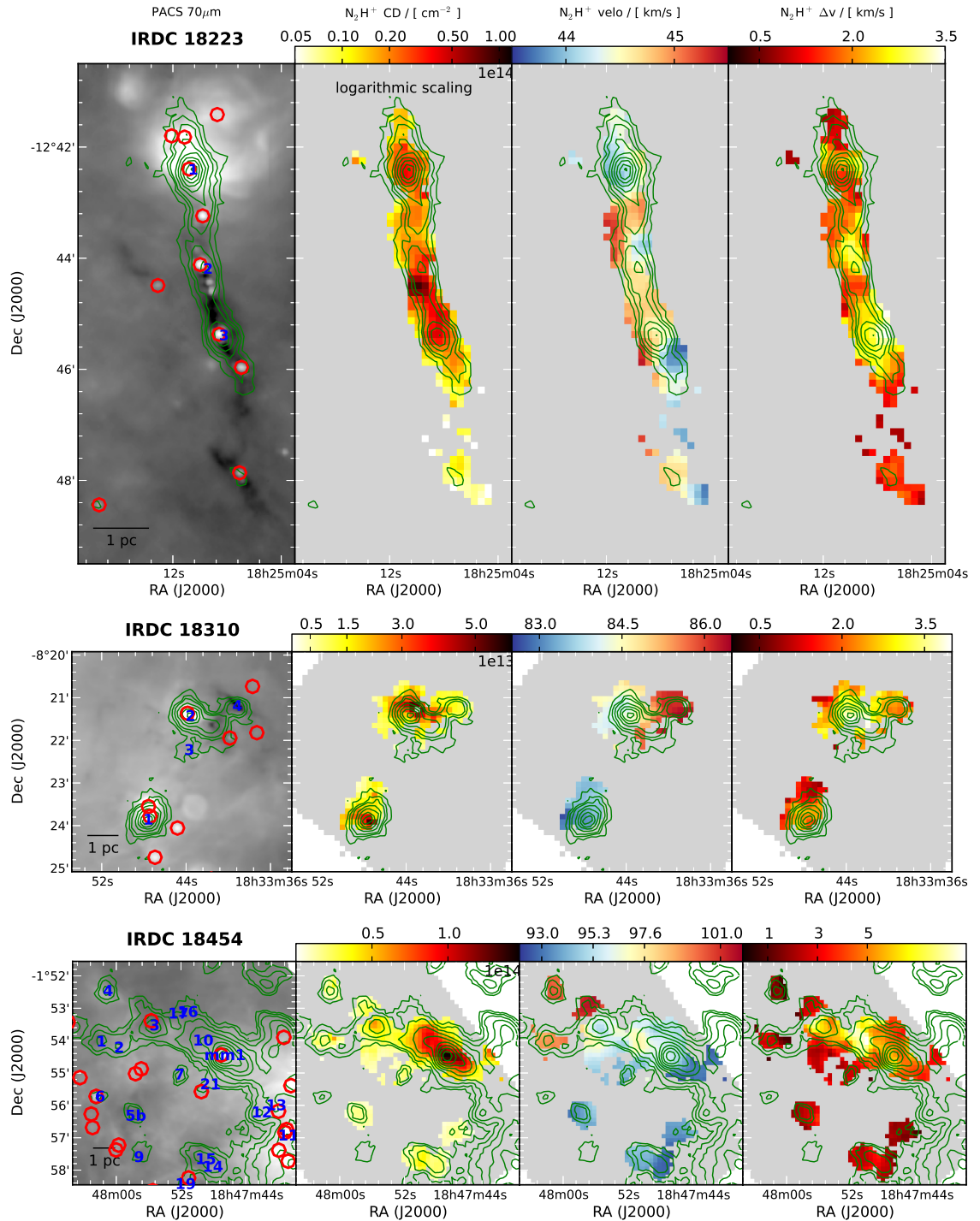


**Figure 3.1:** Parameter maps of the regions IRDC 18223, IRDC 18310, and IRDC 18454 mapped with the Nobeyama 45 m telescope, at top, middle, and bottom panel, respectively. The left panel of each row are the PACS 70  $\mu\text{m}$  maps with the PACS point sources detected by Ragan et al. (2012) indicated by red circles, the blue numbers refer to the sub-mm continuum peaks as given in Table 3.3. The second panel displays the  $\text{N}_2\text{H}^+$  column density derived from fitting the full  $\text{N}_2\text{H}^+$  hyperfine structure. The third and fourth panels show the corresponding velocity and linewidth (FWHM) of each fit. For IRDC 18223, and IRDC 18310 the contours from ATLASGAL 870  $\mu\text{m}$  are plotted with the lowest level representing 0.31 Jy, and continue in steps of 0.3 Jy. The contour levels for IRDC 18454 are logarithmic spaced, with 10 levels between 0.31 Jy and 31 Jy. The column density scale of IRDC 18223 is logarithmic.

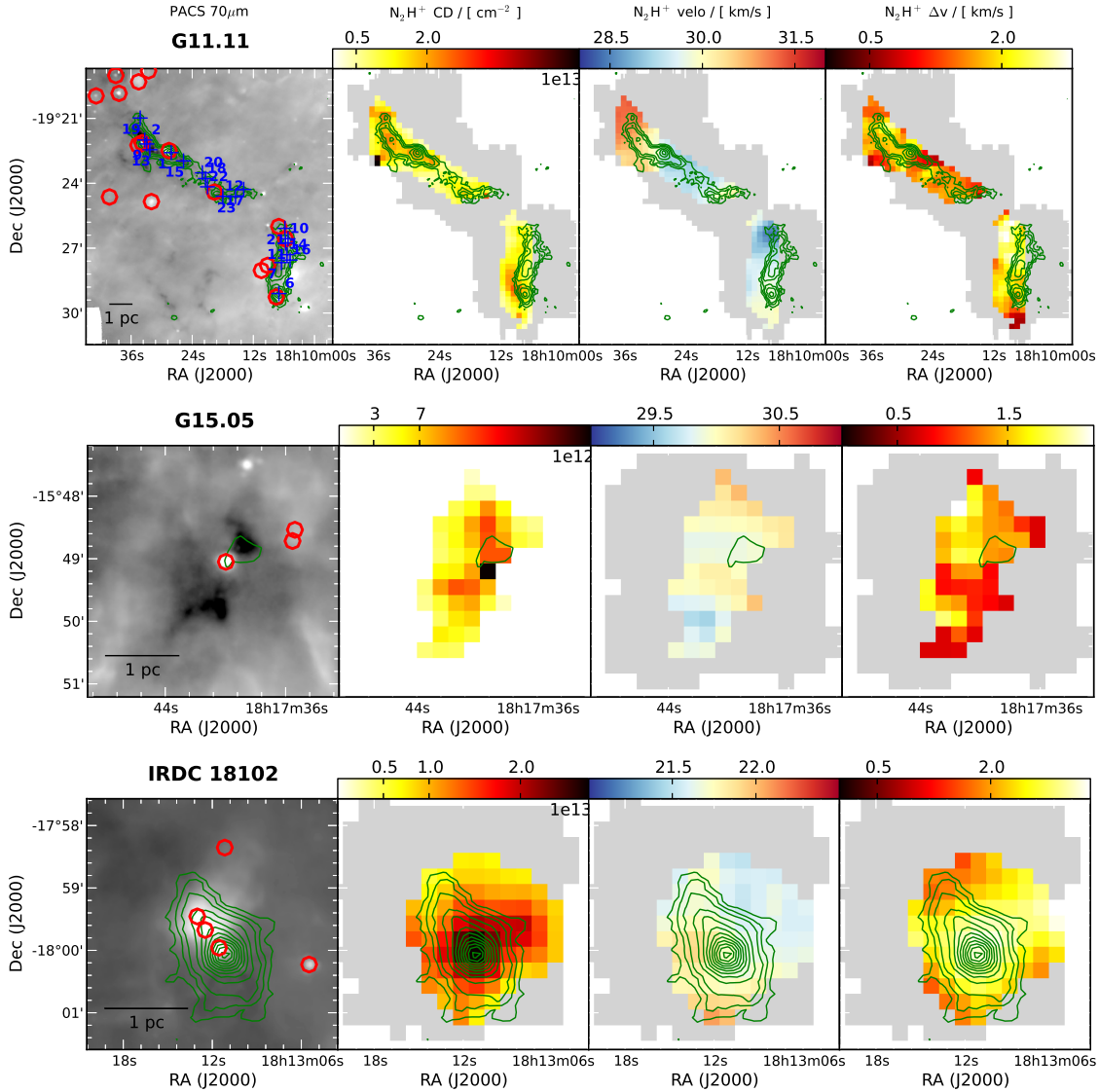


**Figure 3.2:** Parameter maps of the regions G11.11, G15.05, and IRDC 18102, mapped with the MOPRA telescope. The left panel of each row are the PACS 70  $\mu\text{m}$  maps with the PACS point sources detected by Ragan et al. (2012) indicated by red circles, the blue numbers refer to the sub-mm continuum peaks as given in Table 3.3. The second panel displays the  $\text{N}_2\text{H}^+$  column density derived from fitting the full  $\text{N}_2\text{H}^+$  hyperfine structure. The third and fourth panels show the corresponding velocity and linewidth (FWHM) of each fit. The green contours are from ATLASGAL 870  $\mu\text{m}$  at 0.31 Jy, 0.46 Jy, and 0.61 Jy, continuing in steps of 0.3 Jy. The velocity resolution in the G15.05 map is smoothed to 0.4  $\text{km/s}$  to improve the signal to noise and increase the number of detected  $\text{N}_2\text{H}^+$  positions.

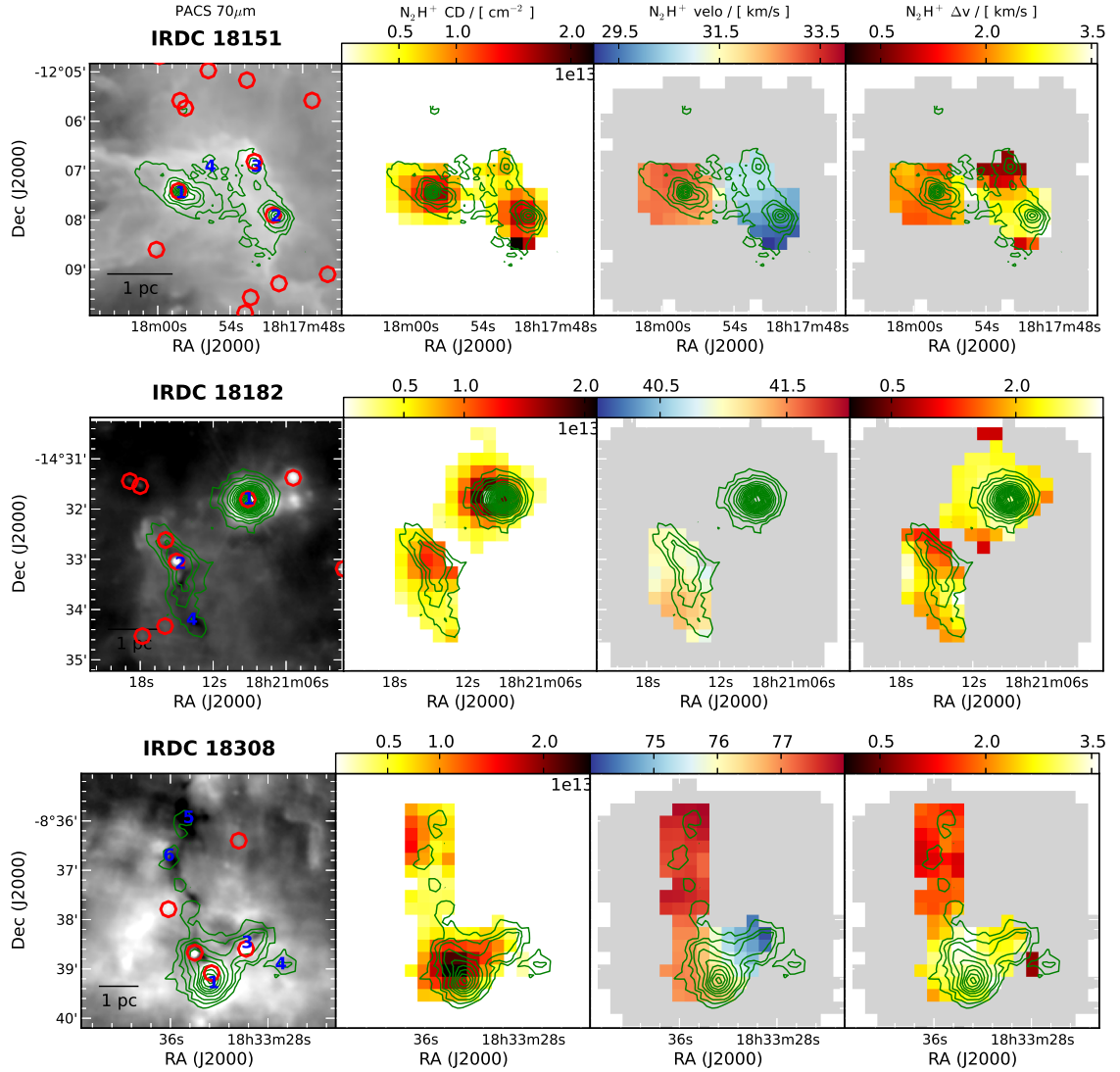


**Figure 3.3:** Parameter maps of the regions IRDC 18151, IRDC 18182, and IRDC 18308, each mapped with the MOPRA telescope. The left panel of each row are the PACS 70  $\mu\text{m}$  maps with the PACS point sources detected by Ragan et al. (2012) indicated by red circles, the blue numbers refer to the sub-mm continuum peaks as given in Table 3.3. The second panel displays the  $\text{N}_2\text{H}^+$  column density derived from fitting the full  $\text{N}_2\text{H}^+$  hyperfine structure. The third and fourth panels show the corresponding velocity and linewidth (FWHM) of each fit. The green contours are from ATLASGAL 870  $\mu\text{m}$  at 0.31 Jy, 0.46 Jy, and 0.61 Jy, continuing in steps of 0.3 Jy. For IRDC 18151 the contours are MAMBO 1.2 mm observations, starting at 60 mJy in steps of 60 mJy. In all three maps the velocity resolution is smoothed to 0.4 km/s.

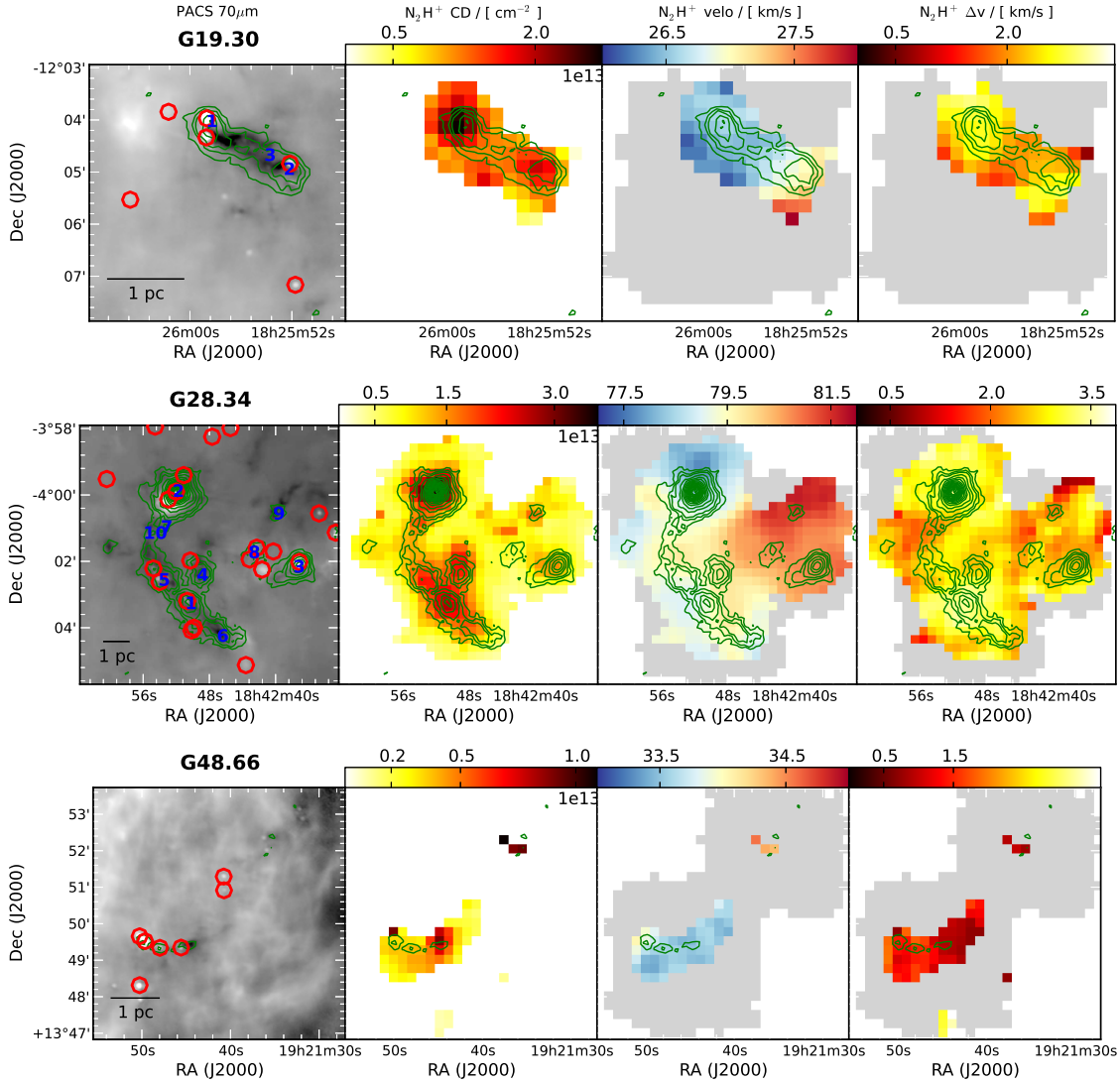


**Figure 3.4:** Parameter maps of the regions G19.30, G28.34, and G48.66, each mapped with the MOPRA telescope. The left panel of each row are the PACS 70  $\mu\text{m}$  maps with the PACS point sources detected by Ragan et al. (2012) indicated by red circles, the blue numbers refer to the sub-mm continuum peaks as given in Table 3.3. The second panel displays the  $\text{N}_2\text{H}^+$  column density derived from fitting the full  $\text{N}_2\text{H}^+$  hyperfine structure. The third and fourth panels show the corresponding velocity and linewidth (FWHM) of each fit. The green contours are from ATLASGAL 870  $\mu\text{m}$  at 0.31 Jy, 0.46 Jy, and 0.61 Jy, continuing in steps of 0.3 Jy. In all three maps the velocity resolution is smoothed to 0.4  $\text{km/s}$ .

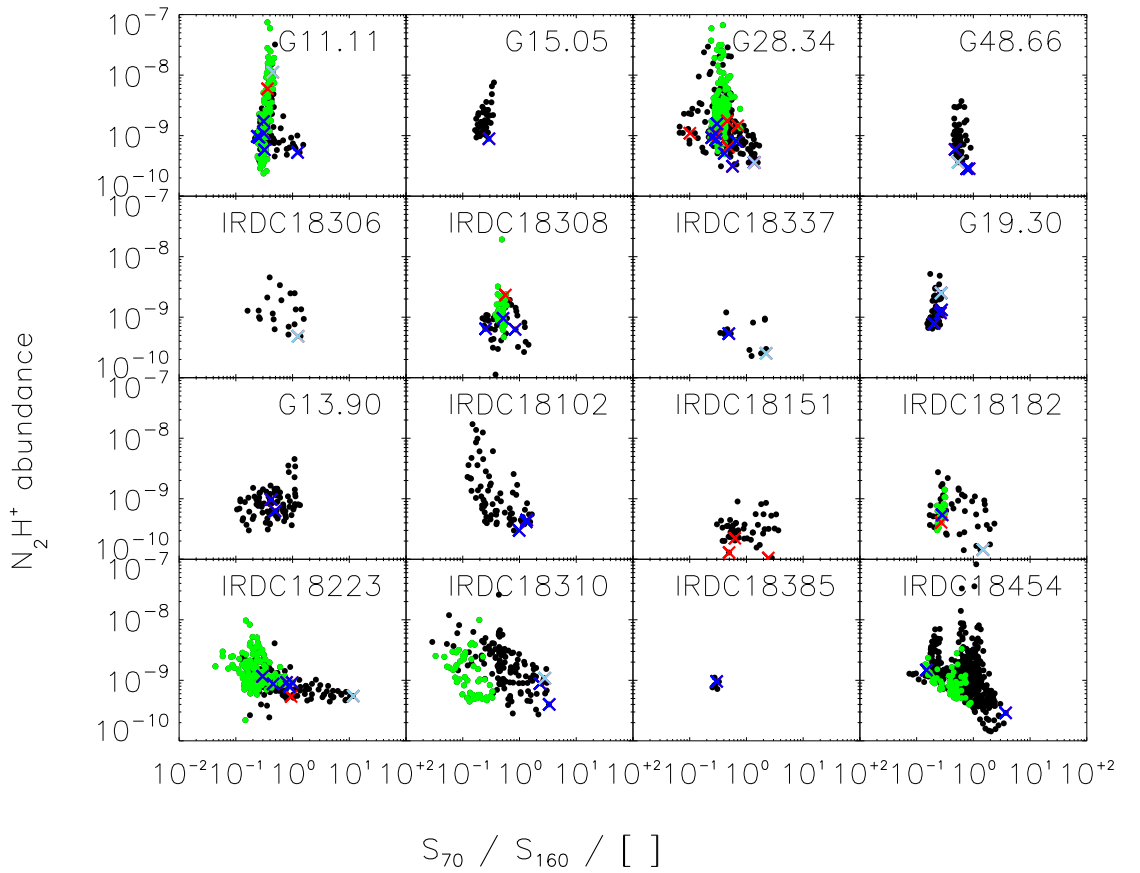


**Figure 3.5:** Plotted is the  $\text{N}_2\text{H}^+$  abundance ratio over the color index between  $70\ \mu\text{m}$  and  $160\ \mu\text{m}$ . Marked by green dots are pixels that lie within IRDCs. Overplotted with red Xs are all PACS sources that have been mapped. Blue crosses also have a  $24\ \mu\text{m}$  detection, while the light blue dots represent source that are saturated at  $24\ \mu\text{m}$ .

by pixel SED fitting is required, which will be done in an independent paper (Ragan et al., in prep.).

To allow a comparison between IRDCs and regions that do not show up in extinction, we marked pixels that lie within regions of high extinction in green. Those regions were selected by eye in the  $70\ \mu\text{m}$  images. As this is a soft criterion we do not aim to be complete but rather selected conservative boundaries around the dark regions.

Figure 3.5 shows no strong overall correlation between the  $\text{N}_2\text{H}^+$  abundance and the flux ratio, but it is significant that pixels of a flux ratio larger than unity have  $\text{N}_2\text{H}^+$  abundances below  $1 \times 10^{-9}$ . However, the reverse statement is not true, pixels of low  $\text{N}_2\text{H}^+$  abundance can still have low temperatures.

On the one hand, IRDC18223 is an example where there seems to be a correlation between the temperature and the  $\text{N}_2\text{H}^+$  abundance. The highest abundance ratios are found at far-IR flux ratios of the bulge of the pixel distribution, while toward higher temperatures the abundance seems to decrease systematically. On the other hand, G11.11

has an almost constant far-IR flux ratio, but its  $\text{N}_2\text{H}^+$  abundance varies over three orders of magnitude.

Marked by an 'X' in Fig. 3.5 are the pixels containing PACS point sources. In addition, we distinguish between sources that have only been detected at  $70\ \mu\text{m}$  and longwards, MIPS-dark sources, and PACS sources that have a  $24\ \mu\text{m}$  counterpart, MIPS-bright sources. If the  $24\ \mu\text{m}$  image is saturated at the given position, sources are considered as MIPS-bright as well. From the figure it can be seen that most embedded PACS sources have  $\text{N}_2\text{H}^+$  abundance ratios below  $1 \times 10^{-9}$  and tend to have higher temperatures than the bulge of the pixel distribution.

### 3.3.3 The large scale velocity structure of clumps and filaments

The velocity structure of the  $\text{N}_2\text{H}^+$  gas is shown in the third panel (second from right) of Fig. 3.1 to Fig. 3.4. As explained in Sect. 3.2.5, we fitted a single  $\text{N}_2\text{H}^+$  hyperfine structure to every pixel and display the resulting peak velocity.

The south-eastern region in the map of IRDC 18182 is the IRDC in the EPoS sample. It already had been known that IRAS 18182-1433, originally targeted by Beuther et al. (2002a), and the IRDC have different velocities and therefore are spatially distinct. All other sources mapped show velocity variations of only a few km/s and are therefore coherent structures.

The source with the largest spread in velocity is IRDC 18454 / W43. The mapped regions in the west, beyond W43-mm1 toward W43-main (which has not been mapped), have the lowest velocities at below 93 km/s, then there is a velocity gradient across W43-MM1 ending east at 97.4 km/s, and in the very south there are two clumps at 100 km/s. However, the velocity map has been derived fitting a single  $\text{N}_2\text{H}^+$  hyperfine structure to each spectrum. Beuther & Sridharan (2007) and Beuther et al. (2012a) have shown that, at least at high spectral and spatial resolution, clump IRDC 18454-1 has two velocity components. Trying to fit each clump peak position with two  $\text{N}_2\text{H}^+$  hyperfine structures, we find that for six continuum peaks, the  $\text{N}_2\text{H}^+$  spectrum is better fitted by two independent components.

While a more detailed description of the double line fits are presented in Sect. 3.3.4, we here want to note that the mapped line velocity is representing either a single component if one is much brighter than the other, or an average velocity of both. Therefore, the uncertainties for IRDC 18454 are significantly larger than for the other regions. Nevertheless, the large-scale velocity gradient is no artifact but is evident in the individual spectra.

Studying the velocity maps in Fig. 3.1 through Fig. 3.4 in more detail, we find two different patterns of velocity structure. On the one hand we find independent clumps that lie within the same region and may now or in the future interact, but are currently separate entities in velocity. A good example is IRDC 18151 plotted in Fig. 3.3. Using  $870\ \mu\text{m}$  as dense gas tracer we resolve two clump complexes separated by  $\sim 1\ \text{pc}$ . Across each clump there are only little velocity variations, but the east and west complex are separated in velocity space by 3.3 km/s. Velocity differences on the order of a few km/s between clumps within the same structure are common and we consider such clumps as spatially connected.

On the other hand, we find smooth velocity gradients across larger structures. Clumps, which may be at different velocities, have connecting dense material with a continuous velocity transition in between. To exclude overlapping, but independent clumps for which either the spatial resolution or our mapping technique mimic a smooth transition we searched for double-peaked velocities and a broadening of the line width in such transition zones.

The velocity maps of G15.05, IRDC 18102, IRDC 18151, IRDC 18182, and G48.66, Fig. 3.1, Fig. 3.2, Fig. 3.3, and Fig. 3.4, immediately reveal that those complexes have no velocity gradients and therefore are of the first type.

For IRDC 18310, shown in Fig. 3.1, the velocity map shows that the IRAS source in the south has a velocity of 83.2 km/s (see also Table 3.3), while the northern complex has larger velocities. Nevertheless, the velocity spread suggests an association between both clumps. In addition, the northern component itself has different velocities toward the east and south, with 86.1 km/s and 84.3 km/s. In between there is a short transition zone with an spatially associated increase in the linewidth (see very right panel of Fig. 3.1). The increase in linewidth suggests that there is indeed an overlap of two independent velocity components, rather than a large scale velocity transition. Using the unsmoothed Nobeyama image at an velocity resolution of 0.2 km/s, the spectra suggest two independent components. Therefore, IRDC 18310 consists of three clumps, each showing no resolved velocity structure.

IRDC 18151, shown in Fig. 3.3, consists of two clumps at different velocities. While the velocities of the western clump agree within 0.5 km/s, the eastern clump has a velocity gradient from the south-east to the north-west with a change in velocity of more than 1 km/s. However, at the velocity resolution of 0.2 km/s we do not detect the lower column density transition region and cannot exclude a smooth transition across both clumps. To overcome the sensitivity issue we smooth the  $\text{N}_2\text{H}^+$  data to a resolution of 0.4 km/s. Still, only a single pixel with a good enough signal to noise ratio connects both dense gas clumps. As we will discuss in Sect. 3.4.4, the found pattern does not suggest a smooth transition.

For IRDC 18454, IRDC 18308, G11.11, G19.30, and G28.34 we find smooth velocity gradients. One of the largest smooth velocity gradients of the sample is found toward the southern part of IRDC 18308, across the HMPO. Although there is an increase in the linewidth map, even in the unsmoothed higher resolution data we cannot find two independent components. Over 3.2 pc the velocity changes by 2.4 km/s, resulting in a velocity gradient of 0.8 km/s/pc. The change in velocity is parallel to the elongation of the ATLASGAL 870  $\mu\text{m}$  emission.

The velocity gradient in the northern part of G11.11 is similarly clear as it is for IRDC 18308 and follows the IRDC. While the very southern tip of the northern filament is at a slightly different velocity, up north it has an almost constant velocity up to the point G11.11-1 and then shows a strong but smooth gradient beyond.

As mentioned before, if considering the length and change in velocity only, the samples largest velocity gradient is found for IRDC 18454. Over a length of 8.4 pc the gradient is 0.9 km/s/pc. However, in between the two endpoints the velocity is not increasing monotonically.

IRDC 18223 shows significant changes in the velocity field, but is not listed among the clumps with smooth velocity gradients. The changes of the velocity are on 0.5 pc - 1 pc scales and show no clear pattern. Nevertheless, at the given velocity resolution of 0.5 km/s we do not find overlapping independent  $\text{N}_2\text{H}^+$  components. Therefore, all the gas on the scales we trace seems to be connected. It is worth noting that the two southern clumps, IRDC 18223-2 and IRDC 18223-3, have a gradient along the short axis of the filament, which might be interpreted as rotation. Velocities in the east are larger than the velocities in the west. In contrast, although less well mapped, the IRAS source in the north, IRDC 18223-1, has a similar velocity gradient, but in opposite direction.

For G13.90, IRDC 18385, IRDC 18306, and IRDC 18337 we lack the sensitivity to draw a conclusion. While IRDC 18385, and IRDC 18306 are not reasonably mapped at all, the data we have for G13.90 and IRDC 18337 suggest a velocity gradient, but with the given sensitivity we do not trace the gas in between the dense clumps, potentially building a smooth transition.

### 3.3.4 The $\text{N}_2\text{H}^+$ linewidth in context of young PACS sources and column density peaks

The right panel of Fig. 3.1 to Fig. 3.4 show the fitted linewidth (FWHM) for the mapped regions.

The distribution of the linewidth is very different for each region and density peak. While it increases toward some of the sub-mm peaks (e.g. IRDC 18102, IRDC 18182-1), for others the peak of the linewidth is on the edge of the sub-mm clumps (e.g. IRDC 18223-1, IRDC 18223-3, G19.30). The IRDCs for which we detect  $\text{N}_2\text{H}^+$  and that have no embedded/detected PACS source often have a smaller linewidth than other clumps of the same region with embedded protostars.

A brief description of the linewidth distribution of each region is given in the Appendix B.1. In the following we discuss a few interesting/notable examples.

While the linewidth in IRDC 18223 increases toward IRDC 18223-2 significantly, the linewidth toward IRDC 18223-1, a well studied HMPO (Sakai et al., 2010), and IRDC 18223-3, an object known to drive a powerful outflow (Beuther & Sridharan, 2007; Fallscheer et al., 2009), increases toward the edges of the dust continuum. Compared to other regions of IRDC 18223, the linewidth at IRDC 18223-3 is elevated, but it broadens further toward the north-west. This aligns very well with the outflow found by Fallscheer et al. (2009) and can be explained by it. IRDC 18223-1 was originally identified as IRAS 18223-1243 and is bright at IR wavelength (down to K band). However, typical tracers of ongoing high-mass star formation as cm emission, water and methanol masers, or SiO tracing shocks are not detected (Sridharan et al., 2002; Sakai et al., 2010). Only the CO line wings found by Sridharan et al. (2002) are indicative of outflows, which could explain the bipolar broadening of the  $\text{N}_2\text{H}^+$  linewidth well. Nevertheless, despite its prominence at IR wavelength and with the luminosity of the PACS point source at its peak of  $2000 L_\odot$  (point source 8 in Ragan et al., 2012), the linewidths at the continuum peak are not exceptional within this region. In contrast, although IRDC 18223-2 is detected at near IR wavelength as well and the PACS point source at its center has a luminosity of only  $200 L_\odot$ , the linewidth

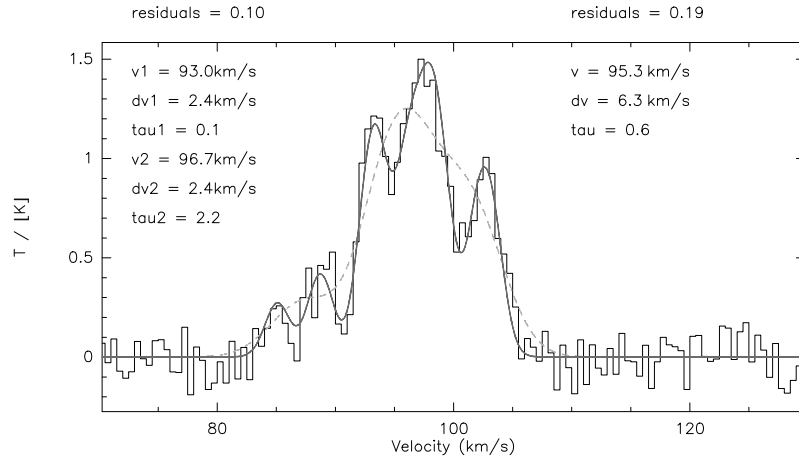


**Figure 3.6:** Spectra of IRDC 18454-4, labeled mm3 in Beuther & Sridharan (2007); Beuther et al. (2012a). While the dashed line shows the single component fit with the fitting parameters to the right, the solid line is the two component fit with its fitting parameters to the left. The given residuals are the results of the *minimize* task in *CLASS*.

is 2.5 kms/s compared to 1.9 km/s for IRDC 18223-1. Since Beuther & Sridharan (2007) find no SiO toward IRDC 18223-1/2 we exclude a strong outflow, and the reason for the line broadening is not clear at all. However, IRDC 18223-2 has not been addressed in such great detail and we cannot entirely exclude an outflow.

We exclude IRDC 18454 from the analysis of the linewidth since, as already mentioned in Sect. 3.3.3, we find multiple velocity components toward several positions. Figure 3.6 displays an example of an  $\text{N}_2\text{H}^+$  spectrum that compares a single component fit to a double component fit. Comparing the residuals of the two different fits as calculated by *CLASS*, for the six clumps in which we find two independent components the residuals are on average reduced by 30%. As for all two component fits, the linewidth decreases compared to a single component fit. However, the linewidths are then on average still larger than for the other clumps listed in Table 3.3.

Similar double velocity component fits toward the peaks are otherwise only possible in G11.11. Here, eight of the clumps are fit better by two independent  $\text{N}_2\text{H}^+$  components. However, different from IRDC 18454 the linewidth of the two components become on average smaller than the linewidth of other clumps in the sample. In addition, the improvement of the residuals is only 20%. Therefore it is unclear whether two independent components are present or the fit is simply improved because of the larger number of free parameters. However, a systematic study of the multiple components is beyond the scope of this paper.

For G13.90, IRDC 18385, IRDC 18306, and IRDC 18337 the mapped areas are not sufficient to draw conclusions.

Similar to Fig. 3.5, Fig. 3.7 correlates the linewidth (FWHM) of  $\text{N}_2\text{H}^+$  to the color index. Since the color index is a proxy of the temperature, a correlation between both quantities could have been expected. However, we do not see any correlation. Figure 3.8 plots the  $\text{N}_2\text{H}^+$  linewidth versus the  $\text{H}_2$  column density, but still, no correlation is found.

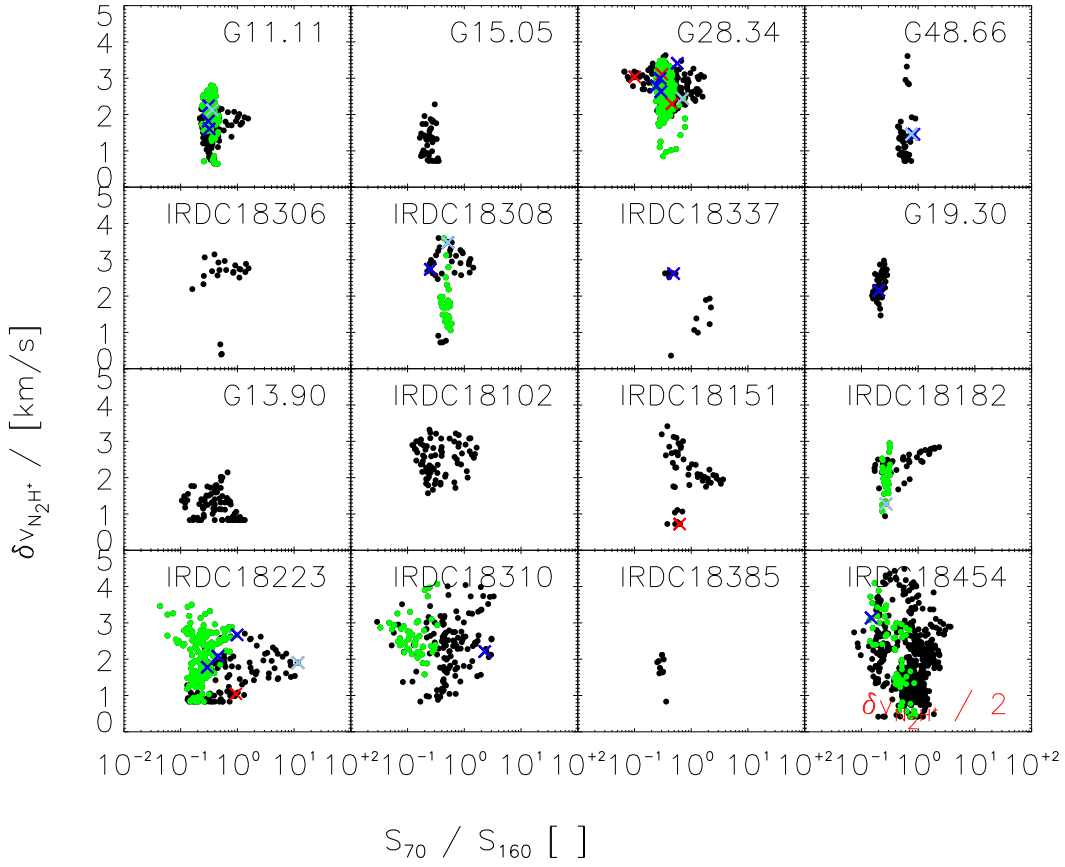


**Figure 3.7:** Plot of the  $\text{N}_2\text{H}^+$  linewidth versus the color index for the  $70\ \mu\text{m}$  over the  $160\ \mu\text{m}$  band. Marked by green dots are pixels that lie within IRDCs. Overplotted with red Xs are all PACS sources that have been mapped. Blue dots also have a  $24\ \mu\text{m}$  detection, while the pale blue dots represent source that are saturated at  $24\ \mu\text{m}$ .

In the context of the linewidth and dust mass, the virial analysis can be used to understand whether structures are gravitationally bound or are transient structures. Following MacLaren et al. (1988), we calculate the virial mass of our clumps via  $M_{vir} = k R \Delta v^2$ . For the clump radius  $R$  we use the effective radius calculated by CLUMPFIND. The geometrical parameter  $k$  depends on the density distribution, with  $k = 190$  for  $\rho \sim r^{-1}$ , and  $k = 126$  for  $\rho \sim r^{-2}$ . Beuther et al. (2002a) and Hatchell & van der Tak (2003) find typical density distributions in sites of massive star formation of  $\rho \propto r^\alpha$  with  $\alpha \sim -1.6$ , in between both parameters. While we list the virial mass for both parameters in Table 3.3, we use the intermediate value of  $k = 158$  in Fig. 3.9.

If we assume the error on our linewidth to be less than 15%, the uncertainties of the calculated virial mass are mainly determined by the geometrical parameter  $k$ . The actual error on the given virial masses is significantly larger since the calculation neglects all physical effects but gravity and thermal motions (kinetic energy). However, for the conceptual quantity we can neglect these effects and estimate the error to be  $\sim 50\%$ .

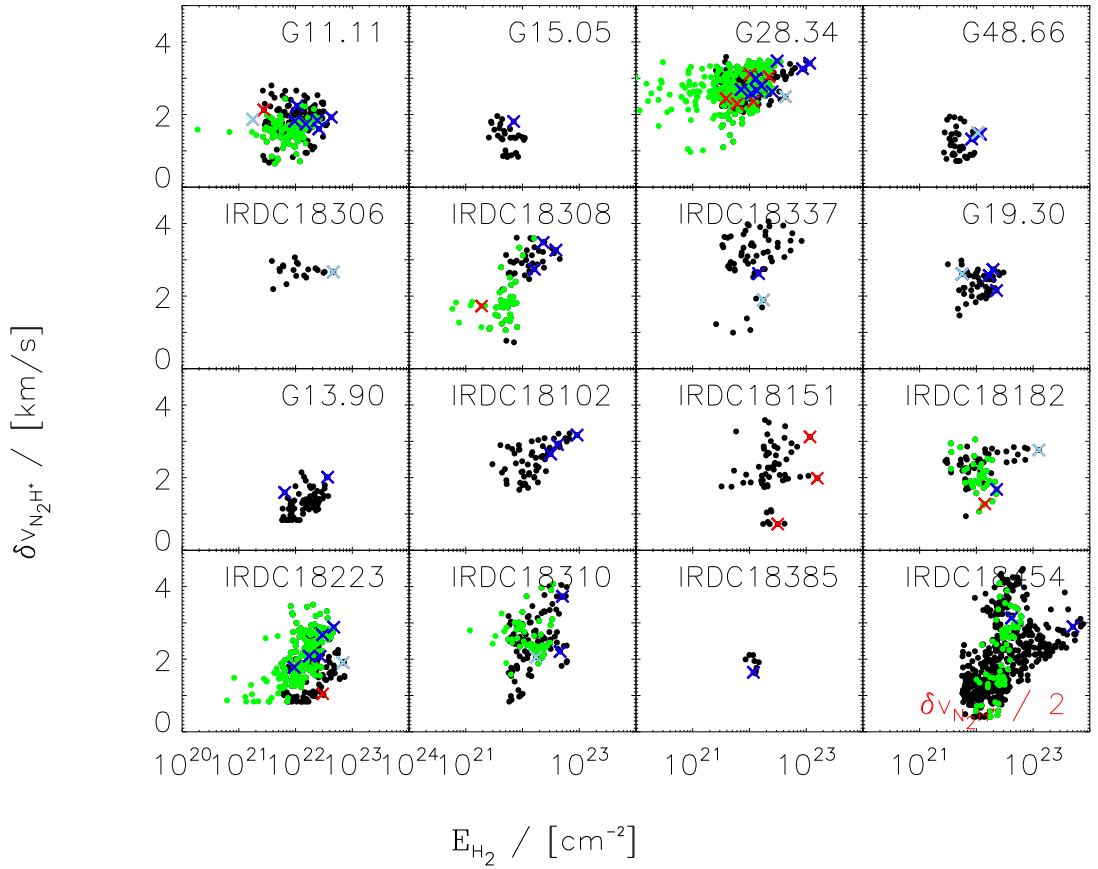


**Figure 3.8:** Plot of the  $N_2H^+$  linewidth versus the dust column density. Marked by green dots are pixels that lie within IRDCs. Overplotted with red Xs are all PACS sources that have been mapped. Blue dots also have a  $24\ \mu\text{m}$  detection, while the pale blue dots represent source that are saturated at  $24\ \mu\text{m}$ .

### 3.4 Discussion of $N_2H^+$ dense gas properties

In the following, we will discuss the kinematic properties of sources we mapped in  $N_2H^+$ , as described above.

#### 3.4.1 Dense clumps and cores

The clump masses in the range of several tens of  $M_\odot$  to a few thousands of  $M_\odot$  show that most regions have the potential to form massive stars in the future, or show signs of ongoing high-mass star formation. One should keep in mind that the listed peak column densities are averaged over the beam. As it has been shown by Vasyunina et al. (2009) assuming an artificial  $r^{-1}$  density profile, true peak column densities are larger by a factor of 20 to 40. This is in agreement with interferometric observations of clumps within our sample (Beuther et al., 2005, 2006; Fallscheer et al., 2011, Beuther et al., *subm.*). Therefore, all peak column densities become larger than  $3 \times 10^{23}\ \text{cm}^{-2}$ , or  $1\ \text{g}/\text{cm}^2$ . This reinforces the

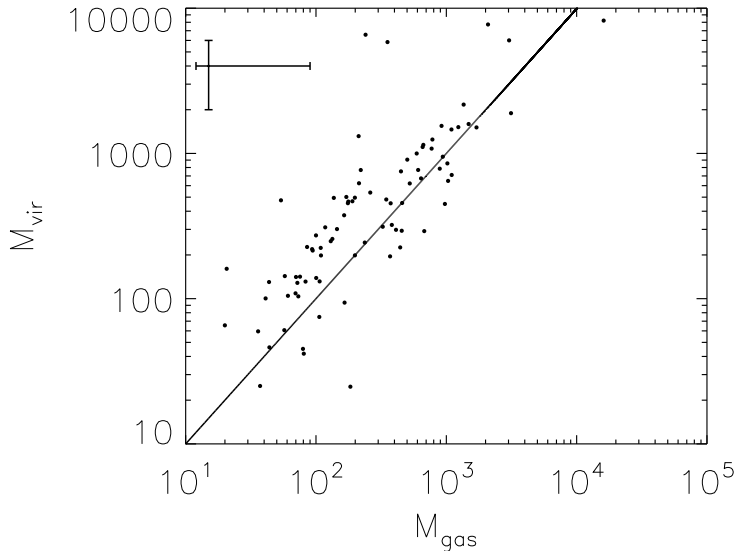


**Figure 3.9:** Plot of the virial mass derived from the  $\text{N}_2\text{H}^+$  line width over the gas mass. The virial mass assumes a geometrical parameter of  $k=158$ , which is intermediate between  $k=126$  for  $1/\rho^2$  and  $k=190$  for  $1/\rho$ . The solid line indicates unity.

view that the mapped clumps are capable of forming massive stars.

The high column densities are also in agreement with the detection of  $\text{N}_2\text{H}^+$  as high density gas tracer.

### 3.4.2 Abundance ratios

In order to understand why the abundance of  $\text{N}_2\text{H}^+$  is expected to vary with embedded sources or temperature, one needs to understand the formation mechanism. The formation of  $\text{N}_2\text{H}^+$  works via  $\text{H}_3^+$  which also builds the basis for the formation of  $\text{HCO}^+$  from CO. Due to the high abundance of CO in cold dense clouds, the production of  $\text{HCO}^+$  is initially dominant and consumes all  $\text{H}_3^+$ . However, if during cloud contraction the temperatures become cold enough for CO to freeze out,  $\text{N}_2\text{H}^+$  can be produced more efficiently and eventually becomes more abundant than  $\text{HCO}^+$ . The situation changes again when CO becomes released from the grains either due to heating or due to shocks. The CO destroys the  $\text{N}_2\text{H}^+$  and forms  $\text{HCO}^+$  instead, making  $\text{HCO}^+$  more abundant again. (For a more detailed discussion see Jørgensen et al. 2004.)

In summary, the early, (more diffuse) cloud phase is dominated by  $\text{HCO}^+$ , while the quiet dense clumps should be dominated by  $\text{N}_2\text{H}^+$ . With the onset of star formation,  $\text{HCO}^+$  is becoming dominant again.

The EPoS sample mainly has been selected to cover regions of ongoing, but early star formation. For the follow-up  $\text{N}_2\text{H}^+$  line survey, we selected regions covering all evolutionary stages. Many of them have both infrared quiet regions at the wavelength range

covered previous to *Herschel* as well as well known and luminous IRAS sources. Together with the *Herschel* data, hardly any region of high column density is genuine infrared dark.

As a result of both the  $N_2H^+$  evolution and the broad range of evolutionary stages covered, we expect a large range of  $N_2H^+$  abundance ratios. As it has been discussed in Sect. 3.3.2, Fig. 3.5 shows the correlation between the  $N_2H^+$  abundance and the  $70\ \mu\text{m}$  to  $160\ \mu\text{m}$  flux ratio as a proxy of the temperature. For all regions, the bulk of all pixels has  $N_2H^+$  abundances ratios of  $1 \times 10^{-9}$ . That is in good agreement with earlier studies of high-mass star-forming regions (Vasyunina et al., 2011, and references therein). At the same time several regions (e.g. G11.11, G28.34, IRDC 18454) show abundance variations of three orders of magnitude. While this is a result of the various evolutionary stages within each region, it is worth to note that it seems not to be correlated to the flux ratio of  $70\ \mu\text{m}$  over  $160\ \mu\text{m}$ . However, as noted in Sect. 3.3.2, all regions that do show an increased temperature have low abundance ratios.

In order to correlate some areas with an evolutionary stage, in Fig. 3.5 we differentiate larger regions that show up in extinction by green dots. We have selected only very obvious regions by hand that may contain faint mid-IR point sources. As Fig. 3.5 shows, these regions are among the coldest within each region. Nevertheless, while for regions where a differentiation was possible the high abundances are found mainly within the marked dark regions, they not necessarily have high  $N_2H^+$  abundances. In contrast to IRDC pixels which mark the earliest and coldest evolutionary stages, the PACS only sources mark regions in which star formation is about to start (red), and the MIPS bright PACS sources indicate ongoing star formation (blue). All pixels connected to a PACS source have low  $N_2H^+$  abundances. Whether this is due to an increase in temperature or probably because of shocks is unclear.

It has been shown in Ragan et al. (2012) that sources with detected  $24\ \mu\text{m}$  counterpart are on average warmer, more luminous, and more massive and therefore a  $24\ \mu\text{m}$  counterpart is indicative of a more evolved source. Nevertheless, the PACS core properties in Ragan et al. (2012) show a large overlap between MIPS bright and dark sources. Therefore, one cannot draw a clear conclusion on the evolutionary stage (temperature, luminosity, or mass) based on a  $24\ \mu\text{m}$  detection alone. This easily explains exceptions as e.g. in G11.11.

### 3.4.3 Signatures of overlapping dense cores within clumps

As we describe in Sect. 3.3.3, we find two independent velocity components toward six of the IRDC 18454 continuum peaks, as well as 7 clumps in G11.11 with double peaked  $N_2H^+$  lines. The two components have velocity offsets of only a few km/s. Since the hyperfine structure of  $N_2H^+$  includes an optically thin component, we can exclude opacity and self absorption effects, a common feature in dense star-forming regions. The two independent velocity components within IRDC 18454 have already been reported by Beuther & Sridharan (2007); Beuther et al. (2012a), and Ragan et al. (in prep.) find multiple velocity components toward G11.11. Combining our  $N_2H^+$  Nobeyama data with PdBI observations at  $\sim 4''$ , Beuther et al. (submitted) reveal multiple independent velocity components toward IRDC 18310-4. These are not resolved within the Nobeyama data alone at the spatial resolution of  $18''$ . Similar multi-component velocity signatures have been found in

high spatial resolution images of dense cores in Cygnus-X (Csengeri et al., 2011a,b), and toward IRDCs by Bühr et al. (in prep.). Therefore, it seems to be a common feature in high-mass star-forming regions.

Using radiative transfer calculations of collapsing high-mass star-forming regions, Smith et al. (subm.) show that such double peaked line profiles may be produced by the superposition of infalling dense cores. Therefore, in high-resolution studies, which filter out the large scale emission, multiple cores along the line-of-sight can be detected. However, comparing our beam sizes of  $\sim 0.5$  pc for IRDC 18454 and  $\sim 0.8$  pc for G11.11 to typical sizes of cores below 0.1 pc, the larger-scale clump gas should be dominating our signal. Therefore it is clear that multiple velocity components due to cores are more likely to be identified in high spatial resolution imaging. While IRDC 18454 is at the intersection of the spiral arm and the Galactic bar, and therefore exceptional in many aspects, G11.11 is likely a more typical high-mass star-forming region, similar to what has been simulated by Smith et al. (2009) and Smith et al. (subm.). If the double peaked line profiles originate from two dense cores within our beam, as suggested by Smith et al. (subm.), the cores within G11.11 would need to be extremely dense or large. Instead, it seems more realistic that we detect the gas of the clump as one velocity component, and the second component is produced by an embedded single core of high density contrast moving relative to its parent clump. For IRDC 18454 we even find double velocity spectra inbetween the peak positions. This suggests that the components are coming from two overlapping sheets, close in velocity. It is unclear whether these sheets are interacting or not.

#### 3.4.4 Accretion flows along filaments?

In Sect. 3.3.3 we presented the velocity structure of the 16 observed high-mass star-forming regions. As we described, 5 complexes have no velocity structure, while 6 regions have smooth large scale velocity gradients. The velocity structure of IRDC 18223 is more complex and does not fit into either of these categories. For 4 regions we lack the sensitivity to draw a conclusion.

Despite the two general appearances, the large scale velocity structure of the clumps is very diverse. In general, structures larger than 1 pc usually show some velocity fluctuations. These can be either steady and smooth, or pointing to separate entities. As expected, this shows that large-scale monolithic collapse, from clumps to single entities, does not occur.

In order to understand the velocity structure of complexes with smooth velocity transitions, Figure 3.10 through Fig. 3.13 visualize the velocity gradients along given lines.

As it has been discussed in Sect. 3.3.3, our velocity map of IRDC 18151 consists of 2 larger structures, IRDC 18151-1 in the east, and IRDC 18151-2 and IRDC 18151-3 in the west. The overall changes within the eastern and western clump are  $\sim 0.5$  km/s and  $\sim 1$  km/s, respectively. However, while the velocity cut through the eastern clump shows hardly any variation, the western clump has a noticeable velocity gradient. To detect at least part of the gas at intermediate velocities, we smoothed the  $\text{N}_2\text{H}^+$  to a velocity resolution of 0.4 km/s. The left part of Figure 3.11 shows the velocity profile across both clumps. While the western clump shows a slight velocity increase toward the east, the eastern clump shows no velocity gradient. Especially, both gradients seem not to match,

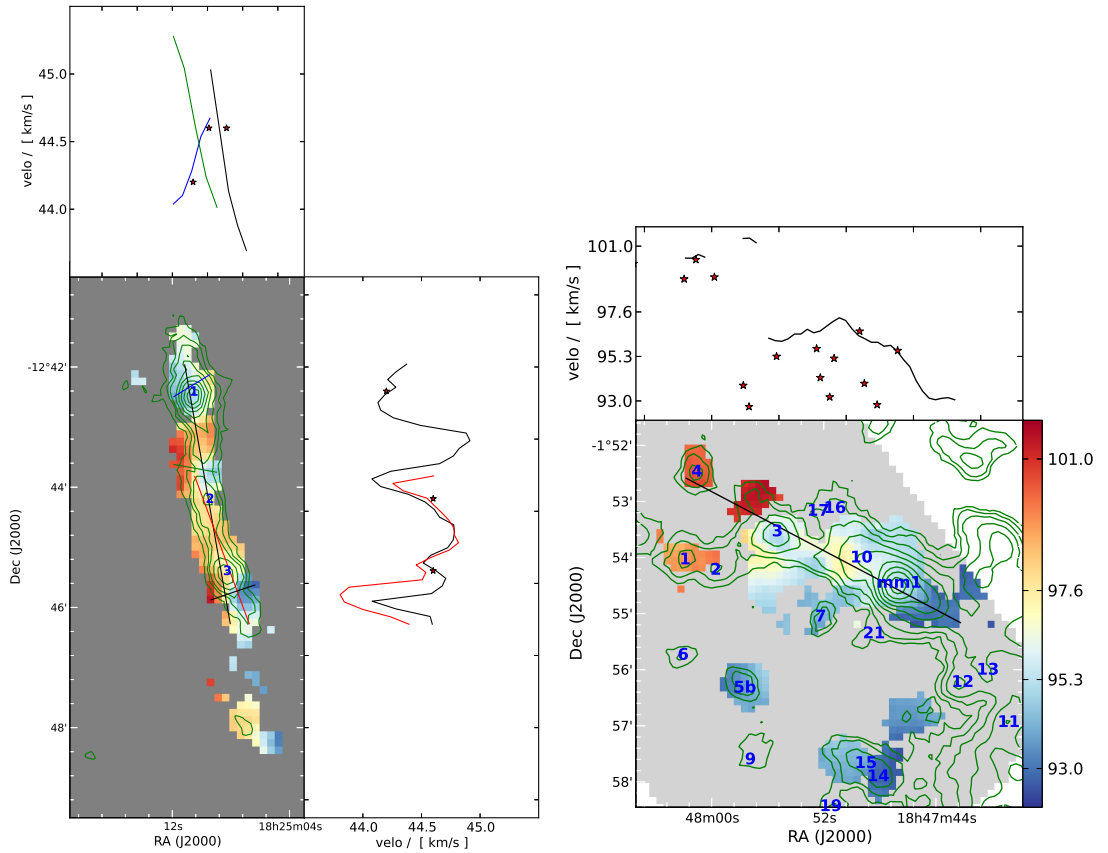


**Figure 3.10:** The left figure shows the profiles of the  $N_2H^+$  velocity of IRDC 18223, the right figure shows a velocity profile of IRDC 18454. The left panel of each figure shows the velocity map with contours from ATLASGAL on top (see also Fig. 3.1). The right and/or top panel show the velocity cuts along the lines marked on the velocity map. The stars mark the velocities of the clump peaks.

and if they interact dynamically, the transition zone would need to be short. Therefore we conclude that both structures are individual components, but in the context of other dense gas tracers both seem to be embedded within the same cloud. If seen from a slightly different angle, the double velocity components discussed in Sect. 3.4.3 could well originate from such a structure.

### Flows along G11.11

A clear smooth transition of the velocity we find toward the northern part of G11.11. Shown by the top profile in the left part of Fig. 3.12, between G11.11-1 and G11.11-12, the differences in velocity are below 0.5 km/s. Along the profile just south of G11.11-1, the velocity starts to increase, with higher velocities toward G11.11-2 and beyond. On the other hand, the profiles perpendicular to the filament, left part of Fig. 3.12, right panel, have almost constant velocities. Only the profile closest to G11.11-1 has a velocity gradient. However, the filament has a bend right at the position of the profile. A profile perpendicular to the actual shape of the IRDC would have no velocity gradient. Therefore,

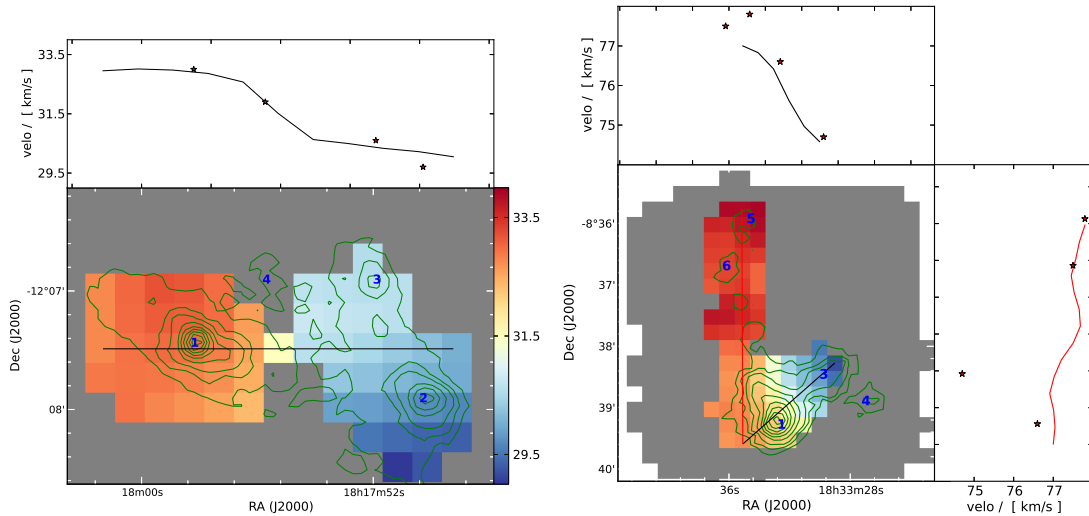


**Figure 3.11:** Left figure: Profile of the  $\text{N}_2\text{H}^+$  velocity of IRDC 18151; right figure: velocity profiles of IRDC 18308. The left panel of each figure shows the velocity map with contours from ATLASGAL on top (see also Fig. 3.3). The right and/or top panels show velocity cuts along the lines marked on the velocity map. The stars mark the velocities of the clump peaks.

we conclude that the velocity gradient is solely along the filament.

Both Tobin et al. (2012) (observationally), and Smith et al. (subm, numerically), suggest large-scale accretion flows along filaments on, and probably producing, central cores. They describe the expected observational signatures for filaments that are inclined from the plane of the sky. Imagine a cylinder with a central core, and material flowing onto the core from both sides at a constant velocity. For simplicity and without loss of generality, we put the central core at rest. Then, on each side of the central object the gas has a constant velocity along the filament. Since the gas is flowing in from both sides onto the core, a constant velocity is observed for both directions. The angle of the filament to the line-of-sight determines the observed velocity component. While Tobin et al. (2012) accounts for a gravitationally accelerated gas flow which should have a velocity jump at its center, the synthetical observations of high-mass star-forming regions performed by Smith et al. (subm.) have a smooth transition. They also find local velocity variations, connected to smaller substructures.

Recalling the velocity structure we find for G11.11, our observations could be explained by such accretion flows along the filament. The filament would need to have an angle such that the south-east is further away from us than the north-west. The almost constant velocity over  $\sim 3\text{pc}$  would be material moving toward G11.11-1, the most massive core in the region. Just before G11.11-1, the velocity starts to increase and we observe the transition across the core. Beyond G11.11-1, the gravitational potential of G11.11-2, the second most massive core in this region, accretes material on its own, and accelerates the gas even further beyond its position.

The scales we trace are an order of magnitude larger than what has been discussed by Smith et al. (subm.) and our resolution is an order of magnitude worse. Because

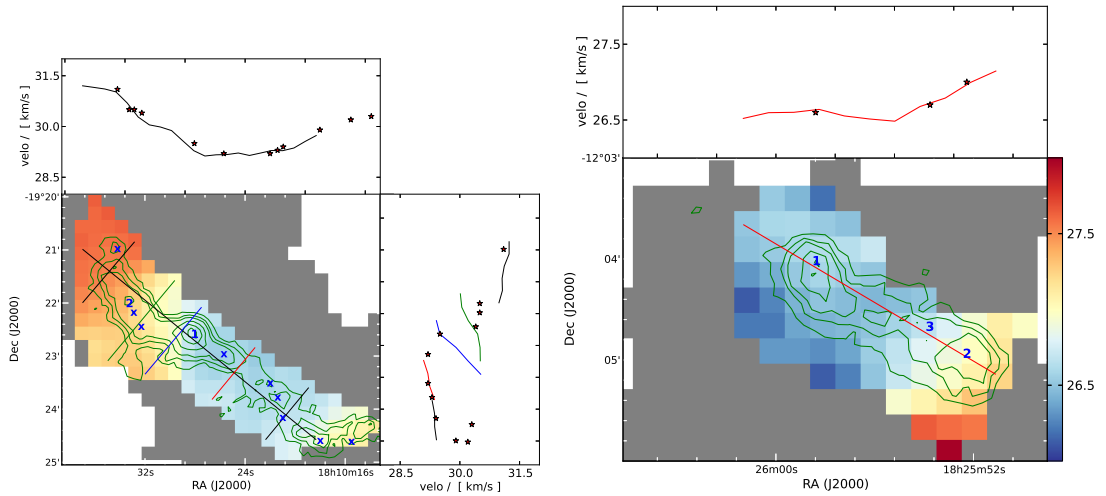


**Figure 3.12:** Left figure: Profile of the  $N_2H^+$  velocity of the northern part of G11.11; right figure: Velocity profile of G19.30. The left panel of each figure shows the velocity map with contours from ATLASGAL on top (see also Fig. 3.2). The top and/or right panels show velocity cuts along the lines marked in the velocity map. The stars mark the velocities of the clump peak.

of the second dense core, we do not observe the theoretically predicted pattern. The increase in velocity could also be explained by solid body rotation of part of the filament. Nevertheless, we propose an accretion flow along the filament as a possible explanation for the observed velocity pattern in G11.11. This view is supported by the fact that star-formation is most active at the center of potential inflow.

### Flows along IRDC 18308

A similar scenario could explain the velocity pattern along the IR dark part of IRDC 18308. The cut along the IRDC ending at the HMPO, see the right part of Fig. 3.11, shows only minor changes in velocity across the IRDC, but then decreases fast but smooth in the vicinity of IRDC 18308-1. The cut does leave a gap to the HMPO and does not fully close up in velocity. As described in Sect. 3.3.3, across the HMPO we find one of the largest velocity gradients in our sample, but the origin is unclear. One possible explanation that would produce a similar velocity profile is solid body rotation. In this picture, the knees at both ends of the profile would be caused by a transition from solid-body rotation to viscous rotation because of the lower densities in the outer regions. However, a full explanation would require a combination of hydrodynamic simulations with radiative transfer calculations. This is beyond the scope of this paper.

### Flows along G19.30?

An example that challenges the picture from above, large-scale accretion flows along the filament, is found toward G19.30, see right part of Fig. 3.12. Along the north-eastern part of the IRDC the velocity is constant over  $\sim 1$  pc, and then it rises toward its one

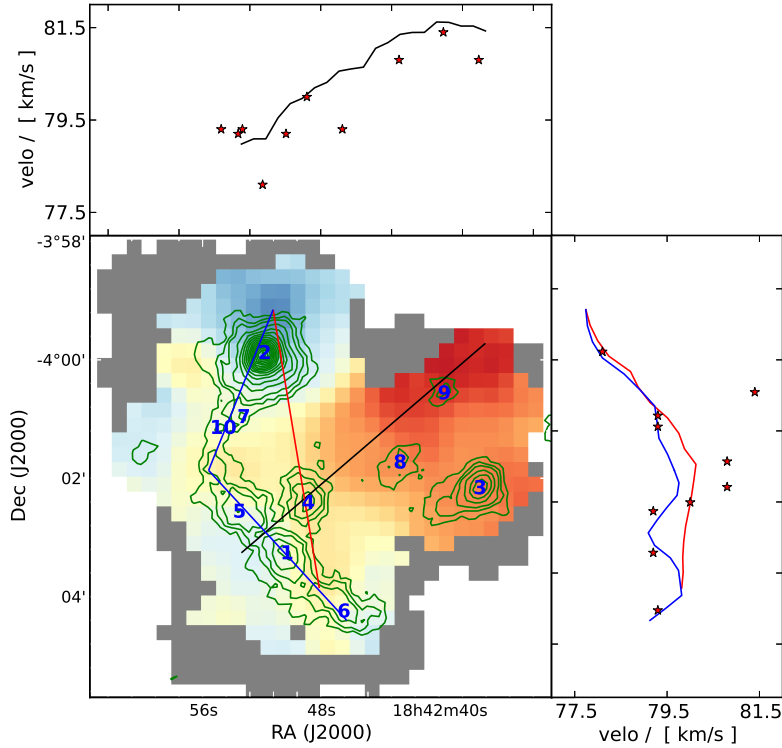


**Figure 3.13:** Profile of the  $\text{N}_2\text{H}^+$  velocity of G28.34. The left panel shows the velocity map with contours from ATLASGAL on top (see also Fig. 3.4). The top and right panels show velocity cuts along the lines marked in the velocity map. The stars mark the velocities of the clump peaks.

end. Therefore, it appears to be the velocity signature of a gas flow along the filament toward G19.30-2. However, the most massive clump, G19.30-1, is at the north-eastern edge of the IRDC. Therefore, the flow is opposite to the gravitational potential. The dust temperatures derived for the cores within G19.30 by Ragan et al. (2012) are higher for the more massive clump G19.30-1, increasing our uncertainties on the mass. Nevertheless, even if we assume the higher dust temperature of 25 K for the whole G19.30-1 clump, and a temperature of 17 K for G19.30-2, both masses become of the same order. The additional clump G19.30-3 close to G19.30-2, is of similar mass as G19.30-2 and therefore could increase the gravitational potential. Still, despite the suggestive observational signature of a gas flow, the mass distribution seems to contradict this picture. This shows that the velocity profile alone is not unambiguous. However, if the flow is primordial and the cores only formed from it, it is independent of the gravitational potential.

### The peculiar case of IRDC 18223

IRDC 18223 is filamentary, but with a more complex velocity structure than the previously discussed regions. Along the filament the velocity seems to be oscillating. The emission peaks of the southern clumps, IRDC 18223-2 and IRDC 18223-3, are at the same velocity of 44.6 km/s and in between the variations are minor. The peak of the clump IRDC 18223-1,

harboring the HMPO IRAS 18223-1243, has a velocity of 44.2 km/s.

Perpendicular to the filament, we find three extreme velocity gradients, shown in Fig. 3.10. Although they are not going directly across the dust continuum emission peaks, each seems to be associated with a clump. A straight forward interpretation would be solid body rotation along the filament axis. However, as mentioned in Sect. 3.3.3, the two lower profiles indicate rotation in contrary direction to the upper most profile. In Sect. 3.3.4 we discuss the possible influence of the powerful outflow within IRDC 18223-3 onto the linewidth distribution. The same outflow could also alter the velocity distribution in its direct vicinity. Nevertheless, a change in rotation orientation along a single filament seems counter intuitive. For the massive filament DR21 within Cygnus X, (Schneider et al., 2010) find three velocity gradients perpendicular to the filament axis, with alternating directions. Suggesting turbulent colliding flows as origin of the filament, they interpret the velocity pattern as a remnant of the external flow motions.

Within IRDC 18223-3, on scales of  $7''$ , Fallscheer et al. (2009) find a velocity gradient in  $N_2H^+$  and  $CH_3OH$ , a high density and shocked gas tracer. They successfully model the  $CH_3OH$  velocity gradient with an rotating and infalling toroid, significantly larger than massive disk candidates (e.g. Cesaroni et al. 2005, for a contradictive example see Boley et al. 2012). However, the small scale velocity gradient presented in Fallscheer et al. (2009) has not only a slightly different orientation (by  $\sim 45^\circ$ ), but is also rotating in the counter direction compared to the gradient presented in Fig. 3.10. This implies that both gradients are independent and have different origins; the small scale infalling toroid is not connecting the large scale envelope to a possibly even smaller scaled disk.

### **G28.34**

A quite large and complicated region is G28.34. Most prominent and clear, it has a strong but smooth east to west velocity gradient. Along the velocity cut given in the top panel of Fig. 3.13, the velocity changes by 2.6 km/s over 7.1 pc. This results in a velocity gradient of 0.4 km/s/pc. The clump emission peaks within the south-eastern component of G28.34, namely G28.34-6, G28.34-1, and G28.34-5, all have the same velocity. However, as the velocity cut along them shows, the velocity of the dense gas between them seems to be oscillating, similar as found for IRDC 18223. Even further north, the emission peaks of G28.34-7, and G28.34-10 are still at the same velocity as the more southern clumps. Only north of those the velocity changes monotonically to smaller velocities on the order of a parsec.

From the smooth velocity transition from east to west, as well as the absence of double peaked  $N_2H^+$  profiles, we conclude that all dense gas within the region is physically connected. However, to fully explain the observed velocity signatures of the complex dense gas morphology in G28.34, again numerical simulations are likely required.

### **IRDC 18454**

The velocity analysis of IRDC 18454 is hampered by the fact that, as discussed in Sect. 3.4.3, several clumps show two independent velocity components at their peak position.

Therefore, the mapped single velocities can either be the stronger of the two components, or an average of both. However, the large scale velocity gradient in east to west direction is clear and no artefact.

### 3.4.5 Discussion of the linewidth distribution

#### Outflow-induced turbulence

As we have described in Sect. 3.3.4, we find no correlation between the linewidth and neither the temperature, nor the  $\text{H}_2$  column density.

The lack of a correlation between the temperature and the linewidth can be explained by the narrow thermal linewidth. At 20 K, the thermal line broadening of  $\text{N}_2\text{H}^+$  is  $\sim 0.18$  km/s (in FWHM), and  $\sim 0.16$  km/s at 15 K. Compared to the observed linewidths of a few km/s, the non-thermal contribution dominates by far and temperature variations of a few K are smaller than our uncertainties of the measured FWHM.

Another possible contribution to the linewidth stems from turbulence. Since the clouds are close to virial equilibrium (see Fig. 3.9), the linewidth should scale with the column density. As mentioned in Sect. 3.3.4, we find no correlation between both quantities either. [NOTE: Is that actually true as I write it? Can one easily quantify the effect? (It can't be too hard to work it out when using  $M=k R \Delta v^2 \dots$ )]

Instead, the spatial resolution of the data prefers molecular outflows as the dominating contribution to the measured linewidths. Examining the  $\text{N}_2\text{H}^+$  linewidth maps of each region, we find clear imprints of known outflows onto the linewidth distribution. A good example in this context is IRDC 18223-3, shown in Fig. 3.1. As we described already in Sect. 3.3.4, Fallscheer et al. (2009) reports the outflow direction in IRDC 18223-3 to be  $\sim 135^\circ$  east of north. As Fig. 3.1 shows, we observe a line broadening along the same axis, with the highest velocities toward the edge. Due to the complex over-all velocity structure it is unclear whether the aligned velocity gradient is connected to the outflow as well. This would suggest the origin of the increased linewidth to be an unresolved velocity gradient. In contrast, shocks connected to bipolar outflows could enhance the turbulence, leading to broader lines. Another possible origin of a linewidth broadening toward the edge of clumps is provided by gravo-turbulent fragmentation, as described in Klessen et al. (2005). Therefore, we cannot assess the physical origin of the linewidth distribution. However, in this particular case the alignment of outflow and linewidth broadening suggests a direct connection.

A similarly clear correlation between the linewidth and outflow we find for IRDC 18102, for which the outflow direction has been observed by Beuther (priv. communication). For G11.11-1, Gómez et al. (2011) observed an outflow in east-west direction, or  $90^\circ$  east of north, while we find a significant line broadening similar to a bipolar outflow with an angle of  $\sim 158^\circ$  east of north.

Although the outflow has not been spatially resolved, the presence of SiO suggests the existence of an outflow toward the northern part of G15.05, while the southern part is SiO quiet (Linz et al., in prep.). Despite both the northern and southern part are IR dark even at  $70 \mu\text{m}$  and the mass distribution peaks in between, the linewidth distribution

in the north is significantly larger than in the south. A possible outflow could explain this linewidth distribution. Using SiO as general tracer of outflows, we find similar correspondence between increased linewidth and the presence of outflows for IRDC 18151-2, G19.30-1, and G19.30-2, and the eastern tip of G48.66.

No SiO has been found toward the IR dark part of IRDC 18182, IRDC 18182-2, and -4, for which the linewidths are among smallest within the region. However, in between the two clumps the linewidth broadens without the presence of known outflows. Therefore, additional factors have to be dominating here, for example superposition of the two independent velocity components.

The four pointings toward G28.34 covering SiO emission (Linz et al., in prep.) agree with the picture of an outflow dominated linewidth distribution. Nevertheless, due to the generally broad lines in that region, the variations are less pronounced as for all other regions.

A particular case seems to be IRDC 18151-1. Fallscheer et al. (2011) reports an outflow connected to it with an angle of  $315^\circ$  east of north, but the linewidth is smaller than in IRDC 18151-2, 1.9 km/s compared to 3.1 km/s, respectively. In addition, it shows hardly any linewidth structure, and therefore differs from the other clumps, discussed so far.

Sridharan et al. (2002) and Sakai et al. (2010) find no SiO toward the two northern clumps of IRDC 18223, IRDC 18223-1, and IRDC 18223-2, but Sridharan et al. (2002) interpret the detection of CO line wings as an indication for an outflow. Therefore, the bipolar line broadening of the edges of IRDC 18223-1 (see Sect. 3.3.4) could be caused by an outflow. In contrast, the linewidth broadens toward the center of IRDC 18223-2. As the large-scale velocity gradient across IRDC 18223-2 is twice as big as for IRDC 18223-1, the line-broadening toward the center could be explained by unresolved small-scale velocity gradients. An alternative explanation for the broadening of the linewidth could be colliding flows, as discussed in Sec. 3.4.4. However, the velocity gradients are not perfectly aligned with the linewidth broadening which would be expected for colliding flows.

We have no information on the SiO or other outflow tracers for IRDC 18310, and IRDC 18308.

### The particular case IRDC 18454

The line width map of IRDC 18454 for a single component fit, given in Fig. 3.1, provides a combination over both components. Therefore, it quantifies the internal motions within each beam and is appropriate for the virial analysis. However, resolving the individual velocity components at the peak positions reduces the line width of the clumps significantly. They become more comparable to the other regions within this survey, but still, the resulting line widths are broader than the average line width that we find for all clumps.

Combining our Nobeyama 45 m  $N_2H^+$  single dish data with observations from the Plateau de Bure interferometer, Beuther et al. (2012a) find two independent velocity components toward IRDC 18454-1 as well. While one of their two components is consistent both in width and velocity with one of our components, the other component is offset by

$\sim 1$  km/s and twice as wide in the single-dish data. This difference can be explained by the better spatial resolution of  $\sim 3.5''$  of the PdBI observations. Although the two fragments Beuther et al. (2012a) resolve within IRDC 18454-1 have very similar velocities, Fig. 7 in their paper shows a velocity spread of a few km/s over the Nobeyama beam size of  $18''$ . However, as already apparent from Fig. 3.1, the linewidth toward IRDC 18454-1 is particularly narrow compared to almost all other clumps within IRDC 18454. This can be explained partly by the absence of any  $70 \mu\text{m}$  PACS source and its distance to W43-mm1.

### 3.5 Infall and outflow signatures

#### 3.5.1 Comparing the $\text{HCO}^+$ self-absorption to $\text{H}^{13}\text{CO}^+$

It has been shown in the past that the line profiles of optically thick emission lines in combination with optically thin lines can be used to study the infall or outflow of gas onto cores (Myers et al., 1996; Smith et al., 2012). A blue skewed line profile of an optically thick transition suggests infall along the line of sight. (For a depicted explanation see Smith et al. 2012.) However, in order to differentiate multiple velocity components from self-absorption an optically thin transition is needed.

Within our survey we find that almost all regions with estimated total gas column densities from the sub-mm emission above  $1 \times 10^{22} \text{ cm}^{-2}$  show self-absorbing  $\text{HCO}^+$  and HNC spectra. From visual inspection, mainly of  $\text{HCO}^+$  in comparison to  $\text{H}^{13}\text{CO}^+$ , we identified clear blue skewed self-absorption profiles over a larger area in IRDC 18102, G15.05, G11.11, and G28.34. Furthermore we find skewed self-absorption profiles toward IRDC 18182-1. However, since we have neglected this HMPO in our  $\text{N}_2\text{H}^+$  studies, we will not further discuss them. While the HMPO IRDC 18308-1 shows both blue and red skewed profiles, the IR dark part of IRDC 18308, IRDC 18308-5, and -6 shows only red skewed  $\text{HCO}^+$  profiles. No asymmetries were found in IRDC 18151, and G48.66. Although the  $\text{H}^{13}\text{CO}^+$  lines of IRDC 18337-4 and G19.30 are at the detection limit, they seem to suggest either a second velocity component (both not seen in  $\text{N}_2\text{H}^+$ ) or asymmetries due to outflows. Therefore, we refrain from an interpretation.

Within this survey paper we constrain our detailed analysis on the clear asymmetric line profiles, seen over a larger area (IRDC 18102, G15.05, G11.11, and G28.34). To quantify the infall we use the method given in (Myers et al., 1996). They have shown by comparison to analytical models that the infall velocity is given by

$$v_{\text{in}} \approx \frac{\sigma^2}{v_{\text{red}} - v_{\text{blue}}} \ln \frac{1 + e \times T_{\text{BD}}/T_{\text{D}}}{1 + e \times T_{\text{RD}}/T_{\text{D}}}. \quad (3.5)$$

Here,  $\sigma$  is the linewidth of an optically thin transition, and  $v_{\text{blue}}$  and  $v_{\text{red}}$  are the velocities of the blue and red shifted emission peaks, respectively. As shown in Fig. 3.14,  $T_{\text{BD}}$ , and  $T_{\text{RD}}$  are the difference between the intensity of the blue and red shifted emission peaks,  $T_{\text{blue}}$ , and  $T_{\text{red}}$ , and the strength of the emission dip  $T_{\text{D}}$ .

To derive these parameters from the spectra of our observations, we have independently fitted the  $\text{HCO}^+$  and  $\text{H}^{13}\text{CO}^+$  spectra smoothed to a velocity resolution of 0.4 km/s at each mapped position. The  $\text{HCO}^+$  spectra were fitted by two independent Gaussian profiles,

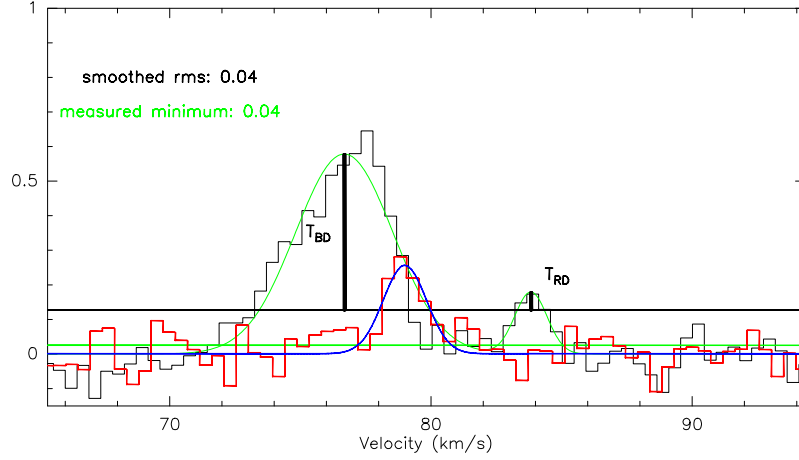


**Figure 3.14:** Comparison of optically thick  $\text{HCO}^+$  and  $\text{H}^{13}\text{CO}^+$  spectrum within G28.34. The black histogram shows the  $\text{HCO}^+$  spectrum, with the sum of the two independent Gaussian fits of the blue and red shifted component plotted in green. The straight green solid line indicates the algorithmically measured minimum of the emission dip, while the black horizontal line depicts the  $3\sigma$  level of the spectrum smoothed twice (not plotted here). The two black vertical lines show the measured  $T_{BD}$ , and  $T_{RD}$ , after subtracting  $T_D$ , here given by the  $3\sigma$ . The red spectrum is  $\text{H}^{13}\text{CO}^+$ , with the fit shown in blue.

determining  $v_{\text{blue}}$  and  $v_{\text{red}}$  as well as  $T_{\text{blue}}$  and  $T_{\text{red}}$ . To determine the strength of the dip  $T_D$  we smoothed the spectrum even further and then searched for the minimum in between the blue and red velocity component. If the emission between both the blue and red shifted peak is below  $3\sigma$  of the again smoothed spectrum, we use the  $3\sigma$  value instead. Together with the linewidth of the optically thin  $\text{H}^{13}\text{CO}^+$  line we then calculated the infall velocity for all spectra that have an integrated  $\text{H}^{13}\text{CO}^+$  line intensity larger than  $5\sigma$ . Since the line detection is proven by a  $5\sigma$  criterion but the peak position is crucial for the infall velocity, we additionally require that the fitted peak intensity of  $\text{H}^{13}\text{CO}^+$  is brighter than twice our rms.

For spectra where we substitute  $T_D$  with its upper limit of  $3\sigma$ , the derived infall velocities are only upper limits. We have compared the upper limits to the values we obtain if we use the measured dip emission. While the discrepancies for G28.34 are on average on the order of 20%, the discrepancies for G15.05 are on average 50%.

Fig. 3.15 display the derived upper limit infall velocities for IRDC 18102, G15.05, G11.11, and G28.34, in which we found blue skewed  $\text{HCO}^+$  line profiles in several mapping pixels. We find the largest infall velocities toward G28.34 with above 1 km/s.

As Fig. 3.15 shows, the majority of each region is in large scale infall motion. However, while we find only a few individual pixels with outward moving gas within IRDC 18102, G15.05, and G11.11, Fig. 3.15 shows red skewed profiles on the entire clump G28.34-3 and its surrounding, also covering the north-west IRDC. In contrast, the IRDC filament connecting from the east to the main structure is among the regions with the highest infall velocities.

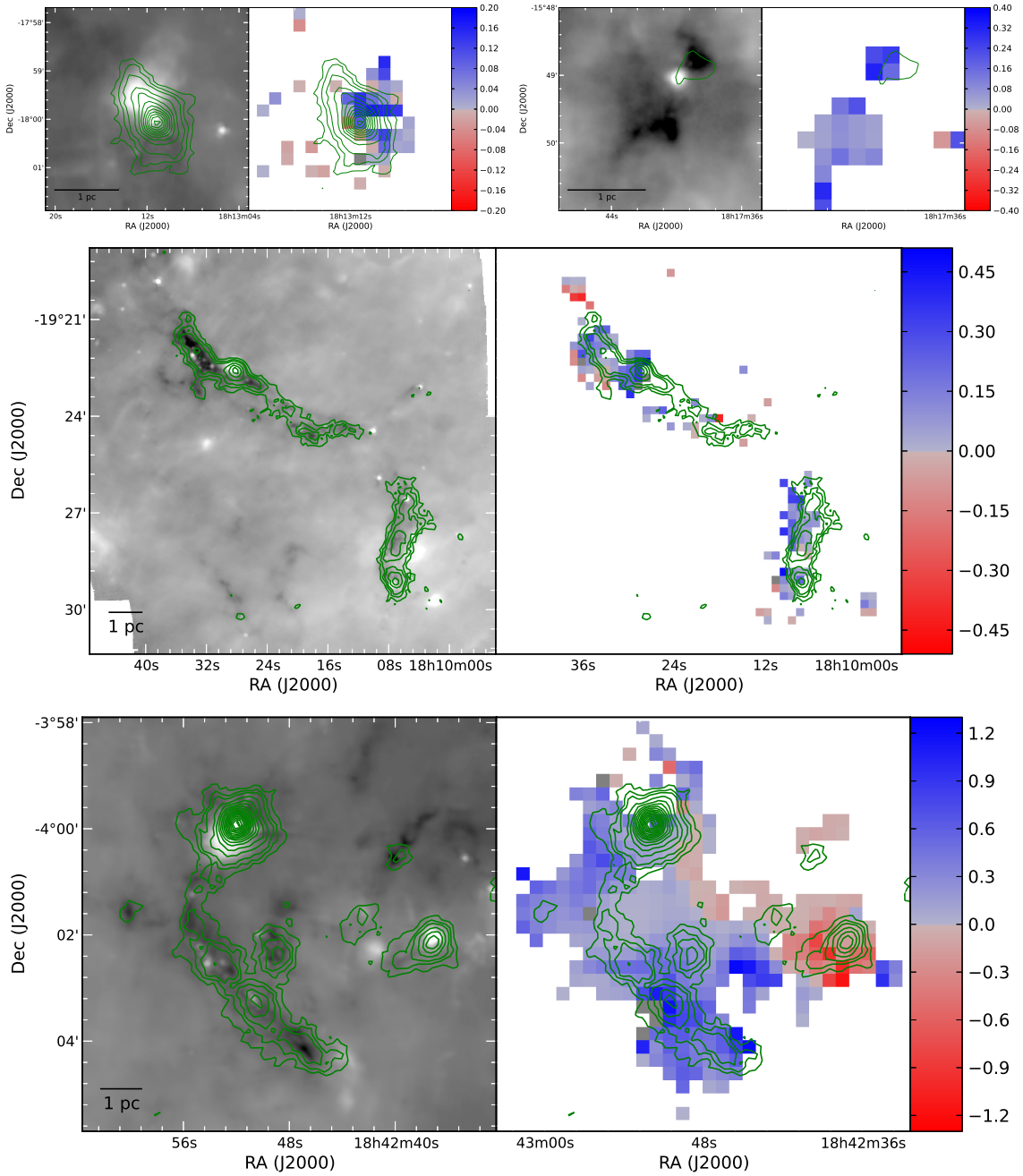


**Figure 3.15:** Infall maps (gas velocity along the line of sight) of IRDC 18102, G15.05, G11.11, and G28.34. The left panels show the 70  $\mu\text{m}$  maps with contours from ATLASGAL. The right panel shows the same contours on top of the gas infall maps, derived from the analysis of the HCO<sup>+</sup> line profile in comparison to the H<sup>13</sup>CO<sup>+</sup> velocities. Note that the plotted infall velocities are upper limits, only.

### 3.5.2 Discussion of the global infall

In Sect. 3.5.1 we describe the detection of blue skewed  $\text{HCO}^+$  profiles and use their the asymmetry to calculate the relative line-of-sight velocity of the gas. For four regions we are able to map the outwards moving and, mainly, in-falling gas.

As Fig. 3.15 shows, three of the four regions are dominated by infall motion of the gas. G28.34 is divided into the eastern part with global infall, and the western part with red skewed  $\text{HCO}^+$  profiles. As mentioned in Sect. 3.5.1, we find the highest infall velocities for G28.34, amounting to more than 1 km/s. Assuming an ISM-like gas composition at 20 K, the thermal sound speed becomes  $\sim 0.2$  km/s. While the infall speed onto IRDC 18102 is below 0.2 km/s everywhere, all other regions show infall in excess of the thermal sound speed. Taking into account that the given infall speeds are only upper limits and may be smaller by a factor of two (see Sect. 3.5.1), both G11.11 and G15.05 could still have sub-sonic motions. However, for G28.34 super-sonic infall motions are very likely.

Similar results were obtained by Schneider et al. (2010) for the DR21 filament. Using the same method to calculate the infall velocities (Myers et al., 1996), they find infall with speeds up to 0.8 km/s. In addition, they used a 1D non-LTE radiative transfer model with global infall to reproduce their observed spectra. The resulting velocities are in good agreement with their values derived using the method given in Myers et al. (1996), affirming its reliability.

In the context of high-mass star-forming regions, Smith et al. (2009) ran smoothed particle hydrodynamical simulations of a  $10^4 M_{\odot}$  molecular cloud, resulting in globally infalling clumps. Using radiative transfer, Smith et al. (subm.) calculate the resulting line profiles of the optically thick  $\text{HCO}^+$  line as well as the isolated, optically thin  $\text{N}_2\text{H}^+$  component. While in low-mass star-forming regions less than  $\sim 50\%$  of the cores in global infall show blue-skewed line profiles, in high-mass star-forming regions they find blue asymmetries on clump scales. The expected infall velocities are on the order of 1.5 km/s. However, the asymmetry in the optically thick  $\text{HCO}^+$  is often small compared to the linewidth, hampering its detection. Therefore, our observations agree very well with prediction of the competitive accretion scenario (Bonnell et al., 2004; Smith et al., 2009).

## 3.6 Conclusions

Complementary to the existing *Herschel*/EPoS data, we mapped 16 massive star-forming regions in  $\text{N}_2\text{H}^+$ . Using CLUMPFIND on sub-mm data, mainly from the ATLASGAL survey at  $870 \mu\text{m}$ , we extracted the clump population that our observations cover. Assuming a constant dust temperature of 20 K and the distances given in Ragan et al. (2012), we calculated both peak column densities and clump masses. With only a few exception, the  $\text{N}_2\text{H}^+$  and total gas column density distribution spatially agrees very well, but the  $\text{N}_2\text{H}^+$  abundance varies in IRDCs by three orders of magnitude.

While five complexes show no velocity structure, six regions have smooth velocity gradients. For three regions the velocity structure is consistent with accretion flows along a filament. For DR 21 Schneider et al. (2010) find a velocity pattern very similar to what we find for IRDC 18223, and suggest that the velocity gradients perpendicular to the

filament are remnants of colliding flow motions the filaments has formed from. For G28.34 and IRDC 18454, the velocity structure is very complex and a detailed modeling is beyond the scope of this work.

The linewidth distribution among the sources is very diverse, in particular, IRDC 18454 stands out. Even after resolving double-peaked line profiles and treating them carefully, its average linewidth is twice the value we find for all other regions. Sources for which the outflow direction is known show a line-broadening along the outflow. In addition, all clumps that have measured SiO show an increased linewidth, while the other clumps show hardly any variations. Therefore, the linewidth on the scale of clumps seems to be dominated by outflows and unresolved velocity gradients.

From a comparison of the optically thick  $\text{HCO}^+$  to the optically thin  $\text{H}^{13}\text{CO}^+$ , we find global gas infall in four regions. While the fastest infall in IRDC 18102 is below 0.2 km/s, the infall velocities in G28.34 become as high as 1.2 km/s. Only for a single clump we find red-skewed line profiles. As it has been shown by Smith et al. (subm.) this could be a line-of-sight effect.

In conclusion, this study supports a very dynamic star-formation scenario. Clumps continuously accrete mass from their surrounding, and cores accrete from their dense filament. Whether the cores form from flows along filaments, or their gravitational potential are the origin of the flows is unclear.

## Chapter 4

# Triggered/sequential star formation? A multi-phase ISM study around the prominent IRDC G18.93-0.03

In the previous chapter we have shown that large-scale gas motions are no exception in high-mass star-forming regions. Here we want to investigate whether a dynamically expanding HII region can affect a starless clump and make it prone to collapse.

This chapter has been accepted for publication in A&A (Tackenberg, Beuther, Plume, Henning, Stil, Walmsley, Schuller, & Schmiedeke, 2012b). Minor changes have been applied to avoid duplications.

### 4.1 Introduction

Based on the Galactic plane survey GLIMPSE (Benjamin et al., 2003), it has become possible to study bubble-like structures in the Milky Way in a statistical sense. Initially, Churchwell et al. (2006) found a “bubbling Galactic disk” and identified 322 bubbles. Today, several compilations of bubbles in the Milky Way exist (e.g. Churchwell et al., 2006, 2007). The most extensive of which has been compiled by “The Milky Way Project” (Simpson et al., 2012), a citizen science project. They visually identified and classified more than 5000 bubbles. Infrared bubbles are defined by their bright  $8\ \mu\text{m}$  emission rims. Although their origin may be manifold, many of the bubbles have shown to be created by a, not necessarily central, ionizing source. In this context, the emission rim originates from UV excited polycyclic aromatic hydrocarbons (PAHs). While all hydrogen ionizing photons are absorbed within the borders of an ionization front, lower energy UV photons pass through the ionization front and may excite the PAHs. In addition, the ionizing source heats its surrounding gas, which expands and drives a shock front beyond the ionization front. In between the shock and ionization front, neutral material can be accumulated. Elmegreen & Lada (1977) discussed the triggering of star formation on the borders of

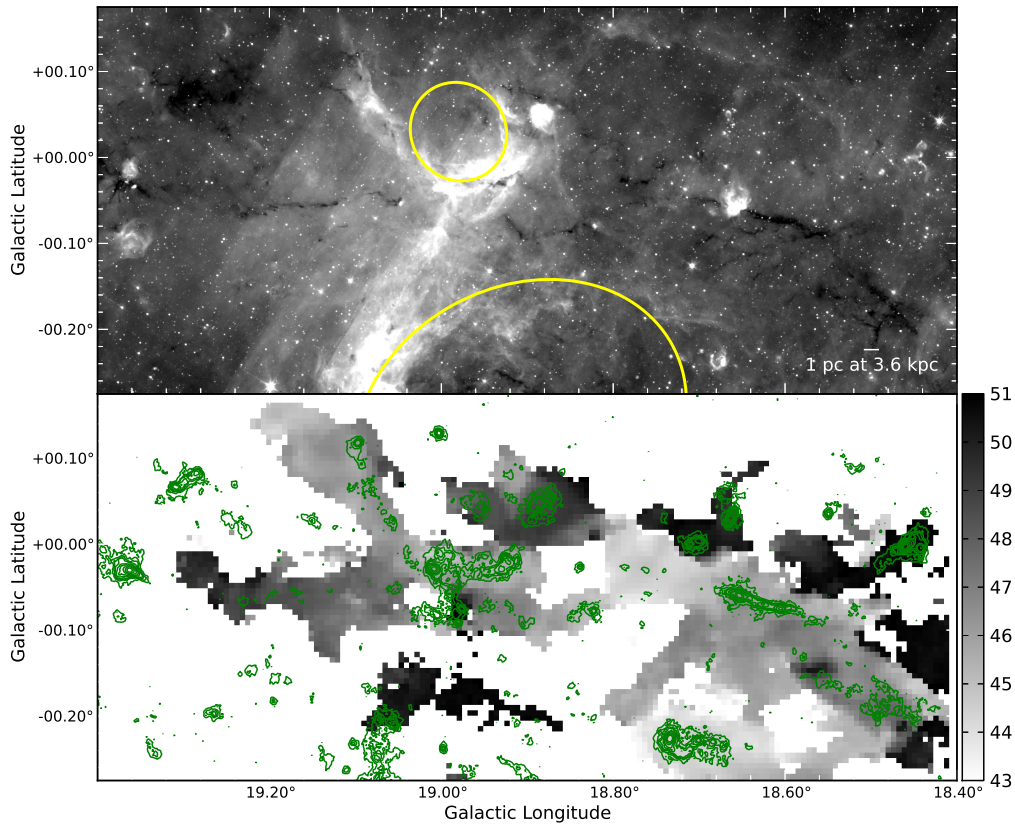


**Figure 4.1:** An IRDC filament along the Galactic plane, spanning across from the *lower right* ( $18.45^\circ$ ,  $-0.20^\circ$ ) to the *upper left* ( $19.30^\circ$ ,  $-0.02^\circ$ ). The *top panel* shows a  $8\ \mu\text{m}$  *Spitzer* image and the color stretch is chosen to bring the IRDC to prominence. The *lower panel* presents the intensity weighted peak velocity (moment 1) map of the GRS  $^{13}\text{CO}$  data. Regions with velocities outside the  $43\ \text{km s}^{-1}$  to  $51\ \text{km s}^{-1}$  are clipped. The green contours are from ATLASGAL with contour levels at  $0.15\ \text{Jy}$  or  $3\sigma$ ,  $0.3\ \text{Jy}$ ,  $0.4\ \text{Jy}$ ,  $0.5\ \text{Jy}$ ,  $0.7\ \text{Jy}$ ,  $0.9\ \text{Jy}$ ,  $1.3\ \text{Jy}$ ,  $1.8\ \text{Jy}$ , and  $2.5\ \text{Jy}$ . The yellow ellipses indicate the bubbles as given in Simpson et al. (2012).

expanding HII regions. Among others, “collect and collapse” describes the collapse of swept up material along a compressed layer. Deharveng et al. (2003) and Zavagno et al. (2006) established “collect and collapse” observationally. A brief overview on triggered star formation is given in Deharveng et al. (2010).

Other results of the GLIMPSE survey are systematical and sensitive studies of infrared dark clouds (IRDCs, e.g. Peretto & Fuller, 2009). Previously discovered by the two infrared satellites ISO and MSX, their high column densities absorb the background emission even at infrared wavelengths and thus become visible as dark patches. With such high column densities, IRDCs are believed to be the cradles of the next generation of stars (Rathborne et al., 2006; Simon et al., 2006). In addition, a rising number of large scale Galactic plane surveys allow one to trace the various stages of star formation. From mm and sub-mm observations of cold, dense clumps and cores (Schuller et al., 2009; Bally et al., 2010) to mid- to near-IR observations of young stellar objects (Benjamin et al., 2003; Carey et al., 2009; Molinari et al., 2010) and stars as well as the ionized and molecular gas (Condon

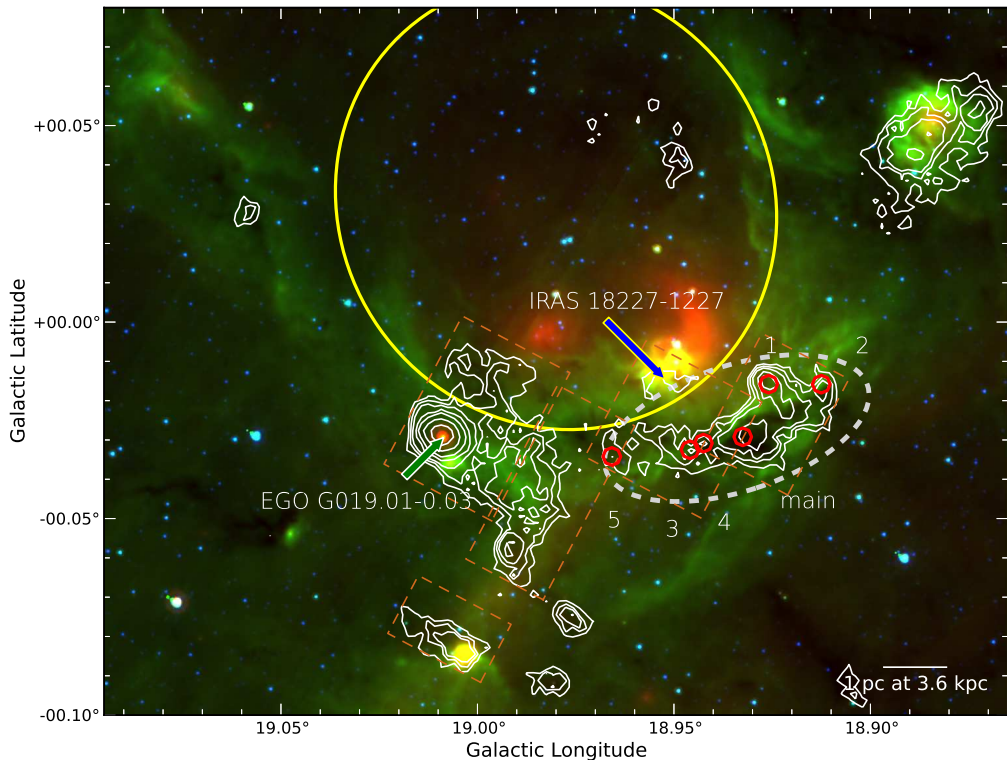


**Figure 4.2:** Three color image of the bubble connected to the long filament, MWP1G018980+00304, composed from the *Spitzer* 3.6  $\mu\text{m}$ , 8  $\mu\text{m}$ , and 24  $\mu\text{m}$  bands in blue, green, and red, respectively. White contours are from ATLASGAL (at 0.3 Jy, 0.4 Jy, 0.5 Jy, 0.7 Jy, 0.9 Jy, 1.3 Jy, 1.8 Jy, and 2.5 Jy) for which the numbers denote the CLUMPFIND peaks, marked by the red circles. The yellow solid ellipse marks the bubble with interpolated bubble dimensions adopted from Simpson et al. (2012). The two arrows mark IRAS 18227-1227, and the massive proto-stellar object EGO G019.01-0.03. While the dashed orange boxes indicate the areas that have been mapped in  $\text{H}^{13}\text{CO}^+$  with the IRAM 30 m telescope, the gray dashed ellipse is drawn around the ATLASGAL contours connected to G18.93.

et al., 1998; Jackson et al., 2006; Purcell & Hoare, 2010), an almost complete picture can be obtained for regions within the Galactic plane.

However, although both filamentary structures and IRDCs have gotten much interest over the last years, extreme IRDCs like the 80 pc long “Nessie” (Jackson et al., 2010) are still rare objects. A similar large scale filament of more than 50 pc length has been presented by Kainulainen et al. (2011). Figure 4.1 shows this filament, spanning over  $\sim 0.87^\circ$ . At a kinematic near distance of  $\sim 3.6_{-0.5}^{+1.0}$  kpc, this translates to a length of  $\sim 54$  pc. (For a discussion of the distance, see Sect. 4.3.2.) Its coherent velocity structure is shown in the bottom panel of Fig. 4.1. Following the low density gas traced by  $^{13}\text{CO}$  along the extinction patch, the smooth velocity transitions suggest that the entire region is spatially connected. Kainulainen et al. (2011) studied the extinction map of the region and estimate the total gas reservoir to be  $4.7 \times 10^4 M_\odot$ . Along the filament at lower longitudes, IRDC 18223 is a well-studied prototype IRDC with ongoing high-mass star formation (e.g. Beuther et al. 2010, and references therein).

A particularly interesting region in the context of triggered star formation is the prominent IRDC G18.93. Being part of the large scale filament described above, its location is also coincident with the rim of a IR bubble just above the filament (indicated by the upper yellow ellipse in Fig. 4.1). We will show that its dense gas, the filament and the bubble have coherent velocities and therefore are all at the same distance. Using CLUMPFIND on  $870\ \mu\text{m}$  dust continuum data we identify six sub-clumps. The most massive clump, denoted G18.93/m, is even infrared dark from near infrared wavelengths up to  $160\ \mu\text{m}$ .

For the particular case of G18.93/m we will address the following questions: do we see evidence that the bubble influences G18.93/m? Do the properties of G18.93/m differ from other high-mass starless clumps?

We will first introduce the data used for the analysis and their implications. In Sect. 4.3 we introduce G18.93 and the neighboring bubble, and supplement a more detailed description in Sect. 4.3.3 and onwards. Section 4.4 describes the signs of triggered star formation we find and discusses their consequences. We summarize the paper in a concluding section.

## 4.2 Description and implications of observations and data

We used various publicly available surveys, as well as IRAM 30 m follow-up observations of the specific region.

### 4.2.1 The cold dust tracing the molecular hydrogen, ATLASGAL

Molecular hydrogen,  $\text{H}_2$ , is hard to trace directly, and no pure rotational transitions are observable from the ground. However, in regions of high particle densities the gas thermally couples with the dust. Cold dust can be observed by its thermal radiation in the Rayleigh-Jeans regime at submm and mm wavelength. The APEX Telescope Large Area Survey of the Galaxy (ATLASGAL, Schuller et al. 2009) covers the full inner Galactic plane at  $870\ \mu\text{m}$  with a resolution of  $19.2''$  and an rms below 50 mJy. Using the Large APEX Bolometer CAmera (LABOCA, Siringo et al. 2009), each position of the inner Galactic plane has been mapped on-the-fly twice, each in different scanning directions. The pointing is on the order of  $4''$  and the calibration uncertainty is lower than 15%. A detailed description of the data reduction is given in Schuller et al. (2009). The submm emission is mostly optically thin.

### 4.2.2 IRAM 30 m observations

We used the IRAM 30 m telescope to map the region around G18.93 identified in the ATLASGAL  $870\ \mu\text{m}$  images (Schuller et al., 2009; Tackenberg et al., 2012a) in  $\text{H}^{13}\text{CO}^+$  and SiO.

$\text{H}^{13}\text{CO}^+$  is a well established and common dense gas tracer with a critical density at 20 K of  $\sim 1.8 \times 10^5\ \text{cm}^{-3}$ . It is generally optically thin and yields information on the bulk

motion of the gas (Vasyunina et al., 2011). SiO becomes released from the dust grains due to shocks and is therefore a well known tracer of shocked gas and molecular outflows (e.g. Schilke et al., 1997).

During our observing run in August 2010 the weather conditions were poor with average precipitable water vapour (pww)  $>10$  mm. Although the weather affected the pointing, it is, nonetheless, better than a third of the 3 mm beam (or  $\sim 9''$ ). We used on-the-fly mapping on 5 boxes to cover all 870  $\mu\text{m}$  continuum emission above 0.3 Jy, or  $2 \times 10^{22} \text{ cm}^{-2}$  (assuming a general dust temperature of 15 K, for further details see Sect. 4.3.3; see Fig. 4.2 for the coverage of the observations). The IRAM 30 m beam width for both  $\text{H}^{13}\text{CO}^+$  and SiO is  $29.9''$  and the 3 mm setup chosen provides a spectral resolution of 40 kHz at 40 MHz bandwidth. This translates to a native velocity resolution of  $0.14 \text{ km s}^{-1}$  at 86 GHz. The data reduction was done using CLASS from the GILDAS<sup>1</sup> package. We subtracted a linear baseline and removed the three central channels to avoid occasional spikes from the backends. The maps have been produced with a pixel scale of  $14.2''$ . With a total integration time of 11.3 h the average rms at a velocity resolution of  $0.25 \text{ km s}^{-1}$  is 0.08 K and 0.05 K for  $\text{H}^{13}\text{CO}^+$  and SiO, respectively.

Simultaneously with the 3 mm observations, we recorded two of the  $\text{H}_2\text{CO}(3-2)$  lines,  $\text{CH}_3\text{OH}(4-3)$ , and  $\text{HC}_3\text{N}(24-23)$  at 1 mm. However, due to the poor weather conditions the average rms noise in the spectra is above 0.32 K. With the given sensitivity, for the region of interest we do not detect any of the higher excitation lines at 1 mm.

### 4.2.3 The large scale cloud complex in HI, VGPS

The ISM is composed primarily of atomic hydrogen. HI (self) absorption features are usually spatially correlated to molecular clouds and IRDCs (Li & Goldsmith, 2003). We used the 21 cm HI observations of the VLA Galactic Plane Survey (VGPS, Stil et al. 2006) to study the large scale distribution of atomic hydrogen. With the VLA in D configuration, the best resolution at 21 cm is  $45''$ . The interferometer data were supplemented with short spacings from the NRAO Greenbank telescope (GBT). To improve the survey's sensitivity to extended, low surface bright emission, the data were reduced to a synthesized beam of  $1'$  at a velocity resolution of  $1.56 \text{ km s}^{-1}$ . The data cubes are sampled to a pixel scale of  $18''$  at  $0.8 \text{ km s}^{-1}$ . The calibration was made to be consistent with the NVSS survey (Condon et al., 1998).

### 4.2.4 A large-scale view of the molecular cloud, GRS

To study the molecular cloud component to its full extent we selected  $^{13}\text{CO}$ , a (well known) low density gas tracer with a critical density  $\sim 1.9 \times 10^3 \text{ cm}^{-3}$ . While it traces the same density range as  $^{12}\text{CO}$ , the isotopologue  $^{13}\text{CO}$  has lower abundances and is therefore optically thinner. The Boston University-FCRAO Galactic Ring Survey (GRS, Jackson et al. 2006) provides spectroscopic  $^{13}\text{CO}$  (1-0) observations of the Galactic plane for Galactic longitudes  $18^\circ \leq l \leq 58^\circ$ . The observations were performed with the single sideband focal plane receiver SEQUOIA, mounted on the Five College Radio Astronomy

<sup>1</sup><http://www.iram.fr/IRAMFR/GILDAS>

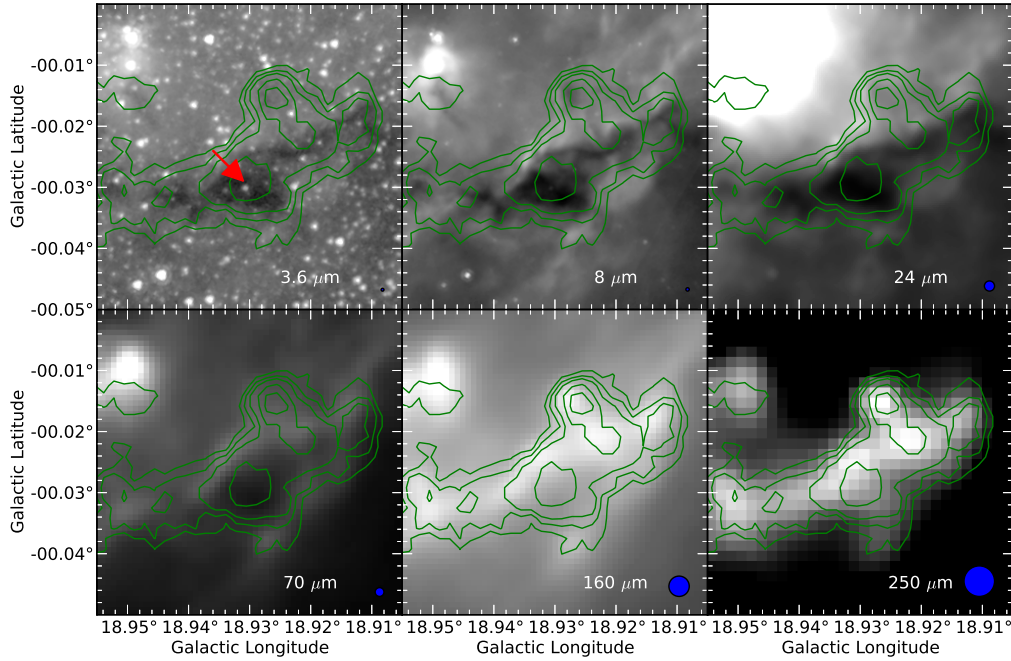


**Figure 4.3:** A multi-wavelength zoom on G18.93/m, the continuum peak connected to the prominent IR extinction feature. The panels are (*from left to right* in reading order):  $3.6\ \mu\text{m}$ ,  $8.0\ \mu\text{m}$ ,  $24\ \mu\text{m}$ ,  $70\ \mu\text{m}$ ,  $160\ \mu\text{m}$ ,  $250\ \mu\text{m}$ , from GLIMPSE, MIPS GAL, and HIGAL. The blue circles in the *bottom right* of each panel indicate the beam sizes, the green contours are from ATLASGAL (at 0.3 Jy, 0.4 Jy, 0.5 Jy, 0.7 Jy, 0.9 Jy, 1.3 Jy, 1.8 Jy, and 2.5 Jy). The colors of the source marked by a red arrow in the first panel are not consistent with typical colors of young stellar objects (class 0/1) (Gutermuth et al., 2008; Robitaille et al., 2008).

Observatory (FCRAO) 14 m telescope in OTF mode. Its angular resolution is  $46''$ , and the publicly available maps are sampled to a grid of  $22''$ . The velocity resolution is  $0.2\ \text{km s}^{-1}$ , the pointing accuracy is better than  $5''$ .

#### 4.2.5 The stellar component of the complex, UKIDSS, GLIMPSE and MIPS GAL

To examine the stellar content and stellar properties, we employed near- and mid-IR surveys. Both the Galactic Legacy Infrared Mid-Plane Survey Extraordinaire (GLIMPSE, Benjamin et al. 2003) and the MIPS Galactic plane survey (MIPSGAL, Carey et al. 2009) are *Spitzer* Legacy Programs. The GLIMPSE survey provides maps of the inner Galactic plane for  $-60^\circ \leq l \leq 60^\circ$  at  $3.8\ \mu\text{m}$ ,  $4.5\ \mu\text{m}$ ,  $5.8\ \mu\text{m}$ , and  $8.0\ \mu\text{m}$ . The resolution is  $1.7''$ ,  $1.7''$ ,  $1.9''$ ,  $2.0''$ , respectively. From MIPSGAL we used the  $24\ \mu\text{m}$  images with a resolution of  $6''$ . Additional near-IR JHK data have been taken from the UKIDSSDR7PLUS data release (Lawrence et al., 2007).

#### 4.2.6 The peak of the SED, HiGal

To further study our the complex, we also use HiGal data as described in Sec. 2.10.3. From a black body fit to the fluxes, we will estimate the temperature of the dust.

#### 4.2.7 The ionized gas, MAGPIS and SHS

In addition to thermal dust and line emission, free-free emission can be observed, which traces ionized gas. A certain amount of ionizing photons per second is required to maintain a given amount of gas in ionized state. This allows a characterization of the ionizing source. However, especially at cm wavelength another significant emission contribution is coming from the cosmic ray electrons' synchrotron radiation. Here, the spectral index can help to distinguish which contribution dominates.

The Multi-Array Galactic Plane Imaging Survey (MAGPIS, Helfand et al. 2006) mapped the 1.4 GHz, or 20 cm, continuum of the first Galactic quadrant partially. Using the VLA in B, C, and D configurations allows a resolution of  $\sim 6''$ , while the extended structures are preserved by including Effelsberg 100 m data (Reich et al., 1990). The ready reduced maps have a pixel scale of  $2''/\text{pix}$ .

While being very susceptible to extinction, the optical  $H_\alpha$  line traces the down cascade of an electron after recombining from ionized to atomic hydrogen. The SuperCOSMOS  $H_\alpha$  survey (Parker et al., 2005) digitized AAO/UKST narrow-band  $H_\alpha$  observations of the southern Galactic plane with a resolution of  $\sim 1''$ .

### 4.3 Results

The employment of the various surveys allows us to draw a comprehensive large scale picture of the cloud complex associated with the IRDC G18.93. In the following we will describe the environment, going from large to small scales. Finally we will use velocity information to study the spatial relations.

#### 4.3.1 A massive IRDC in the vicinity of a bubble

As mentioned in the introduction, a prominent feature along the  $>50$  kpc long filament is the bubble like structure indicated by the yellow ellipse in Fig. 4.1. A second bubble, N24 from Churchwell et al. (2006) and Deharveng et al. (2010) marked by the lower yellow ellipse in Fig. 4.1, is close in projection as well. However, while the filament has a velocity ( $v_{\text{lsr}}$ ) around  $\sim 45 \text{ km s}^{-1}$ , the second bubble has a distinct velocity at around  $60 \text{ km s}^{-1}$  and therefore is at a different distance.

A zoom in on the smaller bubble closer to the filament is shown in Fig. 4.2. It opens towards higher Galactic latitudes and only little  $24 \mu\text{m}$  emission is visible within the bubble. The opening of the bubble resembles a typical ‘‘champagne flow’’ (Stahler & Palla,

2005) with lower density material at higher latitudes. On the lower inner edge of the rim a bright IRAS source is located together with two bright NIR sources.

Directly at the edge of the bubble at lower latitudes, several studies identified infrared dark clouds (IRDCs) and massive dense clumps, e.g. SDC G18.928-0.031 (Peretto & Fuller, 2009), [SMC2009] G18.93-0.01 (Schuller et al., 2009), or BGPS G18.926-0.019 (Rosolowsky et al., 2010). As shown in Fig. 4.2, the ATLASGAL survey at  $870\ \mu\text{m}$  revealed several dense structures along the bubble. The largest structure in Fig. 4.2 is partly following the IRDC filament. In addition, Cyganowski et al. (2008) found an extended green object (EGO) within the rim of the bubble, EGO G19.01-0.03 which drives a bipolar outflow and is characterized as a genuine fast accreting massive young stellar object (Cyganowski et al., 2008, 2011a,b). As shown in Fig. 4.3, the main emission peak of the IRDC shows up in absorption up to even  $160\ \mu\text{m}$ . While absorption of IRDCs usually refers to extinction against the Galactic background from PAHs and very small grains, it is unclear whether the absorption feature at the longer wavelength of  $160\ \mu\text{m}$  implies a lack of emission or simply no grains hot enough to emit in that line of sight. However, the part around EGO G19.01-0.03 and all connected continuum emission towards lower Galactic latitudes does not even show  $24\ \mu\text{m}$  extinction signatures.

Within and along the bubble, there are few additional complexes dense enough to contain dense clumps and become visible at ATLASGAL sensitivity. However, since we want to study the influence of an expanding HII region upon an already existing filament, we will not discuss the continuum emission in the region that is clearly above the filament. Due to its characteristic absorption we will call the IR dark structure defined by the ATLASGAL emission G18.93 (see gray ellipse in Fig. 4.2). For reasons we will discuss in Sect. 4.3.2 we keep the ATLASGAL emission aligned with the Galactic latitude axis connected to EGO G19.01-0.03 separate.

It is interesting to note that both the massive young stellar object EGO G19.01-0.03 and the IRDC filament are at the interface of the bubbles shown in Fig. 4.1.

### 4.3.2 Disentangling the spatial relations of G18.93 and EGO G19.01

From  $^{13}\text{CO}$ , partly shown in Fig. 4.1, it cannot be concluded whether the dense dust for the region of interest seen in ATLASGAL is part of the  $45\ \text{km s}^{-1}$  filament component or the  $60\ \text{km s}^{-1}$  component connected to the second bubble. To address that question and to disentangle the velocity structure of the dense molecular gas, we mapped G18.93 and the dust emission around EGO G19.01-0.03 in  $\text{H}^{13}\text{CO}^+$ , a dense gas tracer.

As shown in Fig. 4.4, the dense gas has two distinct velocity components. Consistent with earlier single spectra (Cyganowski et al., 2011b; Wienen et al., 2012), the IRDC G18.93 shows emission at velocities between  $43\ \text{km s}^{-1}$  and  $47\ \text{km s}^{-1}$ , while the peak of EGO G19.01-0.03 and the ATLASGAL emission directly connected to it have velocities between  $59\ \text{km s}^{-1}$  and  $63\ \text{km s}^{-1}$ . For both components, the dense molecular gas tracer resembles the structure defined by the ATLASGAL emission contours very well. Therefore, one can attribute the same velocities unambiguously to the ATLASGAL emission. That is not obvious from the lower density  $^{13}\text{CO}$  alone. In addition, it is obvious

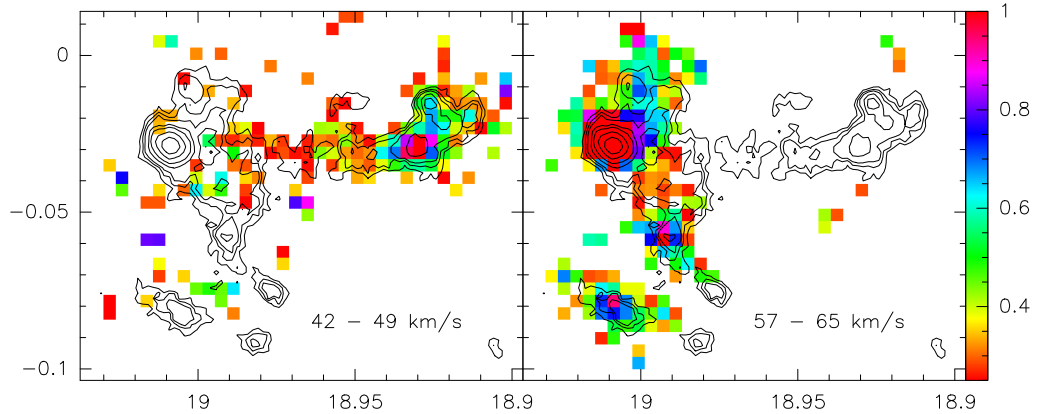


**Figure 4.4:** Color coded map of the  $\text{H}^{13}\text{CO}^+$  emission in  $[\text{K km s}^{-1}]$  for the velocity regime  $42 \text{ km s}^{-1}$  to  $49 \text{ km s}^{-1}$  on the *left*, and  $56 \text{ km s}^{-1}$  to  $65 \text{ km s}^{-1}$  on the *right*. The black contours are from ATLASGAL with levels at 0.3 Jy, 0.4 Jy, 0.5 Jy, 0.7 Jy, 0.9 Jy, 1.3 Jy, 1.8 Jy, and 2.5 Jy.

that G18.93 is part of the long filament and the primary bubble which is connected to it, while EGO G19.01-0.03, a site of massive star formation and its connected material below this region, is at velocities consistent with the larger bubble from Churchwell et al. (2006).

In order to constrain the distance to the filament and the connected bubble, we employ the Galactic rotation curve given in Reid et al. (2009). Assuming a common velocity of  $45 \text{ km s}^{-1}$ , the kinematic near distance becomes 3.6 kpc. From both extinction (Kainulainen et al., 2011) and considerations of the HI absorption feature (see Sect. 4.3.5 for details) we can conclude that the near distance is appropriate. Note that Kainulainen et al. (2011) give a kinematic distance of 4.1 kpc and even larger distances from velocity independent methods. Therefore, error propagation resulting in a distance uncertainty of 0.05 kpc underestimates the uncertainty. We expect the uncertainty rather to be on the order of 0.5 kpc.

### 4.3.3 Details and aspects of the G18.93 complex

So far we have shown that there is a large filament along the Galactic plane that has a consistent velocity structure over more than 50 pc. At  $l = 18.93^\circ$ ,  $b = 0.03^\circ$  the filament becomes very opaque, shows high mid-IR extinction and large gas column densities. Part of it shows IR absorption up to  $160 \mu\text{m}$ . Just above G18.93, a bubble is visible. Its PAH rim visible at  $8 \mu\text{m}$  has a direct interface with G18.93. We will show later that the bubble is an expanding HII region. Therefore, G18.93 is an ideal source in which to study the influence of massive stars on starless clumps and search for imprints of triggering.

#### The dust component of G18.93

As mentioned in Sect. 4.3.2 and shown in Fig. 4.4, the densest gas (and most of the molecular hydrogen) in the complex is concentrated in the regions seen by ATLASGAL

**Table 4.1:** CLUMPFIND decomposition of dust clumps extracted on ATLASGAL 870  $\mu\text{m}$  map.

Sub-clump name	Gal. lon. [ $^{\circ}$ ]	Gal. lat. [ $^{\circ}$ ]	RA(2000) [hh:mm:ss.s]	Dec(2000) [dd:mm:ss]	HiGal peak temp [K]	Peak column density [ $10^{22} \text{ cm}^{-2}$ ]	Mass [ $M_{\odot}$ ]	Angular radius [ $''$ ]	Radius [pc]
1	18.9259	-0.0158	18:25:32.4	-12:26:47	23.0	4.2	248	27	0.46
main	18.9325	-0.0292	18:25:36.0	-12:26:48	21.7	3.5	276	29	0.50
2	18.9125	-0.0158	18:25:30.9	-12:27:29	22.3	2.4	104	21	0.36
3	18.9459	-0.0325	18:25:38.3	-12:26:11	22.5	2.2	107	22	0.38
4	18.9425	-0.0308	18:25:37.6	-12:26:19	22.4	2.1	57	15	0.27
5	18.9658	-0.0342	18:25:41.0	-12:25:10	23.0	1.5	43	15	0.26

at 870  $\mu\text{m}$  (see Sect. 4.2.1).

In order to identify column density peak positions and associate masses to individual clumps, we used the CLUMPFIND algorithm of Williams et al. (1994). Starting at a  $6\sigma$  contour of 0.3 Jy, we chose 0.4, 0.5, 0.7, 0.9, 1.3, 1.8, and 2.5 Jy as extraction thresholds. (For a detailed discussion of the extraction thresholds see Tackenberg et al. 2012a.) The positions of the extracted clumps are listed in Table 4.1 and plotted in Fig. 4.2. We denote the prominent absorption dip and most massive clump G18.93/m.

Assuming optically thin thermal emission, the  $\text{H}_2$  gas column density can be calculated from the dust continuum emission via

$$N_{\text{gas}} = \frac{RF_{\lambda}}{B_{\lambda}(\lambda, T)m_{\text{H}_2}\kappa\Omega}, \quad (4.1)$$

with the gas-to-dust ratio  $R = 100$ ,  $F_{\lambda}$  the flux at the given wavelength,  $B_{\lambda}(\lambda, T)$  the blackbody radiation as a function of wavelength and temperature,  $m_{\text{H}_2}$  the mass of a hydrogen molecule, and the beam size  $\Omega$ . Assuming typical beam averaged volume densities in dense clumps of  $10^5 \text{ cm}^{-3}$  and dust grains with thin ice mantles, the dust mass absorption coefficient from Ossenkopf & Henning (1994) becomes  $\kappa = 1.42 \text{ cm}^2 \text{ g}^{-1}$  at 870  $\mu\text{m}$ . The temperatures are taken from the HiGal temperature map described in Sect. 4.3.3. Because of the sparse resolution, we adopted the temperature at each peak position. The peak column densities at the spatial resolution of ATLASGAL (19.2'') are then between  $1.0 \times 10^{22} \text{ cm}^{-2}$  to  $4.2 \times 10^{22} \text{ cm}^{-2}$ .

With the distance as additional parameter and the integrated flux of the clump, the mass can be calculated in a similar way as given above,

$$M_{\text{gas}} = \frac{Rd^2F_{\lambda, \text{tot}}}{B_{\lambda}(\lambda, T)\kappa}. \quad (4.2)$$

Assuming the kinematic distance of 3.6 kpc, the total mass becomes  $\sim 870 M_{\odot}$ , with clump masses between  $\sim 30 M_{\odot}$  and  $250 M_{\odot}$ . Individual column densities and masses are listed in Table 4.1. The given radius is the effective radius for equating the pixel area of each clump with a theoretical circular area, as calculated by CLUMPFIND.

### Temperature map of G18.93

The dust temperature is not only a necessary quantity for calculating column density and mass estimates, but it is an important physical parameter. As described in Sect. 2.10.3, we

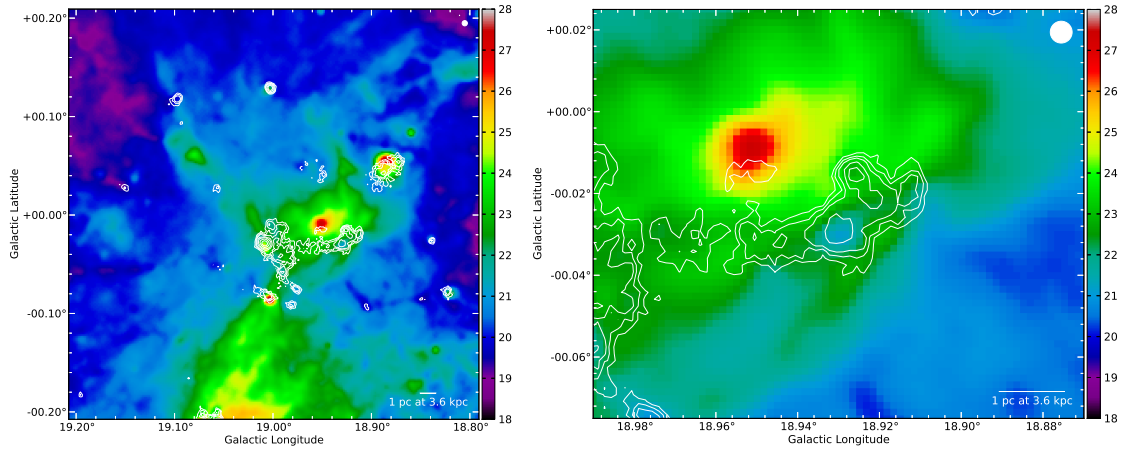


**Figure 4.5:** Color coded temperature maps in [K] of G18.93, shown by the white contours from ATLASGAL (at 0.3 Jy, 0.4 Jy, 0.5 Jy, 0.7 Jy, 0.9 Jy, 1.3 Jy, 1.8 Jy, and 2.5 Jy). The beam size is indicated in the *top right corner*. While the *top panel* presents the large-scale environment, the *bottom panel* zooms into our central IRDC region.

can use the HiGal/*Herschel* survey together with ATLASGAL data to estimate the dust temperature. Smoothing all data to the same resolution, we used frequency-dependent, optically thin dust emission models from Ossenkopf & Henning (1994) to fit every pixel with a single temperature Planck function. (See also Ragan et al. 2012.) A common problem in the context of *Herschel* PACS/SPIRE data is the unknown background contribution. Several efforts have been made to solve that problem, e.g. Stutz et al. (2010); Battersby et al. (2011). In the context of determining the temperature we tested different background levels based on Gaussian fits to the noise distribution in regions with no or little signal. While the absolute temperatures differ up to 10%, the relative temperature distribution is very similar. Therefore we refrain from subtracting any background and focus on the relative changes.

Furthermore, we have compared temperature maps using both HiGal and ATLASGAL, smoothed to a common resolution of  $37''$ , to temperature maps with only three bands,  $70\ \mu\text{m}$ ,  $160\ \mu\text{m}$ , and  $250\ \mu\text{m}$  at a resolution of  $19''$ . Although it is ambitious to fit a curve to only three data points, the peak of the SED is covered and can be reconstructed. The ATLASGAL data has been omitted since the missing background subtraction implies problems with the calibration and worsens the reconstruction of the peak. Comparing the temperatures of both SED fits on regions where differences due to the beam size are negligible, we find very good agreements. We want to point out that omitting the longer wavelength data biases the absolute results towards higher temperatures. However, the relative distribution in the temperature maps are preserved. Therefore, Fig. 4.5 shows the temperature maps at the better resolution of  $19''$ . To have more reliable absolute temperatures for deriving column densities and masses, we use the temperatures derived on all HiGal plus the ATLASGAL data.

As displayed in the top panel of Fig. 4.5, the dust around the IRAS source is hottest and produces a large scale temperature gradient. Nevertheless, all ATLASGAL peaks are colder than their neighborhood, and the temperature dip towards G18.93/m is the largest.

### G18.93/m: a starless clump

Despite its prominence as absorption feature at *Spitzer* wavelengths, Tackenberg et al. (2012a) did not list G18.93/m as a starless clump. Because of a peak in the extended  $24\ \mu\text{m}$  emission within the clump boundaries, the clump had been rejected for consistency. In this detailed study however, we refrain from such rigorous methods and allow an individual inspection of the clump. Using the GLIMPSE color criteria given in Gutermuth et al. (2008), none of the cataloged near- and mid-IR sources within the clump is classified as young stellar object (class 0/I). Using similar GLIMPSE color criteria, Robitaille et al. (2008) did not identify young stellar objects projected onto the clump either. For even younger sources not yet visible at near-IR wavelength, Fig. 4.3 shows that there is no point source longwards of  $8\ \mu\text{m}$  close to the ATLASGAL peak of G18.93/m. To further quantify our sensitivity we estimated the luminosity of objects that still could be embedded in the dust. Using the same assumptions as explained in Sect. 4.3.3, we here fitted two blackbody functions to the point source detection limits of the  $24\ \mu\text{m}$  and  $70\ \mu\text{m}$  images of 2 mJy for MIPS GAL (Carey et al., 2009) and  $\sim 10$  mJy for the  $70\ \mu\text{m}$  HiGal field together with the flux estimates for the absorption peak of G18.93/m at  $160\ \mu\text{m}$  and  $250\ \mu\text{m}$ , 52.0 Jy and 45.1 Jy. The warmer component then has only  $0.1 L_{\odot}$ , corresponding to a low-mass star of  $0.14 M_{\odot}$ . This can be considered as an upper limit for any potential embedded and undetected source.

Additionally indicative of true starless clumps is the absence of SiO emission. Since SiO traces outflows it is commonly used to differentiate between starless clumps and star forming clumps (Motte et al., 2007; Russeil et al., 2010). For the entire G18.93 complex we find no SiO down to column densities of  $\sim 8 \times 10^{11}\ \text{cm}^{-2}$ .

In order to understand whether G18.93/m is pre-stellar or only a transient object, we compare its virial mass to its dust mass. While pre-stellar clumps are gravitationally bound and therefore will eventually form stars in the future, transient clumps are not gravitationally bound. Within such objects, smaller (here unresolved) fragments can still collapse, but the clumps itself will drift apart. As we will discuss in Sect. 4.4.5, we find a double peaked  $\text{H}^{13}\text{CO}^+$  profile at the ATLASGAL peak position of G18.93/m. As shown in Fig. 4.11, the line width of the component we attribute to the IRDC is  $\delta v = 2.1\ \text{km s}^{-1}$ . (For details see Sect. 4.4.5). To calculate the virial mass we use the equation given in MacLaren et al. (1988),  $M_{\text{vir}} = kR\delta v^2$ . For the source radius  $R$  we use 0.5 pc as given in Table 4.1, and the geometrical parameter  $k$  depends on the density structure of the clump and is  $k = 190$  for  $\rho \propto 1/r$ ,  $k = 126$  for  $\rho \propto 1/r^2$ . The mass then becomes  $M_{\text{vir}} = 420 M_{\odot}$  for a geometrical parameter  $k = 190$  or  $\rho \propto 1/r$ , and  $M_{\text{vir}} = 280 M_{\odot}$  with  $k = 126$  or  $\rho \propto 1/r^2$ . Beuther et al. (2002a) and Hatchell & van der Tak (2003) find typical density distributions in sites of massive star formation of  $\rho \propto r^{\alpha}$  with  $\alpha \sim -1.6$ , in between both parameters. Doing a linear interpolation, the suggested virial mass becomes  $360 M_{\odot}$ . Considering all uncertainties, a comparison to the estimated dust mass for G18.93/m of  $280 M_{\odot}$  does not allow a conclusive distinction whether clump G18.93/m is gravitationally bound or not. However, as discussed in Sect. 4.3.3 the dust temperatures derived from SED fitting to *Herschel* data are very uncertain due to missing background levels. Comparing gas temperatures measured with  $\text{NH}_3$  observations (Pillai et al., 2006) to dust temperatures from *Herschel* observations (Henning et al., 2010), we find that despite the efficient dust cooling the ammonia temperatures are usually lower. Thus, the given temperatures are

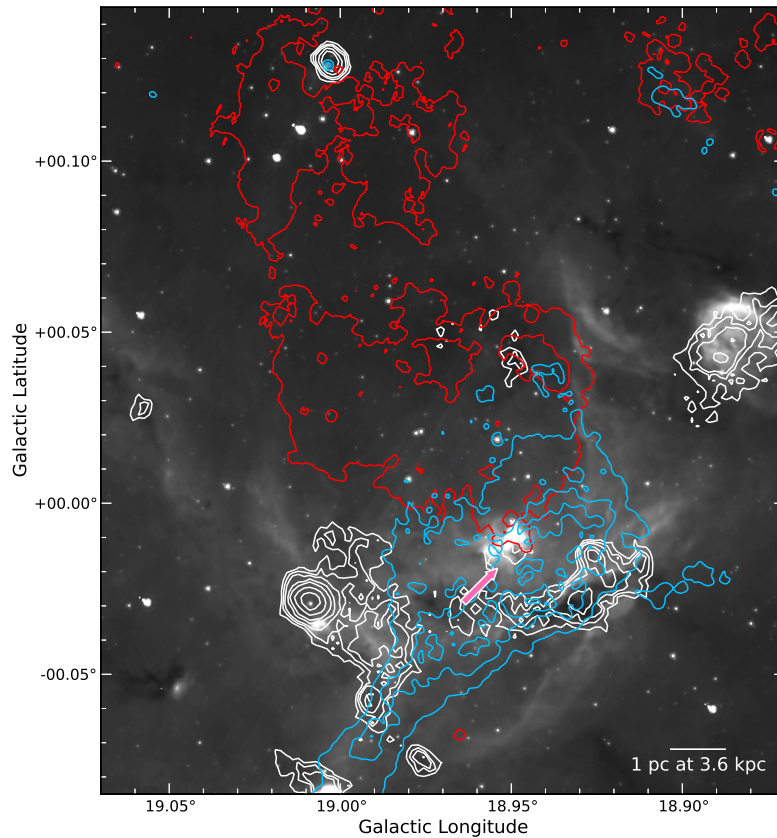


**Figure 4.6:** The ionized gas within and around the bubble. On top of the GLIMPSE  $8\mu\text{m}$  image, the red contours show the  $\text{H}\alpha$  emission from the SuperCOSMOS survey, the blue contours represent the MAGPIS 20 cm emission, and white contours show the ATLASGAL emission (at 0.3 Jy, 0.4 Jy, 0.5 Jy, 0.7 Jy, 0.9 Jy, 1.3 Jy, 1.8 Jy, and 2.5 Jy). The contour levels for the MAGPIS data are 0.002 Jy/beam, 0.003 Jy/beam, 0.004 Jy/beam, and 0.005 Jy/beam. The arrow indicates the peak position of the HII region identified by Lockman (1989).

only upper limits and the clump masses may be higher. Therefore, the virial analysis is consistent with G18.93/m being gravitationally bound, and pre-stellar.

#### 4.3.4 The bubble

According to Simpson et al. (2012), the bubble connected to the filament and described in Sect. 4.3.1, or MWP1G018980+000304, has an effective radius of  $3.44'$ . However, as mentioned before, its appearance is more similar to a “champagne flow” (cf. Fig. 4.2). Since the expansion velocity of an HII region depends on the surrounding density, an inhomogeneous medium leads to asymmetric bubbles. If the ionizing gas reaches the edge of its parent molecular cloud or encounters dense gas, it will fan out towards the empty space (Stahler & Palla, 2005). Therefore, the effective radius and the major- and minor-axis can describe the current appearance of a bubble, but cannot describe the expansion history.

Thus we have to ask: what is the origin of MWP1G018980+00304? Galactic bubbles are usually produced by OB stars or clusters, driving an expanding HII region, or by stellar winds and radiation pressure of late B-type stars (Elmegreen & Lada, 1977; Churchwell et al., 2006; Deharveng et al., 2010; Simpson et al., 2012). For both processes, the exciting source is not necessarily in the middle of the bubble.

Often, (ultra) compact HII regions (UCHIIs) are found connected to the bubble driving source, but e.g. CORNISH (Purcell et al., 2008) does not find an UCHII region inside the bubble. However, despite its high sensitivity at 6 cm of better than 2 mJy, due to interferometry techniques, CORNISH is not sensitive to sources larger than  $12''$  (Hoare et al., 2012). Searching for more extended structure, Lockman (1989) conducted a  $H_\alpha$  radio recombination line single dish survey at 3 cm and detected an HII region at  $l = 18.954$ ,  $b = -0.019$ . As shown in Fig. 4.6, this is right between the IRAS source and G18.93, but measured with a beam of  $3'$ . Although they measure a source velocity of  $v_{\text{LSR}} = (52.3 \pm 1.7) \text{ km s}^{-1}$ , we believe that the bubble and the HII gas are spatially connected. Indeed, velocity offsets between the ionized gas and CO are common (Blitz et al., 1982; Fich et al., 1982). For the same HII region Kuchar & Clark (1997) measure the flux at 4.85 GHz with a beam width of  $4.2'$ . For an estimated source diameter of  $7.0'$  they find 2146 mJy. Using the formula given in Kurtz et al. (1994) and assuming a correction factor for the optical depth of  $a = 0.9922$  (corresponding to a frequency  $\nu = 5$  GHz, and temperature  $T = 9000$  K as given in Mezger & Henderson 1967), this flux translates to the number of Lyman continuum photons  $n_{\text{Ly}} = \log(N_{\text{Ly}}) = 48.4 \text{ s}^{-1}$ .

The blue contours in Fig. 4.6 show the MAGPIS GPS data at 20 cm. The emission peak of the high resolution data at 20 cm agrees well with the extrapolated peak position from Lockman (1989) in the sense that it also lies between the IRAS source and G18.93. However, the GPS data shows 20 cm emission towards the IRDC and beyond. The higher latitude flux within the contour level  $3 \times 10^{-3}$  Jy/beam, without the tail towards lower latitudes, becomes 1.5 Jy. With  $a = 0.9951$  at 9000 K (Mezger & Henderson, 1967), that converts to a Lyman continuum flux of  $n_{\text{Ly}} = 48.2 \text{ s}^{-1}$ . A slightly larger contour drawn along the visual extent of the emission provides a flux of 2.5 Jy, thus 2/3rd bigger. However, with  $n_{\text{Ly}} = 48.4 \text{ s}^{-1}$  the logarithm does not change as much and the given differences can be considered as uncertainty in our measurements. Therefore, the results of Kuchar & Clark (1997) and our measurements agree within the uncertainties.

As mentioned in Sect. 4.2.7, the synchrotron radiation of cosmic ray electrons can also contribute to the cm continuum emission. However, the spectral index  $\alpha$  (with  $S_\nu \propto \nu^{-\alpha}$ ) of the thermal free-free emission is negative in this regime, while the spectral index of the synchrotron radiation is positive. Therefore, we can use the two independent measurements of the continuum emission to at least determine the sign of the spectral index. The slope between the 20 cm, or 1.5 GHz, data point and the 6 cm, or 4.85 GHz, data point is positive, suggesting a negative spectral index, which is in agreement with the expected spectral index for thermal free-free emission. Therefore, the emission is dominated by free-free radiation and we can neglect any synchrotron contribution. Nevertheless, with only two data points we cannot distinguish whether the assumption of optically thin emission is correct. Therefore, the given Lyman continuum fluxes are lower limits.

While the cm continuum is more prominent towards the dust continuum emission, large parts of the bubble are filled by SuperCOSMOS  $H_\alpha$  emission, see Fig. 4.6. As mentioned

in Sect. 4.2.7,  $H_\alpha$  is a complementary tracer of ionized gas. The difference in the spatial distribution can be explained by the optical depth. Since the optical  $H_\alpha$  line is susceptible to extinction,  $H_\alpha$  can only be detected in regions of low visual extinction. However, the near-IR extinction map shows that the visual extinction towards the ATLASGAL emission peaks are larger than  $A_V = 25$  mag.

Using the averaged number of Lyman photons,  $n_{Ly} = 48.3 \text{ s}^{-1}$  to determine the spectral type, the exciting source needs to be at least a main sequence star of type O8.5 (Panagia, 1973; Martins et al., 2005). The extended appearance (and the connected non-detection within CORNISH) and the morphology of the HII suggests that the ionizing source is not extremely young. Nevertheless, the diameter of the bubble does not allow for extremely old bubble-driving sources.

From the mid infrared data, a good candidate for the ionizing source is IRAS 18227-1227, marked in Fig. 4.2. It is very bright at  $24 \mu\text{m}$ , but by  $3.6 \mu\text{m}$  it is no longer the brightest source within its neighborhood. At higher latitudes,  $\sim 16''$  above IRAS 18227-1227, a near-IR source, hardly visible at  $24 \mu\text{m}$ , is another potential candidate to drive the bubble. Although the additional source appears blue in the four IRAC bands from GLIMPSE, the color criteria given in Gutermuth et al. (2008) identify it as young stellar object. At the even shorter wavelengths of the 2MASS and UKIDSS near-IR *JHK* surveys, the second source has a bright neighbor. Nevertheless, its missing detection in the GLIMPSE survey and its blue appearance at NIR wavelength indicates that it is evolved. However, the near infrared colors do not allow a classification or mass determination. While for one its classification as young stellar object (class I) hints to non photospheric emission at near infrared wavelength, the second source shows a significant color excess in the *JHK* color-color diagram indicating non photospheric emission as well. Therefore we can not identify the exact ionizing source with the current data. Nevertheless, as shown before from cm free-free emission, it has to be of spectral type O8.5 or earlier.

Another result one can determine from the different tracers of the ionized gas are the densities above and below the ionizing source. While we have material that is optically thick to visible light suggesting dense gas towards the dust continuum emission, we have optically thin low density material within the bubble and above it. That explains the position of the ionizing source and the “champagne flow”.

#### 4.3.5 The photon-dominated region: a layered structure

What is the observable impact of the HII region on the dense filament, described in Sect. 4.3?

During the evolution of an HII region the temperature difference between the hot ionized gas and the cold environment drives a supersonic shock front beyond the ionization front. In addition, at the interface between an HII region and the neighboring gas a photon dominated region builds up. While hydrogen ionizing radiation with energies above 13.6 eV produces the HII, beyond the ionization front other molecules with lower ionization energies may still be ionized. However, connected to the photon dominated region one expects a layered structure of HII-HI-H<sub>2</sub> (Hollenbach & Tielens, 1997). For our bubble we can directly observe the layers between the presumably ionizing source and the

dense gas of G18.93/m.

While the ionized gas and its structure is directly traced by the cm free-free emission, the ATLASGAL emission connected to G18.93/m represents the cold dust, which is embedded in dense  $\text{H}_2$ . In order to trace the morphology of the atomic hydrogen we employ the VGPS HI survey.

(Hot) HI is so abundant in the Galaxy, that along the Galactic plane, background HI emission is present at all velocities. Therefore, cold sources in the foreground appear as absorption features superimposed on the background HI emission. However, since the HI distribution and temperature vary strongly within the Galactic disk, the observed background varies strongly as well. In addition, individual HI clouds often have sufficiently high column densities to become self absorbing. This complicates the identification of complexes in the HI data.

However, as shown in Fig. 4.7, the absorption dip for the dense gas around G18.93 is very prominent. In order to study the distribution of the atomic hydrogen, we quantified the absorption feature by the following process: (1) we fit the background in the spectra with a third order polynomial omitting the velocity range from  $40 \text{ km s}^{-1}$  to  $50 \text{ km s}^{-1}$ . This determines the large scale background variations, but preserves the signals on small scales; (2) we subtract the fitted function as a baseline; (3) we invert the spectra and fit the now emission peak with a Gaussian. The integrated area of the Gaussian for a constant temperature is proportional to the column density. (NOTE: we stress that the authors do not want to convert the so quantified measure of HI into physical meaningful units, but only take it as relative value). Doing this procedure on all HI spectra around G18.93/m, we obtain the qualitative distribution of the atomic hydrogen.

A problem with this method arises from the free-free continuum. Due to the additional background emission towards the HII region, the absorption dip becomes stronger for the same HI column densities. Therefore, the interpretation of the HI distribution needs to be considered with caution. However, since the peak of the HI and HII emission do not agree, the suggested HI distribution seems to be dominated by the HI column density.

Figure 4.8 shows three physical states of hydrogen. Between the ionizing source and G18.93 a layered structure is visible, with first the ionized gas, then the atomic hydrogen, and then the molecular gas within the IRDC. However, one should keep in mind that the beam of the HI data is on the same order as the spacing between the different peaks.

#### 4.4 Imprints of triggering? Discussing the interaction between G18.93/m and the expanding HII region

So far, most studies of triggered star formation (e.g. Deharveng et al. 2003; Zavagno et al. 2006) have searched for young stellar objects connected to bubbles and HII regions. To understand the statistical significance of triggered star formation, current and future studies make use of the rising number of Galactic plane surveys (Zavagno et al., 2010; Deharveng et al., 2010; Kendrew et al., 2012). Although it has been shown in the past that not all stars on the border of HII regions are necessarily formed by triggering, it becomes clear that triggering might have a significant effect on star formation.

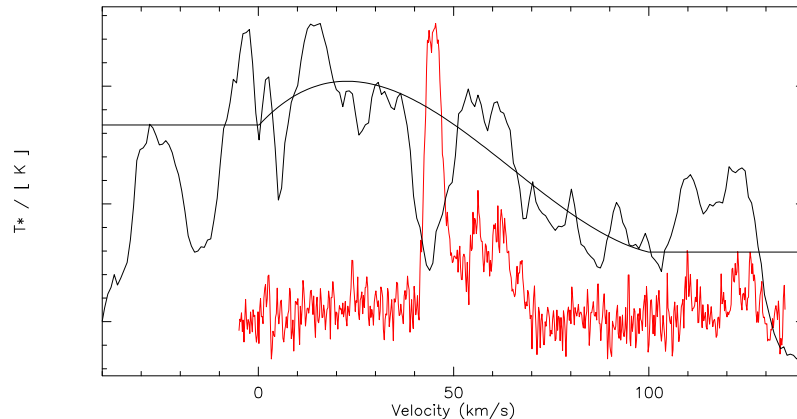


**Figure 4.7:** HI VGPS spectrum of G18.93/m in black with the GRS  $^{13}\text{CO}$  spectrum in red on top. The strong absorption feature of G18.93/m at  $\sim 45 \text{ km s}^{-1}$  in the HI spectrum agrees very well with the  $^{13}\text{CO}$  signature. The smooth line indicates the 3rd order fit to the HI spectrum that has been used to subtract the “continuum”. (For details see text.)

As a next step towards a better understanding of triggered star formation we need to observationally identify the mechanisms that govern the interaction between expanding HII regions and the molecular gas. In this context, detailed studies of individual regions are needed to reveal signatures of triggering before star formation sets in (e.g. Bieging et al. 2009).

In the following section we will explore whether we can see any imprints of the HII region on the starless clump G18.93/m.

#### 4.4.1 Comparison of G18.93/m with typical high-mass starless clumps

As discussed in Sect. 4.3.3, G18.93/m is a starless clump with no IR emission up to  $160 \mu\text{m}$ . While the virial analysis does not allow a firm conclusion as to whether it is bound or not, but if it is bound it would be a proto-type pre-stellar clump. In terms of mass and size it does not stand out. If we compare it to the starless clumps found in Tackenberg et al. (2012a), its clump mass of  $280 M_{\odot}$  is comparable to the average mass of  $315 M_{\odot}$  they find. Note that with the lower dust opacity of  $\kappa = 0.77 \text{ cm}^2 \text{ g}^{-1}$  used in Tackenberg et al. (2012a) as well as the low temperature of 15 K they assume for starless clumps, the clump mass becomes  $900 M_{\odot}$ . Nevertheless, for peculiar sources such as G18.93/m, the elevated dust temperature needs to be taken into account.

If we assume a spherical clump we can calculate the average volume density of G18.93/m to be  $1 \times 10^4 \text{ cm}^{-3}$ . This is significantly smaller than the  $5.0 \times 10^4 \text{ cm}^{-3}$  for the sample of starless clumps presented in Tackenberg et al. (2012a). However, from the detection of  $\text{H}^{13}\text{CO}^+$  with a critical density of  $\sim 1.8 \times 10^5 \text{ cm}^{-3}$ , we know that at least in the central regions the density needs to be higher. Nevertheless, since the average densities of the starless clumps have been calculated with the same assumptions, the results should be comparable. For the formation of high-mass stars, Krumholz & McKee (2008) require a peak column density of  $3 \times 10^{23} \text{ cm}^{-2}$ . With a peak column density of  $4 \times 10^{22} \text{ cm}^{-2}$ ,

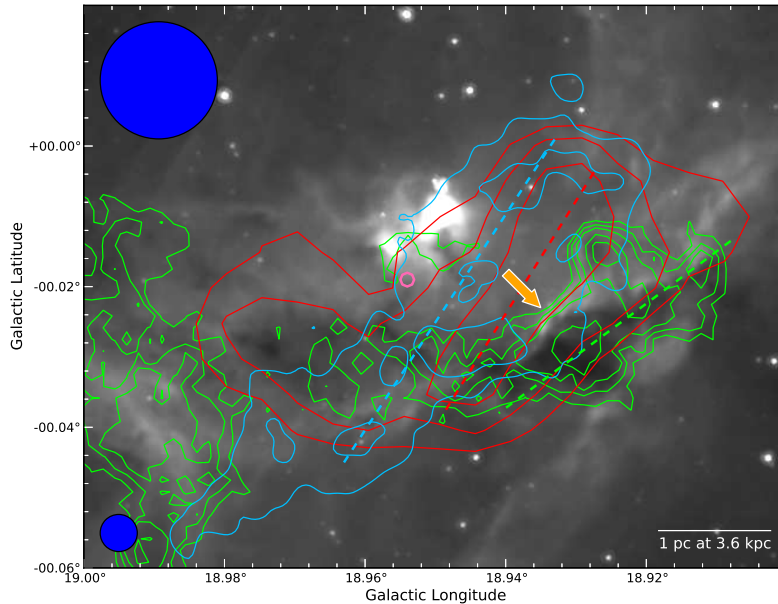


**Figure 4.8:** A layered structure of the hydrogen phase. On top of the  $8\ \mu\text{m}$  GLIMPSE image in gray, the blue contours represent the MAGPIS GPS 20 cm data, the red contours show a measure of the atomic hydrogen at velocities of G18.93 from the VGPS 21 cm line (for details see the text), and the green contours are the cold dust from the ATLASGAL survey, hence the molecular hydrogen. The dashed lines are to guide the eye and indicate the peak positions of the different data. The orange arrow points to  $8\ \mu\text{m}$  excess emission at the edge of the dense gas. The top left circle indicates the beam size of the VGPS data, while the bottom circle shows the beam of ATLASGAL. In this figure, MAGPIS is smoothed to the resolution of ATLASGAL. The contour levels for the GPS 20 cm data are 2 mJy/beam, 3 mJy/beam, 4 mJy/beam, and 5 mJy/beam, and for the ATLASGAL  $870\ \mu\text{m}$  emission 0.3 Jy, 0.4 Jy, 0.5 Jy, 0.7 Jy, 0.9 Jy, 1.3 Jy, 1.8 Jy, and 2.5 Jy.

G18.93/m does not meet their requirements. However, the measured column densities are beam averaged values, true peak column densities are expected to be higher (Vasyunina et al., 2009). Although the expanding HII region might have influenced the starless clump G18.93/m, it does not differ from other starless clumps.

#### 4.4.2 The photon dominated region: a layered structure

While the general distribution of the atomic hydrogen follows the ATLASGAL emission, the peak of HI is elongated towards the gap between the ionizing source and the molecular hydrogen, shown by Fig. 4.8. Towards G18.93/5 (cf. Fig. 4.2), the 20 cm free-free emission is no longer parallel to the cold dust, but crosses the IRDC. However, both extinction and dust emission are significantly lower at the intersection. That implies that there is less dense gas which allows the ionized gas to more easily escape beyond G18.93/5; the ionizing radiation is simply no longer blocked across the full height of the filament.

In the context of star formation, Glover & Clark (2012) have shown that the composition of the gas has hardly any influence on the star formation efficiency. They suggest that

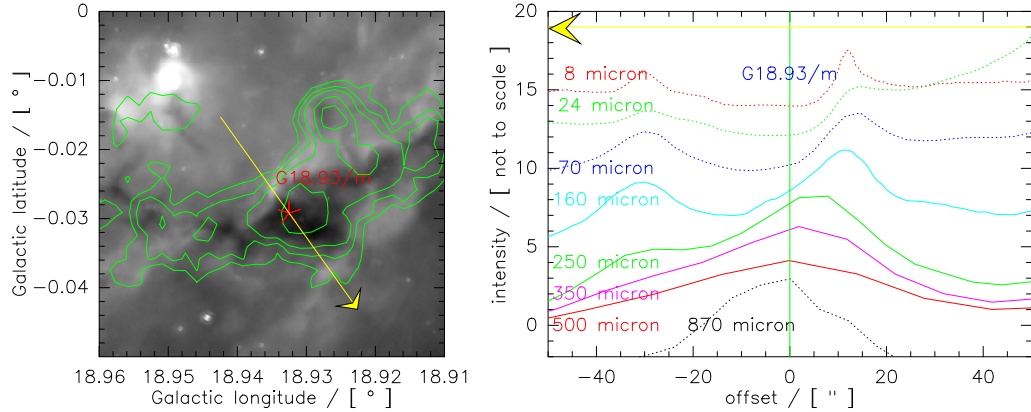


**Figure 4.9:** Profiles of mid-IR data along the cut indicated by the yellow arrow in the *left panel*. While the center of the cut in the *right panel* is G18.93/m, its upper end is chosen to be towards the potential ionizing sources. The different colored profiles in the right panel are of increasing wavelength, starting with 8  $\mu\text{m}$  at the top going to 870  $\mu\text{m}$  at the bottom. The intensities are not to scale, but adopted to fit in the panel. The green vertical line indicates the position of the ATLASGAL continuum peak, the yellow arrow corresponds in direction and length to the arrow in the *left panel*, in which the background image is a GLIMPSE 8  $\mu\text{m}$  image with ATLASGAL contours (at 0.3 Jy, 0.4 Jy, 0.5 Jy, 0.7 Jy, 0.9 Jy, 1.3 Jy, 1.8 Jy, and 2.5 Jy) on *top*.

molecular gas is not a prerequisite for the formation of cold clumps/cores, but that the high (column) densities required also prohibit the destruction of molecules. Hence molecular gas is not a requirement, but form simultaneously. Therefore, the layered structure does not affect the star formation within G18.93. Instead, shielding of the radiation field is most important and the layered structure proves the effectiveness of the shielding.

#### 4.4.3 The temperature distribution

As described in Sect. 4.3.3, the hot ionizing source as well as the IRAS source heat up their environment and produce a temperature gradient across G18.93 (cf. Fig. 4.5). On large scales shown by the top panel of Fig. 4.5, beyond the heating from the ionizing source the fitted dust temperature drops to values between 19 K and 20 K, typical for the ISM (Reach et al., 1995). Within, the temperatures towards the continuum peaks stand out against their direct vicinity. However, all dense clumps are warmer than the general dust/ISM temperature.

A different visualization of the temperature gradient becomes visible if we compare the mid-IR wavelengths. Figure 4.9 shows a cut through G18.93/m for different wavelengths, ranging from 8  $\mu\text{m}$  to 870  $\mu\text{m}$ . While the longest wavelengths trace the column density peak of the cold dust, the SED peak moves along the temperature gradient towards the heating source. Therefore, the shorter wavelengths are offset towards the heating source as well and we can trace its transition directly if we employ the full resolution at all wavelengths. Only the 8  $\mu\text{m}$  band is not consistent with that picture. Since it is dominated by PAH emission, its peak is influenced by the ionizing radiation.

IRDC temperatures elevated above the general ISM temperature of  $\sim 18$  K are differ-

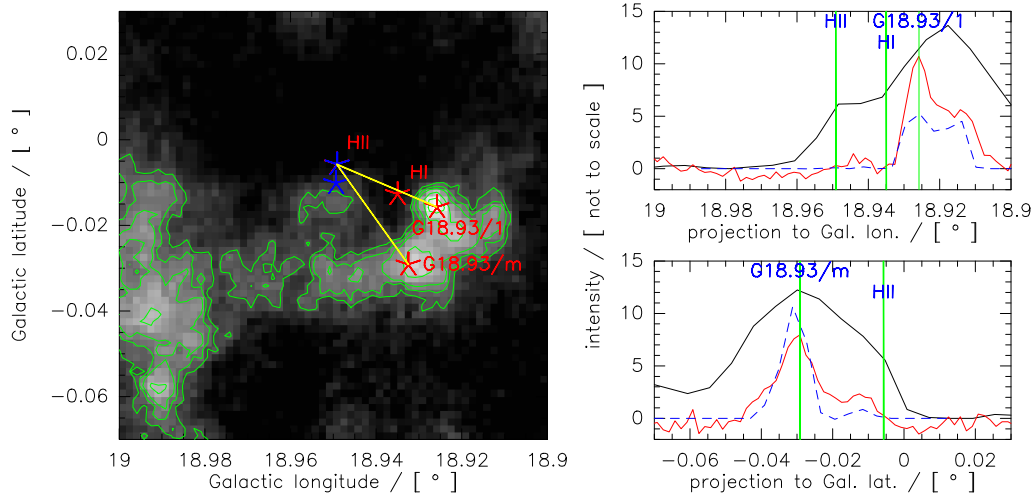


**Figure 4.10:** Profile of  $^{13}\text{CO}$  (black), ATLASGAL (red), and  $\text{H}^{13}\text{CO}^+$  (dashed blue) along the two yellow lines shown on top of the  $870\ \mu\text{m}$  map in the left plot. The position of the peak of HII emission is indicated within both profiles (*right*) and the map (*left*). The *left panel* also gives the two main IRDC peaks. The blue asterisks indicate the position of the IRAS source (lower position) and UKIDSS source (higher position). The green contours from ATLASGAL are at 0.3 Jy, 0.4 Jy, 0.5 Jy, 0.7 Jy, 0.9 Jy, 1.3 Jy, 1.8 Jy, and 2.5 Jy.

ent from typical regions of both low- and high-mass star formation (Peretto et al. 2010; Battersby et al. 2011; Nielbock et al. 2012; Launhardt et al. 2013) in which their temperatures (or the ones of dense cores) drop to temperatures below the ISM value. In contrast to the above studies, Beuther et al. (2012a) find values for IRDC 18454 similar to what we find. In IRDC 18454, the mini starburst cluster W43 raises the general temperature of the IRDC complex to similar temperatures as we find for G18.93. Beuther et al. (2012a) point out that the elevation of the dust temperature raises the Jeans length/mass, and therefore speculate that high-mass star formation may be favored. Hence, it could be that it is not the expansion of the HII region and the connected shock front that promotes the formation of OB associations on the rims of bubbles, but the effects of heating on the environment.

Therefore we conclude that the bubble does have an effect on the temperature of the IRDC, but we cannot distinguish whether this is only due to the heating source or also because of the shock front.

#### 4.4.4 Does the HII region change the shape of the IRDC?

Elmegreen (1998) explains the formation of fingers (or elephant trunk like structures) as a shock wave runs over density enhancements and this has been directly observed (e.g. Motte et al. 2010). For the interface between G18.93 and the neighboring bubble no such structures are visible in Fig. 4.2 nor at other wavelengths available.

In the picture of the “collect and collapse” model the HII region pushes material along. In the vicinity of a pre-existing IRDC, the shock wave mainly penetrates one side of the

IRDC, the one facing the HII region. Thus the IRDC should become asymmetric, with a steeper density profile towards the bubble. Such an asymmetry should be reflected in the projected profiles of the IRDC.

Figure 4.10 shows profiles of various gas tracers along two lines. While the profile through clump G18.93/1 shows a second peak along the profile and is therefore unsuited for comparing the shape of the profile, the cut through G18.93/m seems to be well suited. Figure 4.10 shows that  $^{13}\text{CO}$  is more of an envelope around the entire complex and the HII peak is enclosed within the low density gas. Different from that, the dense gas peak from ATLASGAL data is clearly narrower. However, fitting both sides of the sub-mm continuum intensity distribution of G18.93/m with an exponential function independently, we find no difference between both sides of the profile. At the resolution of the IRAM  $\text{H}^{13}\text{CO}^+$  maps we do not have sufficient data points to do statistically meaningful fits to both slopes, but on the sparse data available, again we find no difference.

Therefore we conclude that at least for G18.93/m the bubble does not seem to influence the density profile of the IRDC.

#### 4.4.5 Imprints of the shock in the dense gas?

After the fast (super sonic) initial expansion of an HII region to the size of a Strömgen sphere, the shock's velocity quickly drops below the sound speed  $v_S$  of the medium. Typical values of  $v_S$  are close to  $10 \text{ km s}^{-1}$  for the hot ionized gas. As the shock front hits the dense gas of G18.93, the expansion velocity drops dramatically, while the lower density gas towards higher latitudes allows an accelerated expansion producing the "champagne flow". However, even the slow shock front should still leave its imprint in the dense gas.

In order to search the potentially shocked gas for velocity peculiarities, we examined  $\text{H}^{13}\text{CO}^+$  spectra at various positions.

For three clumps, Fig. 4.11 compares  $\text{H}^{13}\text{CO}^+$  spectra within the  $8 \mu\text{m}$  rim to spectra at the clump's peak position and positions away from the HII region. Closest to the shock front, the spectra of G18.93/m and G18.93/1, the two right panels of Fig. 4.11, consist clearly of two distinct velocity components of similar strength. Since  $\text{H}^{13}\text{CO}^+$  is expected to be optically thin, we can exclude self absorption. The spectra at the position of the ATLASGAL continuum peaks show two components at the same velocities. However, here one component is significantly stronger than before. At the third position, away from the HII region, G18.93/m shows only a single component, while we do not detect signal for G18.93/1.

A possible interpretation of those spectra could be that one component traces the IRDC, while the second component is shock induced. In that context the rising component towards the peak of the IRDC traces the density distribution of the dense gas. Its distribution is almost symmetric perpendicular to the filament. The second component is bright towards the HII region, but due to the IRDC's high density, the shock has not propagated beyond the peak and therefore no shock component is visible away from the shock front. For the spectra taken across G18.93/4, within our sensitivity limits we cannot find similar clear imprints. Although the spectrum at its peak position has no pure Gaussian profile and a second component is required to fit it, a similar interpretation as

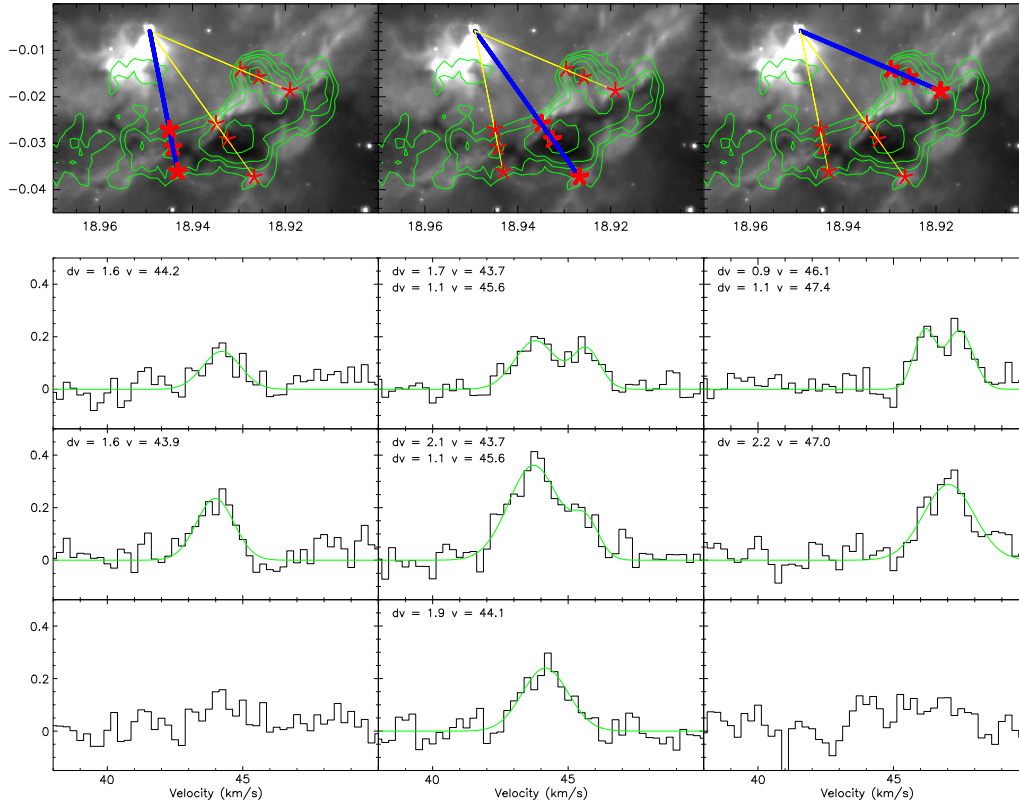


**Figure 4.11:**  $\text{H}^{13}\text{CO}^+$  spectra at positions indicated by bold asterisks in the *top panel*. The positions are chosen to lie along the connection between the UKIDSS near-IR source and the ATLASGAL peak position, with the first spectra at the peak of the GLIMPSE  $8\ \mu\text{m}$  emission. From *left to right* the clumps are G18.93/1, G18.93/m, and G18.93/4. The upper spectra are at positions closer to the ionizing source. Where possible we fitted one, two, or three gaussian components to the spectra. The fitted line widths and peak positions are given in the spectra.

above does not work. In Sect. 4.4.2, we argued that the layered structure breaks down clumps at higher longitudes, because of their lower density. For the same reason, the shock might have had less impact on the dense gas at the center of the filament. Therefore, the imprints in the spectra are not as clear.

It is interesting to note that Klessen et al. (2005) finds similar imprints on quiescent cores. For their modeling of dense cores in which the turbulence is driven on large scales, the velocity dispersion  $\sigma_{\text{turb}}$  of their simulated cores show bow-shaped enhancements (rims) around the continuum emission. In our picture, instead of a large scale convergent flow, the shock introduces turbulence on large scales. The fact that Klessen et al. (2005) measure an increase of line-width instead of two separate velocity components could well be a result of their method for determining  $\sigma_{\text{turb}}$ .

However, the HII region does influence the dense gas of the IRDC. The additional velocity component might give the IRDC additional turbulent support to build more massive fragments.

Another possible imprint of a shock on dense gas could be a broadened line width. Within the limits of our  $\text{H}^{13}\text{CO}^+$  maps, we do not observe such a broadening.

## 4.5 Conclusion

In the middle of a  $>55$  pc long filament is G18.93, a prominent IRDC. While it has the luminous protostellar object EGO G19.01-0.03 at one end, the other end is dark up to  $160\ \mu\text{m}$ . Particularly interesting about G18.93 is its environment; it is located at the projected interface of two IR bubbles. However, it is only spatially coincident with the bubble above the filament, while the bubble at lower latitudes has a different velocity. Using  $\text{H}^{13}\text{CO}^+$  as dense gas tracer we unambiguously attribute kinematic distances to the ATLASGAL continuum emission. Although very close in projection, the high-mass star forming region EGO G19.01-0.03 and its cold dust is not connected to G18.93, but exists at a different distance. From a Galactic rotation curve we determined IRDC G18.93's distance to be 3.6 kpc.

We used CLUMPFIND to decompose the dense gas seen by ATLASGAL into 6 clumps. Together with temperature estimates from HiGal SED fitting, we calculated both the column density and masses of these clumps. The most massive clump is G18.93/m with a gas mass of  $\sim 280 M_{\odot}$ . A comparison of the gas mass to its virial mass of  $360 M_{\odot}$  shows that within the uncertainties it could be gravitationally bound. To determine its evolutionary stage, we first searched the GLIMPSE catalog for young stellar objects using IRAC color criteria, but no young stellar object was found within the boundaries of G18.93/m. Next we visually inspected the longer wavelength images MIPS GAL  $24\ \mu\text{m}$  and HiGal and find no point source at wavelength up to  $160\ \mu\text{m}$ .

In addition, the absence of SiO emission is strongly indicative of no star formation activity. Therefore, we identify G18.93/m as a potential high-mass pre-stellar clump.

Expanding the SED fitting from single positions to all pixels, we produced temperature maps. The sources embedded in the dust connected to IRAS18227-1227 heat the dust and produce a strong gradient across the IRDC. Therefore, all IR dark continuum peaks have temperatures above the general ISM value of  $\sim 19$  K.

In context of the bubble we show that the ‘‘champagne flow’’ structure is produced by an expanding HII region. From measuring the radio continuum flux we estimate the number of Lyman continuum photons and constrain the ionizing source to be at least an O8.5 star.

From VGPS HI spectra we extract a measure of the HI column density. Together with the cm continuum data and the ATLASGAL data we identify a layered structure between the ionizing source and the IRDC, from ionized through atomic to molecular hydrogen.

Finally, we discuss the imprints of the expanding HII region on the starless clump G18.93/m. Our main results are:

- *layered structure*: the ionizing source produces a layered structure towards the IRDC and therefore changes the composition of the hydrogen phase.

- *temperature distribution*: the IRAS source and/or the ionizing source produce a strong temperature gradient across the IRDC. Although the dust temperature at the continuum peaks is reduced compared to their surrounding, their absolute temperatures are above the ISM values. This is atypical compared to most other IRDCs. However, as discussed in Beuther et al. (2012a), the additional support raises the Jeans length which might favor high-mass star formation.
- *density profiles*: in the picture of the “collapse and collect” scenario we would expect the shock front to steepen the density profile of the dense gas. Therefore we compare the emission profile of the cold gas towards and away from G18.93/m. Fitting both wings, we find no difference.
- *imprints within the dense gas*: looking at  $\text{H}^{13}\text{CO}^+$  spectra across the filament, we find emission that resembles the brightness of the ATLASGAL dust continuum. In addition we find a second  $\text{H}^{13}\text{CO}^+$  component, brightest within a PAH rim towards the bubble and not detected away from the bubble. We speculate that this might be a direct imprint of the shock front onto the IRDC.

Therefore, while the additional heating and the shock induced velocity component favor high-mass star formation, we do not find evidence for collapse triggered by the expanding HII region.

## Chapter 5

# Summary, conclusion, and outlook

### 5.1 Summary

#### A search for starless clumps in the ATLASGAL survey

To date, no reliable MIPS GAL point-source catalog is available. Therefore, no previous study incorporated the sensitive MIPS GAL data on scales similar to the  $20 \text{ deg}^2$  we surveyed. To overcome the difficulty of the point source extraction, in Chap. 2 we first excluded clumps with ongoing star formation using established and well-known mid-IR tracers. Then we visually inspected every remaining clumps, searching for faint  $24 \mu\text{m}$  point sources. By inspection we were able to exclude embedded point sources down to  $1.1 L_{\odot}$  to  $27 L_{\odot}$  for 3 kpc to 15 kpc, respectively, thus ruling out the possibility of ongoing high-mass star formation in these clumps.

For an area encompassing  $20 \text{ deg}^2$ , we found 210 starless clumps with high peak column densities, which show that *the dense starless-clump phase exists*. In particular, we found the first starless clump on the far-side of the Galaxy. Despite the varying spatial resolution, the analysis of the clump mass function for clumps on the near and far side of the Galaxy shows that both populations are similar. From the 124 objects likely located on the near side of the Galaxy, only eight regions have the potential to form stars more massive than  $20 M_{\odot}$ , and only a single object is capable of forming a star more massive than  $40 M_{\odot}$ . Therefore, large-scale surveys as this are crucial for the identification of such rare objects.

To answer the question “*What is the lifetime of dense starless clumps?*” we use the most massive starless clumps to estimate their lifetime. Using various assumptions, in particular the Milky Way star-formation rate, we derive it to be between 15 kyr and 60 kyr.

We also tried to identify evolutionary stages later than the starless clump phase. In Sec. 2.10.4 we discuss our ideas and results, and the derived timescales for the formation of massive stars agree with previous estimates. However, difficulties in the classification lead to unsatisfactory uncertainties.

### Kinematics in high-mass star forming regions

The *Herschel*/EPoS program is dedicated to the study of Galactic star formation and observed 45 high-mass star-forming regions with all 6 PACS and SPIRE bands. However, while this allows to trace even the coldest and probably youngest embedded objects in star formation, to give constraints to the question: “*How do clumps and cores form?*” large-scale kinematic information of the gas is required. Therefore, we mapped 16 of the EPoS sources in  $\text{N}_2\text{H}^+$ , a high-density gas tracer, as described in Chap. 3. Due to the hyperfine structure of spectral lines in this molecule, it is useful as a tracer for the column density the line velocity, and the linewidth over a wide range of column densities.

We find that all regions larger than 1 pc show either velocity gradients or fragment into independent structures with distinct velocities. The velocity profiles of several regions with a smooth gradient are consistent with gas flows along the filament, suggesting accretion flows onto the densest regions.

For 10 regions, our observations cover the  $\text{HCO}^+$  and  $\text{H}^{13}\text{CO}^+$  lines as well. Comparing the optically-thick  $\text{HCO}^+$  line to the optically-thin  $\text{H}^{13}\text{CO}^+$  line, we find clearly skewed line profiles across several spectra for four regions. While three of those regions show only blue skewed profiles, suggesting global infall, a small part of G28.34 shows red skewed lines. The infall velocities in G28.34 may even exceed the local sound speed.

Both results, accretion flows and global infall, show that in high-mass star-formation the gas reservoir is constantly replenished. In contrast to the classical picture of low-mass star formation in which the low-mass cores provide the total gas reservoir, cores and clumps in high-mass star formation can accrete material from their surroundings.

### Triggered/sequential star formation? A multi-phase ISM study around the prominent IRDC G18.93-0.03

Our study of the kinematics of high-mass star-forming regions has emphasized their dynamical nature. However, for the studied systems we can only speculate about the origin of the gas motions. In other regions, expanding HII regions are driving parsec-sized bubbles which could produce gas motions leading to the formation of stars. This leads to the question: *Do O/B stars and massive clusters trigger star-formation?* We addressed this question in Chap. 4, by searching for observable influences of the expanding HII region on a starless clump.

We selected a starless clump from a filament  $> 50$  pc long, which lies on the rim of an infrared bubble. The starless clump does not harbor a point source up to  $160 \mu\text{m}$  in the *Herschel*/HiGal data, nor do we detect SiO inside. Using IRAM and GRS observations of  $\text{H}^{13}\text{CO}^+$  and  $^{13}\text{CO}$ , we show that the rim of the bubble and starless clump have the same velocity, and therefore are likely physically associated. From continuum observations, in combination with  $^{13}\text{CO}$  data, the showpiece massive young stellar object, G19.01-0.03, could have been associated with the bubble and presumed to be triggered. Nevertheless, its velocity differs significantly from that of the bubble, revealing that the two objects are not physically connected. To investigate the origin and nature of the bubble, we use centimeter continuum data. We show that the bubble is filled with ionized gas, and infer

the presence of an ionizing source of spectral type O 8.5 or earlier.

Between the ionizing source and the IRDC we find a layered structure, with a transition from ionized hydrogen through atomic to molecular hydrogen. This proves the effective shielding of the UV radiation, but has neither a constructive nor destructive effect on the ability to form stars. Fitting a modified Planck function to the spectral energy distribution, we derive a temperature map for the region. Although the temperature decreases toward the center of the starless clump, it is still higher than the temperature of the general ISM. While common temperatures within IRDCs are below the value of the general ISM, the elevated temperatures in the starless clump could lead to larger fragments, favoring high-mass star formation. In the picture of "collect and collapse", the bubble rim should add mass to the dark clump, altering its density profile. However, comparing the dust emission profile toward and away from the ionizing source, we find no difference in the distribution of cold gas. Therefore, we find no evidence that the expansion of the HII region has influenced the distribution of gas in the starless clump. Finally, we found a second, independent velocity component within the dense gas at the interface between the HII region and the starless clump. As discussed earlier in the thesis, this could be due to multiple cores along the line of sight. Alternatively, the second velocity component could be induced by a shock front, introducing additional turbulence, which would allow the formation of larger fragment.

In summary, while we find no evidence that the starless clump is prone to collapse because of the expanding HII region, it still might favor the formation of higher-mass objects.

### **Additional contributions to other work**

During my PhD I contributed to additional publications. I provide a list of all publications I contributed to, together with their abstracts, in Appendix C.

## **5.2 Conclusion**

This thesis is dedicated to the study of high-mass star formation. We were particularly interested in the early evolutionary stages and the environments in which massive young stellar objects can form. Therefore, we addressed questions related to the starless clump phase and the dynamics of young and massive star-forming regions.

Our results show that in high-mass star formation massive and dense starless clumps exist. Since starless clumps are the starting point in several numerical calculations, our sample of starless clumps can provide initial conditions for such simulations. The short lifetime and the star formation time-scale we derive, show that high-mass star formation is a fast process, taking less than one million years.

The global infall found for four of the star-forming regions and the velocity gradients along the filaments, are consistent with both competitive accretion and colliding flow models, although in competitive accretion no starless clump phase exists. However, in the

context of our results, the quasi-static view of monolithic collapse of an isolated massive core seems unlikely.

### 5.3 Outlook

Based on the starless clump catalog, we were able to estimate the lifetime of dense starless clumps. However, difficulties with the definition of a sample of clumps that eventually will form high-mass stars as well as achieving a full classification hampered our efforts to derive star-formation time-scales. However, both the total star-formation time-scale and the lifetimes of the each evolutionary phase could put constraints on future numerical efforts to understand the underlying physical processes in high-mass star formation. For example the MALT90 project (PI J. Jackson Foster et al., 2011), mapping 16 emission lines of high-mass dense cores, might allow a better classification of the evolutionary stage of such objects. This would improve estimates of the star-formation time-scale.

The starless-clump catalog presented is an ideal sample to study the starless clump phase in great detail. For example, despite the large distance to the starless clumps, current (sub-) millimeter interferometers, such as the Plateau de Bure interferometer (PdBI), the Submillimeter Array (SMA), or the Atacama Large Millimeter Array (ALMA), are capable of resolving the Jeans length within dense clumps. All previous high-resolution studies of dense clumps have resolved sub-structure/fragments. Is this true for all starless clumps? In this context, Beuther et al. (subm.) study the fragmentation properties of a starless clump. However, higher-resolution imaging is required, as well as a more rigorous statistical basis.

Another important aspect of starless clumps is their undisturbed nature. Once star formation sets in, feedback will influence the harboring clumps. Therefore, only in starless objects can one study the physical conditions prevalent during the onset of star formation. For example, Beuther et al. (2012a) study starless clumps in IRDC 18454, but further observations of more typical starless clumps are required.

While we show the dynamics of the large-scale gas in Chap. 4, high-resolution studies should also be able to trace gas motions onto individual cores, if they exist. Such observations could differentiate different star-formation scenarios. In addition, we speculate that the large-scale distribution of the linewidth is dominated by unresolved velocity gradients. Hence, the linewidth measured from interferometric observations is usually smaller. Therefore, high-resolution data is required to study the distribution of the linewidth. This could help to test the gravo-turbulent fragmentation model (Klessen et al., 2005).

While all previous suggestions ideas call for higher-resolution studies, it is also necessary to improve the understanding of the larger scales. We discussed converging large-scale flows as a possible cloud formation mechanism, and the dynamical signatures on scales of 0.1 pc which we find agree with that. However, such flows should also be visible on scales of tens to hundreds of parsecs in atomic hydrogen (Clark et al., 2012), and on scales of tens of parsecs in molecular gas. Among other aspects, the VLA HI/OH/H $\alpha$  Milky Way survey THOR (PI: H. Beuther) will try to address that question. Due to the simultaneous observation of HI and OH, it will also be possible to study the conversion from atomic to molecular gas.

---

Only combining the gas dynamics at all scales will allow us to answer whether the observed flows on small scales are primordial or gravitationally controlled, and whether clouds, clumps, and cores form due to gravity or turbulence.

However, to distinguish the different numerical models of star formation and with it the importance of the underlying physics, the observable signatures of each model need to be calculated. Smith et al. (subm.) has started this effort for the competitive accretion scenario, but more studies are required covering all models.



# Bibliography

- Aguirre, J. E., Ginsburg, A. G., Dunham, M. K., et al. 2011, *ApJS*, 192, 4
- Allen, L. E., Calvet, N., D'Alessio, P., et al. 2004, *ApJS*, 154, 363
- Alves, J., Lombardi, M., & Lada, C. J. 2007, *A&A*, 462, L17
- André, P., Men'shchikov, A., Bontemps, S., et al. 2010, *A&A*, 518, L102
- Bally, J., Aguirre, J., Battersby, C., et al. 2010, *ApJ*, 721, 137
- Bania, T. M., Anderson, L. D., Balser, D. S., & Rood, R. T. 2010, *ApJ*, 718, L106
- Barnard, E. E. 1919, *ApJ*, 49, 1
- Bastian, N., Covey, K. R., & Meyer, M. R. 2010, *ARA&A*, 48, 339
- Battersby, C., Bally, J., Ginsburg, A., et al. 2011, *A&A*, 535, A128
- Beltrán, M. T., Brand, J., Cesaroni, R., et al. 2006, *A&A*, 447, 221
- Benjamin, R. A., Churchwell, E., Babler, B. L., et al. 2003, *PASP*, 115, 953
- Bergin, E. A. & Tafalla, M. 2007, *ARA&A*, 45, 339
- Beuther, H., Churchwell, E. B., McKee, C. F., & Tan, J. C. 2007, *Protostars and Planets V*, 165
- Beuther, H., Henning, T., Linz, H., et al. 2010, *A&A*, 518, L78+
- Beuther, H., Schilke, P., Menten, K. M., et al. 2002a, *ApJ*, 566, 945
- Beuther, H., Schilke, P., Menten, K. M., et al. 2002b, in *Astronomical Society of the Pacific Conference Series*, Vol. 267, *Hot Star Workshop III: The Earliest Phases of Massive Star Birth*, ed. P. Crowther, 341–+
- Beuther, H. & Sridharan, T. K. 2007, *ApJ*, 668, 348
- Beuther, H., Sridharan, T. K., & Saito, M. 2005, *ApJ*, 634, L185
- Beuther, H. & Steinacker, J. 2007, *ApJ*, 656, L85
- Beuther, H., Tackenberg, J., Linz, H., et al. 2012a, *A&A*, 538, A11
- Beuther, H., Tackenberg, J., Linz, H., et al. 2011, *ArXiv e-prints*

- Beuther, H., Tackenberg, J., Linz, H., et al. 2012b, *ApJ*, 747, 43
- Beuther, H., Zhang, Q., Sridharan, T. K., Lee, C.-F., & Zapata, L. A. 2006, *A&A*, 454, 221
- Bieging, J. H., Peters, W. L., Vila Vilaro, B., Schlottman, K., & Kulesa, C. 2009, *AJ*, 138, 975
- Blitz, L., Fich, M., & Stark, A. A. 1982, *ApJS*, 49, 183
- Boley, P. A., Linz, H., van Boekel, R., et al. 2012, *A&A*, 547, A88
- Bonnell, I. A. & Bate, M. R. 2005, *MNRAS*, 362, 915
- Bonnell, I. A. & Bate, M. R. 2006, *MNRAS*, 370, 488
- Bonnell, I. A., Bate, M. R., & Zinnecker, H. 1998, *MNRAS*, 298, 93
- Bonnell, I. A., Vine, S. G., & Bate, M. R. 2004, *MNRAS*, 349, 735
- Bontemps, S., André, P., Könyves, V., et al. 2010a, *A&A*, 518, L85
- Bontemps, S., Motte, F., Csengeri, T., & Schneider, N. 2010b, *A&A*, 524, A18+
- Bronfman, L., Casassus, S., May, J., & Nyman, L. 2000, *A&A*, 358, 521
- Bronfman, L., Nyman, L.-A., & May, J. 1996, *A&AS*, 115, 81
- Carey, S. J., Clark, F. O., Egan, M. P., et al. 1998, *ApJ*, 508, 721
- Carey, S. J., Noriega-Crespo, A., Mizuno, D. R., et al. 2009, *PASP*, 121, 76
- Cesaroni, R., Neri, R., Olmi, L., et al. 2005, *A&A*, 434, 1039
- Chabrier, G. 2003, *PASP*, 115, 763
- Chabrier, G. & Hennebelle, P. 2010, *ApJ*, 725, L79
- Churchwell, E., Povich, M. S., Allen, D., et al. 2006, *ApJ*, 649, 759
- Churchwell, E., Watson, D. F., Povich, M. S., et al. 2007, *ApJ*, 670, 428
- Clark, P. C., Glover, S. C. O., Klessen, R. S., & Bonnell, I. A. 2012, *MNRAS*, 424, 2599
- Commerçon, B., Hennebelle, P., & Henning, T. 2011, *ApJ*, 742, L9
- Condon, J. J., Cotton, W. D., Greisen, E. W., et al. 1998, *AJ*, 115, 1693
- Contreras, Y., Schuller, F., Urquhart, J. S., et al. 2013, *A&A*, 549, A45
- Csengeri, T., Bontemps, S., Schneider, N., Motte, F., & Dib, S. 2011a, *A&A*, 527, A135
- Csengeri, T., Bontemps, S., Schneider, N., et al. 2011b, *ApJ*, 740, L5
- Cyganowski, C. J., Brogan, C. L., Hunter, T. R., & Churchwell, E. 2011a, *ApJ*, 743, 56

- Cyganowski, C. J., Brogan, C. L., Hunter, T. R., Churchwell, E., & Zhang, Q. 2011b, *ApJ*, 729, 124
- Cyganowski, C. J., Whitney, B. A., Holden, E., et al. 2008, *AJ*, 136, 2391
- Dame, T. M., Hartmann, D., & Thaddeus, P. 2001, *ApJ*, 547, 792
- Dame, T. M. & Thaddeus, P. 2008, *ApJ*, 683, L143
- Deharveng, L., Lefloch, B., Zavagno, A., et al. 2003, *A&A*, 408, L25
- Deharveng, L., Schuller, F., Anderson, L. D., et al. 2010, *A&A*, 523, A6
- Diehl, R., Halloin, H., Kretschmer, K., et al. 2006, *Nature*, 439, 45
- Diolaiti, E., Bendinelli, O., Bonaccini, D., et al. 2000, *A&AS*, 147, 335
- Draine, B. T. 2011, *Physics of the Interstellar and Intergalactic Medium*
- Draine, B. T. & Lee, H. M. 1984, *ApJ*, 285, 89
- Draine, B. T. & Li, A. 2007, *ApJ*, 657, 810
- Dunham, M. K., Robitaille, T. P., Evans, II, N. J., et al. 2011, *ApJ*, 731, 90
- Egan, M. P., Price, S. D., Kraemer, K. E., et al. 2003, *VizieR Online Data Catalog*, 5114, 0
- Egan, M. P., Shipman, R. F., Price, S. D., et al. 1998, *ApJ*, 494, L199
- Elmegreen, B. G. 1998, in *Astronomical Society of the Pacific Conference Series*, Vol. 148, *Origins*, ed. C. E. Woodward, J. M. Shull, & H. A. Thronson, Jr., 150
- Elmegreen, B. G. & Lada, C. J. 1977, *ApJ*, 214, 725
- Enoch, M. L., Evans, II, N. J., Sargent, A. I., et al. 2008, *ApJ*, 684, 1240
- Fallscheer, C., Beuther, H., Sauter, J., Wolf, S., & Zhang, Q. 2011, *ApJ*, 729, 66
- Fallscheer, C., Beuther, H., Zhang, Q., Keto, E., & Sridharan, T. K. 2009, *A&A*, 504, 127
- Faúndez, S., Bronfman, L., Garay, G., et al. 2004, *A&A*, 426, 97
- Ferrière, K. M. 2001, *Reviews of Modern Physics*, 73, 1031
- Fich, M., Treffers, R. R., & Blitz, L. 1982, in *Astrophysics and Space Science Library*, Vol. 93, *Regions of Recent Star Formation*, ed. R. S. Roger & P. E. Dewdney, 201–207
- Foster, J. B., Jackson, J. M., Barris, E., et al. 2011, *ArXiv e-prints*
- Gennaro, M., Bik, A., Brandner, W., et al. 2012, *A&A*, 542, A74
- Glover, S. C. O. & Clark, P. C. 2012, *MNRAS*, 421, 9
- Gómez, L., Wyrowski, F., Pillai, T., Leurini, S., & Menten, K. M. 2011, *A&A*, 529, A161

- Green, J. A., Caswell, J. L., McClure-Griffiths, N. M., et al. 2011, *ApJ*, 733, 27
- Griffin, M. J., Abergel, A., Abreu, A., et al. 2010, *A&A*, 518, L3
- Gritschneider, M., Lin, D. N. C., Murray, S. D., Yin, Q.-Z., & Gong, M.-N. 2012, *ApJ*, 745, 22
- Gutermuth, R. A., Myers, P. C., Megeath, S. T., et al. 2008, *ApJ*, 674, 336
- Hacar, A. & Tafalla, M. 2011, *A&A*, 533, A34
- Hartmann, L., Ballesteros-Paredes, J., & Heitsch, F. 2012, *MNRAS*, 420, 1457
- Hatchell, J. & Fuller, G. A. 2008, *A&A*, 482, 855
- Hatchell, J. & van der Tak, F. F. S. 2003, *A&A*, 409, 589
- Heitsch, F., Ballesteros-Paredes, J., & Hartmann, L. 2009, *ApJ*, 704, 1735
- Heitsch, F. & Hartmann, L. 2008, *ApJ*, 689, 290
- Helfand, D. J., Becker, R. H., White, R. L., Fallon, A., & Tuttle, S. 2006, *AJ*, 131, 2525
- Hennemann, M., Motte, F., Schneider, N., et al. 2012, *A&A*, 543, L3
- Henning, T., Linz, H., Krause, O., et al. 2010, *A&A*, 518, L95+
- Hildebrand, R. H. 1983, *QJRAS*, 24, 267
- Hill, T., Motte, F., Didelon, P., et al. 2011, *A&A*, 533, A94
- Hillenbrand, L. A. & Hartmann, L. W. 1998, *ApJ*, 492, 540
- Hoare, M. G., Lumsden, S. L., Oudmaijer, R. D., et al. 2004, in *Astronomical Society of the Pacific Conference Series*, Vol. 317, *Milky Way Surveys: The Structure and Evolution of our Galaxy*, ed. D. Clemens, R. Shah, & T. Brainerd, 156–+
- Hoare, M. G., Purcell, C. R., Churchwell, E. B., et al. 2012, *PASP*, 124, 939
- Hollenbach, D. J. & Tielens, A. G. G. M. 1997, *ARA&A*, 35, 179
- Jackson, J. M., Finn, S. C., Chambers, E. T., Rathborne, J. M., & Simon, R. 2010, *ApJ*, 719, L185
- Jackson, J. M., Rathborne, J. M., Shah, R. Y., et al. 2006, *ApJS*, 163, 145
- Johnston, K. G., Shepherd, D. S., Aguirre, J. E., et al. 2009, *ApJ*, 707, 283
- Johnstone, D., Fiege, J. D., Redman, R. O., Feldman, P. A., & Carey, S. J. 2003, *ApJ*, 588, L37
- Johnstone, D., Wilson, C. D., Moriarty-Schieven, G., et al. 2000, *ApJ*, 545, 327
- Jørgensen, J. K., Schöier, F. L., & van Dishoeck, E. F. 2004, *A&A*, 416, 603
- Kainulainen, J., Alves, J., Beuther, H., Henning, T., & Schuller, F. 2011, *A&A*, 536, A48

- Kainulainen, J., Lada, C. J., Rathborne, J. M., & Alves, J. F. 2009, *A&A*, 497, 399
- Kendrew, S., Simpson, R., Bressert, E., et al. 2012, *ApJ*, 755, 71
- Kessler, M. F., Steinz, J. A., Anderegg, M. E., et al. 1996, *A&A*, 315, L27
- Keto, E. 2003, *ApJ*, 599, 1196
- Kirk, J. M., Ward-Thompson, D., & André, P. 2005, *MNRAS*, 360, 1506
- Klessen, R. S., Ballesteros-Paredes, J., Vázquez-Semadeni, E., & Durán-Rojas, C. 2005, *ApJ*, 620, 786
- Kroupa, P. 2001, *MNRAS*, 322, 231
- Krumholz, M. R., Klein, R. I., & McKee, C. F. 2007, *ApJ*, 656, 959
- Krumholz, M. R. & McKee, C. F. 2008, *Nature*, 451, 1082
- Kuchar, T. A. & Clark, F. O. 1997, *ApJ*, 488, 224
- Kuiper, R., Klahr, H., Beuther, H., & Henning, T. 2010, *ApJ*, 722, 1556
- Kurtz, S., Churchwell, E., & Wood, D. O. S. 1994, *ApJS*, 91, 659
- Lada, C. J. & Lada, E. A. 2003, *ARA&A*, 41, 57
- Ladd, N., Purcell, C., Wong, T., & Robertson, S. 2005, *PASA*, 22, 62
- Launhardt, R., Stutz, A. M., Schmiedeke, A., et al. 2013, *ArXiv e-prints*
- Lawrence, A., Warren, S. J., Almaini, O., et al. 2007, *MNRAS*, 379, 1599
- Lee, K., Looney, L., Johnstone, D., & Tobin, J. 2012, *ApJ*, 761, 171
- Li, D. & Goldsmith, P. F. 2003, *ApJ*, 585, 823
- Linz, H., Krause, O., Beuther, H., et al. 2010, *A&A*, 518, L123
- Liszt, H. S., Burton, W. B., & Bania, T. M. 1981, *ApJ*, 246, 74
- Lockman, F. J. 1989, *ApJS*, 71, 469
- López-Sepulcre, A., Walmsley, C. M., Cesaroni, R., et al. 2011, *A&A*, 526, L2
- Mac Low, M.-M. & Klessen, R. S. 2004, *Reviews of Modern Physics*, 76, 125
- MacLaren, I., Richardson, K. M., & Wolfendale, A. W. 1988, *ApJ*, 333, 821
- Martins, F., Schaerer, D., & Hillier, D. J. 2005, *A&A*, 436, 1049
- McKee, C. F. & Ostriker, E. C. 2007, *ARA&A*, 45, 565
- McKee, C. F. & Tan, J. C. 2003, *ApJ*, 585, 850
- Men'shchikov, A., André, P., Didelon, P., et al. 2010, *A&A*, 518, L103

- Mezger, P. G. & Henderson, A. P. 1967, *ApJ*, 147, 471
- Molinari, S., Swinyard, B., Bally, J., et al. 2010, *PASP*, 122, 314
- Motte, F., Andre, P., & Neri, R. 1998, *A&A*, 336, 150
- Motte, F., Bontemps, S., Schilke, P., et al. 2007, *A&A*, 476, 1243
- Motte, F., Schilke, P., & Lis, D. C. 2003, *ApJ*, 582, 277
- Motte, F., Zavagno, A., Bontemps, S., et al. 2010, *A&A*, 518, L77+
- Mottram, J. C., Hoare, M. G., Urquhart, J. S., et al. 2011, *A&A*, 525, A149+
- Müller, H. S. P., Schlöder, F., Stutzki, J., & Winnewisser, G. 2005, *Journal of Molecular Structure*, 742, 215
- Myers, P. C., Mardones, D., Tafalla, M., Williams, J. P., & Wilner, D. J. 1996, *ApJ*, 465, L133
- Neugebauer, G., Habing, H. J., van Duinen, R., et al. 1984, *ApJ*, 278, L1
- Nielbock, M., Launhardt, R., Steinacker, J., et al. 2012, *A&A*, 547, A11
- Ossenkopf, V. & Henning, T. 1994, *A&A*, 291, 943
- Ott, S. 2010, in *Astronomical Society of the Pacific Conference Series*, Vol. 434, *Astronomical Data Analysis Software and Systems XIX*, ed. Y. Mizumoto, K.-I. Morita, & M. Ohishi, 139
- Panagia, N. 1973, *AJ*, 78, 929
- Parker, Q. A., Phillipps, S., Pierce, M. J., et al. 2005, *MNRAS*, 362, 689
- Perault, M., Omont, A., Simon, G., et al. 1996, *A&A*, 315, L165
- Peretto, N., André, P., Könyves, V., et al. 2012, *A&A*, 541, A63
- Peretto, N. & Fuller, G. A. 2009, *A&A*, 505, 405
- Peretto, N. & Fuller, G. A. 2010, *ApJ*, 723, 555
- Peretto, N., Fuller, G. A., Plume, R., et al. 2010, *A&A*, 518, L98+
- Pilbratt, G. L., Riedinger, J. R., Passvogel, T., et al. 2010, *A&A*, 518, L1
- Pillai, T., Wyrowski, F., Carey, S. J., & Menten, K. M. 2006, *A&A*, 450, 569
- Pineda, J. E., Rosolowsky, E. W., & Goodman, A. A. 2009, *ApJ*, 699, L134
- Pitann, J., Linz, H., Ragan, S., et al. 2013, *ArXiv e-prints*
- Planck Collaboration, Ade, P. A. R., Aghanim, N., et al. 2011, *A&A*, 536, A7
- Poglitsch, A., Waelkens, C., Geis, N., et al. 2010, *A&A*, 518, L2

- Purcell, C. R. & Hoare, M. G. 2010, *Highlights of Astronomy*, 15, 781
- Purcell, C. R., Hoare, M. G., & Diamond, P. 2008, in *Astronomical Society of the Pacific Conference Series*, Vol. 387, *Massive Star Formation: Observations Confront Theory*, ed. H. Beuther, H. Linz, & T. Henning, 389
- Ragan, S., Henning, T., Krause, O., et al. 2012, *A&A*, 547, A49
- Rathborne, J. M., Jackson, J. M., & Simon, R. 2006, *ApJ*, 641, 389
- Reach, W. T., Dwek, E., Fixsen, D. J., et al. 1995, *ApJ*, 451, 188
- Reich, W., Reich, P., & Fuerst, E. 1990, *A&AS*, 83, 539
- Reid, M. A., Wadsley, J., Petitclerc, N., & Sills, A. 2010, *ApJ*, 719, 561
- Reid, M. A. & Wilson, C. D. 2005, *ApJ*, 625, 891
- Reid, M. J., Menten, K. M., Zheng, X. W., et al. 2009, *ApJ*, 700, 137
- Robitaille, T. P., Meade, M. R., Babler, B. L., et al. 2008, *AJ*, 136, 2413
- Robitaille, T. P. & Whitney, B. A. 2010, *ApJ*, 710, L11
- Robitaille, T. P., Whitney, B. A., Indebetouw, R., Wood, K., & Denzmore, P. 2006, *ApJS*, 167, 256
- Rosolowsky, E., Dunham, M. K., Ginsburg, A., et al. 2010, *ApJS*, 188, 123
- Roussel, H. 2012, *ArXiv e-prints*
- Russeil, D., Zavagno, A., Motte, F., et al. 2010, *A&A*, 515, A55+
- Sakai, T., Sakai, N., Hirota, T., & Yamamoto, S. 2010, *ApJ*, 714, 1658
- Salpeter, E. E. 1955, *ApJ*, 121, 161
- Sawada, T., Ikeda, N., Sunada, K., et al. 2008, *PASJ*, 60, 445
- Schilke, P., Walmsley, C. M., Pineau des Forets, G., & Flower, D. R. 1997, *A&A*, 321, 293
- Schlingman, W. M., Shirley, Y. L., Schenk, D. E., et al. 2011, *ApJS*, 195, 14
- Schneider, N., Csengeri, T., Bontemps, S., et al. 2010, *A&A*, 520, A49
- Schöier, F. L., van der Tak, F. F. S., van Dishoeck, E. F., & Black, J. H. 2005, *A&A*, 432, 369
- Schuller, F., Menten, K. M., Contreras, Y., et al. 2009, *A&A*, 504, 415
- Seifried, D., Banerjee, R., Klessen, R. S., Duffin, D., & Pudritz, R. E. 2011, *MNRAS*, 417, 1054
- Shu, F. H. 1977, *ApJ*, 214, 488
- Shu, F. H., Adams, F. C., & Lizano, S. 1987, *ARA&A*, 25, 23

- Siess, L., Dufour, E., & Forestini, M. 2000, *A&A*, 358, 593
- Simon, R., Jackson, J. M., Rathborne, J. M., & Chambers, E. T. 2006, *ApJ*, 639, 227
- Simpson, R. J., Povich, M. S., Kendrew, S., et al. 2012, *MNRAS*, 424, 2442
- Siringo, G., Kreysa, E., Kovács, A., et al. 2009, *A&A*, 497, 945
- Smith, R. J., Clark, P. C., & Bonnell, I. A. 2008, *MNRAS*, 391, 1091
- Smith, R. J., Longmore, S., & Bonnell, I. 2009, *MNRAS*, 400, 1775
- Smith, R. J., Shetty, R., Stutz, A. M., & Klessen, R. S. 2012, *ApJ*, 750, 64
- Solomon, P. M. & Rivolo, A. R. 1989, *ApJ*, 339, 919
- Spitzer, L. 1978, *Physical processes in the interstellar medium*
- Sridharan, T. K., Beuther, H., Saito, M., Wyrowski, F., & Schilke, P. 2005, *ApJ*, 634, L57
- Sridharan, T. K., Beuther, H., Schilke, P., Menten, K. M., & Wyrowski, F. 2002, *ApJ*, 566, 931
- Stahler, S. W. & Palla, F. 2005, *The Formation of Stars*
- Stil, J. M., Taylor, A. R., Dickey, J. M., et al. 2006, *AJ*, 132, 1158
- Stutz, A., Launhardt, R., Linz, H., et al. 2010, *A&A*, 518, L87
- Sunada, K., Yamaguchi, C., Kuno, N., et al. 2000, in *Astronomical Society of the Pacific Conference Series*, Vol. 217, *Imaging at Radio through Submillimeter Wavelengths*, ed. J. G. Mangum & S. J. E. Radford, 19
- Tackenberg, J., Beuther, H., Henning, T., et al. 2012a, *A&A*, 540, A113
- Tackenberg, J., Beuther, H., Plume, R., et al. 2012b, *ArXiv e-prints*
- Tielens, A. G. G. M. 2005, *The Physics and Chemistry of the Interstellar Medium*
- Tobin, J. J., Hartmann, L., Bergin, E., et al. 2012, *ApJ*, 748, 16
- Traficante, A., Calzoletti, L., Veneziani, M., et al. 2011, *MNRAS*, 416, 2932
- Vasyunina, T., Linz, H., Henning, T., et al. 2009, *A&A*, 499, 149
- Vasyunina, T., Linz, H., Henning, T., et al. 2011, *A&A*, 527, A88
- Wang, Y., Zhang, Q., Pillai, T., Wyrowski, F., & Wu, Y. 2008, *ApJ*, 672, L33
- Wienen, M., Wyrowski, F., Schuller, F., et al. 2012, *A&A*, 544, A146
- Wilcock, L. A., Kirk, J. M., Stamatellos, D., et al. 2011, *A&A*, 526, A159+
- Wilcock, L. A., Ward-Thompson, D., Kirk, J. M., et al. 2012, *MNRAS*, 422, 1071
- Williams, J. P., Blitz, L., & McKee, C. F. 2000, *Protostars and Planets IV*, 97

- Williams, J. P., de Geus, E. J., & Blitz, L. 1994, *ApJ*, 428, 693
- Williams, S. J., Fuller, G. A., & Sridharan, T. K. 2004, *A&A*, 417, 115
- Wilson, T. L., Rohlfs, K., & Hüttemeister, S. 2009, *Tools of Radio Astronomy* (Springer-Verlag)
- Wood, D. O. S. & Churchwell, E. 1989, *ApJ*, 340, 265
- Yorke, H. W. & Bodenheimer, P. 1999, *ApJ*, 525, 330
- Yorke, H. W. & Sonnhalter, C. 2002, *ApJ*, 569, 846
- Zavagno, A., Anderson, L. D., Russeil, D., et al. 2010, *A&A*, 518, L101
- Zavagno, A., Deharveng, L., Comerón, F., et al. 2006, *A&A*, 446, 171
- Zinnecker, H. & Yorke, H. W. 2007, *ARA&A*, 45, 481

# Appendix A

## Supplementary material for Chapter 'Starless clumps'

### A.1 Errors and uncertainties

As conventional error propagation breaks down when the uncertainties become larger than a few percent, one can only point out the individual sources of errors and estimate the final uncertainties.

The distance error mainly stems from uncertainties in the Galactic rotation curve and errors in the gas velocities can be neglected. Error propagation including the velocity uncertainties following Reid et al. (2009) suggests uncertainties of smaller than 0.1 kpc. However, owing to intrinsic errors and deviations from the global Galactic rotation we estimate the distance to be uncertain to within 0.5 kpc. This leads to a contribution to the final mass uncertainties ranging from 10% to 50%, that depends on the absolute distance. In addition, individual objects close to the Galactic center that have non-circular orbits may be placed at random distances and contaminate the sample.

In the literature, temperatures of starless cores range from 10 K to 20 K with the bulk at 15 K (Sridharan et al., 2005; Pillai et al., 2006; Vasyunina et al., 2011; Peretto et al., 2010). The temperature estimate here is based on direct observations of 15 out of 210 starless clumps and is in good agreement with earlier studies. A temperature uncertainty of  $\pm 5$  K at 15 K may introduce mass uncertainties of about a factor of two.

The dust properties and the gas-to-dust ratio are very uncertain as well and might contribute another factor of two to the errors. The flux uncertainties are dominated by the calibration uncertainties, which are  $\sim 15\%$  (Schuller et al., 2009).

When calculating the column density as well as the masses, the predominant uncertainties are those of the dust properties and temperatures. For the mass, the uncertainty in the distance is equally important. Altogether, the total uncertainties in the mass may be as large as a factor of five.

## A.2 Full table of starless clumps

Here we present the full table of starless clumps. Please note that it differs from the version on the CDS. The column densities, integrated fluxes, and masses are calculated using the correct beam and a gas-to-dust mass ratio of  $R = 100$ .

Table A.1: Properties of starless clumps.

Global identifier	Gal lon	Gal lat	Ra	Dec	Peak flux	R	Total flux	NH <sub>3</sub> velocity	NH <sub>3</sub> flag	HCO <sup>+</sup> velocity	ve- HCO <sup>+</sup> flag	Near distance	Far distance	Peak column density	Near mass	Far mass	Near flag
	[°]	[°]	[°]	[°]	[Jy/beam <sup>1/2</sup> ]		[Jy]	[km/s]		[km/s]		[kpc]	[kpc]	[10 <sup>23</sup> cm <sup>-2</sup> ]	[M <sub>⊙</sub> ]	[M <sub>⊙</sub> ]	
75	10.6075	-0.3708	272.5993	-19.9382	0.92	36	10.43	-2.9	0	—	0	-0.5	17.0	1.21	0.	37000.	1
76	10.5958	-0.3642	272.5871	-19.9452	0.92	31	7.23	-2.9	0	—	0	-0.5	17.0	1.21	0.	26000.	1
80	10.6858	-0.3075	272.5805	-19.8390	0.86	25	3.72	-1.5	1	-1.7	1	-0.2	16.7	1.13	0.	13000.	1
82	10.1842	-0.4042	272.4125	-20.3249	0.85	21	2.78	10.5	0	9.4	0	1.8	14.7	1.12	110.	7500.	1
83	10.6208	-0.4225	272.6543	-19.9515	0.83	28	5.64	-2.0	1	—	0	-0.3	16.8	1.09	0.	20000.	1
86	10.1658	-0.3342	272.3378	-20.3071	0.81	18	2.18	10.5	0	9.4	0	1.8	14.7	1.07	87.	5900.	1
87	10.1592	-0.3008	272.3032	-20.2968	0.81	18	2.08	10.5	0	9.4	0	1.8	14.7	1.07	83.	5600.	1
94	10.6225	-0.5092	272.7359	-19.9918	0.78	22	3.44	-4.1	0	-3.6	0	-0.7	17.2	1.03	0.	13000.	1
95	10.9825	-0.3692	272.7899	-19.6089	0.78	23	3.33	—	0	-0.6	1	—	16.5	1.03	0.	11000.	0
101	10.1375	-0.3575	272.3449	-20.3432	0.75	17	2.03	10.5	0	9.4	0	1.8	14.7	0.99	81.	5500.	1
105	10.0675	-0.4075	272.3554	-20.4286	0.75	20	2.43	—	0	11.4	1	1.9	14.6	0.99	110.	6500.	1
106	10.1775	-0.4025	272.4075	-20.3300	0.74	13	1.11	10.5	0	9.4	0	1.8	14.7	0.98	44.	3000.	1
111	10.1375	-0.4108	272.3947	-20.3690	0.73	17	1.79	12.9	0	—	0	2.1	14.5	0.96	97.	4700.	1
114	10.1325	-0.4108	272.3921	-20.3734	0.72	15	1.41	12.9	0	—	0	2.1	14.5	0.95	76.	3700.	1
118	10.1342	-0.3475	272.3339	-20.3413	0.71	22	3.08	10.5	0	9.4	0	1.8	14.7	0.94	120.	8300.	1
119	10.5758	-0.3475	272.5613	-19.9547	0.71	17	1.85	-2.9	0	-2.6	1	-0.5	17.0	0.94	0.	6700.	1
121	10.2992	-0.1658	272.2496	-20.1089	0.71	26	4.79	12.8	0	13.6	0	2.1	14.5	0.94	250.	13000.	1
122	11.0575	-0.0958	272.5743	-19.4114	0.70	16	1.72	29.8	0	29.0	0	3.5	13.0	0.92	260.	3600.	1
123	10.5775	-0.3508	272.5653	-19.9548	0.70	19	2.13	-2.9	0	-2.6	1	-0.5	17.0	0.92	0.	7600.	1
140	10.6625	0.0825	272.2059	-19.6708	0.64	21	2.44	—	0	21.1	1	2.8	13.7	0.84	250.	5700.	0
143	10.1958	-0.2892	272.3112	-20.2591	0.62	22	2.64	10.5	0	9.4	0	1.8	14.8	0.82	100.	7200.	1
155	10.6325	-0.4225	272.6603	-19.9412	0.59	18	1.60	-2.9	0	—	0	-0.5	17.0	0.78	0.	5700.	1
156	10.2475	-0.3358	272.3814	-20.2365	0.59	11	0.72	—	0	11.4	1	1.9	14.7	0.78	32.	1900.	0
161	10.2542	-0.3392	272.3880	-20.2322	0.59	12	0.86	—	0	11.4	1	1.9	14.7	0.78	38.	2300.	1
162	11.9139	0.7356	272.2431	-18.2597	0.59	21	2.25	24.0	0	—	0	2.9	13.5	0.78	240.	5100.	1
167	11.0541	-0.0792	272.5571	-19.4062	0.58	19	2.05	29.8	0	29.0	0	3.5	13.0	0.76	310.	4300.	1
168	11.9005	0.7206	272.2501	-18.2786	0.58	19	1.94	—	0	—	0	—	—	0.76	0.	0.	1
169	11.3041	-0.0608	272.6679	-19.1785	0.58	14	1.17	—	0	31.6	1	3.5	12.9	0.76	180.	2400.	1
170	10.5742	-0.7891	272.9724	-20.1689	0.57	25	3.18	—	0	—	0	—	—	0.75	0.	0.	1
173	10.2542	-0.1225	272.1860	-20.1273	0.57	23	2.94	12.8	0	13.6	0	2.1	14.5	0.75	150.	7700.	1
179	10.6192	-0.0325	272.2904	-19.7644	0.56	14	1.16	—	0	64.0	1	5.2	11.3	0.74	390.	1800.	0
181	10.3475	-0.1825	272.2901	-20.0747	0.55	20	2.05	12.8	0	13.6	0	2.0	14.5	0.72	110.	5400.	1
184	10.0275	-0.3525	272.2834	-20.4370	0.55	16	1.35	—	0	—	1	—	—	0.72	0.	0.	0
185	10.6858	-0.2125	272.4921	-19.7931	0.55	11	0.69	29.0	0	29.5	0	3.5	13.0	0.72	100.	1500.	1
188	10.3342	-0.1792	272.2801	-20.0848	0.54	23	2.95	12.8	0	13.6	0	2.0	14.5	0.71	150.	7700.	1
189	11.3508	0.7957	271.8995	-18.7228	0.54	19	1.82	—	0	—	0	—	—	0.71	0.	0.	1

Table A.1: continued.

Global identifier	Gal lon	Gal lat	Ra	Dec	Peak flux	R	Total flux	NH <sub>3</sub> velocity	NH <sub>3</sub> flag	HCO <sup>+</sup> velocity	ve-	HCO <sup>+</sup> flag	Near distance	Far distance	Peak column density	Near mass	Far mass	Near flag
	[°]	[°]	[°]	[°]	[Jy/beam <sup>1/2</sup> ]		[Jy]	[km/s]		[km/s]			[kpc]	[kpc]	[10 <sup>23</sup> cm <sup>-2</sup> ]	[M <sub>⊙</sub> ]	[M <sub>⊙</sub> ]	
191	11.9139	0.7189	272.2584	-18.2678	0.54	11	0.63	—	0	—	0	—	—	0.71	0.	0.	1	
193	11.0575	-0.0875	272.5665	-19.4074	0.54	13	1.00	29.8	0	29.0	0	3.5	13.0	0.71	150.	2100.	1	
197	10.2375	-0.1175	272.1728	-20.1395	0.54	16	1.32	12.8	0	13.6	0	2.1	14.5	0.71	70.	3500.	1	
206	10.1675	-0.4042	272.4039	-20.3395	0.52	10	0.56	12.9	0	—	0	2.1	14.5	0.69	30.	1500.	1	
208	10.1825	-0.2925	272.3075	-20.2724	0.52	14	0.99	10.5	0	9.4	0	1.8	14.7	0.69	39.	2700.	1	
209	10.0192	-0.3525	272.2791	-20.4443	0.52	15	1.26	—	0	—	0	—	—	0.69	0.	0.	0	
215	10.4725	0.0108	272.1746	-19.8717	0.51	17	1.68	66.7	0	—	0	5.3	11.2	0.67	600.	2600.	0	
216	11.7456	-0.1441	272.9701	-18.8317	0.51	17	1.54	—	0	59.1	0	4.9	11.6	0.67	460.	2600.	0	
218	10.1792	-0.2842	272.2980	-20.2712	0.51	14	1.08	10.5	0	9.4	0	1.8	14.7	0.67	43.	2900.	1	
223	11.1041	-0.1358	272.6353	-19.3898	0.51	11	0.56	—	0	—	0	—	—	0.67	0.	0.	1	
231	10.2275	-0.3692	272.4022	-20.2701	0.50	13	0.88	10.5	0	9.4	0	1.8	14.8	0.66	35.	2400.	1	
490	13.2042	-0.1408	273.7027	-17.5499	2.61	37	19.20	51.1	0	53.1	0	4.3	12.0	3.44	4500.	35000.	1	
505	12.7792	-0.1858	273.5309	-17.9447	1.86	26	9.12	36.3	0	36.5	0	3.6	12.8	2.45	1500.	19000.	1	
511	12.7359	-0.1025	273.4323	-17.9429	1.56	35	11.06	55.5	1	55.8	1	4.6	11.8	2.06	2900.	19000.	1	
518	14.4674	-0.0858	274.2811	-16.4129	1.36	34	11.16	38.1	1	41.3	0	3.5	12.8	1.79	1700.	23000.	1	
532	14.3591	-0.6391	274.7358	-16.7705	1.14	34	9.41	21.8	1	—	0	2.4	13.8	1.50	690.	22000.	1	
535	12.8625	-0.2441	273.6266	-17.8994	1.10	39	11.25	36.3	0	36.5	0	3.6	12.8	1.45	1800.	23000.	1	
538	12.8575	-0.2092	273.5918	-17.8871	1.05	29	6.40	36.3	0	36.5	0	3.6	12.8	1.38	1000.	13000.	1	
546	14.4191	-0.1725	274.3367	-16.4966	0.97	21	3.26	—	0	—	0	—	—	1.28	0.	0.	1	
553	12.0212	-0.2091	273.1700	-18.6212	0.93	13	1.15	—	0	—	0	—	—	1.23	0.	0.	0	
559	12.8825	-0.2558	273.6475	-17.8874	0.91	26	4.62	36.7	0	36.8	0	3.6	12.7	1.20	760.	9300.	1	
570	12.9425	-0.2342	273.6576	-17.8244	0.86	28	5.11	36.7	0	36.8	0	3.6	12.8	1.13	840.	10000.	1	
573	14.6857	-0.2241	274.5158	-16.2864	0.85	37	8.04	37.7	1	—	1	3.5	12.8	1.12	1200.	16000.	1	
574	15.0071	0.0092	274.4607	-15.8927	0.83	18	2.14	24.6	1	24.5	1	2.6	13.6	1.09	180.	5000.	1	
583	14.1925	-0.2058	274.2550	-16.7118	0.82	17	1.93	39.4	0	40.2	0	3.6	12.7	1.08	310.	3900.	1	
589	14.1991	-0.2141	274.2660	-16.7099	0.80	22	3.35	39.4	0	40.2	0	3.6	12.7	1.05	540.	6700.	1	
596	14.4691	-0.6107	274.7640	-16.6602	0.77	17	1.83	—	0	—	0	—	—	1.01	0.	0.	1	
599	12.8575	-0.2141	273.5965	-17.8895	0.76	20	2.85	36.3	0	36.5	0	3.6	12.8	1.00	460.	5800.	1	
605	12.9675	-0.2392	273.6747	-17.8048	0.73	22	2.99	36.7	0	36.8	0	3.6	12.8	0.96	490.	6100.	1	
607	12.8059	-0.1725	273.5320	-17.9149	0.73	27	4.64	36.3	0	36.5	0	3.6	12.8	0.96	760.	9400.	1	
610	12.9658	-0.2342	273.6693	-17.8039	0.73	15	1.51	36.7	0	36.8	0	3.6	12.8	0.96	250.	3100.	1	
614	12.3626	0.4207	272.7613	-18.0189	0.72	18	1.96	—	0	30.9	1	3.3	13.1	0.95	270.	4200.	0	
616	12.4376	-0.0542	273.2373	-18.1815	0.72	22	3.08	21.1	0	—	1	2.6	13.8	0.95	260.	7300.	1	
618	13.9092	-0.5041	274.3889	-17.1028	0.72	25	3.85	22.4	0	22.7	0	2.5	13.8	0.95	310.	9100.	1	
621	12.6576	-0.1691	273.4544	-18.0436	0.71	32	6.05	54.9	0	57.6	0	4.6	11.8	0.94	1600.	11000.	1	
623	14.1925	-0.2092	274.2581	-16.7134	0.71	16	1.53	39.4	0	40.2	0	3.6	12.7	0.94	250.	3100.	1	

Table A.1: continued.

Global identifier	Gal lon	Gal lat	Ra	Dec	Peak flux	R	Total flux	NH <sub>3</sub> velocity	NH <sub>3</sub> flag	HCO <sup>+</sup> velocity	ve-	HCO <sup>+</sup> flag	Near distance	Far distance	Peak column density	Near mass	Far mass	Near flag
	[°]	[°]	[°]	[°]	[Jy/beam <sup>1/2</sup> ]		[Jy]	[km/s]		[km/s]			[kpc]	[kpc]	[10 <sup>23</sup> cm <sup>-2</sup> ]	[M <sub>⊙</sub> ]	[M <sub>⊙</sub> ]	
624	14.4574	-0.6074	274.7552	-16.6688	0.71	16	1.44	19.8	0	—		0	2.3	14.0	0.94	92.	3500.	1
625	14.1841	-0.2308	274.2738	-16.7310	0.71	13	1.24	39.4	0	40.4		1	3.6	12.7	0.94	200.	2500.	1
628	14.1858	-0.2275	274.2716	-16.7280	0.70	19	2.31	39.4	0	40.4		1	3.6	12.7	0.92	380.	4600.	1
629	14.1808	-0.4974	274.5174	-16.8605	0.70	22	3.12	19.5	0	18.4		0	2.3	14.0	0.92	200.	7600.	1
630	14.7256	-0.2041	274.5172	-16.2417	0.69	20	2.38	37.5	1	37.3		1	3.4	12.8	0.91	350.	4900.	0
631	14.9805	-0.6089	275.0142	-16.2085	0.68	19	1.90	18.9	0	19.7		0	2.1	14.1	0.90	110.	4700.	0
632	14.2308	-0.1758	274.2464	-16.6639	0.68	22	2.99	37.5	1	—		0	3.5	12.8	0.90	460.	6100.	1
634	12.9309	-0.0742	273.5042	-17.7581	0.66	15	1.36	—	0	—		0	—	—	0.87	0.	0.	0
641	14.6057	-0.6024	274.8238	-16.5358	0.65	16	1.45	—	0	—		0	—	—	0.86	0.	0.	0
650	12.9442	-0.1192	273.5523	-17.7679	0.61	18	1.61	—	0	36.2		1	3.6	12.8	0.80	260.	3300.	1
651	14.3841	-0.1308	274.2811	-16.5076	0.61	13	1.06	—	0	—		0	—	—	0.80	0.	0.	0
655	13.6792	-0.0525	273.8588	-17.0903	0.61	19	1.97	—	0	—		0	—	—	0.80	0.	0.	0
658	12.6826	0.0108	273.3008	-17.9354	0.60	15	1.32	—	0	—		0	—	—	0.79	0.	0.	0
660	12.7025	-0.1442	273.4539	-17.9921	0.60	19	2.03	54.9	0	34.7		1	4.6	11.8	0.79	530.	3500.	1
664	13.2825	0.2275	273.4029	-17.3050	0.60	12	0.76	—	0	—		0	—	—	0.79	0.	0.	1
665	13.0075	-0.3541	273.8009	-17.8245	0.60	13	0.96	14.4	0	14.8		0	1.9	14.4	0.79	44.	2500.	0
669	14.1425	-0.5074	274.5076	-16.8990	0.59	12	0.74	—	0	—		0	—	—	0.78	0.	0.	1
674	14.7723	-0.1725	274.5112	-16.1856	0.57	14	1.06	—	0	37.9		1	3.5	12.8	0.75	160.	2100.	0
677	12.9142	0.4591	273.0047	-17.5170	0.57	18	1.79	33.5	0	32.7		0	3.4	12.9	0.75	260.	3700.	1
678	14.1791	-0.1908	274.2346	-16.7164	0.57	17	1.55	39.4	0	40.2		0	3.6	12.7	0.75	250.	3100.	1
680	12.6875	0.4724	272.8781	-17.7093	0.57	15	1.15	—	0	19.0		0	2.4	14.0	0.75	81.	2800.	1
684	12.9642	-0.2275	273.6623	-17.8021	0.56	12	0.82	36.7	0	36.8		0	3.6	12.8	0.74	130.	1700.	1
690	12.7076	-0.2042	273.5118	-18.0164	0.56	17	1.64	34.1	0	33.8		0	3.5	12.9	0.74	250.	3400.	0
692	13.0342	-0.7491	274.1793	-17.9891	0.56	16	1.39	—	0	—		0	—	—	0.74	0.	0.	1
696	14.4241	-0.0558	274.2321	-16.4368	0.55	13	0.87	—	0	40.3		0	3.6	12.6	0.72	140.	1700.	1
698	14.6140	-0.6090	274.8340	-16.5316	0.55	10	0.58	—	0	—		0	—	—	0.72	0.	0.	1
702	14.1725	-0.5325	274.5454	-16.8844	0.54	11	0.68	19.5	0	18.4		0	2.3	14.0	0.71	43.	1700.	1
703	14.1525	-0.5791	274.5785	-16.9241	0.54	16	1.24	—	0	—		0	—	—	0.71	0.	0.	1
704	13.0075	-0.3591	273.8055	-17.8269	0.54	12	0.83	14.4	0	14.8		0	1.9	14.4	0.71	38.	2200.	0
710	14.6157	-0.6040	274.8302	-16.5278	0.54	11	0.64	—	0	—		0	—	—	0.71	0.	0.	1
712	12.8242	0.3758	273.0360	-17.6360	0.54	10	0.61	—	0	—		0	—	—	0.71	0.	0.	1
715	14.0091	-0.1042	274.0706	-16.8248	0.53	16	1.26	40.6	0	41.4		0	3.7	12.6	0.70	220.	2500.	1
716	12.8759	-0.2408	273.6303	-17.8861	0.53	26	3.49	36.7	0	36.8		0	3.6	12.7	0.70	570.	7100.	1
717	12.2427	-0.7456	273.7791	-18.6834	0.53	13	1.00	—	0	—		0	—	—	0.70	0.	0.	1
723	14.1841	-0.2358	274.2784	-16.7334	0.53	17	1.58	39.4	0	40.2		0	3.6	12.7	0.70	260.	3200.	1
724	14.4158	-0.0658	274.2371	-16.4488	0.53	14	1.14	—	0	40.3		1	3.6	12.6	0.70	190.	2300.	1

Table A.1: continued.

Global identifier	Gal lon	Gal lat	Ra	Dec	Peak flux	R	Total flux	NH <sub>3</sub> velocity	NH <sub>3</sub> flag	HCO <sup>+</sup> velocity	ve-	HCO <sup>+</sup> flag	Near distance	Far distance	Peak column density	Near mass	Far mass	Near flag
	[°]	[°]	[°]	[°]	[Jy/beam <sup>1/2</sup> ]		[Jy]	[km/s]		[km/s]			[kpc]	[kpc]	[10 <sup>23</sup> cm <sup>-2</sup> ]	[M <sub>⊙</sub> ]	[M <sub>⊙</sub> ]	
726	14.4274	-0.0608	274.2383	-16.4362	0.53	13	0.83	—	0	40.3	0	3.6	12.6	0.70	140.	1700.	1	
729	14.4224	-0.0608	274.2358	-16.4406	0.52	11	0.75	—	0	40.3	0	3.6	12.6	0.69	120.	1500.	1	
731	13.9908	-0.1608	274.1135	-16.8678	0.52	14	1.10	40.6	0	41.4	0	3.7	12.6	0.69	190.	2200.	1	
732	14.0008	-0.1125	274.0741	-16.8361	0.52	16	1.41	40.6	0	41.4	0	3.7	12.6	0.69	240.	2800.	1	
733	14.4158	-0.0525	274.2249	-16.4425	0.52	13	0.95	—	0	40.3	0	3.6	12.6	0.69	160.	1900.	1	
737	12.9225	-0.2342	273.6476	-17.8419	0.52	13	0.88	36.7	0	36.8	0	3.6	12.7	0.69	140.	1800.	1	
742	14.8906	-0.1658	274.5634	-16.0783	0.52	11	0.64	—	0	—	0	—	—	0.69	0.	0.	1	
744	14.4408	-0.0625	274.2465	-16.4253	0.52	10	0.57	—	0	40.3	0	3.6	12.6	0.69	94.	1100.	1	
745	12.7142	-0.6407	273.9189	-18.2190	0.51	17	1.45	6.2	1	—	0	1.0	15.4	0.67	19.	4300.	1	
748	14.2375	-0.1658	274.2405	-16.6532	0.51	13	0.82	37.5	0	—	0	3.5	12.8	0.67	130.	1700.	1	
755	12.7159	-0.6357	273.9150	-18.2151	0.51	10	0.51	6.2	0	—	0	1.0	15.4	0.67	6.	1500.	1	
757	13.4958	-0.2158	273.9176	-17.3293	0.51	13	0.94	—	0	—	0	—	—	0.67	0.	0.	1	
758	14.4874	-0.0075	274.2191	-16.3581	0.51	19	1.78	22.2	0	22.9	0	2.5	13.8	0.67	130.	4200.	1	
764	12.7975	-0.1742	273.5294	-17.9230	0.51	14	1.06	36.3	0	36.5	0	3.6	12.8	0.67	170.	2100.	1	
769	13.9775	-0.1242	274.0732	-16.8621	0.51	10	0.53	40.6	0	41.4	0	3.7	12.6	0.67	91.	1100.	1	
771	13.1942	0.0358	273.5349	-17.4743	0.51	23	2.70	48.5	0	49.2	0	4.2	12.1	0.67	600.	5000.	1	
774	13.0342	-0.7524	274.1823	-17.9907	0.50	15	1.22	—	0	—	0	—	—	0.66	0.	0.	1	
776	12.7742	0.3541	273.0307	-17.6902	0.50	16	1.45	17.9	0	18.5	0	2.3	14.1	0.66	94.	3600.	1	
777	12.9608	-0.2325	273.6653	-17.8075	0.50	13	0.99	36.7	0	36.8	0	3.6	12.8	0.66	160.	2000.	1	
780	13.3058	-0.4425	274.0317	-17.6043	0.50	14	0.98	—	0	—	0	—	—	0.66	0.	0.	0	
781	12.8342	0.3941	273.0241	-17.6184	0.50	15	1.09	—	0	—	0	—	—	0.66	0.	0.	0	
787	14.9588	-0.6256	275.0189	-16.2355	0.50	13	0.87	—	0	—	0	—	—	0.66	0.	0.	0	
789	13.2458	0.0442	273.5532	-17.4249	0.50	14	0.96	—	0	50.9	1	4.3	12.0	0.66	220.	1700.	0	
1135	15.1011	-0.6006	275.0658	-16.0983	1.45	28	9.17	19.0	0	17.2	1	2.1	14.1	1.91	520.	23000.	1	
1146	15.1528	-0.6590	275.1447	-16.0802	1.28	33	10.13	19.0	0	19.5	0	2.1	14.1	1.69	580.	25000.	1	
1158	15.0978	-0.5573	275.0244	-16.0808	1.09	35	9.42	—	0	18.8	1	2.1	14.1	1.44	530.	23000.	1	
1176	15.1561	-0.6490	275.1371	-16.0726	0.92	28	5.85	19.0	0	19.5	0	2.1	14.1	1.21	330.	14000.	1	
1188	16.9075	0.7174	274.7462	-13.8836	0.84	19	2.13	—	0	—	0	—	—	1.11	0.	0.	1	
1190	15.2277	-0.8406	275.3482	-16.0996	0.82	23	3.57	—	0	15.6	1	1.8	14.4	1.08	150.	9200.	0	
1192	16.9975	0.9990	274.5347	-13.6711	0.82	22	3.51	—	0	—	0	—	—	1.08	0.	0.	1	
1199	16.9942	0.9324	274.5934	-13.7056	0.79	28	5.67	—	0	—	0	—	—	1.04	0.	0.	1	
1212	15.2760	-0.6057	275.1562	-15.9464	0.73	24	3.41	20.5	0	20.8	0	2.3	14.0	0.96	220.	8300.	1	
1216	15.1244	-0.5590	275.0391	-16.0581	0.72	24	3.56	—	0	19.6	1	2.2	14.0	0.95	210.	8700.	1	
1225	15.2694	-0.6090	275.1560	-15.9539	0.71	15	1.66	20.5	0	20.8	0	2.3	14.0	0.94	110.	4000.	1	
1240	16.9242	0.2408	275.1873	-14.0939	0.63	20	2.19	—	0	—	0	—	—	0.83	0.	0.	1	
1250	15.1477	-0.6173	275.1040	-16.0650	0.61	12	0.91	—	0	—	0	—	—	0.80	0.	0.	1	

Table A.1: continued.

Global identifier	Gal lon	Gal lat	Ra	Dec	Peak flux	R	Total flux	NH <sub>3</sub> velocity	NH <sub>3</sub> flag	HCO <sup>+</sup> velocity	ve-	HCO <sup>+</sup> flag	Near distance	Far distance	Peak column density	Near mass	Far mass	Near flag
	[°]	[°]	[°]	[°]	[Jy/beam <sup>1/2</sup> ]		[Jy]	[km/s]		[km/s]			[kpc]	[kpc]	[10 <sup>23</sup> cm <sup>-2</sup> ]	[M <sub>⊙</sub> ]	[M <sub>⊙</sub> ]	
1251	15.1977	-0.8372	275.3304	-16.1245	0.60	16	1.43	—	0	15.9		1	1.9	14.3	0.79	62.	3700.	0
1255	15.2294	-0.8306	275.3398	-16.0935	0.59	15	1.30	—	0	15.6		0	1.8	14.4	0.78	55.	3400.	0
1260	16.9158	0.2325	275.1909	-14.1051	0.58	13	0.99	—	0	—		0	—	—	0.76	0.	0.	1
1263	17.2108	0.7841	274.8334	-13.5848	0.57	19	1.91	—	0	—		0	—	—	0.75	0.	0.	1
1273	17.0975	0.8857	274.6861	-13.6366	0.55	11	0.68	—	0	—		0	—	—	0.72	0.	0.	1
1277	16.9158	0.2275	275.1954	-14.1075	0.55	14	1.14	—	0	—		0	—	—	0.72	0.	0.	1
1280	17.6673	0.1791	275.6034	-13.4671	0.55	14	1.12	22.6	0	22.5		0	2.2	13.8	0.72	69.	2700.	1
1281	16.9108	0.2225	275.1976	-14.1143	0.55	13	0.89	—	0	—		0	—	—	0.72	0.	0.	1
1284	15.2860	-0.5990	275.1550	-15.9345	0.54	18	1.65	20.5	0	20.8		0	2.2	14.0	0.71	100.	4000.	1
1288	17.6024	-0.7323	276.4011	-13.9512	0.54	15	1.15	44.6	0	—		0	3.5	12.5	0.71	180.	2200.	0
1289	15.6409	-0.4841	275.2234	-15.5673	0.54	28	4.10	-5.1	1	-4.9		0	-0.6	16.8	0.71	0.	14000.	0
1290	15.5043	-0.4258	275.1031	-15.6603	0.53	13	0.92	—	0	39.7		0	3.5	12.7	0.70	140.	1900.	1
1295	15.2677	-0.6040	275.1506	-15.9530	0.53	15	1.12	20.5	0	20.8		0	2.3	14.0	0.70	71.	2700.	1
1299	17.1008	0.8874	274.6862	-13.6329	0.52	15	1.13	—	0	—		0	—	—	0.69	0.	0.	1
1307	16.9242	0.9740	274.5216	-13.7475	0.52	23	2.89	—	0	—		0	—	—	0.69	0.	0.	1
1308	15.7909	-0.4125	275.2311	-15.4013	0.52	13	0.86	—	0	45.9		1	3.8	12.4	0.69	150.	1600.	1
1309	16.3075	-0.5591	275.6170	-15.0143	0.52	14	1.00	—	0	—		0	—	—	0.69	0.	0.	1
1311	15.2144	-0.5823	275.1046	-15.9898	0.52	14	1.03	20.5	0	20.1		1	2.3	14.0	0.69	65.	2500.	1
1312	15.1311	-0.5557	275.0393	-16.0506	0.52	13	0.90	—	0	18.8		0	2.1	14.1	0.69	51.	2200.	1
1313	16.9125	0.6974	274.7668	-13.8886	0.52	21	2.26	—	0	—		0	—	—	0.69	0.	0.	1
1318	16.4325	-0.6708	275.7798	-14.9563	0.51	16	1.34	—	0	—		0	—	—	0.67	0.	0.	1
1319	15.2161	-0.8306	275.3333	-16.1052	0.51	15	1.08	—	0	15.6		0	1.8	14.4	0.67	46.	2800.	0
1320	16.9108	0.2258	275.1945	-14.1127	0.51	13	0.90	—	0	—		0	—	—	0.67	0.	0.	1
1322	16.9242	0.9774	274.5186	-13.7459	0.51	14	1.07	—	0	—		0	—	—	0.67	0.	0.	1
1325	17.0692	0.8207	274.7312	-13.6923	0.51	15	1.17	—	0	—		0	—	—	0.67	0.	0.	1
1328	15.1311	-0.6423	275.1188	-16.0915	0.51	14	0.94	19.0	0	19.5		0	2.1	14.1	0.67	54.	2300.	1
1330	16.9475	0.9407	274.5632	-13.7427	0.51	26	3.59	—	0	—		0	—	—	0.67	0.	0.	1
1334	16.9142	0.2225	275.1992	-14.1113	0.50	11	0.62	—	0	—		0	—	—	0.66	0.	0.	1
1335	15.1427	-0.4907	274.9854	-16.0097	0.50	13	0.93	—	0	20.4		0	2.3	14.0	0.66	59.	2300.	1
1336	16.8992	0.7074	274.7513	-13.8956	0.50	15	1.07	—	0	—		0	—	—	0.66	0.	0.	1
1587	18.1044	-0.3057	276.2542	-13.3080	1.48	33	9.73	51.0	1	56.2		0	3.8	12.2	1.95	1800.	18000.	1
1634	19.5408	-0.4558	277.0764	-12.1071	0.86	14	1.31	64.0	1	63.7		1	4.2	11.6	1.13	290.	2200.	1
1656	18.0994	-0.3407	276.2836	-13.3288	0.72	18	1.92	56.8	1	56.2		0	4.1	11.9	0.95	390.	3400.	1
1661	18.8692	-0.4825	276.7807	-12.7140	0.70	24	3.75	65.8	0	65.8		0	4.4	11.5	0.92	890.	6200.	1
1668	18.0994	-0.3541	276.2957	-13.3350	0.67	22	2.77	49.1	0	—		1	3.7	12.3	0.88	480.	5200.	1
1673	19.5892	-0.0808	276.7601	-11.8898	0.66	18	2.02	—	0	61.1		1	4.1	11.7	0.87	430.	3400.	0

Table A.1: continued.

Global identifier	Gal lon	Gal lat	Ra	Dec	Peak flux	R	Total flux	NH <sub>3</sub> velocity	NH <sub>3</sub> flag	HCO <sup>+</sup> velocity	ve-	HCO <sup>+</sup> flag	Near distance	Far distance	Peak column density	Near mass	Far mass	Near flag
	[°]	[°]	[°]	[°]	[Jy/beam <sup>1/2</sup> ]		[Jy]	[km/s]		[km/s]			[kpc]	[kpc]	[10 <sup>23</sup> cm <sup>-2</sup> ]	[M <sub>⊙</sub> ]	[M <sub>⊙</sub> ]	
1686	18.2310	-0.3474	276.3528	-13.2156	0.60	17	1.54	47.0	0	47.3	0	3.6	12.4	0.79	250.	2900.	0	
1691	18.4943	-0.2008	276.3459	-12.9143	0.57	16	1.39	—	0	—	1	—	—	0.75	0.	0.	1	
1694	19.6308	-0.1625	276.8538	-11.8910	0.56	17	1.56	—	0	—	0	—	—	0.74	0.	0.	0	
1697	19.0592	-0.3008	276.7067	-12.4613	0.56	22	2.65	66.0	0	65.2	0	4.4	11.5	0.74	630.	4400.	1	
1700	18.8559	-0.5325	276.8197	-12.7491	0.55	17	1.52	—	0	—	0	—	—	0.72	0.	0.	0	
1703	18.9425	-0.0308	276.4064	-12.4386	0.55	15	1.27	46.3	0	—	0	3.5	12.4	0.72	200.	2400.	1	
1704	19.1508	0.0275	276.4531	-12.2271	0.55	14	1.00	—	0	92.1	1	5.3	10.6	0.72	350.	1400.	0	
1707	18.7959	-0.4958	276.7578	-12.7851	0.55	17	1.53	65.2	0	65.3	0	4.3	11.6	0.72	360.	2500.	1	
1708	18.0978	-0.3474	276.2888	-13.3334	0.54	15	1.22	49.1	0	56.2	0	3.7	12.3	0.71	210.	2300.	1	
1710	18.0528	-0.2957	276.2203	-13.3490	0.54	15	1.25	49.1	0	56.2	0	3.7	12.3	0.71	220.	2300.	1	
1712	19.7308	-0.6508	277.3432	-12.0293	0.54	11	0.74	—	0	—	0	—	—	0.71	0.	0.	0	
1715	19.0558	-0.2975	276.7021	-12.4627	0.54	15	1.09	66.0	0	65.2	0	4.4	11.5	0.71	260.	1800.	1	
1725	18.8942	0.0492	276.3109	-12.4440	0.53	16	1.38	—	0	49.3	0	3.7	12.2	0.70	230.	2600.	1	
1729	18.1361	-0.3990	276.3542	-13.3236	0.52	15	1.10	—	0	46.8	1	3.6	12.4	0.69	180.	2100.	1	
1732	18.3860	0.1475	275.9782	-12.8472	0.52	12	0.72	—	0	—	0	—	—	0.69	0.	0.	0	
1739	18.4060	-0.2958	276.3898	-13.0368	0.52	16	1.42	—	0	68.5	0	4.5	11.4	0.69	360.	2300.	1	
1743	19.0575	-0.1975	276.6123	-12.4146	0.51	10	0.53	—	0	63.0	0	4.2	11.6	0.67	120.	900.	1	
1744	19.0392	-0.5641	276.9359	-12.6016	0.51	15	1.14	—	0	—	0	—	—	0.67	0.	0.	0	
1748	18.9925	-0.0225	276.4227	-12.3905	0.51	13	0.96	59.8	0	60.0	0	4.1	11.8	0.67	200.	1700.	0	
1750	18.9475	0.0408	276.3439	-12.4007	0.51	13	0.89	—	0	—	0	—	—	0.67	0.	0.	1	
1751	19.0425	-0.5575	276.9314	-12.5955	0.51	16	1.33	—	0	—	1	—	—	0.67	0.	0.	0	
1754	18.7959	-0.4924	276.7548	-12.7836	0.51	20	2.04	65.2	0	65.3	0	4.3	11.6	0.67	480.	3400.	1	
1755	19.8842	-0.5508	277.3254	-11.8471	0.51	14	1.07	43.2	0	44.1	0	3.3	12.5	0.67	140.	2100.	1	
1759	19.7725	-0.1158	276.8789	-11.7439	0.51	11	0.59	—	0	121.2	0	6.2	9.7	0.67	280.	690.	0	
1760	18.9958	-0.0175	276.4198	-12.3852	0.50	20	2.11	59.8	0	60.0	0	4.1	11.8	0.66	450.	3600.	0	
1761	18.1394	-0.3241	276.2877	-13.2857	0.50	21	2.13	49.1	0	56.2	0	3.7	12.3	0.66	370.	4000.	1	
1764	19.7708	-0.1108	276.8736	-11.7430	0.50	11	0.60	—	0	121.2	0	6.2	9.7	0.66	280.	700.	0	
1765	18.9825	-0.0892	276.4783	-12.4305	0.50	10	0.55	63.0	0	—	0	4.2	11.6	0.66	120.	930.	1	
1767	19.5992	-0.9058	277.5119	-12.2641	0.50	15	1.16	—	0	—	0	—	—	0.66	0.	0.	1	
1773	19.0325	-0.5991	276.9644	-12.6237	0.50	19	1.76	—	0	—	0	—	—	0.66	0.	0.	1	

Notes: Columns are identifier, galactic longitude, galactic latitude, right ascension, declination, peak flux, radius as calculated by CLUMPFIND, integrated flux, NH<sub>3</sub> velocity from Wiene et al. (submitted), flag indicating presence of direct NH<sub>3</sub> observation, HCO<sup>+</sup> velocity from Schlingman et al. (2011), flag indicating presence of direct HCO<sup>+</sup> observation, calculated near distance, calculated far distance, peak column density, mass calculated for the near distance,

mass calculated for the far distance, flag indicating the connection to an IRDC. Negative near distances are meaningless; the velocities of those sources place them in the outer Galaxy, while we are looking towards the inner Galaxy. However, their galactic latitude and velocities are also consistent with the near 3 kpc arm at a distance of 5.2 kpc (Dame & Thaddeus, 2008). The  $\text{NH}_3$  flag means that Wielen et al. (submitted) have observed a position within the clump's boundary definition. If the  $\text{NH}_3$  flag is absent but a  $\text{NH}_3$  velocity is given, the velocity is derived from neighboring clumps (see Sec. 2.5 for details). The same yields for the  $\text{HCO}^+$  flag and  $\text{HCO}^+$  observations in Schlingman et al. (2011).

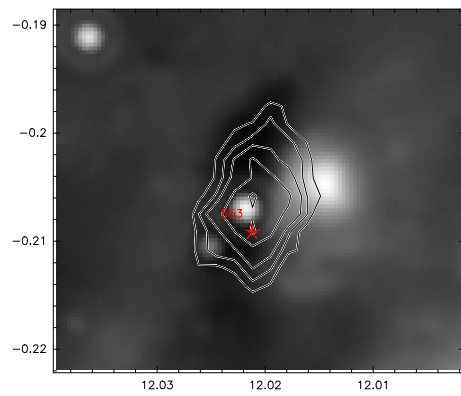
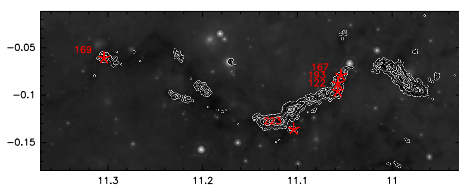
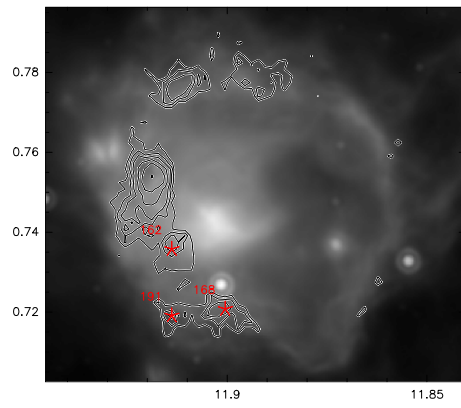
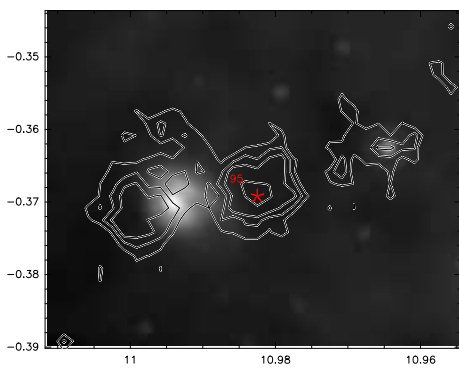
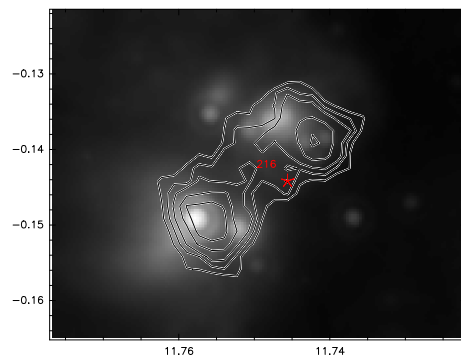
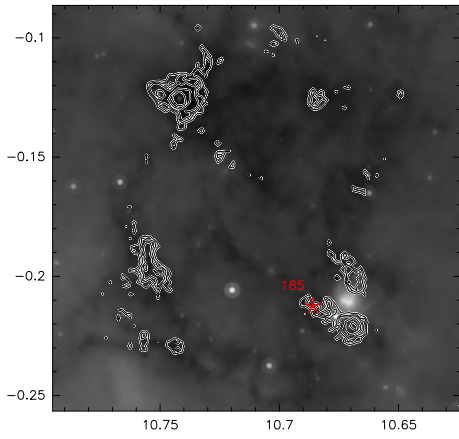
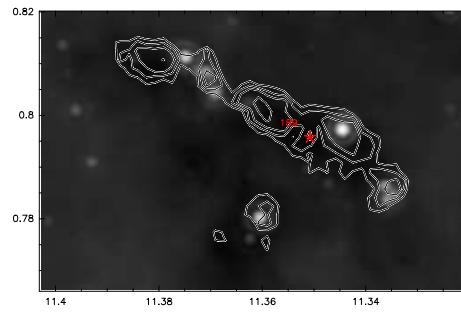
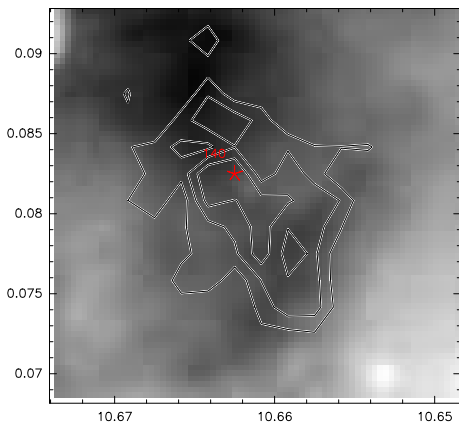
**A.3 Omitted regions**

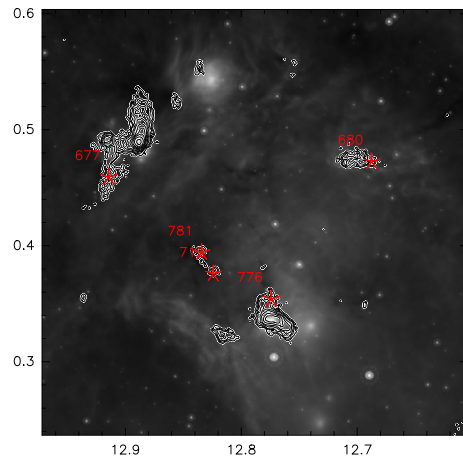
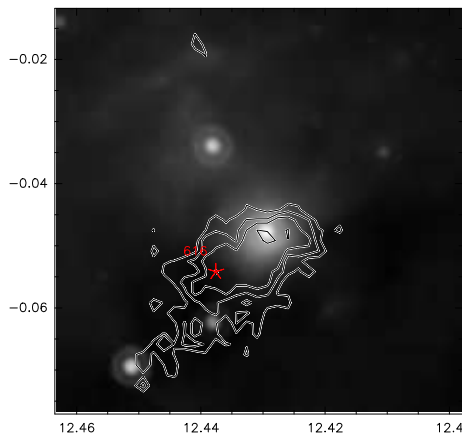
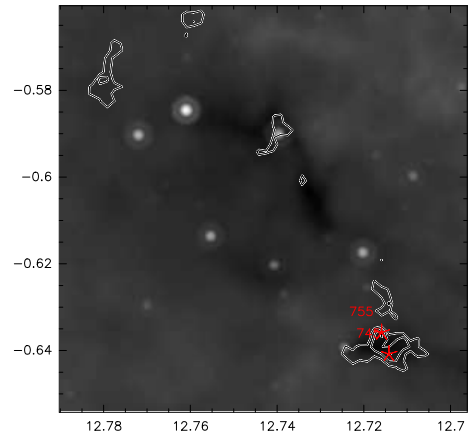
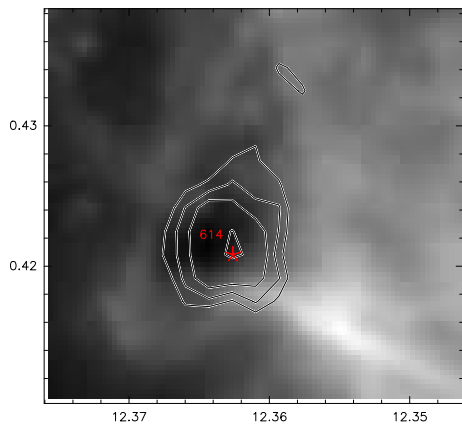
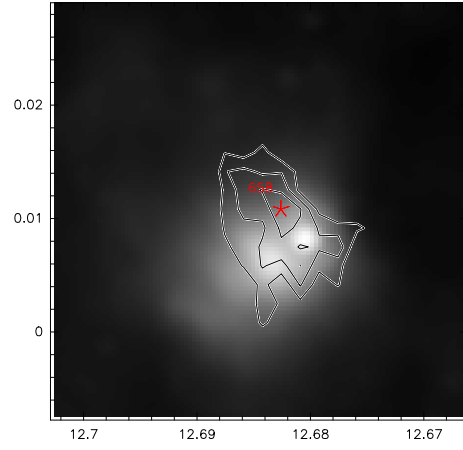
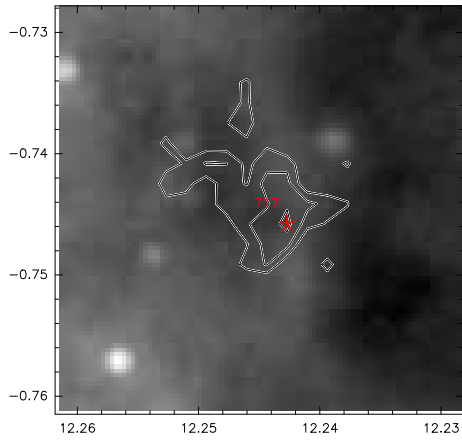
**A.4 Stamps of starless regions**

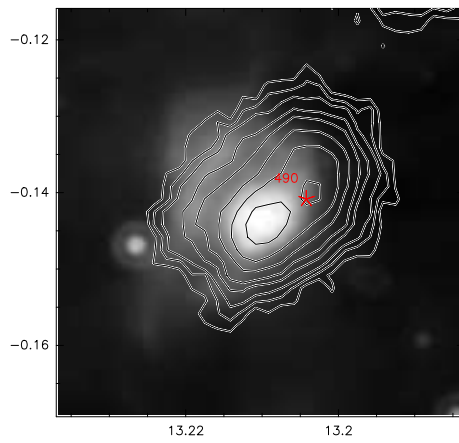
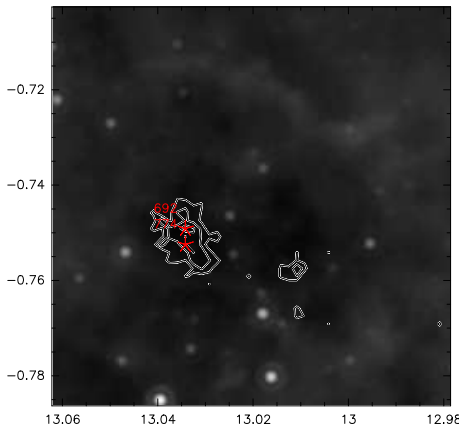
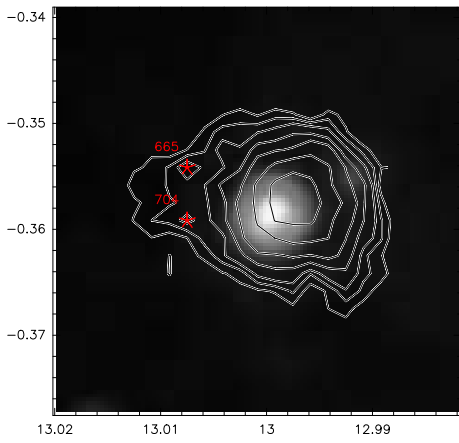
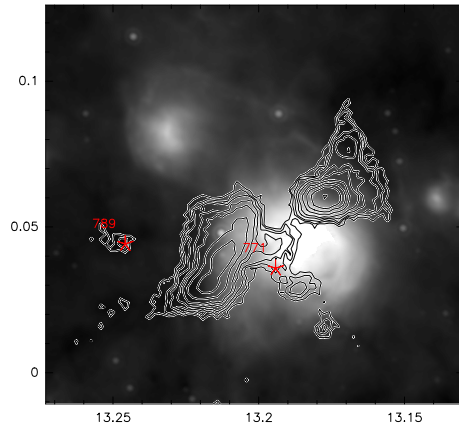
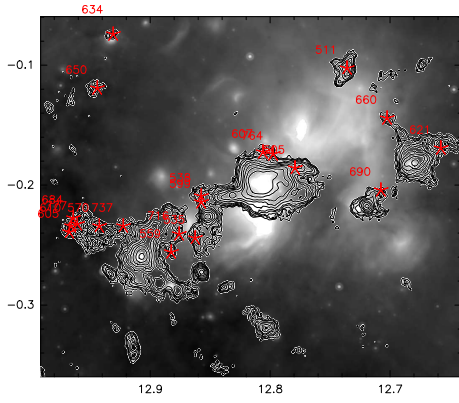
**Table A.2:** Regions listed below were omitted during the classification due to saturation of the  $24\ \mu\text{m}$  data.

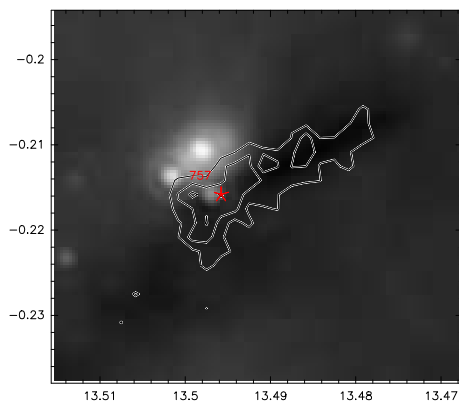
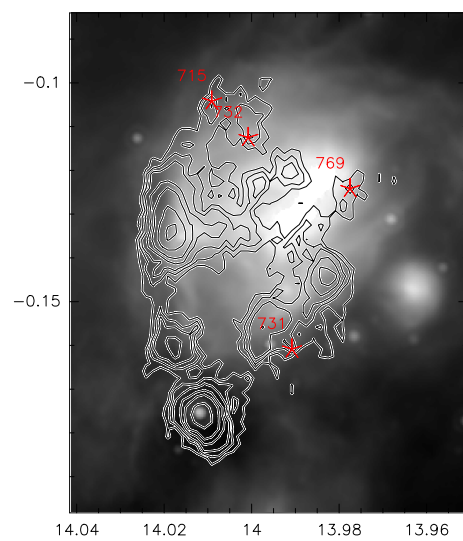
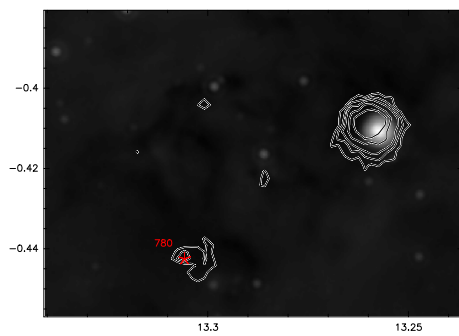
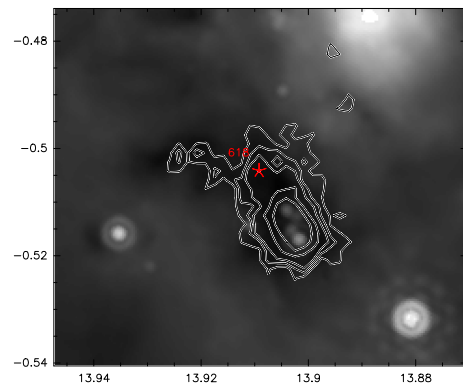
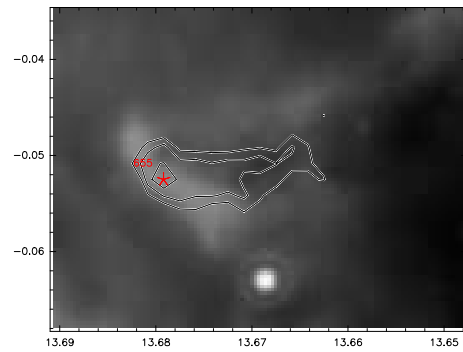
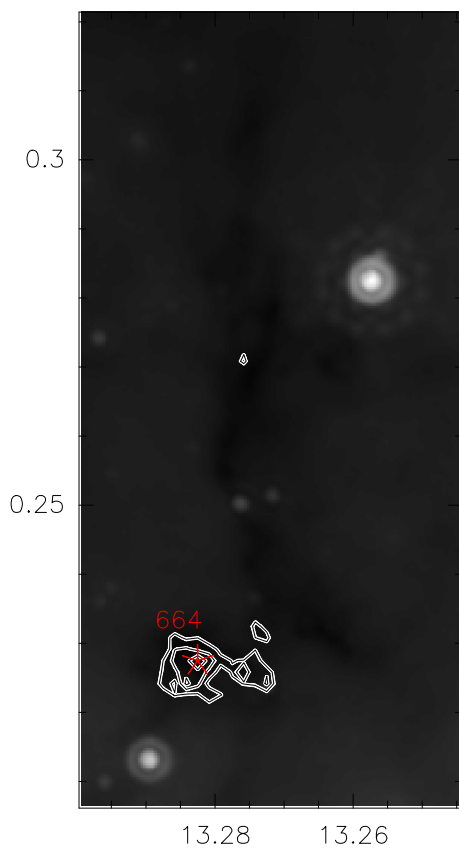
Global identifier	Gal lon [ $^{\circ}$ ]	Gal lat [ $^{\circ}$ ]	Ra [ $^{\circ}$ ]	Dec [ $^{\circ}$ ]	Peak flux [ Jy / beam ]	Total flux [ Jy ]	Radius [ $''$ ]
8	10.3225	-0.1608	272.2570	-20.0861	4.40	45.36	50.
45	10.1325	-0.3775	272.3610	-20.3573	1.30	6.38	28.
59	10.1392	-0.3658	272.3535	-20.3458	1.06	5.59	26.
65	10.1458	-0.3158	272.3103	-20.3157	1.00	7.15	31.
70	10.1808	-0.3692	272.3781	-20.3109	0.94	6.48	29.
79	10.1575	-0.3775	272.3739	-20.3354	0.88	3.34	23.
96	10.1442	-0.3558	272.3468	-20.3365	0.78	2.34	19.
465	14.9838	-0.6956	275.0954	-16.2465	6.60	166.25	74.
467	15.0121	-0.7056	275.1185	-16.2262	5.24	118.69	64.
502	14.9755	-0.7139	275.1082	-16.2624	1.90	27.56	49.
514	15.0022	-0.7255	275.1320	-16.2444	1.45	17.96	44.
519	14.9938	-0.7305	275.1325	-16.2541	1.34	12.58	36.
554	14.9738	-0.7405	275.1318	-16.2765	0.92	4.37	25.
561	14.9755	-0.7372	275.1296	-16.2734	0.91	6.55	28.
617	14.9688	-0.7389	275.1279	-16.2801	0.72	2.42	20.
656	13.9908	-0.1208	274.0768	-16.8488	0.61	1.40	16.
687	12.7975	-0.2275	273.5786	-17.9485	0.56	2.69	23.
707	13.9892	-0.1358	274.0897	-16.8574	0.54	1.52	18.
786	14.9738	-0.7539	275.1441	-16.2827	0.50	1.33	17.
1114	15.0545	-0.6256	275.0659	-16.1512	3.59	28.11	40.
1116	15.0511	-0.6423	275.0795	-16.1620	2.98	46.09	50.
1119	15.0678	-0.6140	275.0617	-16.1339	2.61	22.05	37.
1122	15.0995	-0.6889	275.1461	-16.1414	2.25	22.50	38.
1125	15.0778	-0.6073	275.0605	-16.1220	2.02	21.50	36.
1126	15.1844	-0.6223	275.1266	-16.0351	1.96	37.36	58.
1131	15.1311	-0.6706	275.1448	-16.1048	1.74	21.13	46.
1137	15.1028	-0.6573	275.1187	-16.1235	1.40	31.14	56.
1139	15.0028	-0.7206	275.1277	-16.2415	1.36	9.88	30.
1140	14.9929	-0.7322	275.1335	-16.2558	1.36	11.98	35.
1141	15.1061	-0.6939	275.1539	-16.1378	1.36	12.79	36.
1152	15.1111	-0.7122	275.1732	-16.1421	1.16	11.03	36.

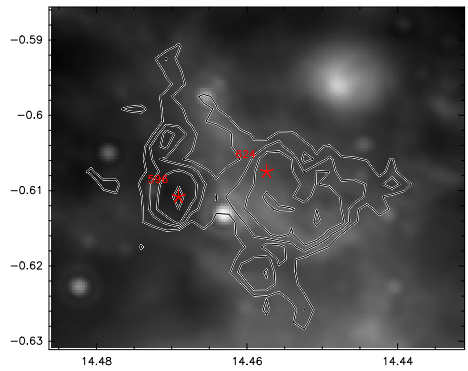
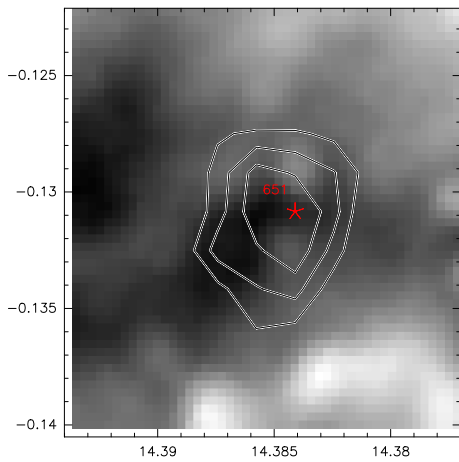
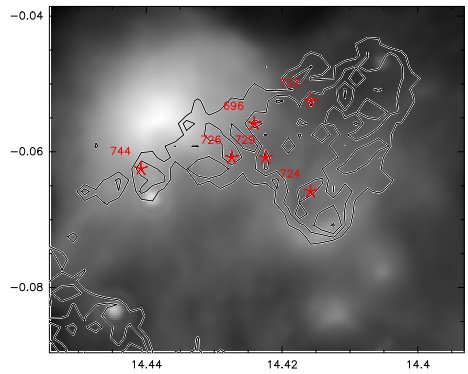
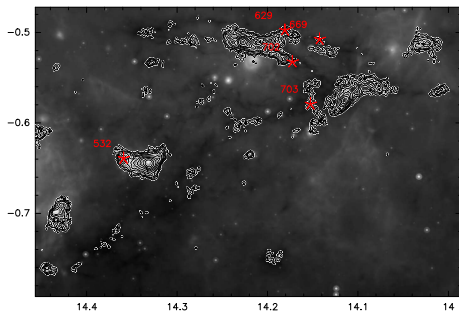
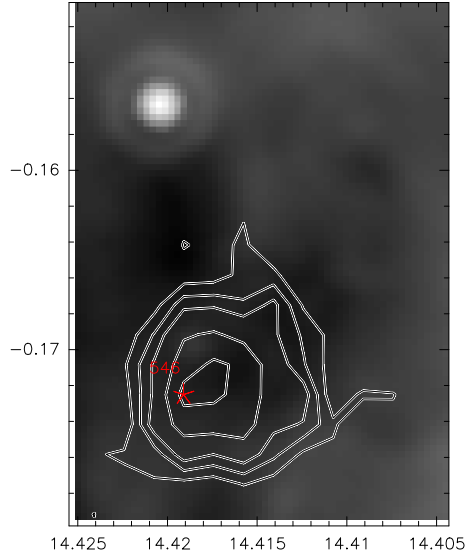
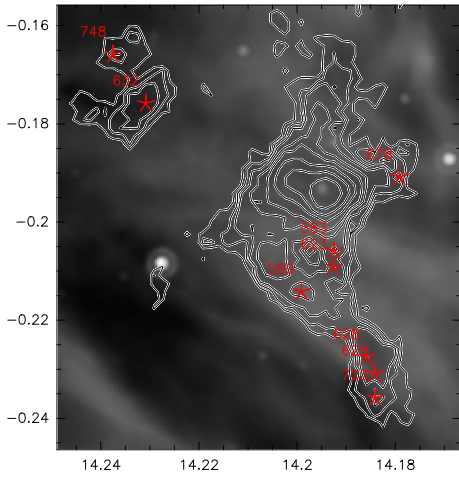


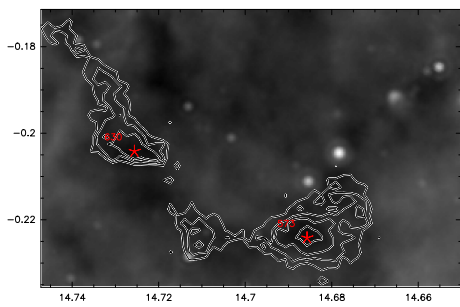
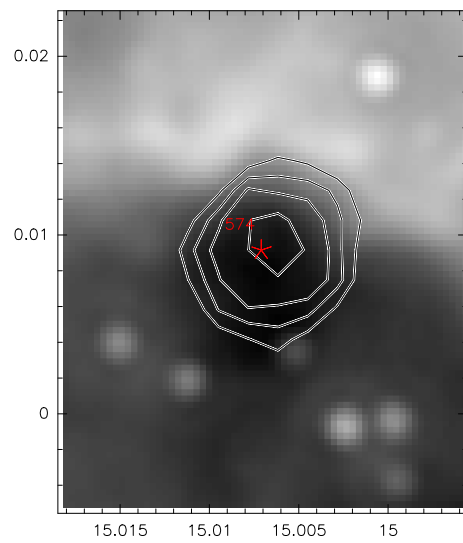
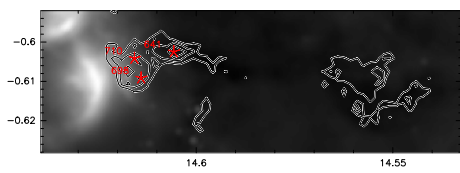
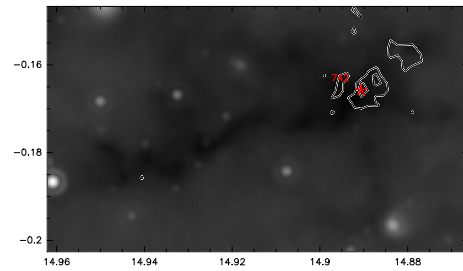
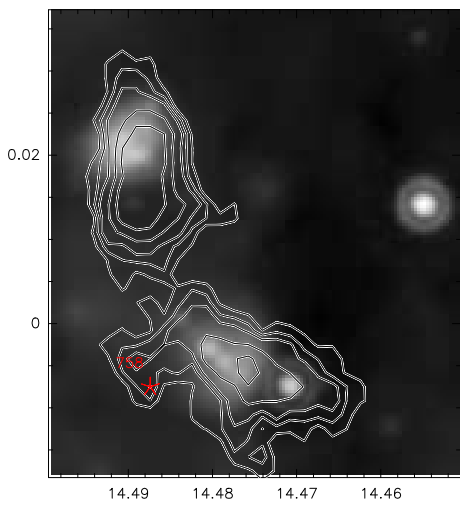
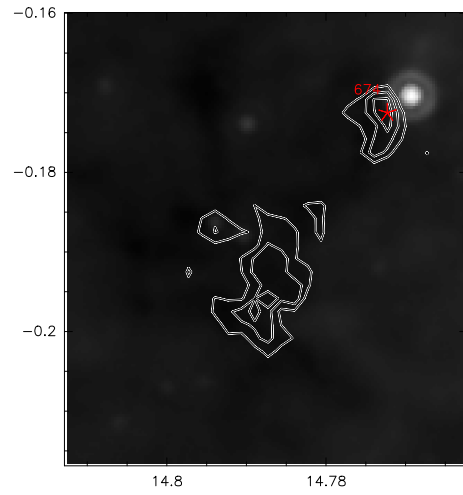
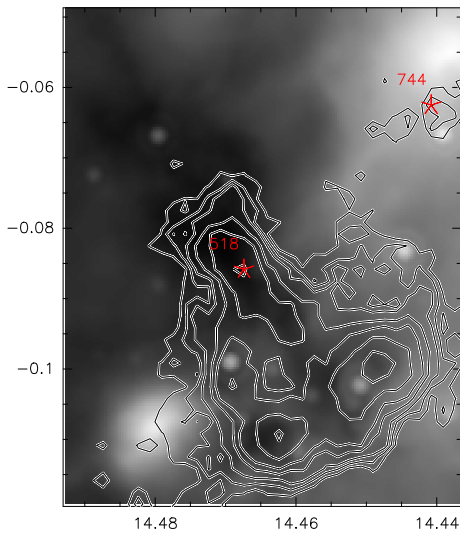


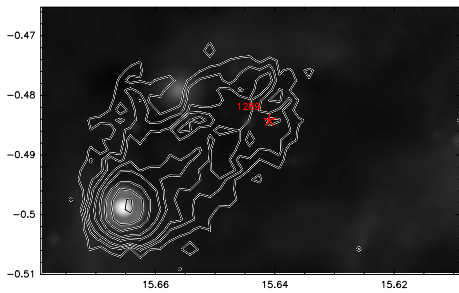
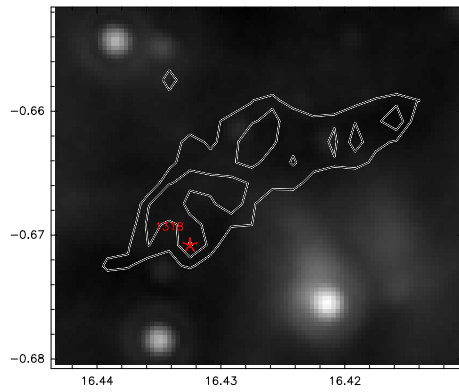
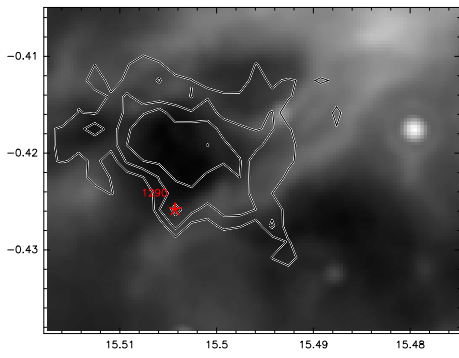
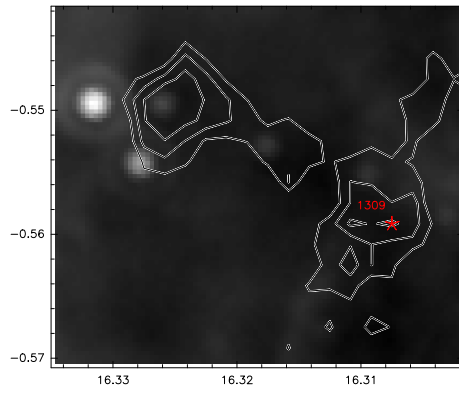
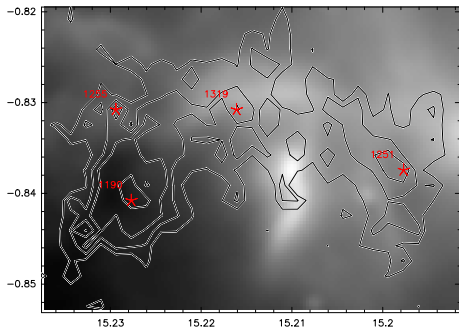
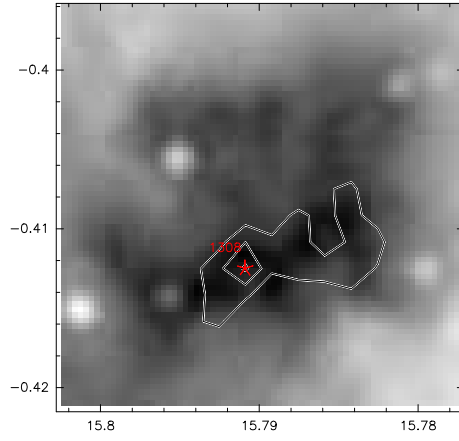
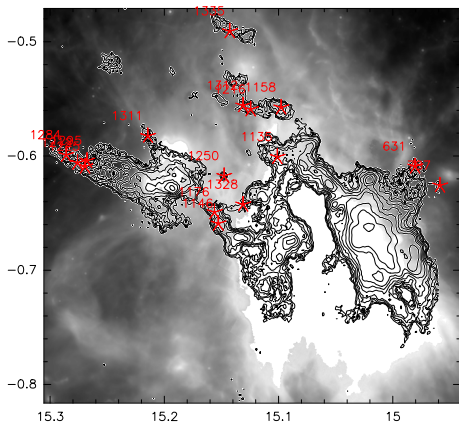


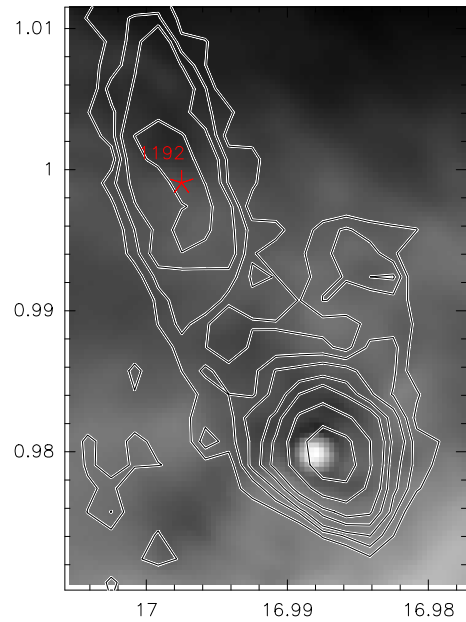
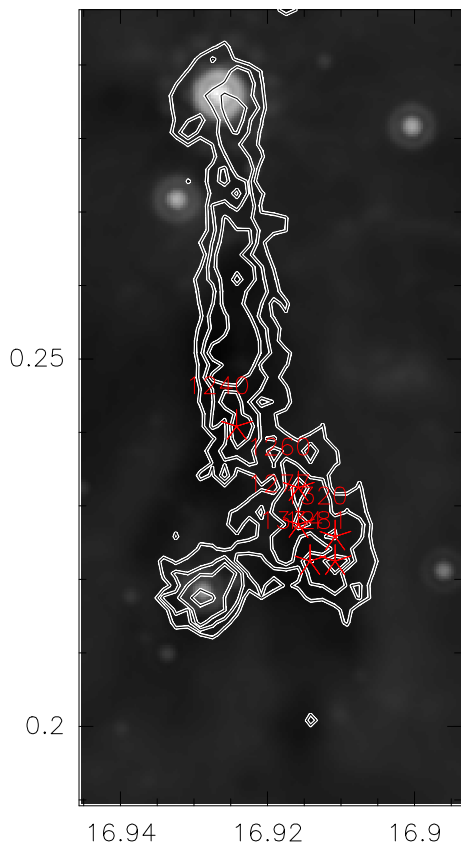
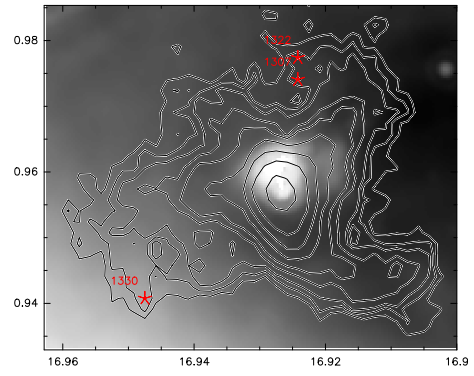
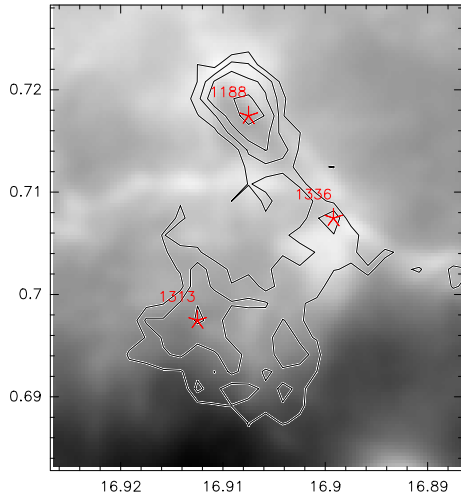




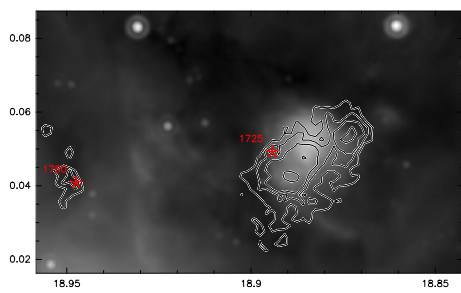
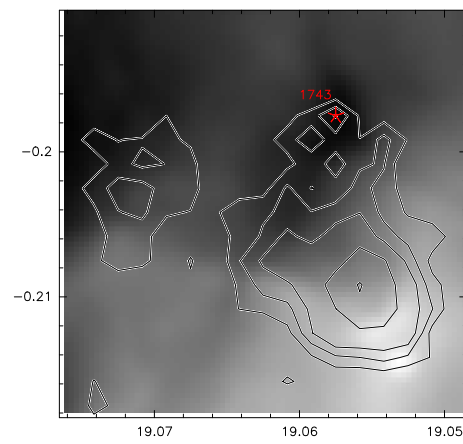
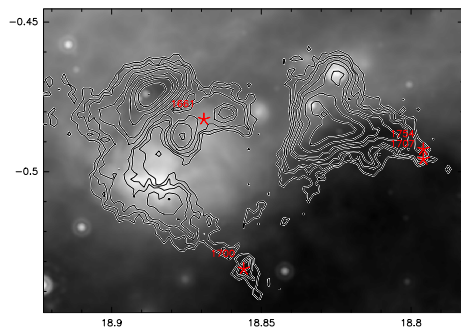
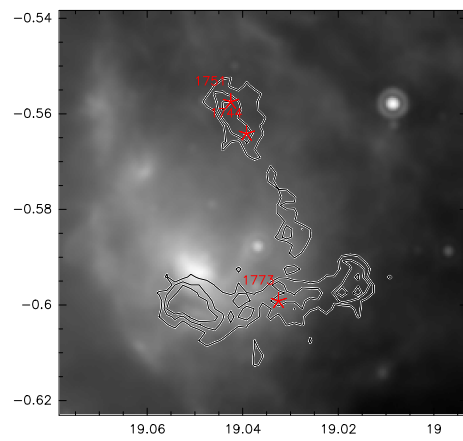
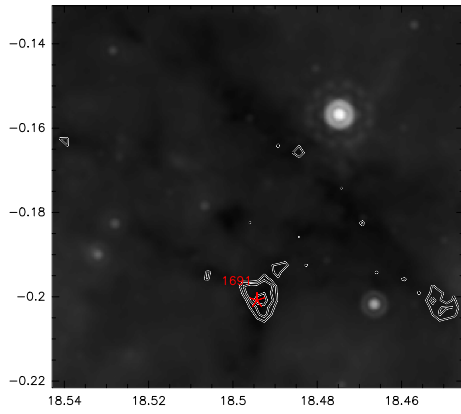
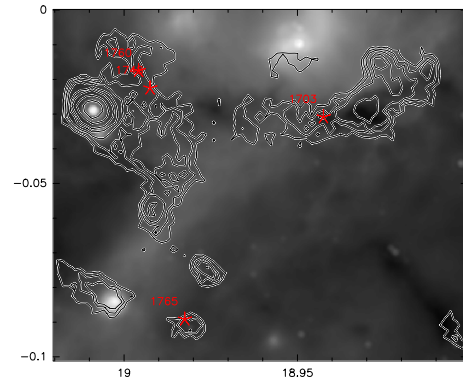
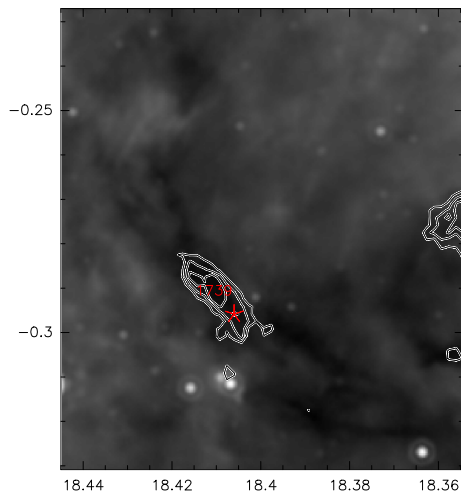


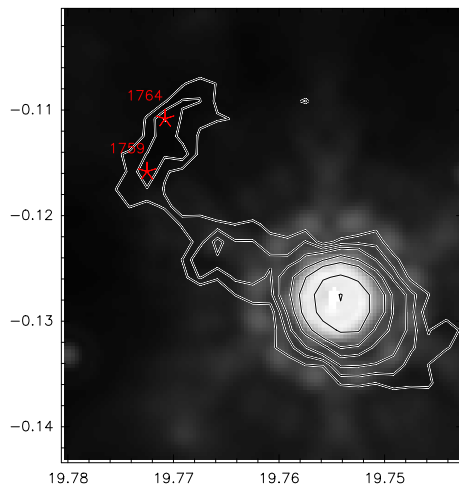
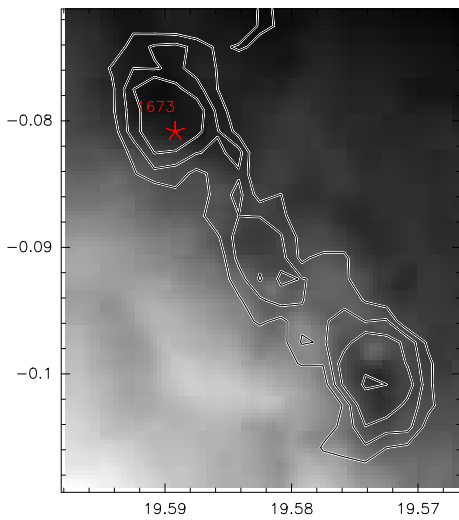
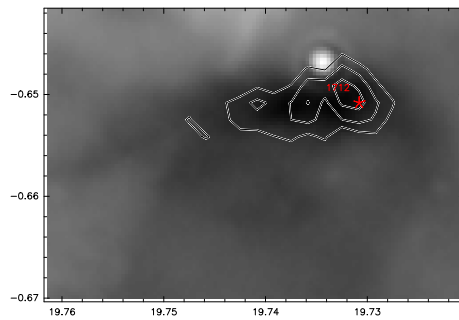
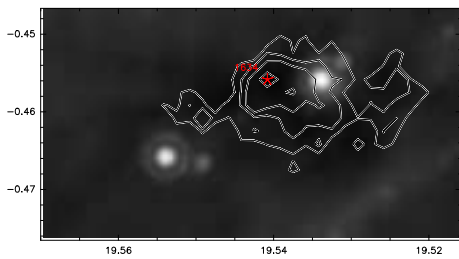
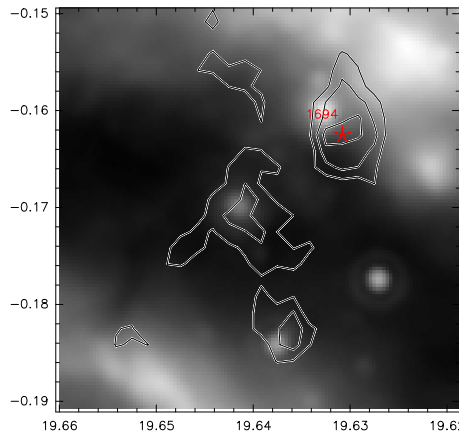
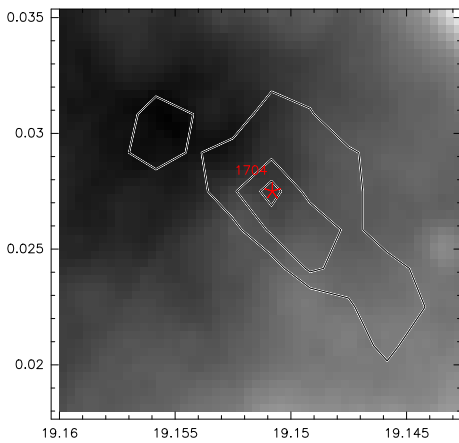
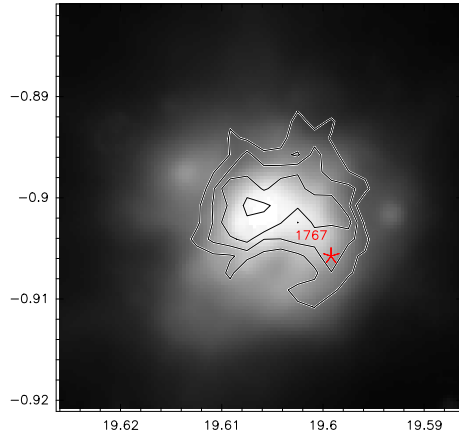
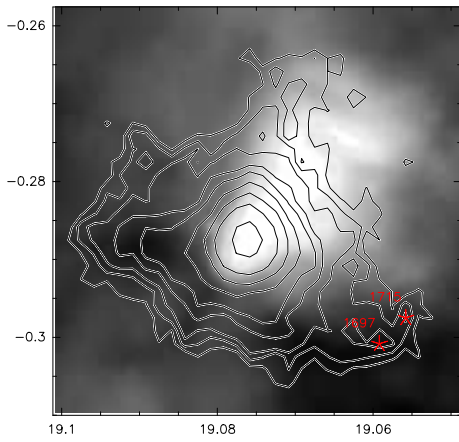


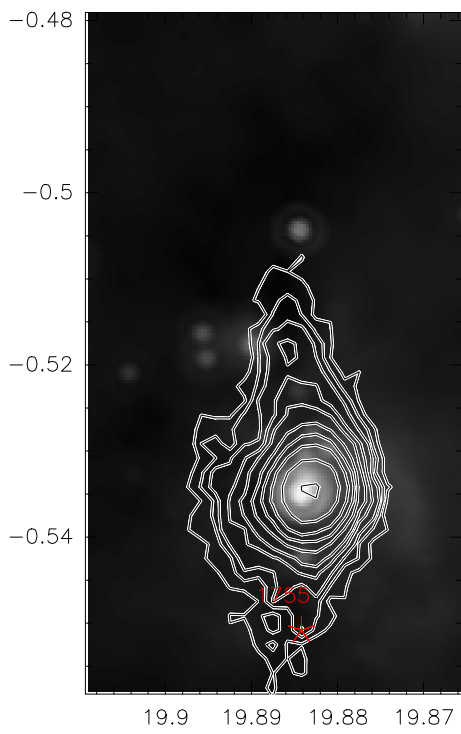












## Appendix B

# Supplementary material for Chapter 'Kinematics of high-mass star-forming regions'

### B.1 Description of the linewidth distribution

*IRDC 18223:* We find a clear increase of the linewidth toward the center of IRDC 18223-2, but IRDC 18223-2 and -3 show an increase toward the edge.

*IRDC 18310:* In IRDC 18310-1 the linewidth increases not toward the sub-mm peak, but toward the detected PACS point sources within. IRDC 18310-4 is a  $70\ \mu\text{m}$  dark region and the the linewidth increases toward its edge. For in between IRDC 18310-2, -3, and -4 the measured increase in linewidth is due to two independent, overlapping components.

*G11.11:* While for the two main peaks of G11.11, G11.11-1, and G11.11-2, the linewidth increases prototypically toward its edges, the other clumps of the northern part shown in Fig. 3.2 show no such clear variation of the linewidth. The systematic offset in the mapping of the southern part of G11.11 does not allow a systematic study of the line parameters. Nevertheless, it is worth noting that the linewidth of the southern part is significantly larger than it is for the northern mapped part.

*G15.05:* .

*IRDC 18102:* We find an increase in linewidth toward the sub-mm peak with its connected PACS point source. An additional broadening of the linewidth from the east to the south is prominent as well.

*IRDC 18151:* In IRDC 18151, IRDC 18151-2 has the largest linewidth with 3.1 km/s. However, it is known to have an outflow (Beuther & Sridharan, 2007) which could explain the broad linewidth. Both brighter at PACS  $70\ \mu\text{m}$  (the associated PACS point source is with  $4026 L_{\odot} \sim 10$  times more luminous than the one connected to IRDC 18151-2) and with a collimated outflow (Fallscheer et al., 2011) as well, thus IRDC 18151-1 has a linewidth of only 1.9 km/s. Along the dust continuum emission away from the center the linewidth increases again. However, the reported outflow is perpendicular to the dust continuum emission and therefore cannot explain the broadening of the linewidth. Despite its still luminous PACS point source of  $184 L_{\odot}$ , IRDC 18151-3 has the smallest linewidth in this region with 0.7 km/s. That is consistent with the fact that López-Sepulcre et al. (2011)

finds no outflows toward that source.

*IRDC 18182:* The well studied HMPO in the north with four outflows connected to it (Beuther et al., 2006) has an increasing linewidth toward its center. The region of interest, the IRDC in the south-east has its smallest linewidth at the peak of IRDC 18182-2. Although there is a PACS continuum source at its peak, Beuther & Sridharan (2007) detect no SiO toward that peak. The southern part of the IRDC, IRDC 18182-4 has slightly larger linewidth.

*IRDC 18308:* While the IR dark filament, connected to IRDC 18308-5 and IRDC 18308-6, has similar linewidth all along between 1 km/s and 2 km/s, the southern complex of IRDC 18308 has linewidths larger than 2.5 km/s. However, the peak of the linewidth is offset to the sub-mm peaks, but is north of IRDC 18308-1. It is interesting to note that the  $\text{N}_2\text{H}^+$  column density is not aligned with the sub-mm continuum peak IRDC 18308-1, and the  $\text{N}_2\text{H}^+$  linewidth peak is offset from the  $\text{N}_2\text{H}^+$  column density peak. While the offset between the continuum and the  $\text{N}_2\text{H}^+$  emission peak of  $\sim 15''$  could be explained by the pointing uncertainties, the offset between the column density peak and the linewidth peak of  $\sim 42''$  are not. Since the linewidth and  $\text{N}_2\text{H}^+$  column density are measured from the same data, positional uncertainties are not an issue for their difference of  $30''$ . As described in 3.3.3, we checked for the peak of the linewidth map whether its spectrum is fit better by two independent  $\text{N}_2\text{H}^+$  velocity components, but only find a single component. Due to the high velocity resolution of 0.1 km/s for that check we can exclude an additional component as cause of that broadening.

*G19.30:* The linewidth distribution in G19.30 peaks toward the two more massive sub-mm peaks G19.30-1, and -2, with an even further increase in linewidth north of G19.30-1. In between P1 and P2, the linewidth is smallest within G19.30-3, but still broad with  $\sim 2$  km/s.

*G28.34:* The linewidth in G28.34 is in general very broad with  $\Delta v > 2$  km/s with only few exceptions. It peaks toward the two main peaks G28.34-1, and -2 with linewidths of up to 3.5 km/s. The minimum in linewidth is found to be in between the two main peaks at G28.34-10 at an linewidth of 2.1 km/s. Using the maps smoothed to a velocity resolution of 0.4 km/s, we find even smaller linewidths along the IR dark filament beyond G28.34-9.

*G48.66:* The linewidths in G48 are narrow compared to other regions mapped within this sample. For the part where  $\text{N}_2\text{H}^+$  is detected, the region with the highest absorption and the embedded but detected PACS sources, the velocity dispersion is broadest, and decreases along the filament to lower column densities.

## B.2 Parameter maps of omitted regions

### B.2.1 Nobeyama 45 m data

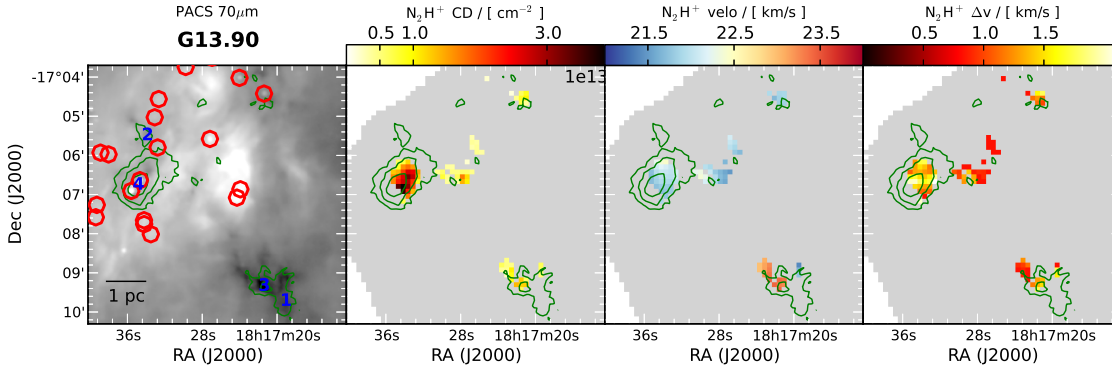


**Figure B.1:** Parameter maps of G13.90 mapped with the Nobeyama 45 m telescope. The left panel is the PACS 70  $\mu\text{m}$  map with the PACS point sources detected by Ragan et al. (2012) indicated by red circles, the blue numbers refer to the sub-mm continuum peaks as given in Table 3.3. The second panel displays the  $\text{N}_2\text{H}^+$  column density derived from fitting the full  $\text{N}_2\text{H}^+$  hyperfine structure. The third and fourth panel show the corresponding velocity and linewidth (FWHM) of each fit. The contours from ATLASGAL 870  $\mu\text{m}$  are plotted with the lowest level representing 0.31 Jy, and continue in steps of 0.3 Jy.

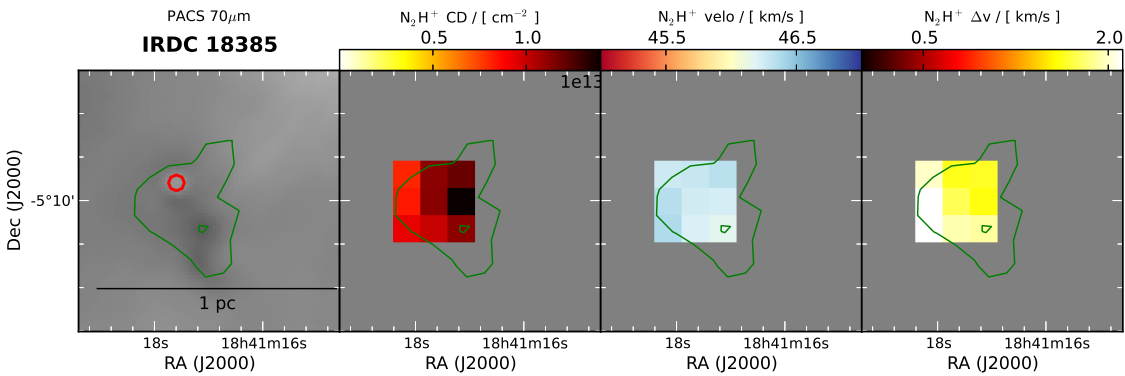


**Figure B.2:** Parameter maps of IRDC 18385 mapped with the Nobeyama 45 m telescope. The left panel is the PACS 70  $\mu\text{m}$  map with the PACS point sources detected by Ragan et al. (2012) indicated by red circles, the blue numbers refer to the sub-mm continuum peaks as given in Table 3.3. The second panel displays the  $\text{N}_2\text{H}^+$  column density derived from fitting the full  $\text{N}_2\text{H}^+$  hyperfine structure. The third and fourth panel show the corresponding velocity and linewidth (FWHM) of each fit. The contours from ATLASGAL 870  $\mu\text{m}$  are plotted with the lowest level representing 0.31 Jy, and continue in steps of 0.3 Jy.

### B.2.2 MOPRA data

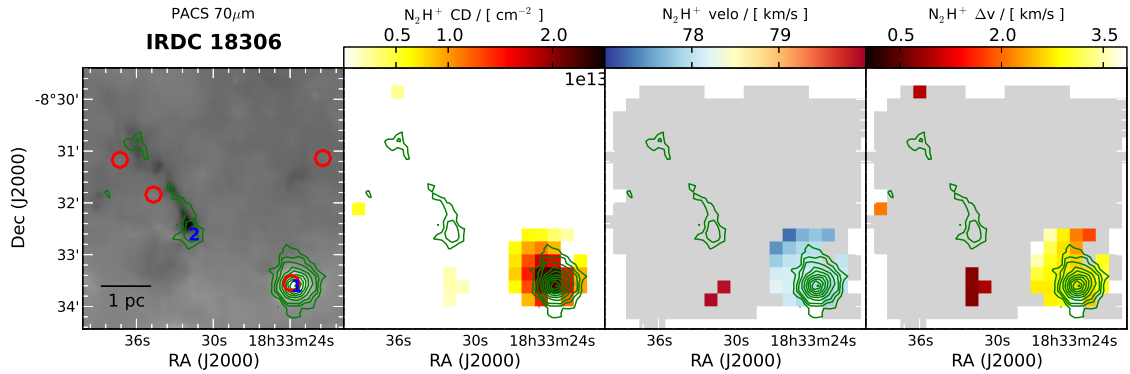


**Figure B.3:** Parameter maps of IRDC 18306 mapped with the MOPRA telescope. The left panel is the PACS  $70 \mu\text{m}$  map with the PACS point sources detected by Ragan et al. (2012) indicated by red circles, the blue numbers refer to the sub-mm continuum peaks as given in Table 3.3. The second panel displays the  $\text{N}_2\text{H}^+$  column density derived from fitting the full  $\text{N}_2\text{H}^+$  hyperfine structure. The third and fourth panel show the corresponding velocity and linewidth (FWHM) of each fit. The contours from ATLASGAL  $870 \mu\text{m}$  are plotted with the lowest level representing  $0.31 \text{ Jy}$ , and continue in steps of  $0.3 \text{ Jy}$ .

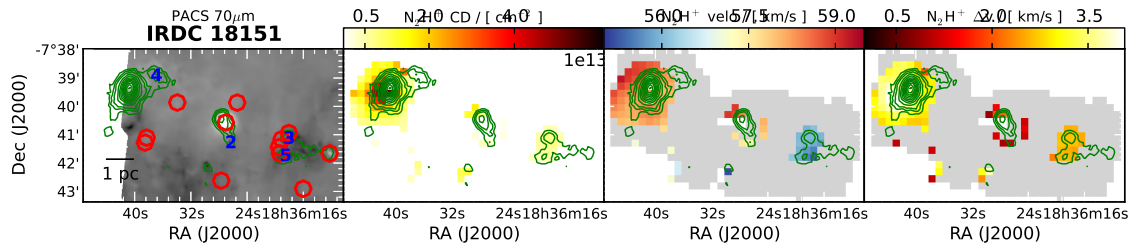


**Figure B.4:** Parameter maps of IRDC 18337 mapped with the MOPRA telescope. The left panel is the PACS  $70 \mu\text{m}$  map with the PACS point sources detected by Ragan et al. (2012) indicated by red circles, the blue numbers refer to the sub-mm continuum peaks as given in Table 3.3. The second panel displays the  $\text{N}_2\text{H}^+$  column density derived from fitting the full  $\text{N}_2\text{H}^+$  hyperfine structure. The third and fourth panel show the corresponding velocity and linewidth (FWHM) of each fit. The contours from ATLASGAL  $870 \mu\text{m}$  are plotted with the lowest level representing  $0.31 \text{ Jy}$ , and continue in steps of  $0.3 \text{ Jy}$ .

## B.3 MOPRA data: Comparing integrated intensities of 5 chemical species

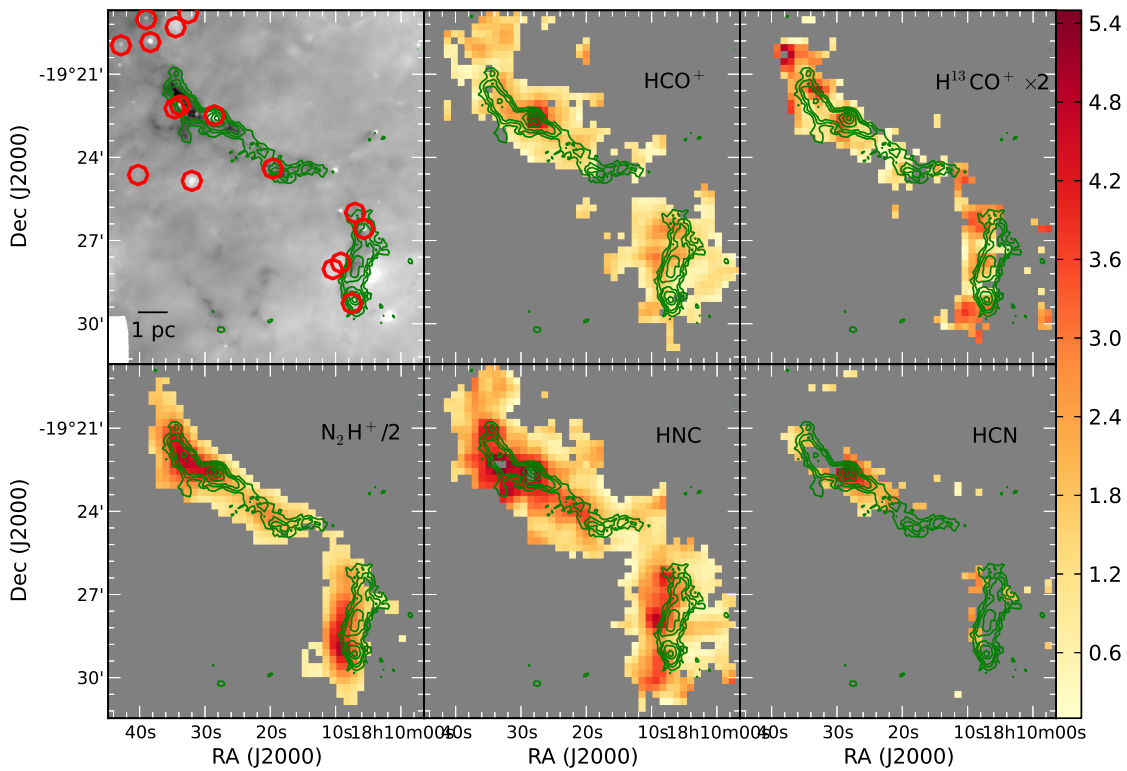


**Figure B.5:** Integrated line intensities of G11.11. The top left panel shows the PACS 70 μm map of the region, with contours from ATLASGAL 870 μm on top. The contour levels start with 0.31 Jy, 0.46 Jy, and 0.61 Jy, and continue in steps of 0.3 Jy. The other panels show the integrated intensities of HCO<sup>+</sup>, H<sup>13</sup>CO<sup>+</sup>, N<sub>2</sub>H<sup>+</sup>, HNC, and HCN, as labeled.

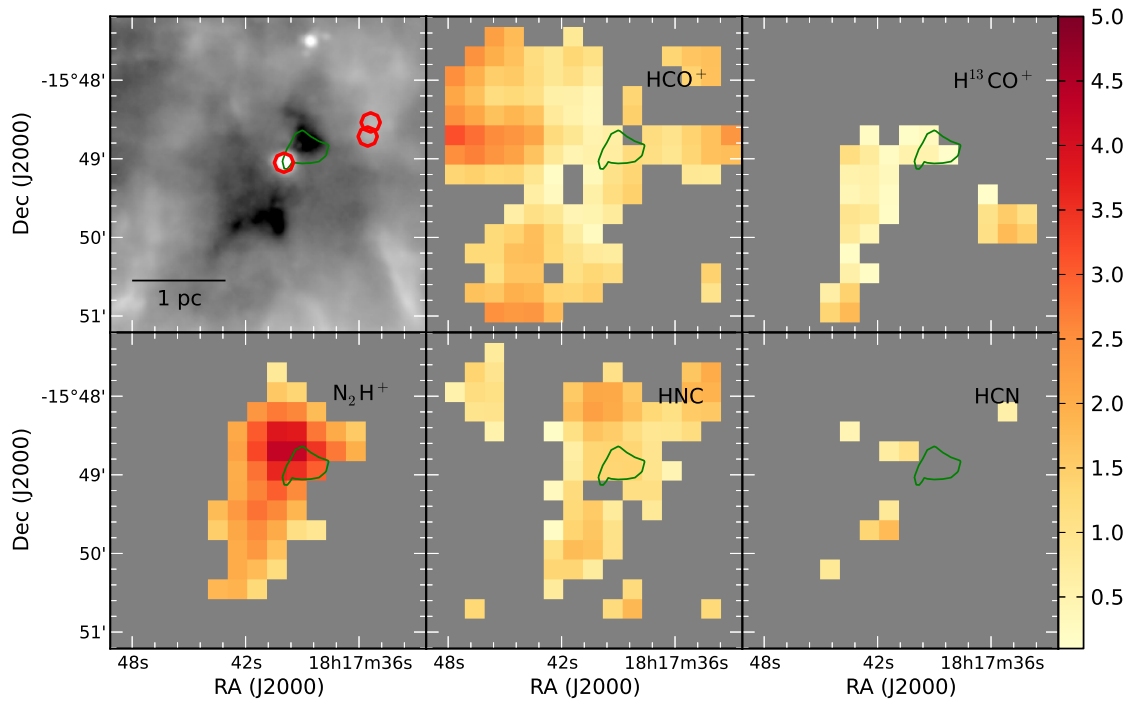


**Figure B.6:** The figure is the same as Fig. B.5, but here plotting G15.05.

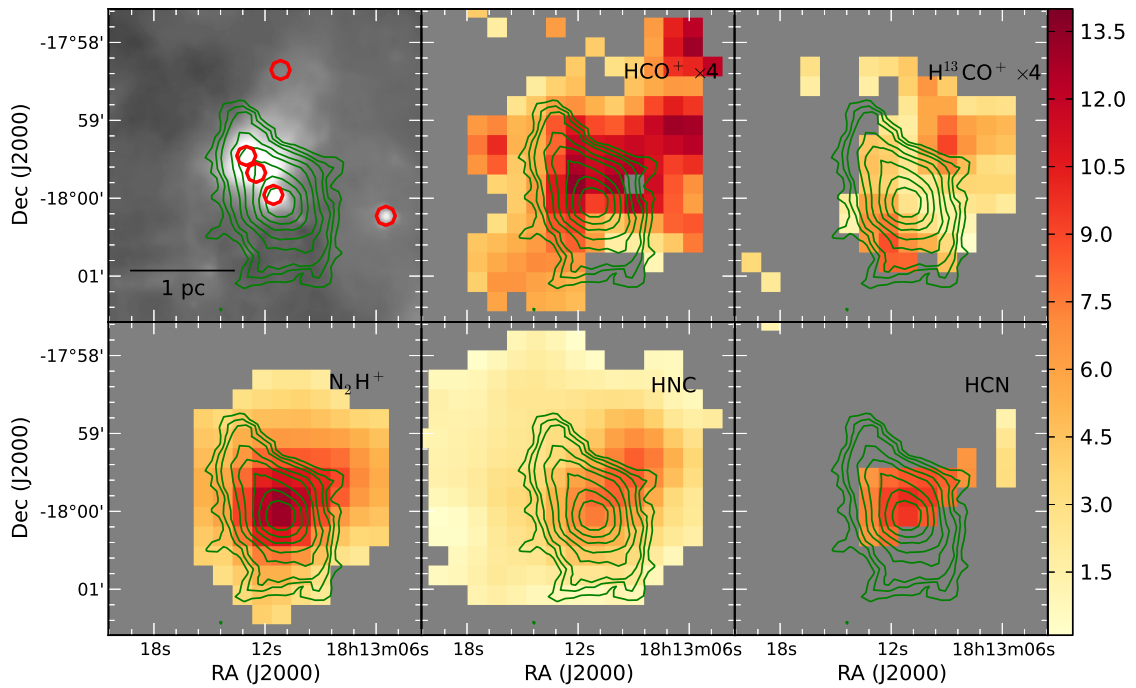


**Figure B.7:** The figure is the same as Fig. B.5, but here plotting IRDC 18102

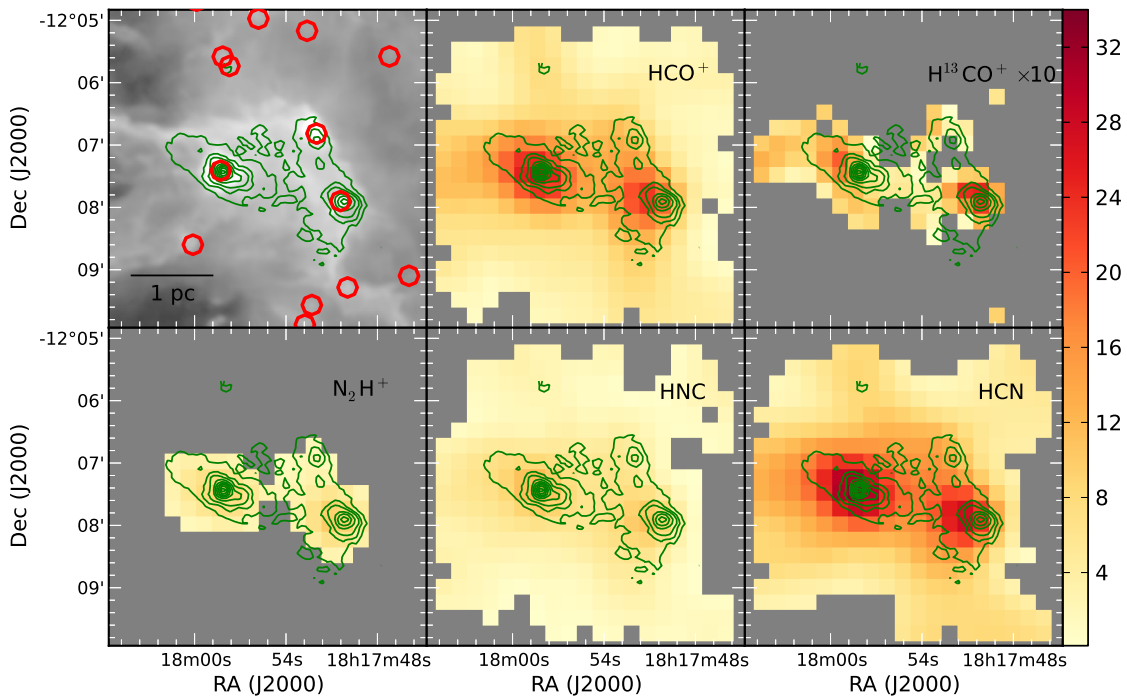


**Figure B.8:** The figure is the same as Fig. B.5, but here plotting IRDC 18151.

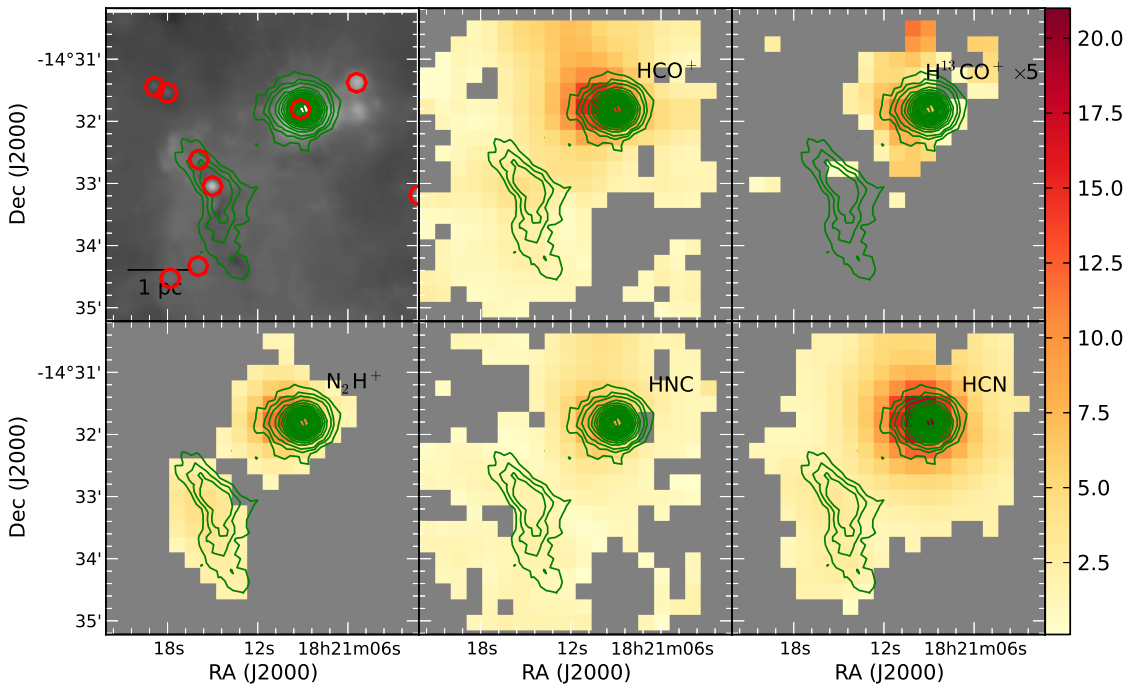


**Figure B.9:** The figure is the same as Fig. B.5, but here plotting IRDC 18182.

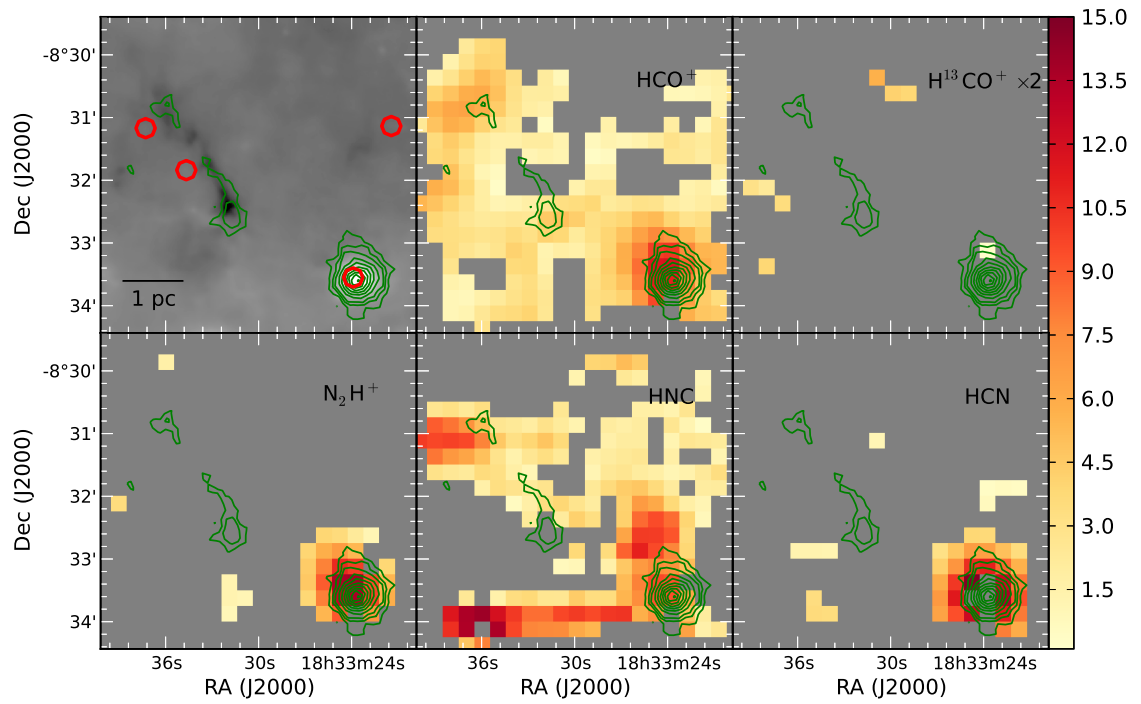


**Figure B.10:** The figure is the same as Fig. B.5, but here plotting IRDC 18306.

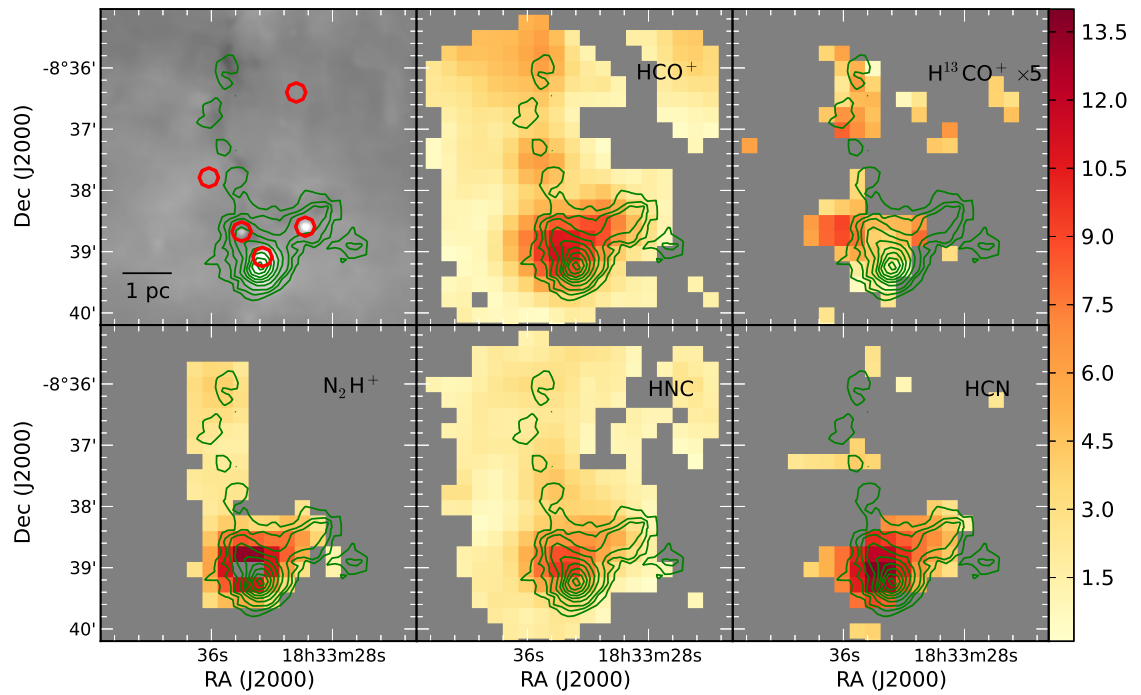


**Figure B.11:** The figure is the same as Fig. B.5, but here plotting IRDC 18308.

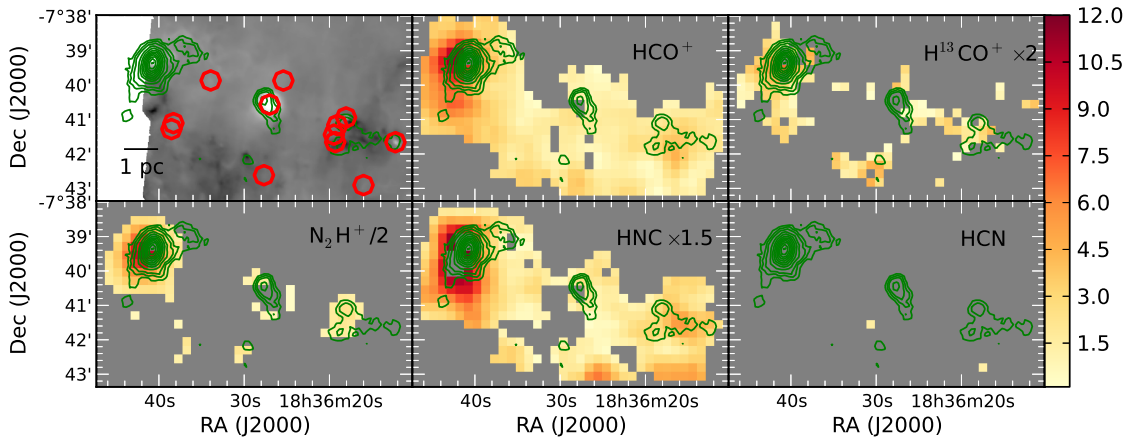


Figure B.12: The figure is the same as Fig. B.5, but here plotting IRDC 18337.

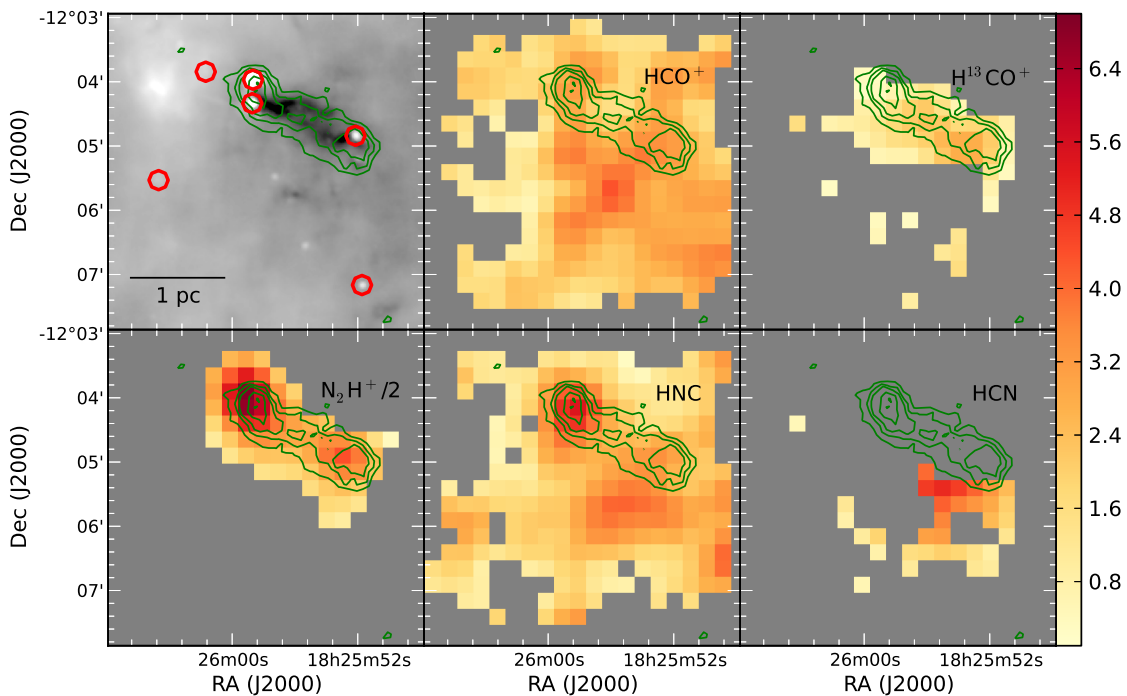
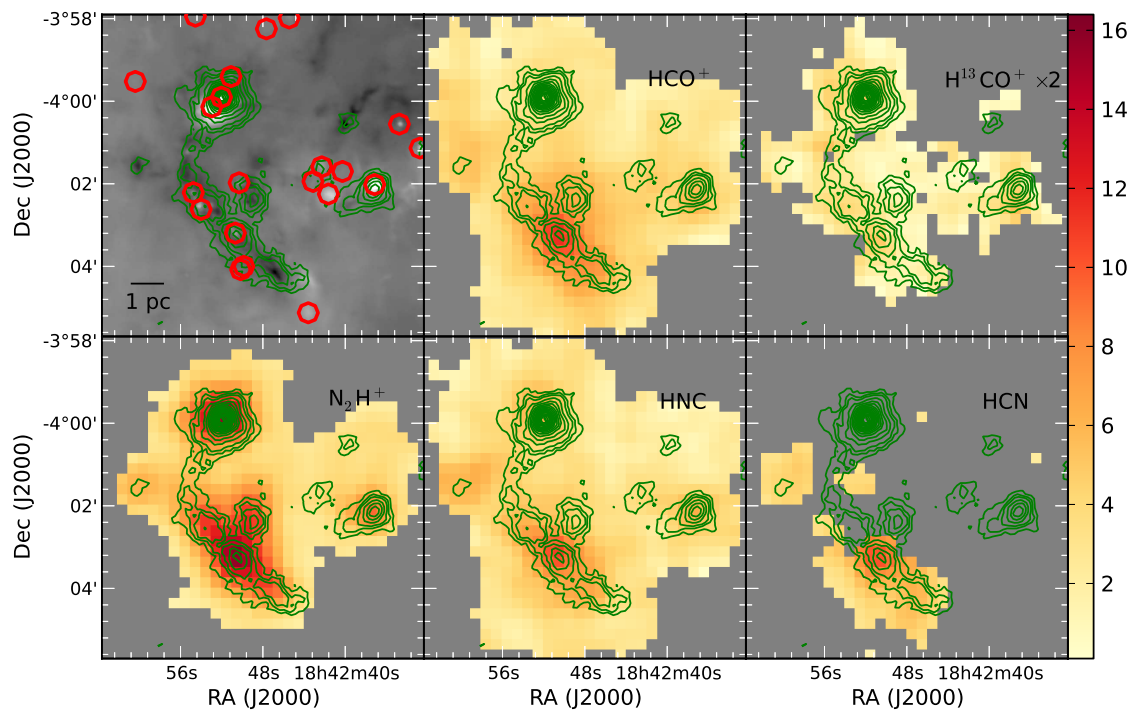
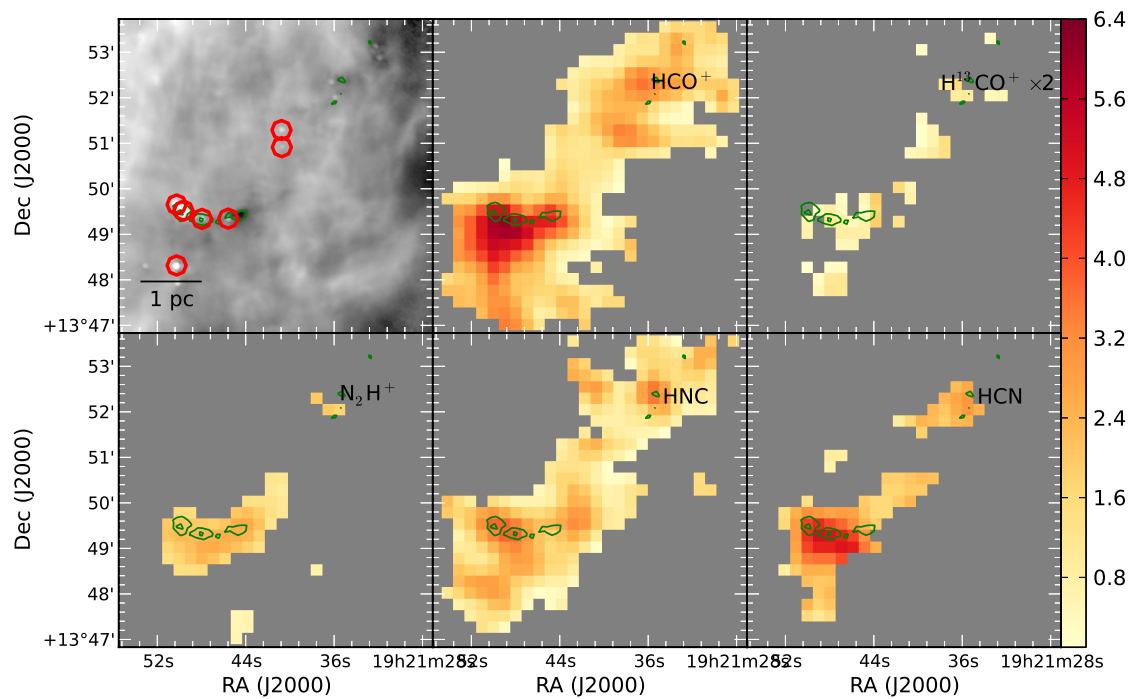


Figure B.13: The figure is the same as Fig. B.5, but here plotting G19.30.



**Figure B.14:** The figure is the same as Fig. B.5, but here plotting G28.34.



**Figure B.15:** The figure is the same as Fig. B.5, but here plotting G48.66.

# Appendix C

## Co-authored papers

### C.1 The earliest phases of star formation - A Herschel key project. The thermal structure of low-mass molecular cloud cores

**Launhardt, Stutz, Schmiedeke, Henning, Krause, Balog, Beuther, Birkmann, Hennemann, Kainulainen, Khanzadyan, Linz, Lippok, Nielbock, Pitann, Ragan, Risacher, Schmalzl, Shirley, Stecklum, Steinacker, & Tackenberg (2013)**

The temperature and density structure of molecular cloud cores are the most important physical quantities that determine the course of the protostellar collapse and the properties of the stars they form. Nevertheless, density profiles often rely either on the simplifying assumption of isothermality or on observationally poorly constrained model temperature profiles. With the aim of better constraining the initial physical conditions in molecular cloud cores at the onset of protostellar collapse, we initiated the Guaranteed Time Key Project (GTKP) "The Earliest Phases of Star Formation" (EPoS) with the Herschel satellite. This paper gives an overview of the low-mass sources in the EPoS project, including all observations, the analysis method, and the initial results of the survey. We study the thermal dust emission of 12 previously well-characterized, isolated, nearby globules using FIR and submm continuum maps at up to eight wavelengths between 100 micron and 1.2 mm. Our sample contains both globules with starless cores and embedded protostars at different early evolutionary stages. The dust emission maps are used to extract spatially resolved SEDs, which are then fit independently with modified blackbody curves to obtain line-of-sight-averaged dust temperature and column density maps. We find that the thermal structure of all globules is dominated by external heating from the interstellar radiation field and moderate shielding by thin extended halos. All globules have warm outer envelopes (14-20 K) and colder dense interiors (8-12 K). The protostars embedded in some of the globules raise the local temperature of the dense cores only within radii out to about 5000 AU, but do not significantly affect the overall thermal balance of the globules.

## C.2 G048.66-0.29: Physical State of an Isolated Site of Massive Star Formation

**Pitann, Linz, Ragan, Stutz, Beuther, Henning, Krause, Launhardt, Schmiedeke, Schuller, Tackenberg, & Vasyunina (2013)**

We present continuum observations of the infrared dark cloud (IRDC) G48.66-0.22 (G48) obtained with Herschel, Spitzer, and APEX, in addition to several molecular line observations. The Herschel maps are used to derive temperature and column density maps of G48 using a model based on a modified blackbody. We find that G48 has a relatively simple structure and is relatively isolated; thus this IRDC provides an excellent target to study the collapse and fragmentation of a filamentary structure in the absence of complicating factors such as strong external feedback. The derived temperature structure of G48 is clearly non-isothermal from cloud to core scale. The column density peaks are spatially coincident with the lowest temperatures ( $\sim 17.5$  K) in G48. A total cloud mass of  $\sim 390 M_{\odot}$  is derived from the column density maps. By comparing the luminosity-to-mass ratio of 13 point sources detected in the Herschel/PACS bands to evolutionary models, we find that two cores are likely to evolve into high-mass stars ( $M > 8 M_{\odot}$ ). The derived mean projected separation of point sources is smaller than in other IRDCs but in good agreement with theoretical predications for cylindrical collapse. We detect several molecular species such as CO, HCO<sup>+</sup>, HCN, HNC and N<sub>2</sub>H<sup>+</sup>. CO is depleted by a factor of  $\sim 3.5$  compared to the expected interstellar abundance, from which we conclude that CO freezes out in the central region. Furthermore, the molecular clumps, associated with the sub-millimeter peaks in G48, appear to be gravitationally unbound or just pressure confined. The analysis of critical line masses in G48 show that the entire filament is collapsing, overcoming any internal support.

## C.3 ATLASGAL - compact source catalogue: $330^{\circ} < l < 21^{\circ}$

**Contreras, Schuller, Urquhart, Csengeri, Wyrowski, Beuther, Bontemps, Bronfman, Henning, Menten, Schilke, Walmsley, Wienen, Tackenberg, & Linz (2013)**

**Context.** The APEX Telescope Large Area Survey of the GALaxy (ATLASGAL) is the first systematic survey of the inner Galactic plane in the sub-millimetre. The observations were carried out with the Large APEX Bolometer Camera (LABOCA), an array of 295 bolometers observing at  $870 \mu\text{m}$  (345 GHz).

**Aims:** Here we present a first version of the compact source catalogue extracted from this survey. This catalogue provides an unbiased database of dusty clumps in the inner Galaxy. **Methods:** The construction of this catalogue was made using the source extraction routine SExtractor. We have cross-associated the obtained sources with the IRAS and MSX catalogues, in order to constrain their nature.

**Results:** We have detected 6639 compact sources in the range from  $330^{\circ} \leq l \leq 21^{\circ}$  and  $-b \leq 1.5^{\circ}$ . The catalogue has a 99% completeness for sources with a peak flux above  $6\sigma$ , which corresponds to a flux density of  $\sim 0.4 \text{ Jy beam}^{-1}$ . The parameters extracted for sources with peak fluxes below the  $6\sigma$  completeness threshold should be used with caution. Tests on simulated data find the uncertainty in the flux measurement to be

$\sim 12\%$ , however, in more complex regions the flux values can be overestimated by a factor of 2 due to the additional background emission. Using a search radius of  $30''$  we found that 40% of ATLASGAL compact sources are associated with an IRAS or MSX point source, but,  $\sim 50\%$  are found to be associated with MSX  $21\ \mu\text{m}$  fluxes above the local background level, which is probably a lower limit to the actual number of sources associated with star formation.

Conclusions: Although infrared emission is found towards the majority of the clumps detected, this catalogue is still likely to include a significant number of clumps that are devoid of star formation activity and therefore excellent candidates for objects in the coldest, earliest stages of (high-mass) star formation.

## C.4 The Earliest Phases of Star Formation (EPoS): a Herschel key program. The precursors to high-mass stars and clusters

**Ragan, Henning, Krause, Pitann, Beuther, Linz, Tackenberg, Balog, Henne-  
mann, Launhardt, Lippok, Nielbock, Schmiedeke, Schuller, Steinacker, Stutz,  
& Vasyunina (2012)**

Context. Stars are born deeply embedded in molecular clouds. In the earliest embedded phases, protostars emit the bulk of their radiation in the far-infrared wavelength range, where Herschel is perfectly suited to probe at high angular resolution and dynamic range. In the high-mass regime, the birthplaces of protostars are thought to be in the high-density structures known as infrared-dark clouds (IRDCs). While massive IRDCs are believed to have the right conditions to give rise to massive stars and clusters, the evolutionary sequence of this process is not well-characterized.

Aims: As part of the Earliest Phases of Star formation (EPoS) Herschel guaranteed time key program, we isolate the embedded structures within IRDCs and other cold, massive molecular clouds. We present the full sample of 45 high-mass regions which were mapped at PACS  $70\ \mu\text{m}$ ,  $100\ \mu\text{m}$ , and  $160\ \mu\text{m}$  and SPIRE  $250\ \mu\text{m}$ ,  $350\ \mu\text{m}$ , and  $500\ \mu\text{m}$ . In the present paper, we characterize a population of cores which appear in the PACS bands and place them into context with their host molecular cloud and investigate their evolutionary stage.

Methods: We construct spectral energy distributions (SEDs) of 496 cores which appear in all PACS bands, 34% of which lack counterparts at  $24\ \mu\text{m}$ . From single-temperature modified blackbody fits of the SEDs, we derive the temperature, luminosity, and mass of each core. These properties predominantly reflect the conditions in the cold, outer regions. Taking into account optical depth effects and performing simple radiative transfer models, we explore the origin of emission at PACS wavelengths.

Results: The core population has a median temperature of 20 K and has masses and luminosities that span four to five orders of magnitude. Cores with a counterpart at  $24\ \mu\text{m}$  are warmer and bluer on average than cores without a  $24\ \mu\text{m}$  counterpart. We conclude that cores bright at  $24\ \mu\text{m}$  are on average more advanced in their evolution, where a central protostar(s) have heated the outer bulk of the core, than  $24\ \mu\text{m}$ -dark cores. The  $24\ \mu\text{m}$  emission itself can arise in instances where our line of sight aligns with an exposed part of

the warm inner core. About 10% of the total cloud mass is found in a given cloud's core population. We uncover over 300 further candidate cores which are dark until  $100\ \mu\text{m}$ . These are possibly starless objects, and further observations will help us determine the nature of these very cold cores.

Herschel is an ESA space observatory with science instruments provided by European-led Principal Investigator consortia and with important participation from NASA.

## C.5 Multiple episodes of star formation in the CN15/16/17 molecular complex

**Gennaro, Bik, Brandner, Stolte, Rochau, Beuther, Gouliermis, Tackenberg, Kudryavtseva, Hussmann, Schuller, & Henning (2012)**

**Context.** We have started a campaign to identify massive star clusters inside bright molecular bubbles towards the Galactic center. The CN15/16/17 molecular complex is the first example of our study. The region is characterized by the presence of two young clusters, DB10 and DB11, visible in the near-infrared, an ultra-compact HII region identified in the radio, several young stellar objects visible in the mid infrared, a bright diffuse nebulosity at  $8\ \mu\text{m}$  coming from PAHs and sub-mm continuum emission revealing the presence of cold dust.

**Aims:** Given its position on the sky ( $l=0.58^\circ$ ,  $b=-0.85^\circ$ ) and its kinematic distance of 7.5 kpc, the region was thought to be a very massive site of star formation in proximity of the central molecular zone. One of the two identified clusters, DB11, was estimated to be as massive as  $104\ M_\odot$ . However the region's properties were known only through photometry and its kinematic distance was very uncertain given its location at the tangential point. We aimed at better characterizing the region and assess whether it could be a site of massive star formation located close to the Galactic center. **Methods:** We have obtained NTT/SofI deep JHKS photometry and long slit K band spectroscopy of the brightest members. We have additionally collected data in the radio, sub-mm and mid infrared, resulting in a quite different picture of the region. **Results:** We have confirmed the presence of massive early B type stars and have derived a spectro-photometric distance of  $\sim 1.2$  kpc, much smaller than the estimated kinematic distance. Adopting this distance we obtain clusters masses of  $\text{MDB10} \approx 170\ M_\odot$  and  $\text{MDB11} \approx 275\ M_\odot$ . This is consistent with the absence of any O star, confirmed by the excitation/ionization status of the nebula. No HeI diffuse emission is detected in our spectroscopic observations at  $2.113\ \mu\text{m}$ , which would be expected if the region was hosting more massive stars. Radio continuum measurements are also consistent with the region hosting at most early B stars.

Based on observations performed at ESO's La Silla-Paranal observatory. Programme ID 085.D-0780.

## C.6 Galactic Structure Based on the ATLASGAL 870 $\mu\text{m}$ Survey

**Beuther, Tackenberg, Linz, Henning, Schuller, Wyrowski, Schilke, Menten, Robitaille, Walmsley, Bronfman, Motte, Nguyen-Luong, & Bontemps (2012b)**

The ATLASGAL 870  $\mu\text{m}$  continuum survey conducted with the APEX telescope is the first one covering the whole inner Galactic plane ( $60^\circ > l > -60^\circ$  and  $b < \pm 1.5^\circ$ ) in submillimeter (submm) continuum emission tracing the cold dust of dense and young star-forming regions. Here, we present the overall distribution of sources within our Galactic disk. The submm continuum emission is confined to a narrow range around the Galactic plane, but shifted on average by  $\sim 0.07$  deg below the plane. Source number counts show strong enhancements toward the Galactic center, the spiral arms, and toward prominent star-forming regions. Comparing the distribution of ATLASGAL dust continuum emission to that of young intermediate- to high-mass young stellar objects (YSOs) derived from Spitzer data, we find similarities as well as differences. In particular, the distribution of submm dust continuum emission is significantly more confined to the plane than the YSO distribution (FWHM of  $0.7^\circ$  and  $1.1^\circ$ , corresponding to mean physical scale heights of approximately 46 pc and 80 pc, respectively). While this difference may partly be caused by the large extinction from the dense submm cores, gradual dispersal of stellar distributions after their birth could also contribute to this effect. Compared to other tracers of Galactic structure, the ATLASGAL data are strongly confined to a narrow latitude strip around the Galactic plane.

## C.7 The onset of high-mass star formation in the direct vicinity of the Galactic mini-starburst W43

**Beuther, Tackenberg, Linz, Henning, Krause, Ragan, Nielbock, Launhardt, Schmiedeke, Schuller, Carlhoff, Nguyen-Luong, & Sakai (2012a)**

**Context.** The earliest stages of high-mass star formation are still poorly characterized. Densities, temperatures and kinematics are crucial parameters for simulations of high-mass star formation. It is also unknown whether the initial conditions vary with environment. **Aims:** We want to investigate the youngest massive gas clumps in the environment of extremely active star formation. **Methods:** We selected the IRDC 18454 complex, directly associated with the W43 Galactic mini-starburst, and observed it in the continuum emission between 70  $\mu\text{m}$  and 1.2 mm with Herschel, APEX and the 30 m telescope, and in spectral line emission of  $\text{N}_2\text{H}^+$  and  $^{13}\text{CO}$  with the Nobeyama 45 m, the IRAM 30 m and the Plateau de Bute Interferometer.

**Results:** The multi-wavelength continuum study allows us to identify clumps that are infrared dark even at 70  $\mu\text{m}$  and hence the best candidates to be genuine high-mass starless gas clumps. The spectral energy distributions reveal elevated temperatures and luminosities compared to more quiescent environments. Furthermore, we identify a temperature gradient from the W43 mini-starburst toward the starless clumps. We discuss whether the radiation impact of the nearby mini-starburst changes the fragmentation properties of the gas clumps and by that maybe favors more high-mass star formation in such an

environment. The spectral line data reveal two different velocity components of the gas at  $100 \text{ km s}^{-1}$  and  $50 \text{ km s}^{-1}$ . While chance projection is a possibility to explain these components, the projected associations of the emission sources as well as the prominent location at the Galactic bar - spiral arm interface also allow the possibility that these two components may be spatially associated and even interacting.

Conclusions: High-mass starless gas clumps can exist in the close environment of very active star formation without being destroyed. The impact of the active star formation sites may even allow for more high-mass stars to form in these 2nd generation gas clumps. This particular region near the Galactic bar - spiral arm interface has a broad distribution of gas velocities, and cloud interactions may be possible.

# D List of Figures

1.1	The GLIMPSE $8\ \mu\text{m}$ and MIPS GAL $24\ \mu\text{m}$ maps of IRDC 18223, named after the bright young stellar object IRAS 18223-1243. In both images, the extinction is clearly visible as dark patch in the center of the image. . . . .	6
1.2	Three color image of IRDC 18223, with $8\ \mu\text{m}$ , $24\ \mu\text{m}$ , and $870\ \mu\text{m}$ in blue, green, and red, respectively. . . . .	7
2.1	Schematic visualization of classification. . . . .	14
2.2	The figures show the clump definition as used in this paper (bottom row), compared to 'classical' $3\sigma$ spacing contour levels (top row). While the left most column shows the ATLAS GAL image of G11.11 with the clump definitions (red), the other columns show two profiles along the lines shown in the left panel ('cut A' and 'cut B'). The red lines indicate the clump borders. . . . .	15
2.3	Clump 67 overplotted on a MIPS GAL $24\ \mu\text{m}$ image. The clump definition are the red solid lines. Overplotted green asterisks are HII regions (Purcell & Hoare, 2010), and blue triangles are GLIMPSE Red Sources (Robitaille et al., 2008). . . . .	18
2.4	RGB image of the Galactic plane with Galactic latitude $l = 10^\circ$ to $20^\circ$ using GLIMPSE $8\ \mu\text{m}$ , MIPS GAL $24\ \mu\text{m}$ , and ATLAS GAL $870\ \mu\text{m}$ , respectively. Overplotted are CO contours from Dame et al. (2001). Starless cores are indicated as circles. . . . .	21
2.5	Histogram of the effective radius derived by CLUMPFIND for all clumps (black), for clumps with IRDC connection (hatched red area), only, and for clumps without any IRDC indication (solid green area). . . . .	22
2.6	Logarithmic histogram plot of the column density (lower x-axis) and flux (upper axis). While the black histogram represents the full sample of starless clumps, the hatched red and filled green histograms correspond to the near and far sample, respectively. (For details, cf. Sect. 2.5.) . . . . .	23
2.7	Artist impression of face-on view of the Milky Way by R. Hurt (SSC-Caltech) / MPIA graphic. Plotted on top are the starless clumps presented here with the distance according to the distance flag in Table 2.1. . . . .	25

2.8	The mass in solar masses is plotted over the distance in kpc. The solid line indicates the sensitivity/completeness limit of our clump extraction, which depends on the distance. The black filled dots represent sources with IRDC associations, and, therefore, the near distance is plotted. The red triangles represent the far solution of sources without an IRDC for which both a far and a near solution can be calculated; in addition, the green asterisks represent the corresponding near solutions. Blue diamonds show sources with such low velocities that only a single solution can be found in the given direction. The error bar in the top right corner indicates uncertainties of a factor of two for the masses and 0.5 kpc for the distance. . . . .	27
2.9	Effective radius in pc over the distance. Colors and symbols are as in Fig. 2.8. . . . .	28
2.10	Clump mass function with the near population plotted in black, the far population plotted in red. Both populations' high-mass tail have been fitted, with the fitting range indicated by the thick horizontal bars at the bottom. The power law indices are fitted to -2.1 and -2.4 for the near and far population, respectively. . . . .	29
2.11	MIPSGAL images of the three most massive starless clumps found in this survey, with (from left to right ) $7400 M_{\odot}$ , $4700 M_{\odot}$ , and $3000 M_{\odot}$ . Green contours are from ATLASGAL, red lines mark the borders of the clumps identified by CLUMPFIND. . . . .	31
2.12	Comparison of the fitted HiGal clump parameters to the evolutionary stage derived from star formation tracers. The left panel shows the temperature distribution of the clumps over the luminosity, the right panel displays the luminosity over the clump mass. The green diamonds represent the starless clumps, the blue squares are infrared bright clumps, and the red triangles indicate the presence of an HII region. . . . .	41
3.1	Parameter maps of the regions IRDC 18223, IRDC 18310, and IRDC 18454 mapped with the Nobeyama 45 m telescope, at top, middle, and bottom panel, respectively. The left panel of each row are the PACS $70 \mu\text{m}$ maps with the PACS point sources detected by Ragan et al. (2012) indicated by red circles, the blue numbers refer to the sub-mm continuum peaks as given in Table 3.3. The second panel displays the $\text{N}_2\text{H}^+$ column density derived from fitting the full $\text{N}_2\text{H}^+$ hyperfine structure. The third and fourth panels show the corresponding velocity and linewidth (FWHM) of each fit. For IRDC 18223, and IRDC 18310 the contours from ATLASGAL $870 \mu\text{m}$ are plotted with the lowest level representing 0.31 Jy, and continue in steps of 0.3 Jy. The contour levels for IRDC 18454 are logarithmic spaced, with 10 levels between 0.31 Jy and 31 Jy. The column density scale of IRDC 18223 is logarithmic. . . . .	55

- 3.2 Parameter maps of the regions G11.11, G15.05, and IRDC 18102, mapped with the MOPRA telescope. The left panel of each row are the PACS  $70\ \mu\text{m}$  maps with the PACS point sources detected by Ragan et al. (2012) indicated by red circles, the blue numbers refer to the sub-mm continuum peaks as given in Table 3.3. The second panel displays the  $\text{N}_2\text{H}^+$  column density derived from fitting the full  $\text{N}_2\text{H}^+$  hyperfine structure. The third and fourth panels show the corresponding velocity and linewidth (FWHM) of each fit. The green contours are from ATLASGAL  $870\ \mu\text{m}$  at 0.31 Jy, 0.46 Jy, and 0.61 Jy, continuing in steps of 0.3 Jy. The velocity resolution in the G15.05 map is smoothed to 0.4 km/s to improve the signal to noise and increase the number of detected  $\text{N}_2\text{H}^+$  positions. . . . . 56
- 3.3 Parameter maps of the regions IRDC 18151, IRDC 18182, and IRDC 18308, each mapped with the MOPRA telescope. The left panel of each row are the PACS  $70\ \mu\text{m}$  maps with the PACS point sources detected by Ragan et al. (2012) indicated by red circles, the blue numbers refer to the sub-mm continuum peaks as given in Table 3.3. The second panel displays the  $\text{N}_2\text{H}^+$  column density derived from fitting the full  $\text{N}_2\text{H}^+$  hyperfine structure. The third and fourth panels show the corresponding velocity and linewidth (FWHM) of each fit. The green contours are from ATLASGAL  $870\ \mu\text{m}$  at 0.31 Jy, 0.46 Jy, and 0.61 Jy, continuing in steps of 0.3 Jy. For IRDC 18151 the contours are MAMBO 1.2 mm observations, starting at 60 mJy in steps of 60 mJy. In all three maps the velocity resolution is smoothed to 0.4 km/s. 57
- 3.4 Parameter maps of the regions G19.30, G28.34, and G48.66, each mapped with the MOPRA telescope. The left panel of each row are the PACS  $70\ \mu\text{m}$  maps with the PACS point sources detected by Ragan et al. (2012) indicated by red circles, the blue numbers refer to the sub-mm continuum peaks as given in Table 3.3. The second panel displays the  $\text{N}_2\text{H}^+$  column density derived from fitting the full  $\text{N}_2\text{H}^+$  hyperfine structure. The third and fourth panels show the corresponding velocity and linewidth (FWHM) of each fit. The green contours are from ATLASGAL  $870\ \mu\text{m}$  at 0.31 Jy, 0.46 Jy, and 0.61 Jy, continuing in steps of 0.3 Jy. In all three maps the velocity resolution is smoothed to 0.4 km/s. . . . . 58
- 3.5 Plotted is the  $\text{N}_2\text{H}^+$  abundance ratio over the color index between  $70\ \mu\text{m}$  and  $160\ \mu\text{m}$ . Marked by green dots are pixels that lie within IRDCs. Overplotted with red Xs are all PACS sources that have been mapped. Blue crosses also have a  $24\ \mu\text{m}$  detection, while the light blue dots represent source that are saturated at  $24\ \mu\text{m}$ . . . . . 59
- 3.6 Spectra of IRDC 18454-4, labeled mm3 in Beuther & Sridharan (2007); Beuther et al. (2012a). While the dashed line shows the single component fit with the fitting parameters to the right, the solid line is the two component fit with its fitting parameters to the left. The given residuals are the results of the *minimize* task in *CLASS*. . . . . 63

- 
- 3.7 Plot of the  $\text{N}_2\text{H}^+$  linewidth versus the color index for the  $70\ \mu\text{m}$  over the  $160\ \mu\text{m}$  band. Marked by green dots are pixels that lie within IRDCs. Overplotted with red Xs are all PACS sources that have been mapped. Blue dots also have a  $24\ \mu\text{m}$  detection, while the pale blue dots represent source that are saturated at  $24\ \mu\text{m}$ . . . . . 64
- 3.8 Plot of the  $\text{N}_2\text{H}^+$  linewidth versus the dust column density. Marked by green dots are pixels that lie within IRDCs. Overplotted with red Xs are all PACS sources that have been mapped. Blue dots also have a  $24\ \mu\text{m}$  detection, while the pale blue dots represent source that are saturated at  $24\ \mu\text{m}$ . . . . . 65
- 3.9 Plot of the virial mass derived from the  $\text{N}_2\text{H}^+$  line width over the gas mass. The virial mass assumes a geometrical parameter of  $k=158$ , which is intermediate between  $k=126$  for  $1/\rho^2$  and  $k=190$  for  $1/\rho$ . The solid line indicates unity. . . . . 66
- 3.10 The left figure shows the profiles of the  $\text{N}_2\text{H}^+$  velocity of IRDC 18223, the right figure shows a velocity profile of IRDC 18454. The left panel of each figure shows the velocity map with contours from ATLASGAL on top (see also Fig. 3.1). The right and/or top panel show the velocity cuts along the lines marked on the velocity map. The stars mark the velocities of the clump peaks. . . . . 69
- 3.11 Left figure: Profile of the  $\text{N}_2\text{H}^+$  velocity of IRDC 18151; right figure: velocity profiles of IRDC 18308. The left panel of each figure shows the velocity map with contours from ATLASGAL on top (see also Fig. 3.3). The right and/or top panels show velocity cuts along the lines marked on the velocity map. The stars mark the velocities of the clump peaks. . . . . 70
- 3.12 Left figure: Profile of the  $\text{N}_2\text{H}^+$  velocity of the northern part of G11.11; right figure: Velocity profile of G19.30. The left panel of each figure shows the velocity map with contours from ATLASGAL on top (see also Fig. 3.2). The top and/or right panels show velocity cuts along the lines marked in the velocity map. The stars mark the velocities of the clump peak. . . . . 71
- 3.13 Profile of the  $\text{N}_2\text{H}^+$  velocity of G28.34. The left panel shows the velocity map with contours from ATLASGAL on top (see also Fig. 3.4). The top and right panels show velocity cuts along the lines marked in the velocity map. The stars mark the velocities of the clump peaks. . . . . 72
- 3.14 Comparison of optically thick  $\text{HCO}^+$  and  $\text{H}^{13}\text{CO}^+$  spectrum within G28.34. The black histogram shows the  $\text{HCO}^+$  spectrum, with the sum of the two independent Gaussian fits of the blue and red shifted component plotted in green. The straight green solid line indicates the algorithmically measured minimum of the emission dip, while the black horizontal line depicts the  $3\sigma$  level of the spectrum smoothed twice (not plotted here). The two black vertical lines show the measured  $T_{BD}$ , and  $T_{RD}$ , after subtracting  $T_D$ , here given by the  $3\sigma$ . The red spectrum is  $\text{H}^{13}\text{CO}^+$ , with the fit shown in blue. 77

- 3.15 Infall maps (gas velocity along the line of sight) of IRDC 18102, G15.05, G11.11, and G28.34. The left panels show the  $70\ \mu\text{m}$  maps with contours from ATLASGAL. The right panel shows the same contours on top of the gas infall maps, derived from the analysis of the  $\text{HCO}^+$  line profile in comparison to the  $\text{H}^{13}\text{CO}^+$  velocities. Note that the plotted infall velocities are upper limits, only. . . . . 78
- 4.1 An IRDC filament along the Galactic plane, spanning across from the *lower right* ( $18.45^\circ$ ,  $-0.20^\circ$ ) to the *upper left* ( $19.30^\circ$ ,  $-0.02^\circ$ ). The *top panel* shows a  $8\ \mu\text{m}$  *Spitzer* image and the color stretch is chosen to bring the IRDC to prominence. The *lower panel* presents the intensity weighted peak velocity (moment 1) map of the GRS  $^{13}\text{CO}$  data. Regions with velocities outside the  $43\ \text{km s}^{-1}$  to  $51\ \text{km s}^{-1}$  are clipped. The green contours are from ATLASGAL with contour levels at  $0.15\ \text{Jy}$  or  $3\sigma$ ,  $0.3\ \text{Jy}$ ,  $0.4\ \text{Jy}$ ,  $0.5\ \text{Jy}$ ,  $0.7\ \text{Jy}$ ,  $0.9\ \text{Jy}$ ,  $1.3\ \text{Jy}$ ,  $1.8\ \text{Jy}$ , and  $2.5\ \text{Jy}$ . The yellow ellipses indicate the bubbles as given in Simpson et al. (2012). . . . . 82
- 4.2 Three color image of the bubble connected to the long filament, MWP1G018980+00304, composed from the *Spitzer*  $3.6\ \mu\text{m}$ ,  $8\ \mu\text{m}$ , and  $24\ \mu\text{m}$  bands in blue, green, and red, respectively. White contours are from ATLASGAL (at  $0.3\ \text{Jy}$ ,  $0.4\ \text{Jy}$ ,  $0.5\ \text{Jy}$ ,  $0.7\ \text{Jy}$ ,  $0.9\ \text{Jy}$ ,  $1.3\ \text{Jy}$ ,  $1.8\ \text{Jy}$ , and  $2.5\ \text{Jy}$ ) for which the numbers denote the CLUMPFIND peaks, marked by the red circles. The yellow solid ellipse marks the bubble with interpolated bubble dimensions adopted from Simpson et al. (2012). The two arrows mark IRAS 18227-1227, and the massive proto-stellar object EGO G019.01-0.03. While the dashed orange boxes indicate the areas that have been mapped in  $\text{H}^{13}\text{CO}^+$  with the IRAM 30 m telescope, the gray dashed ellipse is drawn around the ATLASGAL contours connected to G18.93. . . . . 83
- 4.3 A multi-wavelength zoom on G18.93/m, the continuum peak connected to the prominent IR extinction feature. The panels are (*from left to right* in reading order):  $3.6\ \mu\text{m}$ ,  $8.0\ \mu\text{m}$ ,  $24\ \mu\text{m}$ ,  $70\ \mu\text{m}$ ,  $160\ \mu\text{m}$ ,  $250\ \mu\text{m}$ , from GLIMPSE, MIPS GAL, and HIGAL. The blue circles in the *bottom right* of each panel indicate the beam sizes, the green contours are from ATLASGAL (at  $0.3\ \text{Jy}$ ,  $0.4\ \text{Jy}$ ,  $0.5\ \text{Jy}$ ,  $0.7\ \text{Jy}$ ,  $0.9\ \text{Jy}$ ,  $1.3\ \text{Jy}$ ,  $1.8\ \text{Jy}$ , and  $2.5\ \text{Jy}$ ). The colors of the source marked by a red arrow in the first panel are not consistent with typical colors of young stellar objects (class 0/1) (Gutermuth et al., 2008; Robitaille et al., 2008). . . . . 86
- 4.4 Color coded map of the  $\text{H}^{13}\text{CO}^+$  emission in  $[\text{K km s}^{-1}]$  for the velocity regime  $42\ \text{km s}^{-1}$  to  $49\ \text{km s}^{-1}$  on the *left*, and  $56\ \text{km s}^{-1}$  to  $65\ \text{km s}^{-1}$  on the *right*. The black contours are from ATLASGAL with levels at  $0.3\ \text{Jy}$ ,  $0.4\ \text{Jy}$ ,  $0.5\ \text{Jy}$ ,  $0.7\ \text{Jy}$ ,  $0.9\ \text{Jy}$ ,  $1.3\ \text{Jy}$ ,  $1.8\ \text{Jy}$ , and  $2.5\ \text{Jy}$ . . . . . 89
- 4.5 Color coded temperature maps in  $[\text{K}]$  of G18.93, shown by the white contours from ATLASGAL (at  $0.3\ \text{Jy}$ ,  $0.4\ \text{Jy}$ ,  $0.5\ \text{Jy}$ ,  $0.7\ \text{Jy}$ ,  $0.9\ \text{Jy}$ ,  $1.3\ \text{Jy}$ ,  $1.8\ \text{Jy}$ , and  $2.5\ \text{Jy}$ ). The beam size is indicated in the *top right corner*. While the *top panel* presents the large-scale environment, the *bottom panel* zooms into our central IRDC region. . . . . 91

- 4.6 The ionized gas within and around the bubble. On top of the GLIMPSE  $8\ \mu\text{m}$  image, the red contours show the  $\text{H}\alpha$  emission from the SuperCOSMOS survey, the blue contours represent the MAGPIS 20 cm emission, and white contours show the ATLASGAL emission (at 0.3 Jy, 0.4 Jy, 0.5 Jy, 0.7 Jy, 0.9 Jy, 1.3 Jy, 1.8 Jy, and 2.5 Jy). The contour levels for the MAGPIS data are 0.002 Jy/beam, 0.003 Jy/beam, 0.004 Jy/beam, and 0.005 Jy/beam. The arrow indicates the peak position of the HII region identified by Lockman (1989). . . . . 93
- 4.7 HI VGPS spectrum of G18.93/m in black with the GRS  $^{13}\text{CO}$  spectrum in red on top. The strong absorption feature of G18.93/m at  $\sim 45\ \text{km s}^{-1}$  in the HI spectrum agrees very well with the  $^{13}\text{CO}$  signature. The smooth line indicates the 3rd order fit to the HI spectrum that has been used to subtract the “continuum”. (For details see text.) . . . . . 97
- 4.8 A layered structure of the hydrogen phase. On top of the  $8\ \mu\text{m}$  GLIMPSE image in gray, the blue contours represent the MAGPIS GPS 20 cm data, the red contours show a measure of the atomic hydrogen at velocities of G18.93 from the VGPS 21 cm line (for details see the text), and the green contours are the cold dust from the ATLASGAL survey, hence the molecular hydrogen. The dashed lines are to guide the eye and indicate the peak positions of the different data. The orange arrow points to  $8\ \mu\text{m}$  excess emission at the edge of the dense gas. The top left circle indicates the beam size of the VGPS data, while the bottom circle shows the beam of ATLASGAL. In this figure, MAGPIS is smoothed to the resolution of ATLASGAL. The contour levels for the GPS 20 cm data are 2 mJy/beam, 3 mJy/beam, 4 mJy/beam, and 5 mJy/beam, and for the ATLASGAL  $870\ \mu\text{m}$  emission 0.3 Jy, 0.4 Jy, 0.5 Jy, 0.7 Jy, 0.9 Jy, 1.3 Jy, 1.8 Jy, and 2.5 Jy. . . . . 98
- 4.9 Profiles of mid-IR data along the cut indicated by the yellow arrow in the *left panel*. While the center of the cut in the *right panel* is G18.93/m, its upper end is chosen to be towards the potential ionizing sources. The different colored profiles in the right panel are of increasing wavelength, starting with  $8\ \mu\text{m}$  at the top going to  $870\ \mu\text{m}$  at the bottom. The intensities are not to scale, but adopted to fit in the panel. The green vertical line indicates the position of the ATLASGAL continuum peak, the yellow arrow corresponds in direction and length to the arrow in the *left panel*, in which the background image is a GLIMPSE  $8\ \mu\text{m}$  image with ATLASGAL contours (at 0.3 Jy, 0.4 Jy, 0.5 Jy, 0.7 Jy, 0.9 Jy, 1.3 Jy, 1.8 Jy, and 2.5 Jy) on *top*. . . . . 99
- 4.10 Profile of  $^{13}\text{CO}$  (black), ATLASGAL (red), and  $\text{H}^{13}\text{CO}^+$  (dashed blue) along the two yellow lines shown on top of the  $870\ \mu\text{m}$  map in the left plot. The position of the peak of HII emission is indicated within both profiles (*right*) and the map (*left*). The *left panel* also gives the two main IRDC peaks. The blue asterisks indicate the position of the IRAS source (lower position) and UKIDSS source (higher position). The green contours from ATLASGAL are at 0.3 Jy, 0.4 Jy, 0.5 Jy, 0.7 Jy, 0.9 Jy, 1.3 Jy, 1.8 Jy, and 2.5 Jy. . . . . 100

- 4.11  $\text{H}^{13}\text{CO}^+$  spectra at positions indicated by bold asterisks in the *top panel*. The positions are chosen to lie along the connection between the UKIDSS near-IR source and the ATLASGAL peak position, with the first spectra at the peak of the GLIMPSE  $8\ \mu\text{m}$  emission. From *left to right* the clumps are G18.93/1, G18.93/m, and G18.93/4. The upper spectra are at positions closer to the ionizing source. Where possible we fitted one, two, or three gaussian components to the spectra. The fitted line widths and peak positions are given in the spectra. . . . . 102
- A.1 MIPS GAL  $24\ \mu\text{m}$  image with ATLASGAL contours on top. Starless clumps are marked with a red asterisk. The numbers correspond to the global identifier given in Table 2.1. . . . . 131
- B.1 Parameter maps of G13.90 mapped with the Nobeyama 45 m telescope. The left panel is the PACS  $70\ \mu\text{m}$  map with the PACS point sources detected by Ragan et al. (2012) indicated by red circles, the blue numbers refer to the sub-mm continuum peaks as given in Table 3.3. The second panel displays the  $\text{N}_2\text{H}^+$  column density derived from fitting the full  $\text{N}_2\text{H}^+$  hyperfine structure. The third and fourth panel show the corresponding velocity and linewidth (FWHM) of each fit. The contours from ATLASGAL  $870\ \mu\text{m}$  are plotted with the lowest level representing 0.31 Jy, and continue in steps of 0.3 Jy. . . . . 146
- B.2 Parameter maps of IRDC 18385 mapped with the Nobeyama 45 m telescope. The left panel is the PACS  $70\ \mu\text{m}$  map with the PACS point sources detected by Ragan et al. (2012) indicated by red circles, the blue numbers refer to the sub-mm continuum peaks as given in Table 3.3. The second panel displays the  $\text{N}_2\text{H}^+$  column density derived from fitting the full  $\text{N}_2\text{H}^+$  hyperfine structure. The third and fourth panel show the corresponding velocity and linewidth (FWHM) of each fit. The contours from ATLASGAL  $870\ \mu\text{m}$  are plotted with the lowest level representing 0.31 Jy, and continue in steps of 0.3 Jy. . . . . 146
- B.3 Parameter maps of IRDC 18306 mapped with the MOPRA telescope. The left panel is the PACS  $70\ \mu\text{m}$  map with the PACS point sources detected by Ragan et al. (2012) indicated by red circles, the blue numbers refer to the sub-mm continuum peaks as given in Table 3.3. The second panel displays the  $\text{N}_2\text{H}^+$  column density derived from fitting the full  $\text{N}_2\text{H}^+$  hyperfine structure. The third and fourth panel show the corresponding velocity and linewidth (FWHM) of each fit. The contours from ATLASGAL  $870\ \mu\text{m}$  are plotted with the lowest level representing 0.31 Jy, and continue in steps of 0.3 Jy. . . . . 147

---

B.4	Parameter maps of IRDC 18337 mapped with the MOPRA telescope. The left panel is the PACS 70 $\mu\text{m}$ map with the PACS point sources detected by Ragan et al. (2012) indicated by red circles, the blue numbers refer to the sub-mm continuum peaks as given in Table 3.3. The second panel displays the $\text{N}_2\text{H}^+$ column density derived from fitting the full $\text{N}_2\text{H}^+$ hyperfine structure. The third and fourth panel show the corresponding velocity and linewidth (FWHM) of each fit. The contours from ATLASGAL 870 $\mu\text{m}$ are plotted with the lowest level representing 0.31 Jy, and continue in steps of 0.3 Jy. . . . .	147
B.5	Integrated line intensities of G11.11. The top left panel shows the PACS 70 $\mu\text{m}$ map of the region, with contours from ATLASGAL 870 $\mu\text{m}$ on top. The contour levels start with 0.31 Jy, 0.46 Jy, and 0.61 Jy, and continue in steps of 0.3 Jy. The other panels show the integrated intensities of $\text{HCO}^+$ , $\text{H}^{13}\text{CO}^+$ , $\text{N}_2\text{H}^+$ , HNC, and HCN, as labeled. . . . .	148
B.6	The figure is the same as Fig. B.5, but here plotting G15.05. . . . .	149
B.7	The figure is the same as Fig. B.5, but here plotting IRDC 18102 . . . . .	149
B.8	The figure is the same as Fig. B.5, but here plotting IRDC 18151. . . . .	150
B.9	The figure is the same as Fig. B.5, but here plotting IRDC 18182. . . . .	150
B.10	The figure is the same as Fig. B.5, but here plotting IRDC 18306. . . . .	151
B.11	The figure is the same as Fig. B.5, but here plotting IRDC 18308. . . . .	151
B.12	The figure is the same as Fig. B.5, but here plotting IRDC 18337. . . . .	152
B.13	The figure is the same as Fig. B.5, but here plotting G19.30. . . . .	152
B.14	The figure is the same as Fig. B.5, but here plotting G28.34. . . . .	153
B.15	The figure is the same as Fig. B.5, but here plotting G48.66. . . . .	153

# E List of Tables

2.1	Properties of starless clumps. The full table is available in the Appendix A.1.	20
2.2	Overview of typical clump properties for near and far clumps. The origin of the uncertainties is explained in Appendix A.1.	24
2.3	Lifetimes of starless clumps calculated for different sets of parameters. Estimates are calculated using different Milky Way star formation efficiencies for opacities for both the cold ISM (Hildebrand 1983, H83) and dense but cold regions (Ossenkopf & Henning 1994, OH94).	30
3.1	Observed IRDCs.	47
3.2	Summary of the different dust data used, and the corresponding properties. The column densities have been calculated under the assumptions given in Sec. 3.2.6 for 20 K. The last column is the column density corresponding to the lowest emission contour used within <i>CLUMPFIND</i> .	49
3.3	870 $\mu\text{m}$ ATLASGAL clump properties.	52
3.3	continued.	53
4.1	CLUMPFIND decomposition of dust clumps extracted on ATLASGAL 870 $\mu\text{m}$ map.	90
A.1	Properties of starless clumps.	122
A.1	continued.	123
A.1	continued.	124
A.1	continued.	125
A.1	continued.	126
A.1	continued.	127
A.2	Regions listed below were omitted during the classification due to saturation of the 24 $\mu\text{m}$ data.	130

# Acknowledgments

In context of this thesis I'm deeply indebted especially to two people. On the one hand my beloved wife Nina. From the decision to go to Heidelberg to probably a few month after the defense, we had and have to agree on plenty of compromises. Thank you for that and a lot more (you know best...) On the other hand I have to thank Henrik Beuther. He was not only a superb supervisor, but also a great guy to discuss science, life, children, and everything else. My thesis would not have been so enjoyable with a different supervisor.

I want to thank Thomas Henning for giving me the opportunity to write this thesis and pay me, my family, and my travel during that time. He co-supervised this thesis and the scientific discussions with him brought-up fruitful input, new ideas, and structure.

I want to thank Rene Plume for his invitation to Calgary. I had a good time in Canada, and it gave me the opportunity to invite my son Jonas to his first overseas travel.

I want to thank Simon Glover for co-refereeing this thesis, and Stephanie Hansmann-Menzemer to complete my thesis committee. I thank the Max-Planck Research School (IMRPS) for Astronomy and Cosmic Physics for their financial support.

I thank Katharine and Paul for reading and correcting my English on parts of this thesis.

I thank all my co-authors for their contributions science chapters.

The co-authors of the two published chapters and I wish to thank the anonymous referees for their careful reading and helpful comments. They substantially enhanced both the science and appearance of the papers.

Before the long list of technical acknowledgments I want thank all members of the MPIA for the productive and highly encouraging working environment.

This publication is partially based on data acquired with the Atacama Pathfinder Experiment (APEX). APEX is a collaboration between the Max-Planck-Institut für Radioastronomie, the European Southern Observatory, and the Onsala Space Observatory. This work is based, in part, on observations made with the Spitzer Space Telescope, which is operated by the Jet Propulsion Laboratory, California Institute of Technology under a contract with NASA. This research has made use of the NASA/ IPAC Infrared Science Archive, which is operated by the Jet Propulsion Laboratory, California Institute of Technology, under contract with the National Aeronautics and Space Administration. PACS has been developed by a consortium of institutes led by MPE (Germany) and including UVIE (Austria); KU Leuven, CSL, IMEC (Belgium); CEA, LAM (France); MPIA (Germany); INAF-IFSI/OAA/OAP/OAT, LENS, SISSA (Italy); IAC (Spain). This develop-

ment has been supported by the funding agencies BMVIT (Austria), ESA-PRODEX (Belgium), CEA/CNES (France), DLR (Germany), ASI/INAF (Italy), and CICYT/MCYT (Spain). SPIRE has been developed by a consortium of institutes led by Cardiff University (UK) and including Univ. Lethbridge (Canada); NAOC (China); CEA, LAM (France); IFSI, Univ. Padua (Italy); IAC (Spain); Stockholm Observatory (Sweden); Imperial College London, RAL, UCL-MSSL, UKATC, Univ. Sussex (UK); and Caltech, JPL, NHSC, Univ. Colorado (USA). This development has been supported by national funding agencies: CSA (Canada); NAOC (China); CEA, CNES, CNRS (France); ASI (Italy); MCINN (Spain); SNSB (Sweden); STFC (UK); and NASA (USA). This publication makes use of molecular line data from the Boston University-FCRAO Galactic Ring Survey (GRS). The GRS is a joint project of Boston University and Five College Radio Astronomy Observatory, funded by the National Science Foundation under grants AST-9800334, AST-0098562, & AST-0100793. The International Galactic Plane Survey is supported through a Collaborative Research Opportunities grant from the Natural Sciences and Engineering Research Council of Canada. The National Radio Astronomy Observatory is a facility of the National Science Foundation operated under cooperative agreement by Associated Universities, Inc. The UKIDSS project is defined in Lawrence et al. (2007). UKIDSS uses the UKIRT Wide Field Camera (WFCAM; Casali et al. 2007) and a photometric system described in Hewett et al. (2006). The pipeline processing and science archive are described in Irwin et al. (2008) and Hambly et al. (2008). We have used data from the 7th data release.